Characterization, Modeling and Control of the μWalker

This thesis has been completed in partial fulfillment of the requirements of the Dutch Institute of Systems and Control (DISC) for graduate study.

The research described in this thesis was undertaken at the Control Engineering Department of the Faculty Electrical Engineering, Mathematics and Computer Science at University of Twente, the Netherlands. This work was performed within the framework of STW project TES.5178, called Micro Scanning Probe Array Memory.

Printed by Wöhrmann Print Service, The Netherlands

ISBN: 90-365-2398-2

CHARACTERIZATION, MODELING AND CONTROL OF THE μWALKER,

— A MICRO ACTUATOR FOR DATA STORAGE —

PROEFSCHRIFT

ter verkrijging van de graad van doctor
aan de Universiteit Twente, op gezag van
de rector magnificus, prof. dr. W.H.M. Zijm,
volgens besluit van het College van Promoties,
in het openbaar te verdedigen op
vrijdag, 22 september 2006
om 15.00 uur

door
Mihail Pătraşcu
geboren op 14 september 1978
te Boekarest, Roemenië

Dit proefschrift is goedgekeurd door:

Prof. Dr. Ir. S. Stramigioli, promotor

L'expérience est la source unique de la vérité:
elle seule peut nous apprendre quelque chose de nouveau;
elle seule peut nous donner la certitude.

Experience is the unique source of truth:
only she can learn us something new
and give us certainty.

H. POINTCARÉ, LA SCIENCE ET L'HYPOTHÈSE

Summary

We, people, always want more. Ever increasing demands for computing performance and storage capacity call for disruptive technologies of digital data storage. An additional fact is the miniaturization of many consumer electronics devices that are present on the market. The combination of these two ingredients has raised discussions whether for instance the hard-disk storage principle could be partially substituted by new technologies, which better meet the desired present and future specifications.

μSPAM (Micro Scanning Probe Array Memory) is one of the projects related to data storage, where we seek to build a prototype of a probe storage read and write device. The work presented in this thesis is on two-dimensional positioning in the read/write system.

The first necessary step was to characterize the μWalker, an existing micro electro-mechanical actuator, as this is considered to be the basic stone for the positioning system in μSPAM.

Based on the knowledge obtained by measurements, a number of physical models were developed and simulated. These models are able to predict the effects of varying actuator dimensions and or material properties on the overall performance. Such predictions are very interesting, because they accelerate the development of the positioning system considerably.

Based on simulation results, a range of new devices were designed and tested. Many of them are based on the original μWalker actuator and now include electrostatic sensors, 2D motion or other features.

The control of such MEMS actuators is a totally different topic, with lots of opportunities for future research. Real time closed-loop control in MEMS proves a hard task, especially the integration of sensors, actuators and the control system in the small volume which is required. Both open- and closed-loop control ideas are worked out and the open-loop case is validated.

Samenvatting

De toenemende vraag naar meer rekencapaciteit en dataopslag opent perspectieven voor nieuwe technologieën voor opslag van digitale data. Een bijkomend verschijnsel is de miniaturisatie van de meeste consumenten-electronica produkten. Deze twee factoren hebben geleid tot vraagtekens omtrent de toekomst van de harde schijf technologie en tot het thema of er niet wellicht andere dataopslaprincipes als betere kandidaten uit de bus kunnen komen.

Één van de projecten die zich met dit vraagstuk bezighoudt, is μSPAM (in het Engels: Micro Scanning Probe Array Memory), waarbij we ernaar streven een prototype te ontwerpen van een dataopslagmedium dat gebaseerd is op het probe storage concept. In dit proefschrift wordt vooral ingegaan op het positioneren van het lees- en schrijfsysteem in twee dimensies.

De eerste noodzakelijke stap binnen dit onderzoek was het karakteriseren van een bestaande micromotor, genaamd de μWalker. Dit is tevens het basisontwerp voor het tweedimensionaal positioneren binnen μSPAM.

Een aantal fysische modellen werden vervolgens ontwikkeld, gebaseerd op de kennis die uit de karakterisatieprocedure voortvloeide. Met deze modellen kunnen we de prestaties van actuatoren onderzoeken, alvorens deze te fabriceren. Zulke voorspellingen, vanuit de modellering en simulatie, kunnen het zoeken naar een optimale actuator behoorlijk vergemakkelijken en versnellen.

De volgende stap was het ontwerpen van nieuwe actuatoren. Vele van hen zijn gebaseerd op de oorspronkelijke μWalker en hebben een toegevoegde waarde door aanwezigheid van sensoren of het kunnen bewegen in twee richtingen.

Voor wat betreft de regeltechniek van MEMS actuatoren voor μSPAM, het blijkt redelijk ingewikkeld om een real-time lus te sluiten met de beschikbare actuatoren. Bovendien is het integreren van de sensoren, actuatoren en het regelsysteem op zo’n schaal problematisch. Er worden twee manieren van regelen behandeld, open en gesloten lus. Het open-lus regelsystem is tevens gevalideerd.

Contents

Nomenclature

Abbreviations and Acronyms

AFM	Atomic Force Microscopy/Microscope
CCD	Charge-Coupled Device, technology used for camera chips
CMOS	Complimentary Metal-Oxide Semiconductor
DV	Digital Video
FPGA	Field Programmable Gate Array
FPS	Frames Per Second
GPS	Global Positioning System
LPCVD	Low-Pressure Chemical Vapor Deposition
LSQ	Least-Squares Method
MESA+	Institute for Nanotechnology at the University of Twente
MEMS	Micro-electromechanical Systems
MMIS	Magnetic Media Information Services
MFM	Magnetic Force Microscopy, used for imaging the magnetic field gradient and its distribution above the sample surface resolution in the order of a few nanometer
MST	Microsystems Technology
PDA	Personal Digital Assistant
PVR	Personal Video Recorder
RAMAC	Random Access Method of Accounting and Control, the first computer disk storage system invented by IBM in 1956
RPM	Rotations Per Minute

SEM	Scanning Electron Microscope, device which scans the surface of an object by an electron beam; the reflected electrons contain information about the texture (nanometer resolution)
μSPAM	Micro Scanning Probe Array Memory, acronym for both the project and the future probe storage prototype
STW	Stichting Techniek en Wetenschap
TEM	Transmission Electron Microscopy, where resolutions down to atoms can result from bombarding a thin material and analyzing the electrons passing through the sample (sub nanometer resolution)
VHDL	Very High Speed Integrated Circuit Hardware Description Language
μWalker	code name for the electrostatic stepper motor used in the μSPAM project for positioning

Constants

E_{pSi}	160.10^9	Pa	Young's modulus of poly silicon
ϵ_0	$8.85419 \cdot 10^{-12}$	$A.s/V.m$	Dielectricum constant or permittivity in vacuum
ϵ_{Si_RN}	7.6	—	Dielectric permittivity of silicon nitride
λ_{BpSi}	45.3	$W/(m.K)$	Thermal conductivity of boron-doped poly silicon
ν_{BpSi}	0.01-0.1	$\Omega.m$	Specific resistance of boron-doped poly silicon
μ_0	$4\pi \cdot 10^{-7}$	$V.s/(A.m)$	Permeability in vacuum (from [4])
ρ_{pSi}	2330	kg/m^3	Material density of poly silicon

Units and Scales

GB	gigabyte, generally 1024MB
Gb	gigabit or 2^{30} bits, where 8 bits $= 1$ byte
MB	megabyte or $2^{20} = 1.048.576$ bytes of data

Chapter 1

Introduction

The target of this first chapter is to warm up the reader with some background facts about data storage. The state of the art is shortly enlighten, followed by a micro introduction to the immense world of MEMS. The motivation of this work is encapsulated into the thesis objective. This chapter ends with an outline of the remaining chapters.

1.1 Background on data storage

Data storage has been around for thousands of years. As far as we can tell, it all begun with drawings on walls and stones, by means of which people could pass on their experience to their descendants. This art is still practiced by many people even at present times. Unfortunately some of them tend to imitate our ancestors too literally, by drawing on street walls and transportation systems.

In recent years, the necessity to store information has increased exponentially. As soon as digital storage media became available, about 50 years ago, the amount of stored data exploded. According to [88], with the advent of the internet people now have access to more information than the total written data that was existent on the globe one century ago [88]. One thing remains the same, however: data must be stored and retrieved in a safe way. At present, the most cost effective data storage medium fabricated in mass production is the hard disk. It has been around for five decades and is clearly the most established digital data storage technology available.

Nowadays the dimensions of electronics devices tend towards miniaturization and indeed storage media are a part of it. The hard disk architecture has followed the trend by introducing the Micro-drive®, a one-inch sized hard disk [3].

A remarkable development in the consumer products is that most digital video camera producers still rely on magnetic storage media and more specifically on digital tapes. Most manufacturers have been waiting a long time for the chance to get rid of the tape-based DV[1] and introduce a more compact storage device that reduces the actual devices to pocket-size dimensions. Indeed, in January 2005 JVC presented the first consumer cam-corder based on a micro-drive storage medium. On a 4Gb micro-drive, between 60 and 300 minutes can be recorded, depending on the preset recording quality. The storage medium is of course interchangeable and can be plugged into computer card readers for fast data access.

The adventure of JVC is not a consequence of random effects. From the prospects of Fig. 1.1, it is clearly visible that the hard-disk will tend to enter the consumer products market aggressively during the next few years.

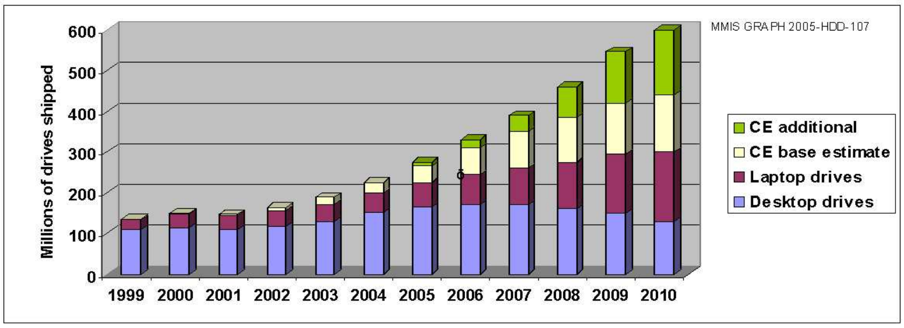

Figure 1.1: Expected growth rates for hard-disk drives as consumer applications gain dominance (Printed with permission of MMIS).

In Fig. 1.1, ”CE base estimate” represents the sell estimations made in July 2004, while ”CE additional” was added one year later (July 2005) due to accelerated developments in the small-sized hard-disk industry, of which the micro-drive is the most outstanding example.

If we may believe the prognosis shown above, we are at the edge of a break-through in consumer electronics drives, and in 2010 the market volume should approach the PC hard-disk market (composed of laptop and desktop drives).

With time, a few other technologies have emerged, which partly compete with the hard-disk – especially in consumer electronics. Amongst them is the Flash (non-volatile) memory, which is presently used in memory sticks. Producing large flash memory devices in order to compete with the hard disk is too expensive and therefore not feasible for the foreseeable future. This technology is furthermore restricted by the relatively short device life time. On the other hand, flash memory has interesting performance characteristics. Especially the access time and the power consumption are better than for the hard-disk. The main niche for flash memory is consumer electronics, where

---

[1] For this and all other acronyms, please see Nomenclature.

reduced storage capacities are acceptable provided limited volume, like for instance digital still cameras, MP3 players and alike. The expected market trends for Flash-RAM show the same increasing tendency as is the case of the hard-disk industry.

The gap in storage capacity between the compact, yet more expensive flash and the somewhat larger hard-disk is closing slowly but surely. The gap comprises the future portable PDA's, digital still cameras, PVR's, portable video game consoles, the upcoming generation of mobile phones and GPS automotive/traffic applications. This gap is seen as the main target for novel storage devices based on techniques like for instance probe storage.

Lower cost per MB, lower power consumption, and high data density are necessary, but not sufficient constraints imposed by the state of the art technologies of today. Due to the inertia of the hard disk technology, it becomes very hard for non-established technologies to earn a part of the market pie. The only way for a new technique like probe storage to compete, is by providing large scalability, lower price per item, higher data density, and above all, a large, for the foreseeable future unconstrained scalability. The scalability issue is intrinsically solved in the probe storage concept, and this is one of the base columns on which this technology resides, along with high density and small format. This also explains why probe storage truly is a disruptive technology, and not just an innovation of the current trends.

Although no probe storage devices exist on the market today, it is more than probable that sooner or later they will be there for the evident reason that the projected data density is at least an order of magnitude higher than that of hard-disk technology, where thermal instability of bits plays an increasing role.

1.2 State of the art compact storage media

With small exceptions, IBM was and still is the driving force behind the research of non-volatile data storage technologies. After the first computer disk storage system in 1956, the 305 RAMAC, IBM continued to be the research and market leader of magnetic recording media, bringing to light numerous inventions and innovations across decades [11].

One of their latest mass-market based inventions is the micro-drive, actually the smallest magnetic data storage device in the world. By September 2005, Seagate shipped the first 8GB micro-drives on the market, Hitachi following shortly thereafter with a $10GB$ version. At dimensions of 40x30x5mm^3 and a weight of only $14g$, it approaches the memory cards available today. The $20GB$ version is due to be shipped in 2006, according to Hitachi – requiring a data density of $230Gbit/inch^2$. Such a high density will be reached with perpendicular recording [70].

When looking at probe storage, which is a relatively new concept by itself, it also has first been proposed by IBM under code name Millipede (Fig. 1.2)

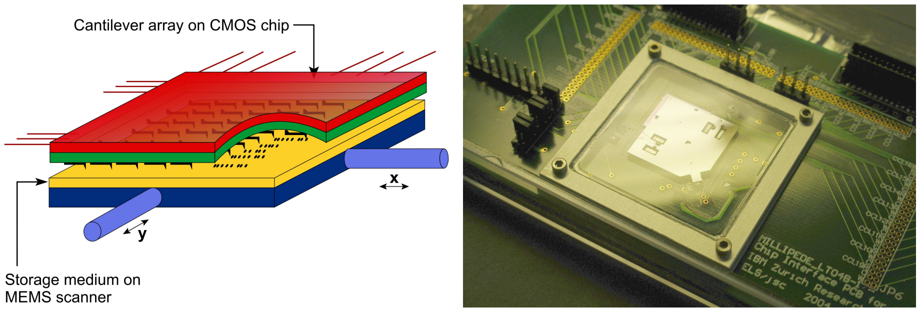

Figure 1.2: The millipede in the conceptual stage (left) and a recent prototype (right). Courtesy of IBM Zurich Research Laboratory. Unauthorized use not permitted.

[12, 15, 22, 52, 44, 97]. The concept of probe storage will be elaborated to a larger extent in Chapter 2.

The μSPAM project of which this thesis is a part of, has many similarities with the Millipede concept. Both projects incorporate a large number of read and write heads, named data tips or probes. Each head owns a certain area with data bits exclusively. The estimated prototype dimensions of the two projects have been chosen to fit into the SD format (24x32x2,1 mm^3). The projected overall specifications in terms of performance are similar too (for the μSPAM, see Chapter 2).

At present some differences can be distinguished. For instance the positioning system differs as well as the medium type, which is magnetic in μSPAM and a polymer in the Millipede project. It has been shown that a polymer medium permits data densities beyond the range of magnetic storage.

On the other hand, the μSPAM prototype theoretically shows more parallelism due to a different actuation principle for read/write. Whereas the Millipede only features one 2D magnetic actuator for all the data on the device, the μSPAM contains about 100 independently working tiles that work in parallel. This parallelism can be used to limit power consumption according to read/write load, to increase redundancy, to scale effectively towards more parallelism[2] and to reduce the amount of data loss in case of a failing actuator.

Other projects related to probe storage techniques include Resistive Probe Storage supported by Samsung and several Korean Universities [42, 46], the Ultra-High-Density Data Cache Project running at Carnegie Mellon University and Intel [12, 41], the Planar Electrostatic Micromover by Hewlett Packard [49] and Nanochip's Probe-Array Storage Chips [22].

For the sake of backwards-compatibility and effective market entrance, most

---

[2] For the Millipede, scaling up towards more parallelism means that the mass increases leading to larger seek times, which is inconvenient.

of the projects mentioned above aim at delivering a prototype which has standard interface and dimensions, like the SD card format.

1.3 Micro-electromechanical Systems

The concept of probe storage would not have been feasible without the advent of micro-electromechanical systems, or MEMS[3]. The IMST 2005 White book [3] emphasizes the need for MEMS micro-actuators to improve tracking in storage devices.

Generally, MEMS refers to systems with structures between about 0.5 and 500 μm that involve both electronic and mechanical elements and which perform one or more tasks like for instance actuation, sensing and display.

Fabrication of micro-devices relies on lithographic techniques borrowed from the microelectronics industry, which implies the use of thin-film fabrication methods. Nowadays not only silicon serves as bulk material but also glass, quartz, ceramic, plastic and metal are used. The results are 2D shapes, which have been extruded in 3D [43, 79, 32, 72].

Regarding the aggregation of electronics, sensors, actuators and packaging into one system, there are two possibilities. The subsystems can either be assembled in a late stadium of the fabrication process, or they can be integrated one into the other as soon as possible. For instance, depending on the microfabrication possibilities at hand, both the micro-mechanical actuators and the CMOS electronics could be realized on top of each other during one single set of fabrication processes in the clean-room. At present this method is hardly used due to the complexity of the processes involved. The sub-parts in the μSPAM project are only assembled in a late stadium of the fabrication. In fact, most of the probe storage projects recognize and incorporate assembly as a very important step during fabrication.

The number of applications where MEMS devices are used, has been expanding very fast during the last couple of years [43]. According to market analysis [79], the top sales of MEMS includes accelerometers and pressure sensors for the automotive and medical industries, ink-jet printer heads, displays and disk heads for the consumer market. One concrete example of overwhelming market success are MEMS microphones. With more than 100 million microphones sold worldwide in 2005 – which is about 5% of the total market – and an expected 450 million to be sold in 2008 [82].

In the MEMS research field, there are many other devices searching their way to the market. Invasive drug delivery, surgery [68], genomic research, defensive and offensive weaponry [66] are only a few examples. As a concrete example, Fig. 1.3 represents a gear system, which can be driven by a motor functioning on the bimetal effect up to 250.000 RPM.

---

[3] In Europe, the acronym MST is used instead of MEMS; strictly spoken, MST is more inclusive.

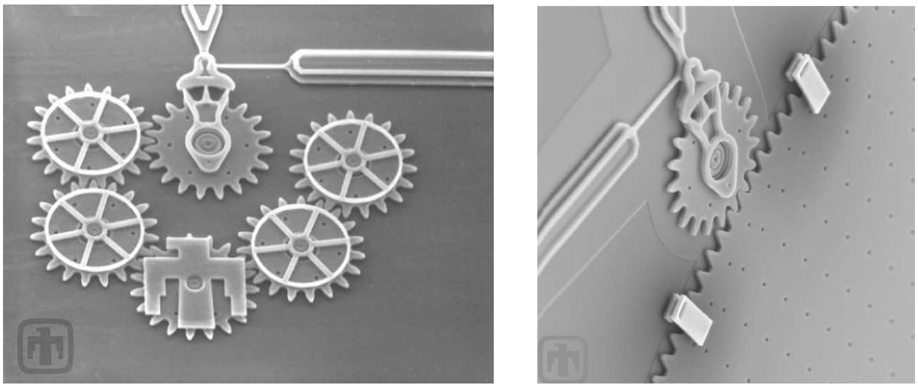

Figure 1.3: Gear wheels actuated by bimetal actuators. Courtesy of Sandia National Laboratories, SUMMiT^{TM} Technologies http://www.mems.sandia.gov.

Probe storage is just a small part of this ever increasing set of applications. The field is a descent of atomic force microscopy (AFM) and it can be used for non-volatile mass storage and other more dedicated tasks, like parallel AFM scanning and molecular or even atomic manipulation. More about AFM will follow in Chapter 2.

Let us first recognize that on one side the variety of MEMS actuators is huge. Even steam micro-engines and micro pumps can be found in literature. On the other side, as to now no probe storage standard has been established yet. Instead, there are a number of dispersed projects. An important question arises here: Is such a specially designed MEMS actuator like the μWalker really comparable to other dedicated actuators with different target specifications? Especially when we compare the μWalker with actuators from projects with different applications than probe storage, this question seems ill-posed.

A range of surveys [13, 18, 28, 31] on electrostatic micro motors are available but again depending on the application, different sets of target specifications hold. To give a parallel, imagine the usefulness of comparing a magnetic coil of a hard-disk head with a coil used in a relay for a mini trains railway system. Different applications clearly lead to a different optimization for each device. This makes straight comparison between actuators subjective and without purpose in the view of the author.

More likely, it seems useful to compare devices at a project level and concentrate on standardization of performance specifications like is the case with the hard-disk industry. The reader who is still interested in a straight comparison between the μWalker and other MEMS actuators, is referred to the recent survey presented in Appendix A of [73].

1.4 Thesis objective

Within the μSPAM project, there are a number of key issues, each of them tackled by one or more researchers working in the project. More about this follows in Chapter 2. One of these issues in μSPAM is about reading and writing, especially about the actuator which moves the medium in two dimensions with respect to the read and write heads.

For the sake of performance, displacements must be performed with velocities in the order of a few cm/s, for a range of about 100μm on both axes and with very high accuracy, typically under 30nm. Fulfilling these specifications is the task of the μWalker, a MEMS based micro actuator initially designed and fabricated by E. Sarajlic, a former member of the μSPAM project [73, 74, 75]. The predecessor of the μWalker was developed by N. Tas and is presented in [86].

The μWalker is the main subject of research treated in this thesis. During the research presented in this work, a number of improvements have been proposed, some of which are listed hereunder. During initial measurements [75], it turned out that further characterization and optimization of the μWalker was necessary, before an aggregation of all sub-parts of μSPAM could become possible.

For achieving the positioning velocity and accuracy required, a closed-loop control system is very valuable, if not necessary. The integration of the actuator with a proper sensor for real-time displacement measurements turned out to be somewhat involved in practice. This is because of limitations in the fabrication process. Therefore, a number of models of the actuator were required to make controller design possible in software. In this way, both device optimization and controller design could be done in software, until the sensor integration is ready. Increased decoupling of the x and y displacements was also an issue to be taken into account during the development of new prototypes. A new type of 2D displacement device is presented. Last but not least, the walking range of the original μWalker prototype was too limited compared to the target range of about 100 μm for each axis. From the above, the thesis objective can be stated as follows:

"Develop and validate a model of the μWalker which can be used for prototype optimization and controller design. Furthermore, design new prototypes which better match the target specifications of the μSPAM project and pave a way for closed-loop control."

1.5 Outline

Chapter 2 provides the reader with some basic facts about the μSPAM project in general, and especially the prototype design specifications to be met. One version of the micro-actuator called μWalker is shortly introduced, thereby choosing a general set of dimensions from an existing specimen. This set constitutes the starting point of the research presented here.

The following chapter is on characterization based on measurements. The first part is a concise introduction to matters of scaling in physical systems. After presenting the practical setup, a diversity of measurements are elaborated in order to aquire useful information for the models and to increase insight in the microscopic phenomena taking place during the movements.

Chapter 4 is about modeling and simulation of the μWalker. Results are presented which help optimize the micro-actuator with respect to the tasks it has to fulfill in a probe storage system. Additionally, models predict the power consumption per step.

Design optimization is the topic of Chapter 5, with an emphasis on dimensions and performance. New types of devices are presented here, which are based on the basic μWalker introduced in Chapter 2.

The first steps towards tracking control are presented in Chapter 6. Again, actuator performance plays a key role here, with total system performance as underlying target. Various results on open- and closed loop control are elaborated. Finally, Chapter 7 concludes the thesis with a general review, discussion and final conclusions to be drawn from this research.

Chapter 2

The μSPAM Project and the μWalker

Before starting to dig into the worlds of modeling simulation, characterization and control, this introductory chapter on the μSPAM project and the μWalker is meant to acquaint the reader with the concept of probe storage and some basics on the actuator under study, the μWalker. The introductory section on μSPAM was also been presented in [53, 54, 98].

2.1 Probe Storage and Atomic Force Microscopy

The concept of probe storage was derived from AFM and therefore a short introduction of the Atomic Force Microscopy is useful before proceeding. AFM is a relatively novel method to measure surface roughness down to the atomic scale. According to Fig. 2.1, the surface to be observed – in this case an array of data points – is being literally scanned by a probe with a tip, whose curvature is in the order of only a few nm.

AFM measurement methods can be divided in contact and non-contact types. With contact AFM, the probe touches the surface very softly. The deflection of the probe as a result of texture and roughness of the underlying surface is then sensed with a reflected laser beam and a detector. The information from the detector is then conditioned, analyzed and stored. What results is a three dimensional reconstruction of the surface under observation. AFM can be used both for conducting and non-conducting, hard and soft media. In practice, very soft materials are often being scanned with other techniques (MFM, SEM, TEM, etc).

For inventing the AFM, Gerd Binnig and Heinrich Rohrer – both working with the IBM Research Laboratory in Zurich – received the Nobel Prize[1]

---

[1] In fact the Nobel Prize was shared with Ernst Ruska, who invented the first electron micro-

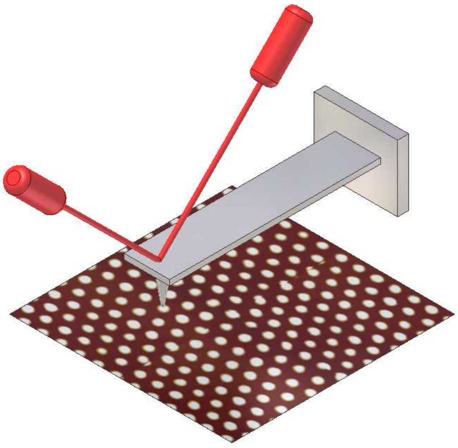

Figure 2.1: Sketch of an AFM scanning setup.

in Physics in 1986. The idea of probe storage emerged in the eighties, when several researchers were investigating the possibility to use the AFM for other purposes than only surface scanning.

While probe storage can be seen as a proud descendant of the AFM, it is hard to blur the stamp that IBM has put on this technique. We need to generalize the concept in order to give a correct definition of probe storage in a more broad sense than merely the implementation of IBM, the Millipede.

Altogether, according to the author, probe storage is a technology that makes several nanometer wide indentations or other local modifications to the medium properties, with the scope of storing information in a compact, safe and cheap way. Data channel parallelism is widely implemented, with virtually unlimited prospects for further increase.

2.2 μSPAM – Idealism or perspective?

The essential target of the μSPAM project is to investigate the feasibility of a novel storage device based on probe recording [1, 5]. Within μSPAM, the following sub-groups can be distinguished: MEMS fabrication [73, 74, 75], probe development [71, 92, 93, 94], tip-sample approach [38], modeling, simulation and control [40, 60, 56, 57], magnetic medium [47] and power dissipation and performance related issues [54].

Figure 2.2 gives an impression of the final prototype, which includes some of the vital components needed for probe storage: many (thousands of) probes,

---

scope in 1933; Dr. Binnig and Dr. Rohrer both got 25% each, while Ernst Ruska received 50%.

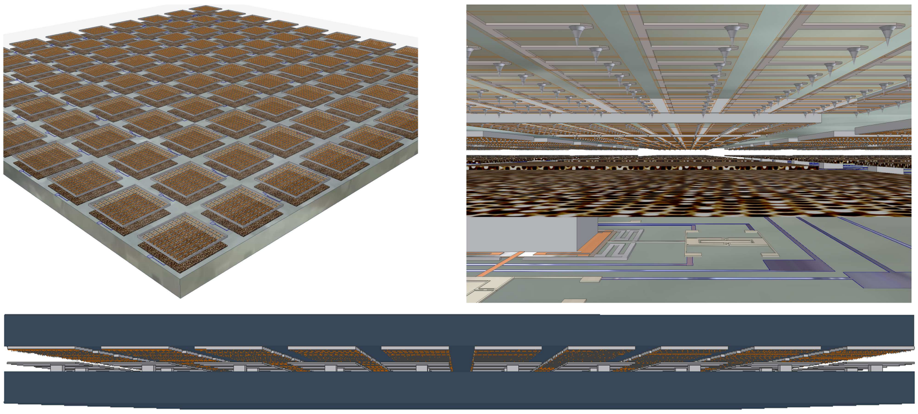

Figure 2.2: Overview of the μSPAM device, consisting of data clusters arranged in an array.

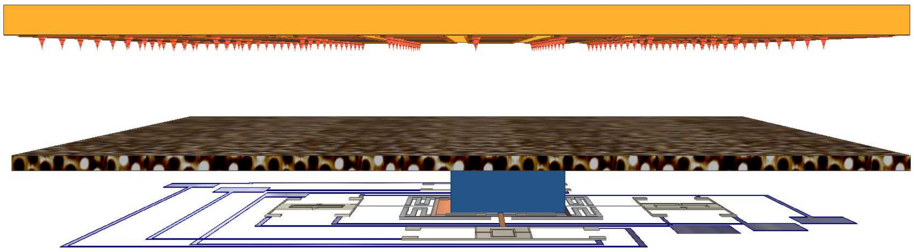

Figure 2.3: Close-up of one cluster, showing the probe array frame (on top) and the magnetic medium attached to the positioning device underneath.

medium sliders with very high density and MEMS motors for actuation. In this case 100 identical clusters can move independently from each other, for increased parallelism and reduced access time. The dimensions proposed do not exceed 15x15x2mm^3, packaging included. Wiring for actuation and data channels was left out of the picture for the sake of clarity.

The clusters consist basically of a 2D MEMS actuator for x-y positioning, a 100μm x100μm magnetic medium attached above the actuator and an array of read/write probes (Fig. 2.3). Each of the probes owns a part of the magnetic medium exclusively, for reading and writing.

The probes are actuated individually or in small clusters in the vertical direction and do not touch the magnetic medium during read/write cycles, unlike the contact AFM method. This is necessary for taking into account the surface curvature and roughness of the magnetic medium.

Table 2.1: General design specifications for μSPAM.

Property	Target
scanning speed (mm/s)	> 2
scanning precision (nm)	≈ 10
seek velocity (mm/s)	> 40
power consumption read/write (W)	< 1
power consumption (standby) (μW)	1
dimensions ($mm \cdot mm \cdot mm$)	$15 \cdot 15 \cdot 2$
total capacity ($GBytes$)	> 2
max. data rate ($Mbit/s$)	$100 - 300$
access time (ms)	< 2.5

The number of actuated clusters varies in time according to the demands. Decoupling the clusters has the advantage that we can optimize performance with respect to power dissipation.

Moreover, some clusters are able to read, while other write at the same time, such that bandwidth in principle does not drop if the data of the two processes is on different clusters. Thus, all probes fixed on the same cluster follow the same planar motion, while the vertical motion is controlled individually for each probe. Provided a very flat medium with asperities not greater than a few nm, vertical position tracking can be done for a number of probes at the same time to reduce complexity and interface or wiring bottlenecks.

By starting from the project proposal targets and projecting into the future, Table 2.1 can be obtained (see also [5]). The information in this table forms the basic set of specifications which is used further on in this work.

2.3 MEMS actuation for μSPAM

According to the above, it is not hard to see that the performance of the two dimensional MEMS actuator directly influences the total system performance. The minimum desired performance of the MEMS actuator to be used in μSPAM follows directly from Table 2.1. This issue will be elaborated in more depth in Chapters 3 and 4.

2.3.1 Harmonica, shuffle motor and comb drive

Initially, there were three types of devices available to choose from in μSPAM, namely the harmonica drive, shuffle motor and comb drive[2]. All three can be

---

[2] The harmonica and shuffle were designed and fabricated by E. Sarajlic, the comb drive by A. A. Kuijpers.

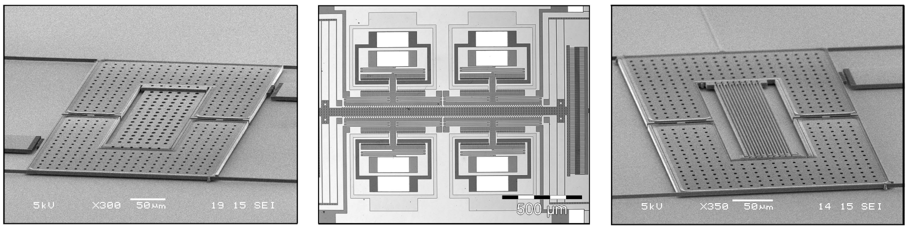

Figure 2.4: Left: Shuffle motor. Center: Comb drive. Right: Harmonica drive.

Table 2.2: Some details about the three micro actuator candidates for μSPAM.

Properties	Shuffle	Comb drive	Harmonica
dimensions (mm)	0.41 x 0.29	2 x 1,5	0.44 x 0.29
max. velocity (mm/s)	3.6	125	0.6
life time (expressed in m)	1500	not measured	not measured
force delivered (mN)	1.72	0.001	1.7
input signals (1D/2D)	4/6	3/5	4/6
step size, if applicable (nm)	45	n.a.	8
input voltage (V)	$\leq$55	30	$\leq$ 70
travel range for 1D (μm)	±70	± 30	±100

produced at the MESA+ Clean-room of the University of Twente and are electrostatically actuated (Fig. 2.4).

Table 2.2 describes certain characteristics of one typical prototype from each of these three classes of actuators. The information was collected from [35, 73].

Looking back at the probe storage concept in general and at μSPAM in particular reveals that device size, delivered force and traveling speed, range and life time are the most essential features when considering such a MEMS actuator for positioning in a probe storage system. The number of actuator signals, the step size and the input voltage are less vital, yet important factors for the sake of the overall system complexity, positioning accuracy and low power supply voltage which is necessary in mobile applications.

Seen from this perspective and based on the information gathered in Table 2.2, the shuffle motor turns out to be the best option of the three. The somewhat lower velocity is compensated for by the force delivered. Also scalability towards lower actuation voltages is more favorable for the μWalker.

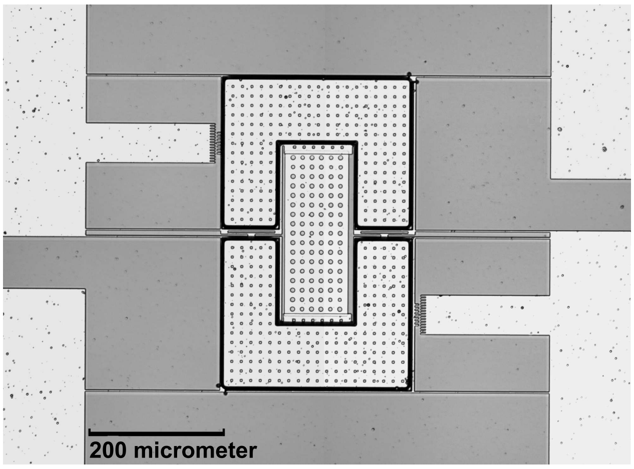

Figure 2.5: Microscope snapshot of the basic μWalker.

2.4 A light on the μWalker

Now that the shuffle motor has been justified as the proper device for μSPAM, it is useful to have a closer look at the working principle and dimensions. A number of design details are enlighten, which will become more relevant later on.

Electrostatic actuation, plate bending and stick-slip are the basic phenomena which are used for the propulsion of the motor under consideration. Basically, when a voltage is applied to one leg, this part snaps to the ground due to the temporal electro-mechanical instability created by the voltage potential. As the leg touches the surface, the electrostatic force keeps the leg from shifting in either direction – of course, up to a certain limit, as will be concluded in Chapter 3. Two factors influence this limit, namely leg area and the applied leg voltage. The legs can move freely when not actuated and they stick to the underlying surface when actuated. As we will see later on, this effect can be modeled roughly by a stick-slip phenomenon – however strictly spoken the actual dynamics is more complex due to vertical displacement of the structure when entering or leaving the stick region.

When a potential is applied to the plate, it bends and if the voltage is sufficient, the plate snaps to the ground. Certain conditions for the electro-mechanical instability in the plate apply, as will be shown in Chapter 4. By this bending, the Euclidian distance between the ends of the plate decreases and as a result the distance between the two legs decreases a fraction. This is exactly the size of one step.

Now, by properly snapping and releasing both legs and the plate, displacement can be obtained in both directions. The μWalker basic motion can be compared to a wide range of feet-less creatures moving over a solid surface, like for instance worms and sea lions.

2.4.1 Basic walking principle

There are a variety of ways to produce steps, only the basic walking principle is considered in this chapter. Step size, applied force, repeatability and maximum velocity all depend on the actuation chosen. Although the basic walking principle is described in detail in literature [57, 73], the essentials are reviewed for the sake of completeness.

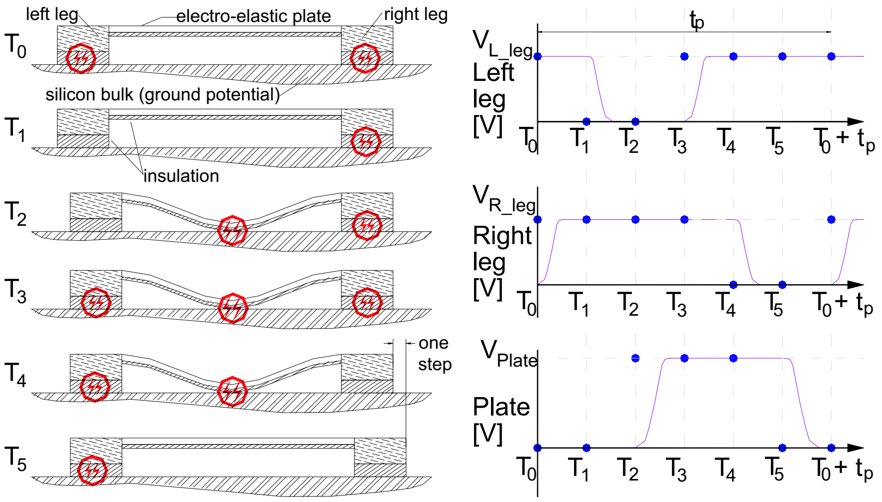

(a) Schematic illustration of the motion (b) Typical actuation for one step.

Figure 2.6: One basic step is produced by six actuation sequences.

The sequence in Fig. 2.6 is used for making one step to the right. It starts with both legs actuated (T_0). The left leg is released, and directly thereafter the plate is attracted to the ground, thus decreasing the distance between the legs by exactly one step (T_1 and T_2). In the fourth sub-sequence the free leg is again clamped, followed by releasing of the other leg (T_3 and T_4). Finally, releasing the plate and actuating both legs again brings the system back to the first sub-sequence (T_5 and T_0). At this point, one step to the right has been completed. Actuating the sequence in the opposite way (in the left part of Fig. 2.6(a) from T_5 down to T_0) yields a step in the opposite direction, namely to the left. In practice, the walking sequence resides on repetitively performing

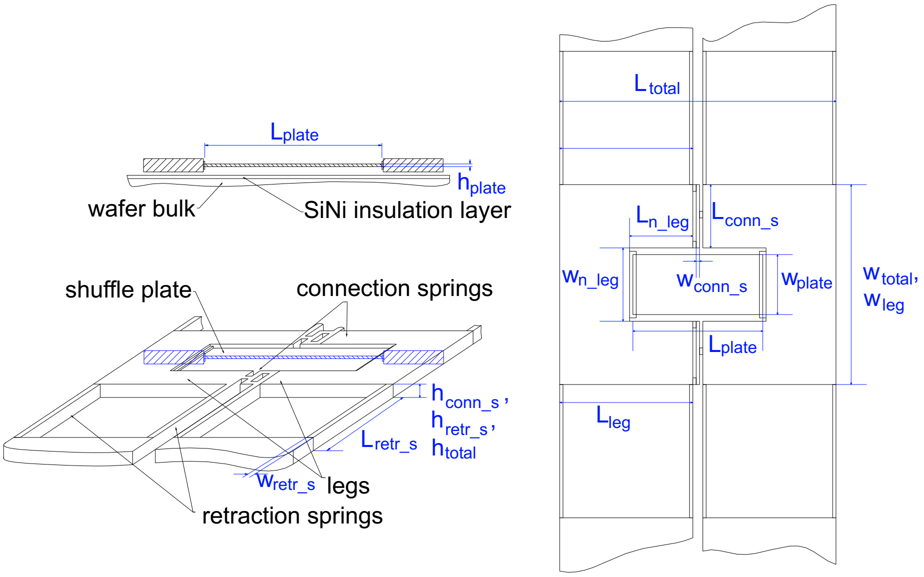

Figure 2.7: Sketch with μWalker dimensions. Please see Tab. B.2 for the explicit values.

steps at a high rate. Deliberately complex tracking tasks can be achieved by combining the sequence presented above with other actuation sequences for holding the device at one position, going back to rest and making smaller steps than the unit step as presented in Fig. 2.6(a). Appendix E goes into more detail regarding signal generation, especially towards higher level actuation which is needed in future FPGA designs for feedback control.

2.4.2 Dimensions and the mechanical structure

As remarked in the Introduction, the μWalker presented in this section is chosen to have the basic set of dimensions from which improvements and control will take place in later chapters[3]. Hence unless otherwise stated, this configuration is used as the basic set further on in this work.

The most relevant dimensions of the μWalker are sketched in Fig. 2.7 and summarized in Appendix B, Table B.2.

The mechanical structure of the device includes a number of beams, which act as springs in both the vertical and horizontal direction.

The eight retraction springs in Fig. 2.7 have a dual purpose. At least three of the springs are necessary for electrical connection of the bond pads and the de-

---

[3] Please remind that this device was first designed and fabricated by Edin Sarajlic from the TST Group.

vice sub-parts, namely the two legs and the center plate. The other five springs have been added to complete the mechanical symmetry and to increase the vertical stiffness of the structure, making it more robust and increasing step repeatability. Thus, the retraction springs keep the sub-parts suspended from the substrate, unless the parts are voltage activated and stick to the surface (Chapter 3). Due to this fact, the contact area of a moving leg is strictly spoken reduced to less than ten contact points. Actually when looking at the free leg, only the array of bumps which are most close to the connection springs may still touch the surface, due to the high vertical stiffness of the connection springs and due to the fact that the other leg is clamped (see next subsection).

The function of the small connection springs which connect both legs is mainly to align the two legs. Also, a small amount of potential energy is stored in the first part of the step making, when the plate is attracted to ground; this energy is released in the last sequence of the step, when the plate is released. Some concepts to improve symmetry, reduce planar rotation of the legs and increase the connection springs potential energy are presented in Chapter 5.

2.4.3 Bumps for stiction reduction

At this point it is useful to present some more details about the material properties at the contact surface between the μWalker parts and the walking surface, as they are crucial for characterizing the capacitance of the loads and also later on for a proper understanding of the motion of each part during one step.

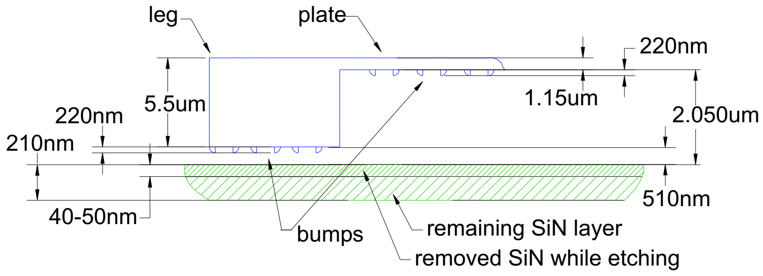

Figure 2.8: Close-up sketch of the plate and legs shape.

Figure 2.8 shows the most significant materials and dimensions. These values were either derived from the process document (Appendix J) or otherwise estimated from SEM pictures. In this picture, the bumps play a central role for many reasons, most important of which is that they reduce the contact area between the part and the walking surface. The Van der Waals forces which are intrinsically present due to quantum mechanical effects between the atoms of the two contact surfaces, hardly play a role. Reference [17] reports that Van der Waals forces fall rapidly with increase in distance, and estimates a true area of contact of only 1% of the apparent area[4], which implies a Van der Waals force reduced to 1% of the initial. The assumption that these forces do not play a role in the current design becomes even more evident if one considers that the apparent contact area of the parts with bumps have been drastically reduced from the initial size to only a few contact points which are relatively hard and brittle (silicon nitride). Furthermore, [17] mentions that gaps greater than $100nm$ do not lead to any significant Van der Waals effects. When the μWalker parts are not actuated or actuated under pull-in, the distance between the parts and surface the surface is about 300-$500nm$ at least, such that these forces do not play any significant role (Fig. 2.8).

Also surface tension can be reduced by decreasing the amount of humidity in the surroundings of the device, or by applying a flow of (dry) nitrogen over the device, which keeps moisture away.

There seems to be an optimum of the humidity rate, however. A too low percentage of humidity and the lack of charge carriers in the insulators (bumps and walking surface) slow down the process of neutralizing or removing the static charge induced by friction. More about this will be mentioned in Section 3.3, page 40.

As an anticipating remark regarding scaling and electrostatics (Chapter 4), a further advantage of the electrostatic forces applied in the system is that – unlike other types of forces at the micro scale, like for instance Van der Waals forces – they do not depend very much on the surface roughness, but only on the distance between the part and the wafer bulk. So the contact area is reduced considerably, but the electrostatically applied force is not influenced much by the texture. These thoughts will be confirmed by extensive measurements on motion reproducibility later on in Chapter 3.

The conclusion to be drawn here is that phenomena which become important at an atomic scale such as Van der Waals forces and surface tension do not play a distinguishing role in the design of the μWalker, mostly due to the bumps applied on the parts and because of the hard walking surface.

2.4.4 Fabrication process

Surface micro machining and vertical trench isolation are the basic ingredients for the fabrication of the devices under study. A number of design and fabrication details will be presented, which greatly affect the performance of the electrostatic actuators.

The kernel of the process document, Appendix J, describes the processing steps for the fabrication of the wafer used in Chapters 3 and 5. It relies on work presented in [73].

---

[4] The apparent area is here the area in case the two surfaces would have been completely smooth.

Increasing the vertical stiffness of the retraction springs would be beneficial for the actuation speed and step reproducibility. Unfortunately, as the device material (poly silicon) is deposited – a process which takes time and is prone to errors – it is not feasible to increase the thickness of the device (and especially of the retraction beams) more than at present. Put simply, the present fabrication process limits the vertical stiffness of the structure, which in turn limits the actuator performance and the coupling of the two perpendicular axes for the two dimensional case. Using bulk micro machining technology would help in this case, however the processes needed are not well-known at the time of writing. As usual, new technologies give novel opportunities to the present electrostatic actuators [73].

Silicon nitride is used at the contact points between the actuators and the wafer bulk because nitride has attracting properties such as very good electrical insulation (more than $4M\Omega$ for one bond) and high material hardness for low friction and reduced wear. The concept of using hemispherical or circular bumps in order to reduce the contact surface beyond photolithography resolution has been reported earlier in the MEMS literature [16, 83, 100].

As a last remark concerning the bumps, the reader is being warned against misconceptions found in some references in literature. For instance [64] is – to the knowledge of the author – the first book to shortly describe the μWalker and its walking principle. In Subsection 7.2.8, the authors of [64] claim: ..."*it is not desirable to have the elastic plate make contact with the substrate*" and that hence the ..."*steps of the motor are limited by the pull-in phenomenon*". Regarding the first citation, it may be clear that due to the integrated circular bumps, the contact surface is drastically reduced, so that unintended stiction hardly plays a role. This fact also follows from measurements which are subject of Chapter 3. Moreover, actuating the μWalker above the pull-in voltage of the plate turns out to be the only way to have repeatable micrometer large displacements with nanometers accuracy, which makes the second statement untrue! Thus, in the best interpretable way, the information mentioned in [64] is outdated.

The walking surface consists of a $210nm$ thick silicon nitride layer deposited by LPCVD. The surface smoothness should be smaller than about $10nm$, as it is of critical importance for correct operation. Furthermore, the thickness of this layer could influence the performance of the actuator, as will be shown in Chapter 4.

2.5 Concluding remarks

The μSPAM project has been shortly reviewed, together with some basics about probe storage and AFM. One part of the μSPAM project is an electrostatic actuator, the μWalker, which is the main topic of the research. Some basic properties of the device have been presented to acquaint the reader with the motion concept. Several fabrication related topics concluded this part.

In the following chapter, the measurement setup is shown, followed by thorough characterization of the μWalker by means of diverse measurements. As will soon become clear, some of the most important parameters needed later on in models could only be estimated from indirect measurements.

Chapter 3

Setup and characterization of the μWalker

Scaling of actuators is the first topic of the chapter, with an accent on MEMS actuators and down-scaling. Then, the setup for μWalker characterization is shortly introduced, which includes the procedure for taking measurements. Interpretation of a number of results needed for modeling and simulation is the main part of the chapter. Parts of the work presented in this chapter can be found in [57, 58, 61].

3.1 Scaling and MEMS actuators

3.1.1 General

Laws and relations between elements at different scales is a very general topic, which extends from biology to astronomy. Whereas in life sciences scaling is of descriptive nature mainly to investigate basic differences between species at different scales [43], in MEMS design the question often posed is, which types of forces become predominant at different scales. For instance, the effects of inertia are less important compared to the human scale ($1m$). As mass and therefore inertia goes with third power of the dimension, the mass moment of inertia scales with fifth power! Even for the μWalker which has total dimensions up to $0.5mm$, gravity does not play a role any more compared to the other forces. To the contrary, other effects such as viscous drag, surface tension and quantum effects (Van der Waals forces, see page 19) do become dominant with decreasing scale. As a general rule, surface effects become relatively more important than body or volume forces during miniaturization. A consequence is that thermal isolation and storage become more difficult, whereas cooling or radiation is very efficient. This is because heat is stored in a mass and thus volume, which decreases fast with decreasing dimensions. Ref. [64] introduces dimensionless factors to generalize the scaling problem. We will constrain ourselves here to present a comparison between the different forces acting at the micro and nano scale.

It must be mentioned that energy sources and energy conversion methods are of great interest for successfully and efficiently performing the required tasks. The most interesting micro devices are those, whose useful energy content is relatively high, compared to inertia and other forces opposing the motion. Because energy sources scale down rather poorly (Table 3.1), most micro actuators receive the required energy from a macro scale power supply, like is the case with our μWalker.

3.1.2 Basic magnetic and electrostatic conversion principles

Amongst the available energy buffer types at micro scale, one electrical and one magnetic energy case are shortly considered, each with a predefined shape. Note that the topology of the device does affect the scaling laws, so the scaling rules should be used with care.

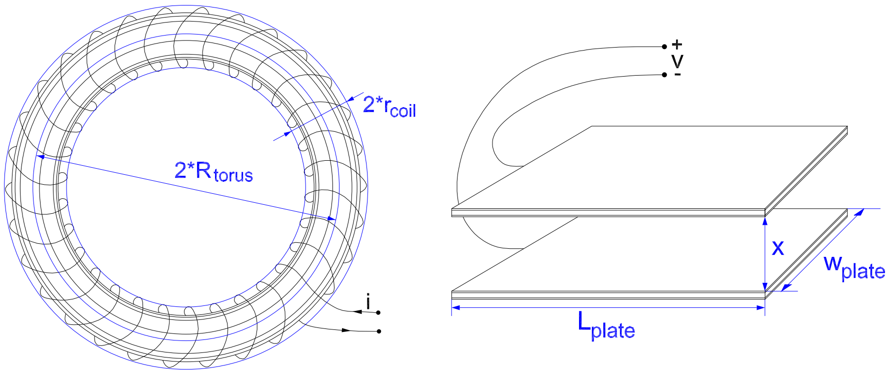

(a) Conductive coil winded around a torus.

(b) Two conductive plates with different potentials.

Figure 3.1: General topologies of magnetic and electrostatic actuators.

Starting with the magnetic domain, assume a solenoid coil like in Fig 3.1(a). If the toroid sectional area is defined as $A_{coil} = \pi r_{coil}^2$, with r_{coil} the sectional radius of the toroid and $R_{torus} >> r_{coil}$, then the magnetic force between the winding and the torus inside the winding can be expressed as in Eq. 3.1.

$$F_{magn} = \frac{A_{coil}\lambda^2}{2\mu}, \tag{3.1}$$

where $\mu = \mu_0 \mu_r$ is the magnetic permeability of the solenoid material and λ is the magnetic field density:

$$\lambda = L\,i\,, \qquad L = \frac{\mu n^2 A_{coil}}{2\pi R_{torus}} \tag{3.2}$$

The number of windings is denoted by n. Thus, Eq. 3.1 becomes:

$$F_{magn} = \frac{\pi r_{coil}^2 \left(\mu n^2 \pi r_{coil}^2 i\right)^2}{2\mu \left(2\pi R_{torus}\right)^2} \Rightarrow F_{magn} = \frac{\mu \pi n^4 r_{coil}^6 i^2}{8R_{torus}^2} \tag{3.3}$$

Consider now a variable α representing the order of the spatial dimension of F_{magn}, which is written in exponents of the space dimension γ. Then ψ gives information about scalability effects:

$$\psi_{F_{magn}} \propto \frac{[\gamma^6]}{[\gamma^2]} \propto [\gamma^4]$$

This means, that a coil with ten times smaller dimensions reduces the electromagnetic force by 10.000. Note that implicitly, we assume that the current does not need to scale down, such that the current density can be deliberately high. If the current density cannot be decreased further, then the spatial dimension in the order of $\psi \approx \gamma^6$ for this configuration. So for decreasing dimensions, the magnetic force generated with a solenoid will be less and less effective.

The second example is about a couple of identical electrostatic plates. A potential difference is applied, which implies an attractive force $F_{el.st.}$ between the plates:

$$F_{el.st.} = \frac{\epsilon_0 \epsilon_r A_{plate} V_{in}^2}{2x^2}, \tag{3.4}$$

where A_{plate} is the plate area, V_{in} the applied voltage, x the distance between the plates and ϵ_0, ϵ_r the dielectric constant and dielectric material coefficient, respectively. In line with fig. 3.1(b), if we consider the electrostatic force between two capacitor plates as given by Eq. 3.4, then the spatial dimensionality is zero:

$$\psi_{F_{el.st.}} \propto \frac{[\gamma^2]}{[\gamma^2]} \propto [\gamma^0]$$

In words, scaling does not influence the electrostatic force. Analogue to the solenoid example, this derivation holds only in the case that the input, in this case V_{in} can remain constant for smaller structures. In reality however, as the inter-plate distance decreases, the breakdown voltage of the insulator structure is reached (see also the discussion on page 55). Decreasing the voltage linearly with the scale is a solution, which then yields a scale factor of $[\gamma^2]$ – whence the varying factor in Tab. 3.1.

3.1.3 Scaling rules

Before showing Table 3.1 with the main quantities of interest for this work, the effect of scaling on a number of additional physical quantities are presented below. The mass of an object scales with its volume, i.e.:

$$m = \rho_m L_m w_m h_m \Rightarrow \psi_m \approx [\gamma^3]$$

The inertial force described by Newton's Second Law is one dimension higher, $\psi \approx [\gamma^4]$:

$$F_m = m \cdot a \Leftrightarrow F = m\frac{d^2x(t)}{dt^2} \Rightarrow \psi_{F_m} \approx [\gamma^3] \cdot [\gamma^1] = [\gamma^4]$$

In general, the moment of inertia of a mass rotating around an axis can be written as:

$$J = \int\int\int r^2 \mathrm{dm} \Rightarrow \psi \approx [\gamma^2] \cdot [\gamma^3] = [\gamma^5]$$

The torque τ_m is defined as the product of the force applied and the radius between the center of rotation and the point where the force is exerted:

$$\tau_m = F_m \cdot r_m \Rightarrow \psi \approx [\gamma^4] \cdot [\gamma^2] = [\gamma^6]$$

In line with Chapter 4, page 92, bending of a thin beam-like spring with length L, width w, height h and Young's modulus E in the linear range goes with the square of the dimension scale, just like the axial force (on page 92):

$$\begin{aligned}
F_{bending} &= ky, \quad k = \frac{16\,E\,w\,h^3}{L^3} \Leftrightarrow F_{bending} = \frac{16E\,w\,h^3\,y}{L^3} \Rightarrow \\
\psi_{F_{bending}} &\approx \frac{[\gamma^4]}{[\gamma^3]}[\gamma^1] = [\gamma^2] \\
F_{axial} &= E\,A\frac{\delta L}{L}, \quad A = w\,h \Rightarrow \\
\psi_{F_{axial}} &\approx [\gamma^2] \cdot \frac{[\gamma^1]}{[\gamma^1]} = [\gamma^2]
\end{aligned}$$

Heat dissipation scales with surface area ($\psi \approx [\gamma^2]$), while heat storage depends on the volume ($\psi \approx [\gamma^3]$), so that conservation of heat at small scale becomes problematic. The same holds for other types of energy storage like fuel cells; the dependency on volume size makes it unattractive for miniaturization:

$$\psi_{en\_storage} \approx [\gamma^3]$$

From [43], the surface tension (or capillary forces) scale as $\psi \approx [\gamma^1]$, which makes it possible for various insects to walk on water, for instance.

Table 3.1: Scaling factors relevant for the μWalker.

Physical quantity	Spatial dimension α ($\psi \approx \gamma^{\alpha}$)	Unit
Van der Waals force	-1	N
surface tension (capillary)	1	N
electrostatic force (see page 25)	0-2	N
spring bending force	2	N
spring axial force	2	N
heat dissipation	2	$\approx m^2$
heat conservation	3	$\approx m^3$
energy storage	3	$\approx m^3$
mass	3	kg
inertial force	4	N
moment of inertia	5	$kg.m^2$
torque	5	$N.m$
magnetic force (see page 25)	4-6	N

According to [17], the (always attracting) Van der Waals force between a sphere and a plane can be described by:

$$F_{vdW} = \frac{hr}{8\pi z^2},$$

where h is the (materials dependent) Lifshitz-van der Waals constant and z is the separation between the two surfaces. Here, we can see that as the the scale decreases, the force becomes more important:

$$\psi_{F_{vdW}} \approx \frac{[\gamma^1]}{[\gamma^2]} = [\gamma^{-1}]$$

This force can become dominant at distances between roughly 5 and $100nm$.

3.1.4 Concluding remarks

While electromagnetic actuators are limited by the maximum current density through the supply wires in order to form the electromagnetic field, the electrostatic ones are constrained by the break-down voltage properties of the material(s) between the electrode plates (see later on in this chapter). Altogether, the electrostatic force is a surface force, while for magnetic forces, the actuator volume is of importance. This fact makes fabrication of electrostatic actuators more convenient with the surface micro machining techniques available today.

Slightly different scaling exponents are found in literature [43], where the applied voltage or current is assumed to depend linearly with one spatial dimension, but in the general case this does not need be so. Anyway, the gap of two spatial orders in γ between the electrostatic force and the magnetic force remains valid.

Table 3.1 also shows why Van der Waals forces should hardly matter for the μWalker design: the spatial dimension is negative, which means that only at very small distances will their effect be present. But as the surface of the μWalker parts was made ’rough’ on purpose by adding a texture with bumps, the area of contact is reduced and as a consequence the forces are not expected to be of noticeable importance.

The so-called Trimmer notation was specially developed in order to deal with scaling matters and is not treated nor used in this work. More about it can be found in [43, 89].

3.2 Practical setup

3.2.1 General

(a) The setup placed in a dust-free environment.

(b) The actuation and acquisition part.

Figure 3.2: Illustrations of the μSPAM setup at the Control Engineering Laboratory, University of Twente.

Realizing a setup for measurements with nanometer resolution requires a range of dedicated equipment. Some parts are used for conditioning of the environment, like the soft-wall modular clean-room in Fig. 3.2(a), other for actuation, data acquisition, processing and storage (Fig. 3.2(b)).

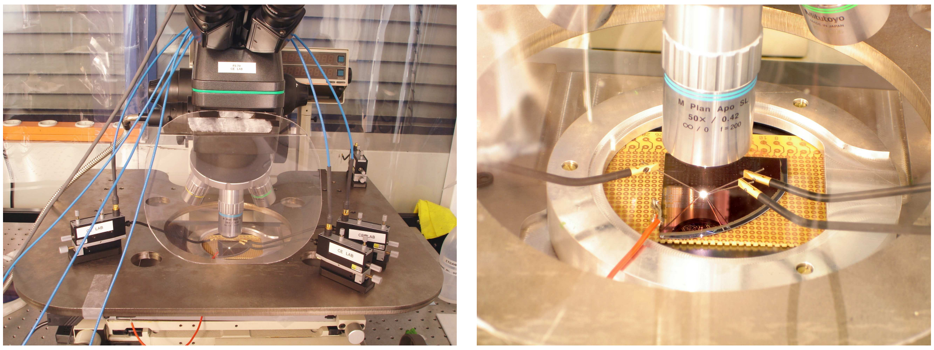

(a) The microscope and dedicated probe station.

(b) Close-up of the central part.

Figure 3.3: The probe station and the microscope under attention.

The core of the setup consists of an optical microscope with dedicated probe station and image recording capabilities, Fig. 3.3. A virtual magnification of about 3500x is realized, when the camera image is projected on a 19$inch$ monitor.

3.2.2 In-plane video measurement techniques

From the beginning, the need for measurements for characterization and control was recognized. So far, though, it turned out that combining a micro actuator with a micro (position) sensor is tough. Even considering the vast micromachining equipment and knowledge available at MESA+, the complexity of the actuator fabrication process (Appendix J) and the aggregation of a sensor using the same fabrication steps is still a big challenge.

At the moment, measurements are taken by actuating the device and at the same time recording the movements in one dimension with a microscope and a digital camera. Unfortunately, the current affordable cameras combined with the setup microscope do not admit resolutions much lower than about 100nm. The pixel size of about 4μm – of the fire-wire camera is the main bottleneck.

As the measurement accuracy should be roughly an order of magnitude lower, under 10nm, a different way was investigated to measure sub-pixel resolution movements [96]. The technique resides on recording a pattern of white and dark regions, and on measuring the shift in phase of this pattern, which is directly proportional to the displacement. The resolution has thus been improved to about 5nm. which is more than sufficient for the characterization targets of this chapter. More information about the optical path and resolution can be found in Appendix A.

The FS 70 microscope is the basic part of the setup, and therefore some basic characterization is useful. First, it was discovered that drift in the mechanical structure itself is considerable, and cannot be ignored. The microscope would sometimes even go out of focus within one hour after setting. Temperature differences could be a cause of this unwanted effect, but so far no direct correlation was found between the temperature gradient and drift. Altogether, an uncertainty of $120 nm/min$ has been established by repetitive experiments, provided that temperature does not fluctuate more than $5°C$. As a consequence, measurements should be taken as fast as the video capturing software and hardware permits, in order to reduce the effect of this drift uncertainty.

After the data has been recorded in uncompressed AVI format, it is processed with Matlab in order to obtain information about the displacement. Unfortunately, the amount of video data to be processed does not allow for real-time results with the current configuration. A real-time operating system, combined with frame grabbing from the fire-wire camera and FPGA control could be used to close the loop at a bandwidth limited by 30fps.

3.2.3 Fringes setup

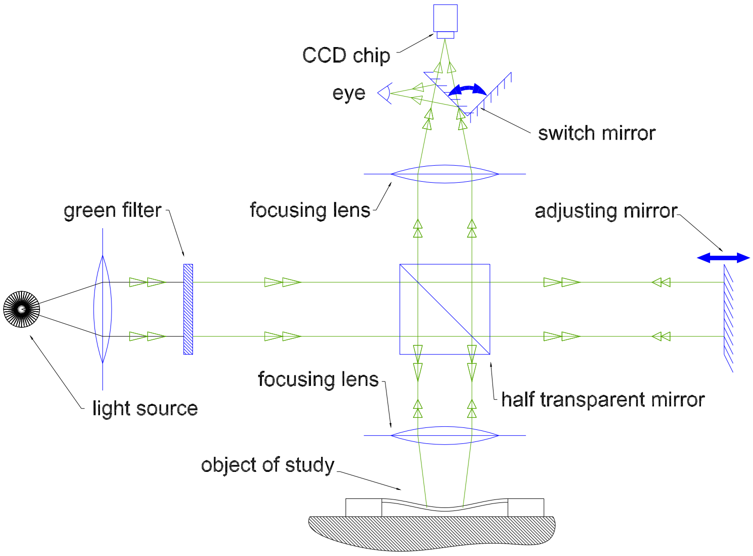

Figure 3.4: Obtaining height information of the μWalker parts with a light interferometry-based microscope setup.

The basic idea behind light interferometry (Fig. 3.4) and fringes measurements is that by making use of the wave properties of light and polarized filters/mirrors, one can obtain wave-like patterns on the object of study. The method is called Michelson interferometry and is described in [4], [26].

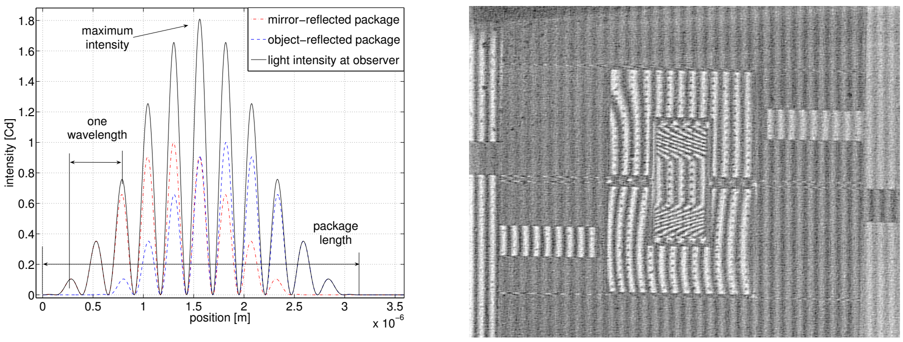

(a) Basic principle of light interferometry resides on convolution of energy packages.

(b) Illustration of an image obtained with the interferometry setup.

Figure 3.5: From packages of light to topological information of the sample.

To clarify the working principle some more, consider Fig. 3.5(a). A source produces light which is then filtered such that only a narrow bandwidth (typically around $530nm$) can pass. The energy packages obtained in this way are now split by a half transparent mirror. One half is reflected towards the object, whereas the other passes through and reaches a mobile and fully reflective mirror.

The light package is thus reflected by both the object of study and the adjusting mirror, after which it reintegrates in the half transparent mirror. The obtained energy package is directed towards the CCD camera or the eye by a system of lenses and mirrors.

The result is an interference pattern which is composed of concentric rings or almost parallel lines, also called Frizeau fringes [4]. The lines are present if the adjusting mirror inside the microscope is slightly tilted, such that the center of the concentric rings is shifted and the radii of the observed circles are relatively large, thus making it approximate a parallel pattern.

Referring to Fig. 3.4, moving the microscope mirror horizontally or the object of study vertically by half a wavelength leads to a shift of exactly one interference fringe.

An important remark here is that the length of the light package in time must be sufficient, at least a number of times the wavelength. If this is not the case, then the object of study and the mirror must be at exactly the same distance with respect to the half transparent mirror. Indeed, having a light source which produces relatively broad energy packages in time presents an advantage, as then interference appears more often than once. This is illustrated in Fig. 3.5(a), where the energy content of the packages reflected by the mirror and object sum up to give the light intensity at the observer.

Consider now Fig. 3.5(b). As the wave length of the green light used is around 530nm, a shift of seven fringes on the plate results in a vertical difference of the object of about 1.855μm. This value corresponds roughly with the design dimensions in Fig. 2.8, where the plate can bend about 1.59μm. Worn-out or malformed bumps are a possible cause for the slight difference of about 265nm.

In this way, sub-micron differences in height can be monitored. The images obtained are digitized, and later on processed or inspected visually. With this kind of interferometry measurements, information about the pull-in voltage of the legs, the area of the legs which sticks, the plate, the distance between plate and ground and the plate stick distance have been obtained.

3.2.4 Actuation setup

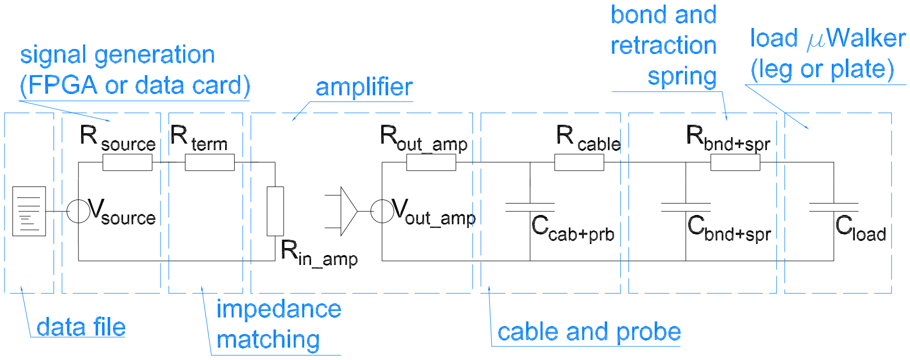

Figure 3.6: Sketch of basic components used for actuation.

In this subsection, the main components used for actuation are presented schematically. There are three independent channels as in Fig. 3.6, for the μWalker legs and the plate.

The steps needed for actuation of the μWalker are loaded from a data file and generated either by Labview™ and a data card, or by an FPGA card with PCI interface. In the latter case, a D/A converter are used to link the FPGA to the amplifier (the D/A convertor is not shown in Fig. 3.6). The resistance R_{term} matches the source (R_{source}) and the load impedance (R_{in_amp}). The voltage amplifier was customly developed for this setup and features six channels based on the PA98 amplifier chip from APEX Microtechnology. It has a range of ± $100V$ and slew rates above $500V/\mu s$. The output resistance of the amplifier, R_{out_amp}, was experimentally matched to the load in order to minimize ringing and signal degradation. In this way, a compromise was established between the amplifier output slew rate and signal ringing. Low-capacity coax cables[1] ($C_{cab+prb}$, R_{cable}) connect the amplifier output to the probes, which make contact with bonds on the wafer ($R_{bnd+spr}$, $C_{bnd+spr}$). The signal is then directed via the retraction springs of the actuator to the actual load C_{load}, which is either the μWalker plate or one of the legs (Fig. 2.5). In practice, the load is much smaller than the bond capacity ($C_{load} << C_{bnd+spr}$).

Typical values for the lumped elements in Fig. 3.6 are listed in Table B.1, Appendix B. Calculations about the load capacitance for the legs and the plate are enlighten in Appendix C. The model presented here is being used in Chapter 4 to draw conclusions about efficiency, power consumption and more.

3.2.5 Other equipment

For the desired accuracy to be obtained. i.e. smaller than one step size, the measuring environment should be free of substantial external vibrations and the device to be measured must be protected from dust particles.

Due to the nature of the MEMS device under attention, even sub-micron particles can damage the actuators permanently. For this reason, a class 1000 environment[2] is used to clean the air flowing over the wafer with actuators [43].

An active damping table (with air pressure) is used to damp out external shocks above $\approx 7Hz$. As most of the eigen frequencies of the MEMS structures on the wafer are far above this frequency –typically three orders of magnitude or more, vibrations are reduced to a negligible value.

3.3 Characterization of the μWalker

The reason for presenting a rather extended number of diverse measurements of the μWalker in this section is because first the reader should acquire some 'feeling' of what is going on when such a shuffle motor shows displacement and second to build a basis for the modeling and simulation part in Chapter 4, where validation based on the results presented here is crucial. Some of the results derived have a more general value than merely characterization of the

---

[1] To keep the drawing schematic, only a simple capacitor between the signal line and ground is present in Fig. 3.6; a more realistic model would represent a lumped-model of the cable impedance, as the cable is of course symmetric.

[2] Quantitatively, class 1000 means that a particle count does not exceed 200 particles of a size of $1\mu m$ or larger or about 2000 particles of a size of $0.1\mu m$ or larger in a volume of one cubic foot.

μWalker – they give estimates of wear, stiction and other topics which are supposed to be of significant interest for the MEMS community in general and for friction related experiments on micro scale in particular.

There is a certain variation in the dimensions of the devices which were used for measurements. Nevertheless, the results from the types of μWalker tested are not expected to vary noticeable from measurements which would have been done on the device with dimensions as in Table B.2. Of course it is remarked when other than the standard device is being used.

Originally, a number of measurements about the μWalker have already been presented in [73]. These were mostly about pull-in, step size, displacement as a function of different voltages and output force. The measurements presented in this work are inherently related to the work presented in [73], and they gratefully build on the knowledge available there. Generally, the results presented here also have a statistical label in terms of mean and standard deviation values derived from a number of measurements under identical conditions, as knowledge about the repeatability of motion is of the highest importance.

This section contains only measurement results and interpretations and is divided in three in an effort to sort out the measurements done in one of the many possible ways. The first subsection is about typical characteristics of one or more μWalker parts, while the second is more related to the overall device performance, including wear and life time.

3.3.1 Parts level

Plate stick region

When a high enough voltage called pull-in voltage is applied to the plate, this will snap to the ground and a part of it will stick, giving rise to one step. This sticking part depends on the voltage applied and to a smaller extent on the state of the legs (clamped or not). During the development of the energy-based model presented in Chapter 4 and [40], predictions were made about the part of the plate which would stick when the pull-in voltage is applied. This would be 50% of the total plate length, or more if the voltage is higher than the pull-in voltage.

Interferometry images reveal that the area of the plate that sticks at pull-in is smaller than half of the total plate area. By recording different frames like the one in Fig. 3.5(b) for a range of input voltages, one obtains Fig. 3.7. Each data point is based on one measurement. The three sub-figures represent the percentage of the plate that sticks, and which depends about linearly on the plate voltage applied. The visible peaks in Fig. 3.7 raise the appeal to repeat the measurements for each data point in the figure in order to characterize noise. Since according to the (linearized) theory in Chapter 4 the plate stick percentage is linearly related to step size, these measurements are in agreement

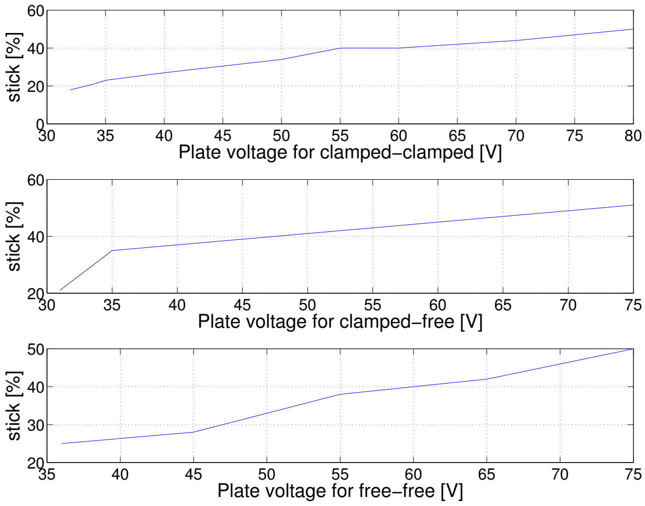

Figure 3.7: The stick percentage as a function of applied plate voltage for three situations.

with [73]. The state of the legs, namely clamped-clamped, clamped-free and free-free, does have some influence. On one hand, as a clamped leg decreases the distance between the plate and the walking surface, the stick area is being increased. On the other hand, clamping the legs means that they cannot shift sideways, so that axial tension in the plate occurs, which in turn decreases the stick area compared to the case when no legs are clamped. In conclusion, it is not trivial to draw any hard conclusions based on the data acquired thus far. In Chapter 4, this plate stick phenomenon is studied from a modeling point of view.

The measurement just presented was obtained with the interferometer setup. The results of the rest of this section follow from experiments with the camera setup from Section 3.2, page 29.

Relation between maximum range and plate voltage

For the reliability and result impact of upcoming more complex measurements, it is very important to use proper actuation voltages. Therefore a characterization of the maximum range of the μWalker with respect to the applied plate and legs voltage is considered necessary. The influence of the voltage applied to the legs is treated later in this subsection.

Let us concentrate on the plate voltage first, while assuming that the shape

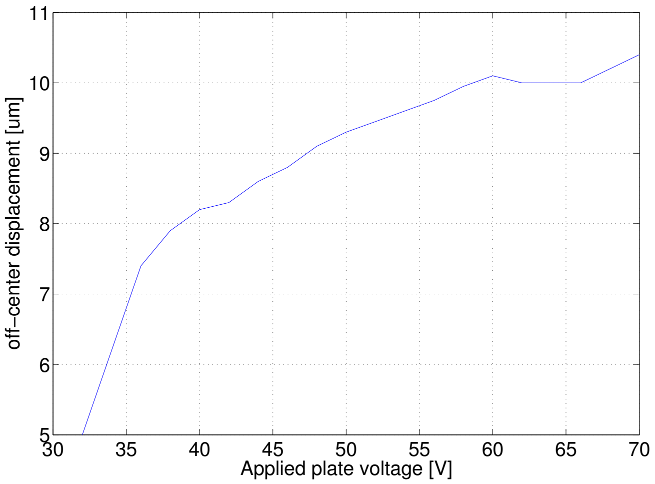

Figure 3.8: Maximum range as a function of the plate input voltage (each data point in the plot was measured three times and averaged).

of the legs voltage signals are the same each time[3]. Here, the actuation sequence consists of taking 200 steps into one direction and then measuring the displacement. From Fig. 3.8 it follows that a plate voltage of about $60V$ would be optimal from the point of view of maximal range and avoiding charge build-up (to be discussed later on in this chapter). Also here we see the presence of measurement noise, as for values larger than $60V$ the maximum displacement varies.

If we convert the recorded displacement into a counteracting force exerted by the eight retraction springs then the maximum force exerted by the μWalker under the present circumstances is about $1.39mN$. The way the springs force is calculated is subject of Chapter 4, page 92 and on.

Plate push and pull force

One of the most interesting subjects of this research is to discover the main limiting factors of the current μWalker design and propose improvements. In this experiment, we seek to find out the factor that leads to a decrease in the step size as the μWalker approaches the end of the range.

From the basic actuation principle introduced on page 17 and reviewed in Fig. 3.9, only the retraction (from sequence T_1 to T_2) and the release (from T_4 to T_5) of the plate yield planar motion of parts of the device. As such, at least one of these two sub-sequences is responsible for the decreased step size measured

---

[3] The amplitude of the legs voltage was $35V$.

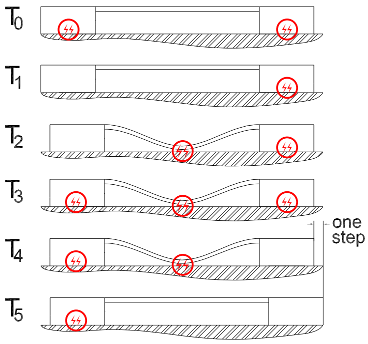

Figure 3.9: One-step sequence of the μWalker (revisited).

close to one end of the actuation range.

In sub-sequence T_2 from Fig. 3.9, the electrostatic force applied exceeds the bending force required for equilibrium. As a consequence, the plate sticks to the surface, thus storing some energy into the bending of the plate and dissipating the rest during the impact. Sequence T_5 is used to release the stored bending energy in the plate.

In other words, the bending force in the plate must be smaller than the electrostatically applied force, otherwise the plate dynamics would not become unstable and the plate would not clamp to the surface. Because the electrostatic force must always be larger for pull-in to occur, some energy is lost at each impact.

Reasoning in this way, before discussing the measurements it can be predicted that the bending energy released in sub-sequence T_5 could be the limiting factor because the electrostatic energy should always be larger, otherwise the plate would not feature pull-in and stick to the surface at all.

The measurements consist basically of moving a number of steps, typically 10, 20 or 40, then clamping one leg and after that actuating the plate a number of times while monitoring the position of the free leg. After this, the μWalker is again shifted a number of steps and the whole actuation sequence is repeated.

This is illustrated in Fig. 3.10(a) for the push sequence. The μWalker is at the right of the steady-state position and the left leg is fixed. The plate voltage is turned on and off which makes the plate enter and leave the pull-in phase. During plate actuation, the left leg remains clamped. Due to this situation, every time the plate voltage is switched to zero potential, the right leg which is free, now shifts a little to the right as the bending energy is released.

This displacement – called push step size – is plotted in Fig. 3.11(a) for different positions of the uWalker along it's range. Effectively, Fig. 3.11(a) represents the step size due to the bending force which was stored in the plate, and which is also called push force.

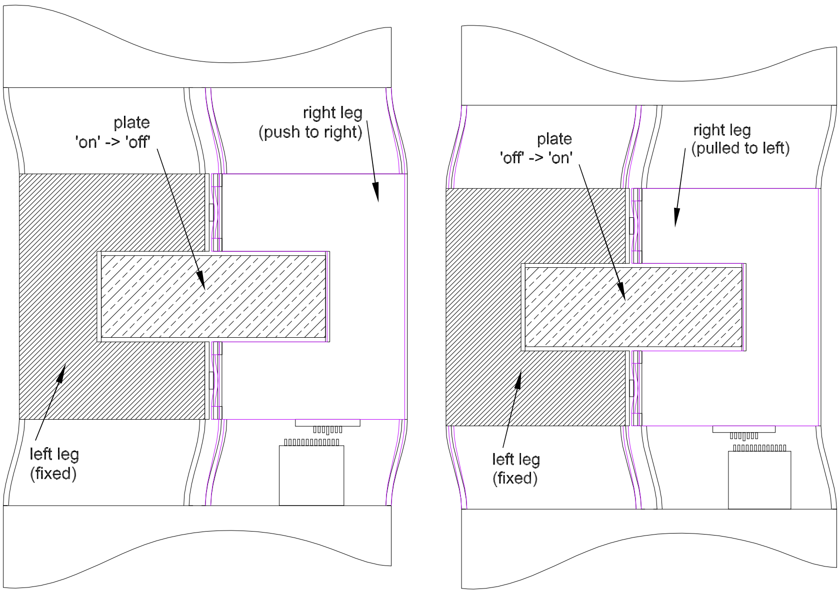

(a) Measuring the push force...

(b) ... and the pull force.

Figure 3.10: Schematic view of how the push and pull force are derived.

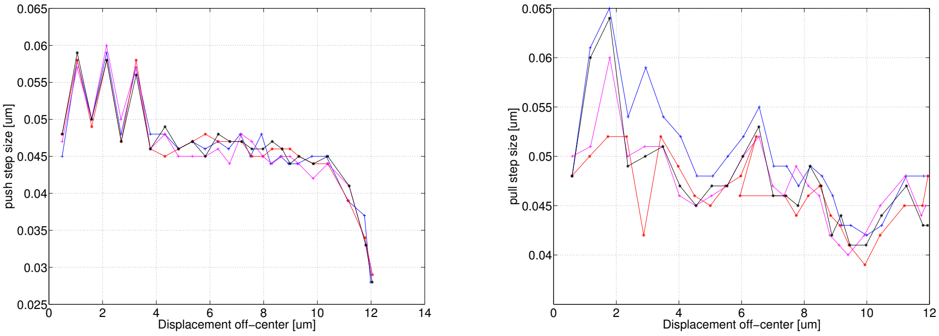

(a) Push step size related to off-center displacement.

(b) Characterization of pull step size.

Figure 3.11: These measurements indicate that the plate bending force is the limiting factor.

In Fig. 3.11(a), the step size jumps up and down about $10nm$ from one measurement to the next. It would be weak to attribute this to stochastic effects, as all four measurements indicate the same behavior at small displacements around steady-state. One plausible explanation is surface charge induced in the insulating materials. Although bi-polar signals were used to make steps, a constant potential had to be applied to the sticking leg during the on-off switching of the plate. The sticking of the leg (due to a constant potential on the leg) might have caused the fluctuation.

This phenomenon could be attributed to the sign of the leg potential every time the leg had to be clamped to the surface for measurements. To be more precise, during the odd measurements (lower step sizes left in Fig. 3.11(a)) a positive leg stick voltage was applied, during the even measurements negative voltages were applied. Probably, a net negative charge was present on the walking surface and/or the shifting leg bumps prior to the measurements, such that the step size varies every time. For higher counter forces of the retraction springs (above $4\mu m$ displacement), this effect becomes of second order and actually disappears as the displacement is increased.

Although the exact origin of the varying step size is not exactly known, for our purpose it is irrelevant as to us it matters what happens at the end of the range, namely around $12\mu m$. To be more precise, it can be seen that the step decreases towards zero at the end of the range. Technically, the plate bending force is not high enough to stretch the retraction springs even more and the step size decreases towards zero. This leads to the conclusion that the bending energy stored in the plate indeed limits the range and the applied force of the μWalker.

Conversely, for capturing the pull step size due to the electrostatics, the device is moved in the opposite position (left of steady-state, see Fig. 3.10(b)). Also here, the left leg is fixed as the potential of the plate is switched on and off a number of times. During the switch from off to on, the displacement of the right leg is recorded, which is free to move.

The displacement obtained in this way tells something about the applied electrostatic force minus force it takes to the bend the plate. No noticeable limitation on performance can be observed in Fig. 3.11(b). At the end of the range, the step size is still about $45nm$.

Altogether, Fig.3.11 shows that for the pull case, the step size remains about constant up to the maximum range, whereas for the push case it decreases. Thus the electrostatic force – here called pull-force – is not a limiting factor on the range or the exerted force of the μWalker.

If the applied electrostatic force would be insufficient, then for positions close to the end of the range, a clear decrease in step size would be seen in both Fig. 3.11(a) and 3.11(b). However, this is not the case.

Some ideas to improve the μWalker design from this perspective are presented in Chapter 5. The reader is referred to Appendix E for more information about actuation signals.

Stiction and the effect of charge on the legs

Initial measurements point out that if the μWalker is actuated more than a few seconds, it starts to behave differently than initially. The standard deviation of the step size increases, with other words the variation in step size grows. Moreover, when after such a sequence the μWalker inputs are set to zero such that the retraction springs bring it back to steady state, it turns out that the device remains at the same position (with the retraction springs bent) for a time, before jumping to the zero position. In one case it remained fixed about $1.23\mu m$ away from steady-state, where the horizontal counter force in the springs is about $5.5\mu N$! This implies the existence of a vertical force induced by the charge particles.

This effect is very probably due to the charge which is induced in both the bumps and the walking surface which are placed between the two capacitor poles, namely one part of the μWalker and the wafer bulk. They are very good insulators and hence the di-electricum constant is high. Due to lack of charge carriers, the electric charge which is inserted in these components cannot flow away easily, even if both poles are set to ground potential.

Another potential cause could be the static charge induced between the part bumps and the walking surface as a result of friction between these components. The charge produced in this way would be even more difficult to get rid of, as it emerges at the surface contacts. Leaking to the ground potential involves that the charges should pass all the way through the bumps or the silicon nitride walking surface (both about $200nm$ thick), and this takes time.

To reduce this effect, the voltages applied to the μWalker were changed, such that now both positive and negative voltages are applied. This is called bi-polar actuation from now on – in contrast to the basic, uni-polar actuation presented earlier in Fig. 2.6(a). Figure 3.12 is a proposed way of actuation, composed of 12 sub-sequences and which produces two steps. By switching between positive and negative voltages, there is theoretically no net amount of charge induced in the insulators, provided an even number of steps.

There is a clear difference between actuation with uni-polar and bi-polar voltages for the plate and the legs. Figure 3.13 shows ten measurements done on the same device consecutively, the left side with ten with uni-polar voltages, the right with bi-polar. The μWalker performed 200 steps into one direction, after which it was fixed to the surface and the displacement was measured. When using bi-polar actuation, the mean step size, the total displacement decreased from $9.88\mu m$ to $8.01\mu m$, but more important, the standard deviation of the end position of the ten measurements decreased from $0.310\mu m$ to $0.0623\mu m$! This means, that by using bi-polar actuation, the predictability of a certain sequence is indeed much better, in the sense that the μWalker end posi-

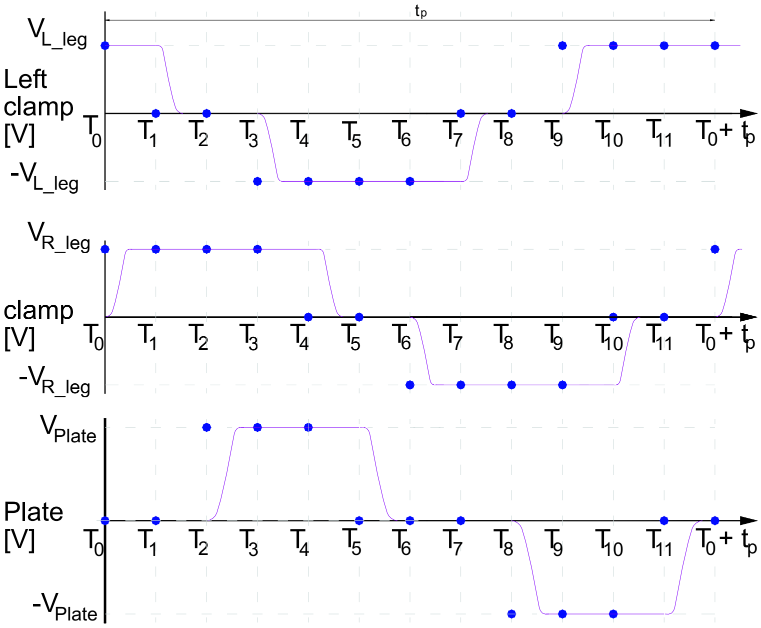

Figure 3.12: Actuation with bi-polar signals for two steps.

tion is each time about the same. From here on, only bi-polar actuated voltages are used for measurements.

Coefficient of stiction and actuation speed dependency

One of the most interesting results presented in this chapter is on determining the coefficient of stiction between the surface and the bumps of one leg, a result which can be interpreted in a more general sense than merely for the μSPAM project in particular.

Generally, the measurements are taken in the following way (see Fig. 3.14):

- the plate voltage is set to zero for about one second in order to have a known initial position (from start to $1.1s$);
- 500 consecutive steps in one direction are taken, to make sure that the maximum range has been reached[4] (between $1.1s$ and $3.6s$);
- at this point, the device is being clamped to the surface for one second by applying a constant voltage on one of the legs while keeping the other

---

[4] The range is being reached after about 350 steps, after which the μWalker slips during the next 150 steps.

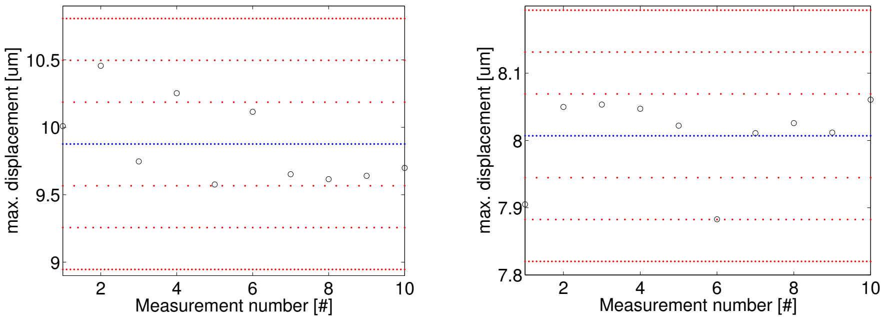

(a) Unipolar actuation.

(b) Bipolar actuation.

Figure 3.13: The total displacement after 200 nominal steps clearly shows a difference in mean and standard deviation between the uni-polar and bi-polar actuation. The tested device has a plate length of 236 μm compared to the standard type.

leg and the plate released; as soon as this happens, the device will slip more or less, depending on the exact voltage applied to the leg (between 3.6s and 4.6s);

- in the end, all parts are set to zero potential, so that the μWalker instantly goes back to steady-state (from 4.6s until the end).

The data in Fig. 3.14 corresponds to 20V actuation of the leg while holding it into position. Now, by repeating such a measurement five times, a surprisingly good estimation of the step turns out to hold: the mean of all five trials is 6.84μm, with a standard deviation of only 13.5nm (assuming an equally distributed set around the mean value).

Now, we can repeat this set of five data points for other voltages than 20V while the leg sticks to the surface, namely we may choose a range of interest between 15V and 35V. By doing so, Fig. 3.15(a) is obtained. In a nut shell, higher voltages of the clamped leg in Fig. 3.14 mean that the vertically applied electrostatic forces are higher, and so the device will stick earlier, on its way from maximum range to zero position. The results are interesting, because they give us information about the μWalker offset during the stick period as a function of the applied leg voltage.

A small intermezzo about dynamics is considered useful here. A related, rather interesting issue was to investigate whether the displacement in Fig. 3.15(a) depends on the actuation speed. In other words, the question to ask is if there will be a change in the position at stick if the actuation steps are pro-

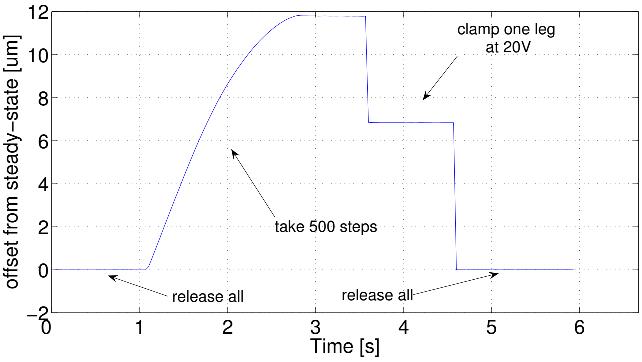

Figure 3.14: Example of actuation with bi-polar signals.

cessed faster. To test this, new actuation signals were made for $120 Samples/s$, $12k Samples/s$ and $120k Samples/s$, respectively. Altogether, three orders of magnitude were covered (Fig. 3.15(b).).

The shape of the four graphs shows resemblance. The $120 Samples/s$ data set does show a small dip between roughly $21V$ and $28V$ but this may have been caused by a particle which temporarily entered between one leg and the walking surface. Furthermore, there is a tendency towards smaller offset with increasing actuation velocity (the data plot of the 'slowly' actuated μWalker lies above the 'fast' actuated one). This could be explained by considering the assumption that at high actuation velocities, the effect of insulation charging is of less importance, compared to the 'slow' actuation of $120 Samples/s$, where the long actuation time may still have induced an amount of charge, thus adding an unknown stick force to the vertical balance of forces in the respective leg, and increasing the offset in this way. This intermezzo is concluded by the remark that the actuating speed does not drastically alter the shape or the values of the offset. From here on, $1200 Samples/s$ (or 200 μWalker steps per second) shall be the standard velocity during measurements.

The data from Fig. 3.15(a) is further processed by calculating the vertical force which corresponds to the applied voltage on the leg during the stick period. The vertical counter force of the retraction springs, which prevent the device from excessive wear by retracting the legs while they are not actuated, is subtracted from the applied force in order to obtain the net vertical force applied to the leg. Assuming that the μWalker will slip as long as the retraction force is larger than horizontal anti-slip force induced by the vertical electrostatic force, then only when the retraction force of the springs is smaller than the horizontal anti-slip force (induced by the vertically applied electrostatic force), will the device stop from moving towards zero position. Note that inertia effects of the leg hardly matter at this scale, as the leg mass is very reduced

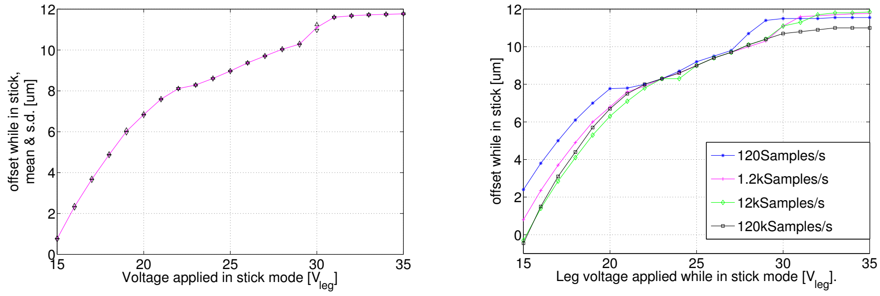

(a) Displacement during stick at 1200$Samples/s$.

(b) Displacement in stick at four different actuation velocities.

Figure 3.15: Distance from steady-state where the μWalker sticks, depending on the applied leg voltage.

($2.2{\cdot}10^{-10}\,kg$) while stiction is omnipresent. This allows us to temporally disregard effects due to inertia dynamics.

The horizontal force in the retraction springs is calculated using linear beam theory, see also Chapter 4. Altogether, it now becomes possible to plot the horizontal anti-slip force as a function of the vertical net applied force on the leg.

Figure 3.16(a) is gives this relation, which is only by estimation linear. From here, the coefficient of stiction, or $\mu_{stiction}$, can be derived, which is defined as the horizontal force over the vertical force applied at a certain moment in time.

An important note here is that theoretically, the coefficient of stiction should be the same for all data in the graph of Fig. 3.16(b). This condition holds only if the area of contact is the same in all cases. Apparently, this area is not equal (visual inspection with the interferometry setup indeed shows that the legs are generally bent and not straight – Fig. 3.5(b)), such that a varying amount of bumps makes contact with the walking surface.

More explicit, a description of the possible causes for the variation of $\mu_{stiction}$ follows next. Four regions could be distinguished in the plot for the coefficient of stiction, with the vertical net force varying between:

- 0.9-2.0: Initially, it is expected that there is only one row of bumps touching the surface, which cannot produce any significant anti-slip force; as the applied voltage increases, the legs bend more towards the walking surface and there is an increasing number of additional bumps which join the process of stiction, which in turn leads to more contact points and accordingly to a roughly linear increasing of the coefficient of stiction.

- 2.0-2.2: as the leg is now getting parallel to the walking surface, the angle

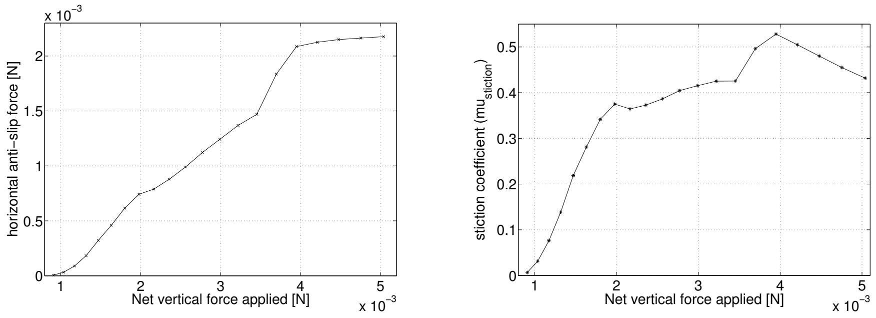

(a) Relation between the horizontal force and the vertically applied force.

(b) Determination of the coefficient of stiction.

Figure 3.16: Derivation of $\mu_{stiction}$ as a function of the vertical force (μWalker shape with 180μm plate).

of the sharp supposedly inner (hollow) side of the bumps has increased to about 90°; this leads to a slightly smaller force of stiction compared to the case where the leg only touched the surface by the bumps of one array and where there was a small angle between the leg and the silicon nitride layer, making the bumps in a way act as a claw or a scratch.

- 2.2-3.5: $\mu_{stiction}$ is constant, only slightly increasing around the value of 0.4; only a small amount of extra bumps add to the stiction area, as the leg is now practically flat on the surface, and bumps from different parts of the leg are in good contact with the ground.

- 3.5-4.0: at the moment, this effect is not well understood, but it is probable that certain bumps dig themselves into very small dips which are present onto the silicon nitride walking layer.

- 4.0-5.0: finally, increasing the applied vertical force does not influence the coefficient of stiction anymore, because the μWalker is already at the maximum range; it will not slip back and stay at this range for a high enough vertical force, but increasing this force will not drive the device beyond it's range, of course; this part can be disregarded generally, as it is beyond normal operation.

The research for the stiction coefficient is being concluded by comparing the results obtained above with the plots of the horizontal anti-slip force and coefficient of stiction for a μWalker with different retraction springs dimensions, namely 100μm instead of 200μm. Figure 3.17(b) was derived in the same

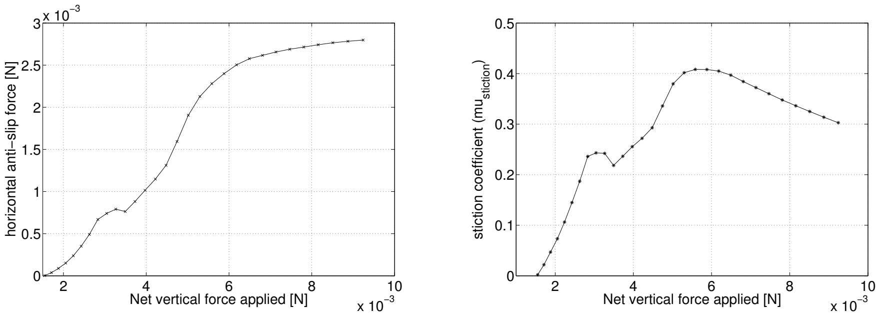

(a) Relation between the horizontal force and the vertically applied force.

(b) Determination of the coefficient of stiction.

Figure 3.17: Derivation of $\mu_{stiction}$ as a function of the vertical force (for a shorter μWalker plate and shorter retraction springs).

way as presented previously. Note the resemblance of the plots with the previous case and a slightly lower maximum stiction coefficient in the latter case of about 0.4.

3.3.2 Device level

The following parts concentrate more on the device level measurements and conclusion drawn therefrom.

Range and force as function of applied voltage

For the sake of maximization of range and force, it was considered necessary to find out which voltages are optimal, i.e. which combination of plate and legs voltages yield a (nearly) maximum range for the standard μWalker design.

To obtain this information, a measurement was completed for each point in the set $\{V_{plate}\,\mathbf{X}\,V_{leg}\} = \{20, 25, 30...70\}\,\mathbf{X}\,\{20, 25, 30, ...60\}$. Thus, a total of 99 data points were obtained, by processing 500 steps and then deriving the final position. The results have been plotted in Fig. 3.18(a). Because the stiffness of the springs is supposed to depend on the cubic power of the deflection, Fig. 3.18(b) is better to see the small differences which are present between the different points with applied voltages of $40V$ and above. If only maximum range is being seen as a criterion, then the highest point in the figure is at $V_{plate} = 60V$ and $V_{leg} = 55V$, with very small differences between this point and its neighbors.

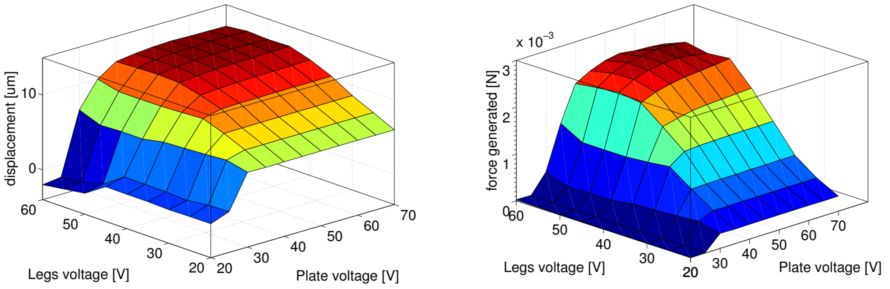

(a) Relation between input voltages and total range.

(b) Corresponding force as function of inputs.

Figure 3.18: Search for the voltage inputs yielding the maximum range of the actuator into one direction.

Mean and S.D. of displacements

In this part of the section, an effort is presented to better estimate the variation of end position of one hundred identical actuation sequences, featuring 20 steps into one direction and a hold time, followed by a jump back to steady state.

Figure 3.19 reveals a surprising resemblance between the 100 identically actuated sequences. The mean size of the movement was found out to be 1.033μm and the standard deviation only 6.52nm!

Assuming that the stiffness of the retraction springs is about constant in this range (according to calculations it is within 5% difference for the deflection of about 1μm), also the 20 steps are considered to be equally large, within the accuracy of the measurements of about 10nm. The step size for the standard μWalker is thus 51.65nm.

Step size dependency on load

The target here is to find out how the step size decreases with increasing load, where in this specific case the load is well-known and only present due to bending of the retraction springs. During the simulations and also for the real prototype, the inertia of the read/write medium is present which adds more dynamics to the system (Chapter 2).

This time a bi-polar potential of 55V was applied to the plate and legs, while making steps towards one end of the range. The actuation rate was only two steps per second, such that the exact position of one leg during each step

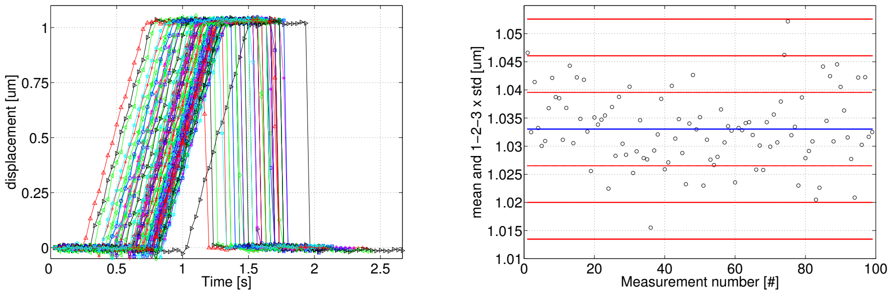

(a) Sequence of 20 steps, 100x repeated.

(b) Corresponding mean values.

Figure 3.19: Actuation reproduction and step size.

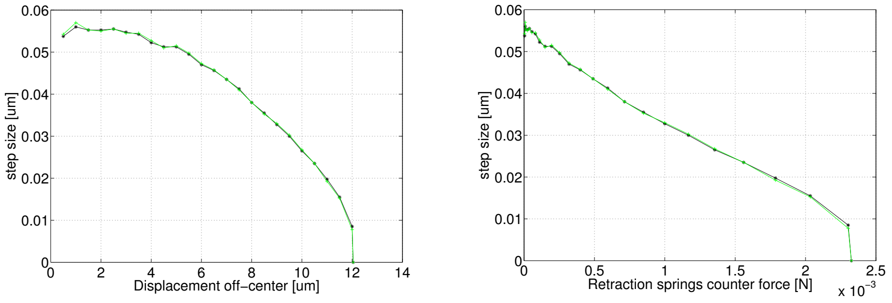

(a) Relation between step size and position.

(b) Step size and the retraction springs load.

Figure 3.20: The step size depends about linearly on the counter force (device with standard dimensions used for testing, two consecutive measurements taken).

could be determined in an accurate way. The step size was measured (off-line) after every 500nm of displacement and plotted in Fig. 3.20(a). Figure 3.20(b) with the step size and the springs counter force is obtained by relating the displacement in the Fig. 3.20(a) to the load of the retraction springs, which is subject of Chapter 4. The data obtained could be approximated by a linear relation between step size and applied counter force, of course within the working range (-12μm .. 12μm).

Roughly estimated, the linear behavior complies with the measurements at the end of Chapter 8 in [73]. It is unknown to the author which type of μWalker was tested there, how the total force was derived and what this force is composed of – the springs connected to one leg only or of all retraction springs.

The load plotted in Fig. 3.20(b) is generated by all eight springs which act on the device. Due to the stick and slip way of propulsion, each step actually only 'sees' half of the springs, namely 4, because the other leg is then clamped. However, it was considered more useful to plot the total force generated by the device, as it is a characteristic value of global importance in the design optimization procedure.

Steps smaller than 50nm

In the μSPAM project and in all probe storage projects in general, it is crucial that the positioning of the probes exactly at the center of the data tracks happens very accurately. Although the future probe tips are expected to have integrated side-way actuators with a range which is enough to cover one track, it seems interesting to mention that also the μWalker can be used to make such small displacements. The device accuracy is thus not limited to 26nm which corresponds to half of the step size.

For reducing unnecessary complexity, the positive unipolar case is explained here, whereas the bipolar case can be derived in a straightforward way. A quick comparison between the basic step (Chapter 2, page 17) and Fig.3.21(a) learns that now at $[T_1]$ and $[T_2]$ a voltage V_α is applied, where $0 < \|V_\alpha\| < V_{L\_Leg}$. V_α is actually the value of the left leg voltage during the second and third sequence of each step.

The consequence is that while the distance between the right and left leg decreases during the plate actuation in $[T_2]$, some stick will occur to the left leg due to V_α. This stick is the cause of the decreased step size, $\Delta_{intra-step}$.

Let us define $\Delta_{step}(V_\alpha)$ over $0 \leq V_\alpha < V_{L\_Leg}$. For $V_\alpha < 10V$, it can be assumed that the step size is the same as the full step (Chapter 2): $\Delta_{intra-step} \approx \Delta_{full-step} = 52nm$. However for $V_\alpha > 31V$, $\Delta_{step} \approx 0nm$ so the step size is zero.

Figure 3.21(b) gives the relation between V_α and $\Delta_{intra-step}$ for $10V \leq V_\alpha < 31V$. Each of the data points shown is the mean of five identical measurements, except at $28V$, where two of the five values were outside $MEAN \pm 2 * STD$

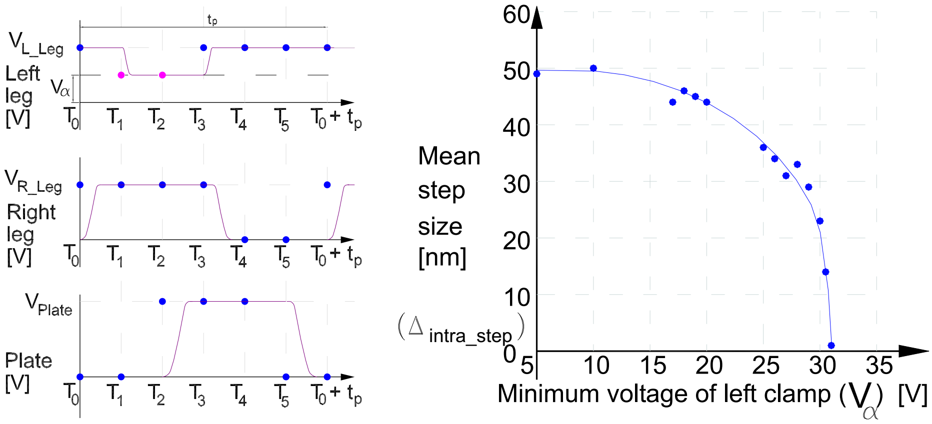

(a) Actuation sequence for a sub-nominal step.

(b) Impact of varying V_α on the step size $\Delta_{intra-step}$.

Figure 3.21: Realization of intra-steps, steps smaller than the nominal step.

and were excluded. The five measurements needed for each of the points in Fig. 3.21(b) have been obtained after measuring a sequence of 200 consecutive steps and calculating the mean step size over all steps. Given set of dimension parameters of the standard μWalker, the step $\Delta_{step}(V_\alpha)$ can be as:

$$\Delta_{step} := \begin{cases} 0 & : \quad 31 \leq V_\alpha < V_{nominal} \\ \Delta_{intra-step} & : \quad 10V \leq V_\alpha < 31V \\ \Delta_{full-step} & : \quad 0 \leq V_\alpha < 10V \ , \end{cases} \tag{3.5}$$

with $\Delta_{intra-step}$ a best-fit curve of deliberate shape and order, see Fig. 3.21(b). These results have been included in [57].

Wear and estimated life time

The influence of wear on performance and especially on the life time is of crucial importance for the target application, probe storage. Some attention has been paid to this topic, in order to quantify the performance degradation with time, and also the total expected life time.

From destructive tests after the end of the life time of a device was reached, it was discovered that the μWalker parts touch the surface but not all bumps have the chance to wear or even come into contact with the walking surface.

Figure 3.22 shows the state of the walking surface after failure. The device completed about 4.39m of total displacement until failure, in a total time of

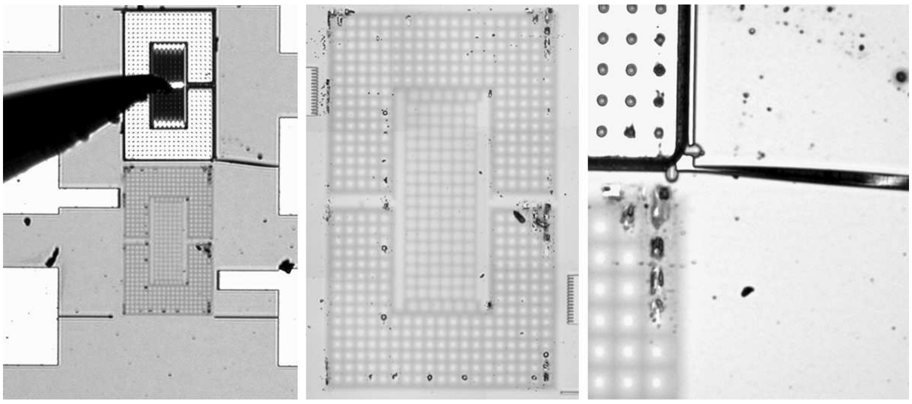

Figure 3.22: Results of destructive testing on a μWalker.

about 16 minutes. Left, the actuator was turned over in order to be able to detect the cause of failure and rate of wear. No visible irregularities could be observed at the device parts, but note that the height of the bumps in the μWalker – probably the most important parameter – is very hard to measure.

However, some material deposition due to abrasive and/or adhesive wear can be observed on the walking surface, especially at the contacts around corners and edges of both legs (middle photograph). Appendix D describes four main mechanisms of wear. Typically, about 20 wear spots can be seen for each leg, most of them grouped in clusters of four or five, like in the right picture. Apparently this actuator failed due to a short circuit between the lower leg and the ground potential of the bulk. This happened near the right connection springs as can be seen in the right picture of Fig. 3.22. This type of failure happened more often with different μWalkers while actuated at 16.000 steps per second or more.

The next μWalker shifted for about 190m during more than 27hrs (Fig. 3.23(a)) before failure. The difference between wear of the left and right part of the device is probably caused by a difference in vertical stiffness of the retraction springs. For instance, the height of the stiffness springs is very important, designed as h_{retrs} Fig. 2.7. Even small, local changes of this parameter can influence the vertical stiffness in a such way that wear patterns like in Fig. 3.23(a) result. We also see some regions around the connection springs to the right of the picture, where material seems to have been deposited due to adhesive wear.

The device in Fig. 3.23(b) shows the most wear of the three tests. Most of the legs bumps have been in contact with the surface and show signs of wear. Excessive wear patterns are present at the corners of the legs and at the bumps in the edge arrays of the actuation plate. Traces of adhesive wear are clearly vis-

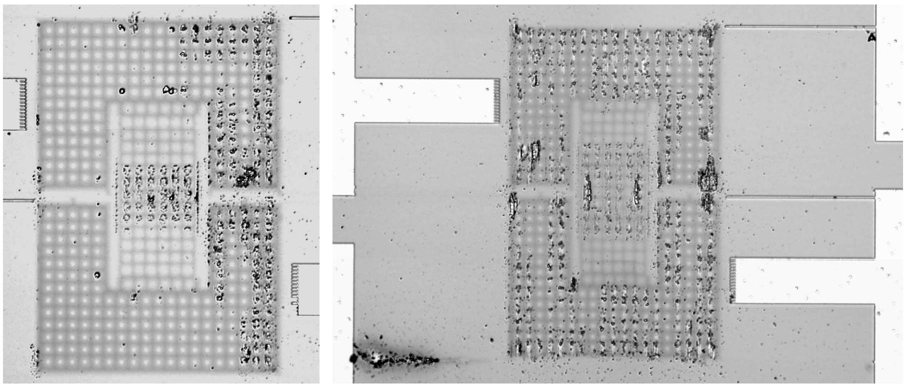

(a) Partial wear. (b) Excessive wear, resulting in short circuit.

Figure 3.23: Photographs of advanced wear patterns.

ible, especially under the legs and at the outer part of the plate center. Finally, note a possible short circuit with the bulk which has caused the left lower retraction spring to melt.

It is not completely known why some devices break down rather fast, while other perform many more steps. Variation of the silicon nitride walking layer over the wafer could be a reason, but also impurities in this layer could lead to premature break-down. Alien particles which find themselves between the surface and the μWalker have been observed sometimes, expecially under the plate. This too has a negative effect on life time.

Finally, for sure the height and the exact shape of the μWalker bumps are both crucial. A lower variation and better control of these two parameters yields a normal load at the contact points which is more evenly distributed among the bumps. This, in turn, increases life time because points of excessive adhesive wear like the regions in in Fig. 3.23(b) are now avoided – or at least postponed for a later time in the life cycle.

In a nut shell, the operation life of the device can be characterized by a number of steps. Depending on the operating speed, wear becomes visible sooner or later. Eye inspection shows the presence of foreign particles (poly silicon) or intrinsic particles (probably silicon nitride) which have changed color due to excessive heat. Especially wear of the walking surface is clearly observable by looking at the thin white traces up and down the steady-state position of the bumps.

If the operating speed is elevated, then the temperature at the contacts increases up to a point where the material (silicon nitride) on both the bumps

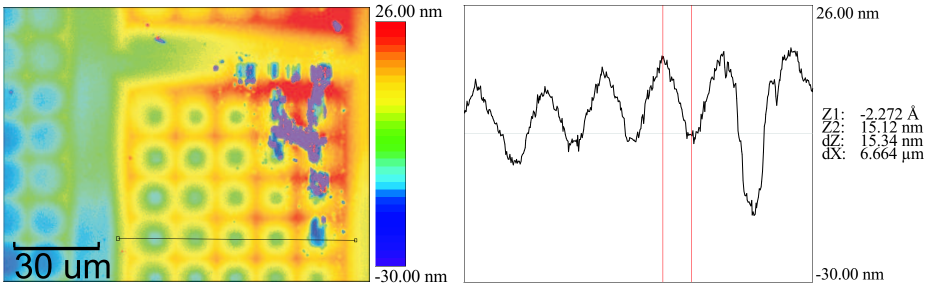

(a) Close-up of the right connection of the legs, done with an automatic interferometry-based setup...

(b) .. and the corresponding height along the line segment of the left plot.

Figure 3.24: Height-information of the μWalker in Fig. 3.22.

and the surface starts to create microscopic welding points. Furthermore, due to the very fast repetitive movements, the boundary layer made of oxides or other materials cannot grow fast enough, so that the silicon nitride layers can be better protected and adhesive wear is reduced.

The fact that each μWalker that has reached the end of its life time after fast actuation (40.000 steps per second) ends up welded to the walking surface, and that relatively high forces must be exerted with probe tips in order to release it, enforces this thought. As soon as such welding points appear, the rate of wear is accelerated and short thereafter the end of the life time is reached.

To have a better idea about the final state of the walking surface after the device malfunction took place, let us consider Figs. 3.24 and 3.25. Here we can see the topology of a part of the walking surface, recorded by an automated light interferometry setup. Of course, the μWalker was removed in advance for exposing the walking surface. The different colors express the local height: red parts (top of the scale) represent higher altitude, whereas blue and magenta shapes at the bottom of the scale represent low regions, mostly regions with excessive wear.

Figure 3.24(a) is a close-up of the walking surface under the right connection of the legs of the device in Fig. 3.22. Due to a small tilt of approximatively $20nm$, the base color changes slightly from the lower left to the upper right corner. Remark the line segment in this figure. The height information measured along this segment is plotted in Fig. 3.24(b). A scale of different remarks follow from this plot. First, the wear patterns due to bumps are clearly visible, as well as wear in the form of scratches caused by the edge of the lower leg. Second, the number of bumps which have been in contact in this region is reduced to six.

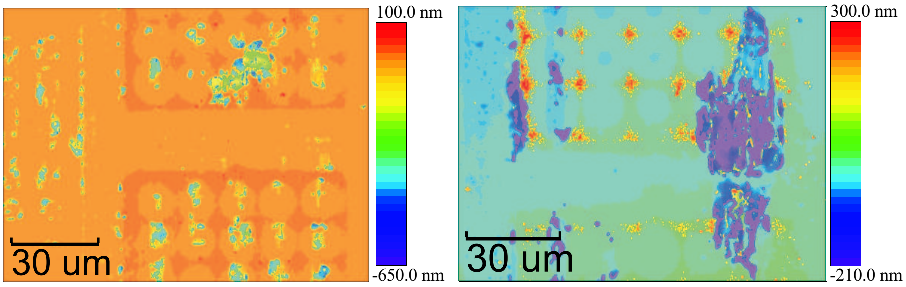

(a) The right connection of the two μWalker legs.

(b) Zooming the same region for the excessively worn actuator.

Figure 3.25: Height-information of the μWalkers in Figs. 3.23(a) and 3.23(b), respectively.

Regarding the plot in Fig. 3.24(b), note the repetitive pattern of $14\mu m$, which is exactly the distance between the center points of two neighboring bumps. Perhaps the most interesting part is the fact that we can derive the shape and rate of etch which has changed the flat walking surface into a landscape with repetitive well structures. These wells are formed in one of the final steps in the fabrication process, when the sacrificial layer needs to be removed. For more information see Appendix J and especially Fig. J.1. Because the etchant removes the intended oxide layer via the holes in the bumps, the walking surface is indeed etched away at a certain rate, depending on the exposure time, concentration and some other factors. Directly under the bump the etching time is slightly longer and it decreases towards the center region between two bumps. This gives rise to the wells of depth in the order of $15nm$.

Figures 3.25(a) and 3.25(b) show a close-up of about the same region, but of μWalkers which performed more steps and thus feature more advanced wear. In Fig. 3.25(a), the thin yellow/green vertical line left of the center indicates that the edge of the μWalker plate has been touching the surface repeatedly. Note also the extensive wear which has taken place at the upper leg. The cause could be the presence of a foreign particle, as the wear pattern shape is from one bump to the other in a diagonal way.

Figure 3.25(b) is from a device which has developed excessive wear. The magenta wear patterns are visible. Other patterns indicate wear of the edge of the upper leg with the walking surface. The small red regions are most likely displaced surface particles, brought together at cross-points where the leg bumps did not come into contact with the surface.

It seems plausible that except wear, other phenomena also play a role, like field emission for example. Voltage breakdown is treated in detail in [34]. It

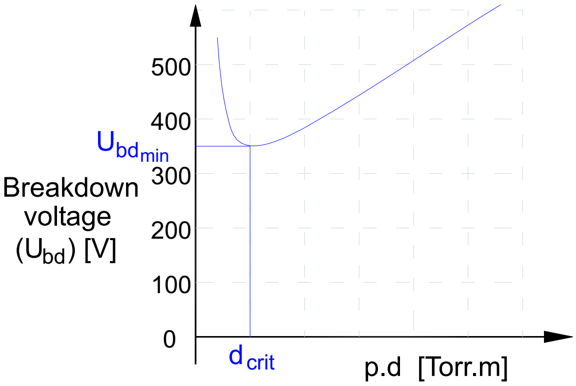

Figure 3.26: Paschen curve for air at a constant pressure (inspired by [80]).

can occur between device parts and the bulk under the layer after wear has decreased the insulating layer where the μWalker walks on.

The Paschen curve for air in Fig. 3.26 is a widely used tool in the design of high voltage components and actually suggests that as the distance between the electrodes decreases under a critical value d_{crit} for constant pressure, the breakdown voltage V_{bd} starts to increase [34]. Left of d_{crit}, the distance is small compared to the mean free distance of an electron in air (0.5μm), such that less and less collisions take place before an electron reaches the anode. This explains the expected increase in breakdown voltage V_{bd}. Surprisingly, recent experiments show that the breakdown voltage actually decreases drastically for distances smaller than about 4μm [80]. Due to the decreasing homogeneity of the electric field, the Paschen curve is not valid anymore. In fact, it becomes about linearly dependent on the air gap, so that for gaps under 1μm in air, the breakdown voltage is smaller than 50V. One possible explanation for this phenomenon is that material asperities and dissociated impurities initialize a field emission process, which finally leads to a conductive vapor plasma that expands towards the anode. When the distance between cathode and anode has been bridged by this plasma, breakdown occurs. Breakdown voltages of 29V have been reported for air gaps of 0.25μm [80].

Put shortly, possible impurities in the silicon nitride layer and excessive wear of the device parts and the walking surface can trigger partial discharges, which then cause local material melting, poly silicon deposition on the walking surface, as well as melting of one or more retraction springs. Melting of the retraction springs is caused by the fact that the breakdown current and finally the short circuit current gives rise to a too high current density, given the limited conductor cross-section of 2μx5.5μm.

Due to the time consuming nature of wear tests, only a few quantitative results were successfully ended and they are shown in Fig. 3.27. It is expected

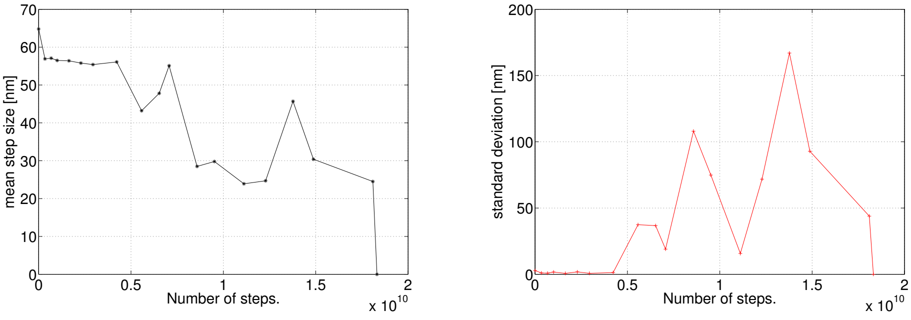

(a) Mean step size between 10 test runs.

(b) Standard deviation.

Figure 3.27: Step size as a function of number of processed steps.

that the step size of a μWalker changes with time, as the device approaches the end of its life time.

In the beginning, the step size increases a little, probably because this device, just like any other moving mechanical system, needs to be run in. To be more explicit, there still are small rests from the sacrificial layer, which have not been etched away. As a consequence, these peaks first have to get worn, before the μWalker walks in an optimal way.

After some time of normal operation, more and more wear increases the roughness of the walking surface, the bumps are not effective anymore and the distance between the plate/legs and the bulk decreases, thus increasing the chance for short circuit. To capture this expected decrease in step size, 24-hour runs were started; here, the actuator moves up and down a few hundred of steps continuously. After this, a short test consisting of only 40 steps is recorded ten times. The mean total displacement of the ten tests is then considered to contain information about wear and life time.

So far, no direct correlation was found between device step size and temperature or humidity. The values for the temperature and humidity were logged continuously during the wear process (Fig. 3.27) and the values are between 17.4-23.2°C and 20-36%, respectively.

Looking at Fig.3.27, it can be concluded that after $4.25{\cdot}10^9$ steps the variation of the end position in the test runs increased from under $3nm$ to above $37nm$. Using the step size information from the test runs, a total distance of about $746m$ has been calculated ($18.3{\cdot}10^9$ steps). In [75], a distance of $1500m$ has been reported, which roughly agrees with the measurements presented here. In contrast with [75], a remarkable performance deterioration has been observed here after the first 4.25 billion (or $\cdot 10^9$) steps, equivalent to $240m$ of walked distance.

To have an idea about the walked distance at the micro scale, one rather dared comparison with the macro world follows. If a nominal step ($52nm$) would be compared to the step of a person in hurry ($\approx 1m$), then the distance the μWalker walked until the appearance of deterioration in step standard deviation would be about $4.25{\cdot}10^6 km$, or eleven times the Euclidean distance to the moon! Scaling does seem an interesting and useful topic, after all!

Chapter 4

Modeling and simulations

After bringing up reasons for physical modeling of the μWalker, some rigorous attention is paid to results from analytical modeling of different parts of the device, especially the middle plate of the actuator. The plate is namely the propulsion element which influences performance most. The second part of this chapter is about practical issues related to modeling and simulation in 20-sim. Some models of the μWalker are introduced, followed by simulation results. A short review concludes the present chapter. A number of references treating several model parts of the μWalker have been aggregated into this part [40, 60, 56, 57, 62, 63].

4.1 Analytical modeling

4.1.1 Motivation

Because the target of the μWalker actuator is to be used in probe storage or related applications, it should become possible to somehow simulate its behavior, in order to minimize development time and cost due iterative runs in the clean-room [60, 61]. Reference [78] also mentions that computational prototyping can be far more economical than physical prototyping, provided that the model is sufficiently accurate and the simulations are fast.

This discussion shall be carried on in Chapter 5, for now it is considered enough to present the context, in order to justify the need for an accurate model, which can be used to simulate the actuator.

There is another reason for having a model at hand. Imagine the real possibility that for control purposes, a feed-back signal is needed, but that for some reasons no sensor (signal) is available. With a model based on and validated with off-line measurements, it still becomes possible to research interesting topics on control – be it purely in software for the time being. This is topic of Chapter 6.

Hopefully the reader is now convinced of the necessity of an accurate model. The next question which might arise is why yet another model, as there already exist general models for plates, for bending beams and so on. Most of these models were developed separately, and not with an eye on integration. To the impression of the author, the interaction between the several sub-parts of the actuator is of such a nature that simply glueing together some results and models from literature would not be a successful approach, for the target of device optimization presented above.

What is even more important, the final model should feature as many physical parameters (material properties, dimensions) as possible so that insight can be used to help the optimization procedure.

Finally, the models of parts of the μWalker which were available in the beginning are not always accurate enough. As an illustration, consider the pull-in voltage of the plate, which is one of the most crucial parameters for the final design. Countless measurements indicate that the value is between 32 and $40V$ for the standard actuator[1] as shown in Fig. 2.5. Yet many references [1, 73, 86, 84] use Eq. 4.1 in some flavor or another for deriving the pull-in voltage.

$$V_{pull-in} = \sqrt{0.75 \frac{E_{poly} h_{plate}^3 h_{gap}^3}{\epsilon_0 L_{plate}^4}} \tag{4.1}$$

Actually, if Table B.2 is consulted and we assume $h_{gap} = 2.050\mu m$ from Fig. 2.8, then $V_{pull-in} \approx 10.4V$, which is clearly not even close to the measured values.

4.1.2 Beam theory revisited

Let us start the quest for a competent model of the μWalker plate by revising shortly some basic beam theory. The plate is only fixed at the two ends and thus does not behave like a membrane. Therefore the influence of the Poisson's ratio is considered negligible.

Moreover an important approximation is made, namely that all sections along the length of the plate follow the same motion as a function of time. This is illustrated in Fig. 4.1 with four sections denoted as $S(w)$. In other words, at any given time it holds that all $S(w)$ with $0 < w < w_{plate}$ are identical, where w_{plate} is the width of the plate like in Fig. 2.7. Measurements confirm that this can be assumed in general. Now it is possible to use beam theory instead of plate theory, which simplifies the results considerably. The equation of the Euler beam in case of an applied force distribution is given as:

$$EI \frac{\partial^4 w(x)}{\partial x^4} - \sigma_0 w_{plate} h_{plate} \frac{\partial^2 w(w)}{\partial x^2} = F_{el.st}(x), \tag{4.2}$$

---

[1] The exact pull-in voltage depends on factors such as the state of the legs, the dimension of the retraction springs, etc.

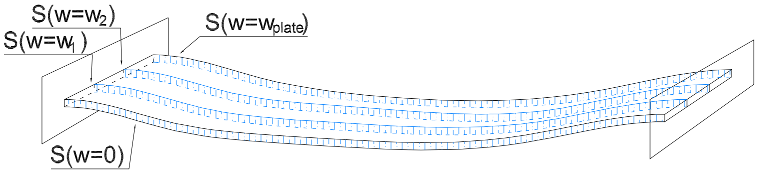

Figure 4.1: Sketch of a long plate clamped at two ends, indicating that the shape of all section $S(w)$ are identical at all times.

where E is the Young's modulus of the material, I is the moment of inertia, $w(x)$ is the shape of the plate along x with $0 \leq x \leq L_{plate}$, σ_0 is the axial stress, h_{plate}, w_{plate} are as in Table B.2 and $F_{el.st}(x)$ the distribution of the electrostatic force applied. The factor $\sigma_0 w_{plate} h_{plate}$ is sometimes called the tension in the beam or plate.

Basically, there are two different internal components in the equation of the plate which are present in our case, namely the bending and stress parameters. Although Eq. 4.2 is hard to solve analytically, some short remarks are mentioned. First, note that the axial stress component, the term which includes the second derivative with respect to x, has opposite sign than the bending term, meaning that it counteracts pure bending, strictly spoken. For small deflections (smaller than about 5% of plate length), the stress component can be neglected compared to bending. This is an often made assumption in practice.

When no axial stress is present (no doubly-clamped plate), then the second factor vanishes, giving the Timoshenko approach [21]:

$$EI\frac{\partial^4 w(x)}{\partial x^4} = F_{el.st}(x) \tag{4.3}$$

In this case, assuming a certain load distribution and a shape for the plate is enough to solve the equation, like in Appendix F.

The other extreme case is when the bending energy of a beam is negligible, string theory comes into play:

$$-\frac{\partial^2 w(x)}{\partial x^2} = \frac{F_{el.st}(x)}{\sigma_0 w_{plate} h_{plate}} \tag{4.4}$$

If a point load at the center is assumed, then the shape becomes similar to the equal sides of an isosceles triangle, instead of taking over a predefined form or the form of the load distribution. The axial stress σ_0 and the force exerted in order to elongate the plate by ΔL are defined as:

$$F_{axial} = EA_{plate}\frac{\Delta L}{L_{plate}} \text{ and } \sigma_0 = E\frac{\Delta L}{L_{plate}}, \tag{4.5}$$

with $A_{plate} = w_{plate}h_{plate}$ the cross-section of the plate, and $\frac{\Delta L}{L_{plate}}$ the strain induced by the axial stress.

Later on, it will be shown that the second term of Eq. 4.2 can be left out in certain parts of the model (connection springs), as it does not have any noticeable influence. For other parts (retraction springs) the effect of axial stresses is indeed important for the overall model accuracy and it will be incorporated accordingly.

Appendix G presents an estimation of the axial stress for the particular case when a (vertical) force distribution induces a well-defined shape of the plate and the ends are fixed. Using line integrals [10], the axial stress is defined in this way. The conclusion drawn is that the force needed to stretch the plate and thus alter step size is high (up to $8.5mN$), so that step size is hardly influenced by the axial stress under normal conditions.

4.1.3 Plate stability analysis

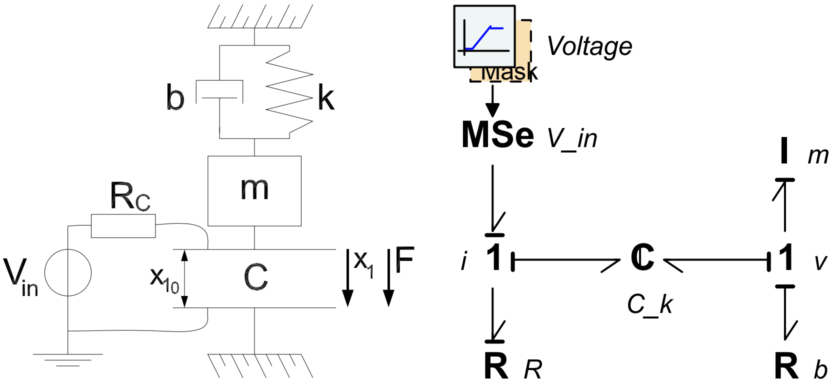

(a) Lumped elements used to model the electro-mechanical plate of the μWalker.

(b) Bond graph representation of the same plate.

Figure 4.2: Plate modeling in the iconic and bond graph representation.

Physical model

In this subsection we investigate the stability of the μWalker plate under the assumption that the dynamics is described by interconnected linear components. Figure 4.2(a) introduces a number of lumped elements. Amongst them is capacitor C with one movable plate. This part couples the electrical and mechanical domains dynamically. Another central component is the vertical plate stiffness denoted by k. Part d represents air damping and m the equivalent plate mass. These last two components do not influence the stability points we are looking for.

We further remark that voltage actuation is used (V_{in}). From a physical point of view, the presence of resistance R is necessary. This necessity is hereafter explained using bond graphs – however the reader which is not familiar nor interested in bond graphs can skip the following part in the belief that element R is indeed a necessary component.

Bond graphs and causality

Detailed information on bond graphs can be found in [7, 9, 90]. The interaction between the mechanical and electrical domains is in our case achieved by a two-port $\mathbb{C}$ element (Fig.4.2(b)). This element represents the transduction of the moving capacitor plate, thus connecting the electrical and mechanical domains. While determining the causality of the model [90], the $\mathbb{C}$ ports have a flow-in causality, as the element is composed of coupled C and k.

In order to avoid causality conflicts, the component R must be added. At the $1:i$ junction in Fig.4.2(b), MSe imposes an effort and the $\mathbb{C}$ port requires flow-in preferred causality. The resistance R solves this conflict by imposing the flow on the junction.

The relation between the states x_1(plate position), x_2(charge) and the inputs F(force), V_{in}(applied voltage) of the linear $\mathbb{C}$ element can be found from the energy $E(x_1, x_2)$ or the co-energy $E^*(F, V_{in})$:

$$E(x_1, x_2) = \frac{1}{2}k{x_1}^2 + \frac{1}{2C}{x_2}^2 \quad \Rightarrow \tag{4.6}$$

$$F = \frac{\partial E(x_1, x_2)}{\partial x_1} = k\, x_1 \quad \text{and} \quad V_{in} = \frac{\partial E(x_1, x_2)}{\partial x_2} = \frac{x_2}{C},$$

$$E^*(F, V_{in}) = \frac{1}{2k}F^2 + \frac{1}{2}C{V_{in}}^2 \quad \Rightarrow \tag{4.7}$$

$$x_1 = \frac{\partial E^*(x_1, x_2)}{\partial F} = \frac{F}{k} \quad \text{and} \quad x_2 = \frac{\partial E^*(x_1, x_2)}{\partial V_{in}} = C\, V_{in}$$

Now we can write the relation between the states and the inputs in matrix form:

$$\begin{bmatrix} x_1 \\ x_2 \end{bmatrix} = \begin{bmatrix} k^{-1} & d \\ d & C \end{bmatrix} \cdot \begin{bmatrix} F \\ V_{in} \end{bmatrix} \Longleftrightarrow \begin{bmatrix} F \\ V_{in} \end{bmatrix} = \frac{1}{k^{-1}C - d^2} \begin{bmatrix} C & -d \\ -d & k^{-1} \end{bmatrix} \cdot \begin{bmatrix} x_1 \\ x_2 \end{bmatrix} . \tag{4.8}$$

Physically, d represents the polarization of matter between the capacitor plates. In this case, there is no polarizing material so $d = 0$. This was also considered in the (co-)energy functions above.

Strictly spoken, the energy is being expressed in state variables, whereas the co-energy is a function of the inputs of the system. Note that the energy function can be used to investigate stability in the sense of Lyapunov [81]. In the next part, the critical points are investigated for the whole system using characteristic polynomials.

Critical points and stability

The system dynamics of the total system in Fig. 4.2 can be described in the general form $\dot{x} = f\left(x, u\right)$, with x the state vector containing position x_1, capacitor charge x_2 and mobile plate velocity x_3; the input vector u has only one input, namely the applied voltage V_{in}.

In so doing, we can determine the dynamics as follows:

$$\begin{bmatrix} \dot{x_1} \\ \\ \dot{x_2} \\ \\ \dot{x_3} \end{bmatrix} = f(x,u) = \begin{bmatrix} x_3 \\ \\ \frac{V_{in}}{R} - \frac{x_2\left(x_{1_0} - x_1\right)}{R\epsilon_0 A_{plate}} \\ \\ -\frac{k}{m}x_1 - \frac{b}{m}x_3 + \frac{{x_2}^2}{2\epsilon_0 A_{plate} m} \end{bmatrix}, \tag{4.9}$$

where $A_{plate} = h_{plate}\, w_{plate}$ is the area of one capacitor plate.

We find the equilibrium equations by solving $f(x,u) = 0$:

$$\frac{x_2\left(x_{1_0} - x_1\right)}{R\,\epsilon_0\, A_{plate}} = \frac{V_{in}}{R} \quad \Rightarrow \quad x_2 = \frac{\epsilon_0\, A_{plate}\, V_{in}}{x_{1_0} - x_1} \tag{4.10}$$

$$-\frac{{x_2}^2}{2\epsilon_0\, A_{plate}\, m} = -\frac{k}{m}x_1 \quad \Rightarrow \quad x_1 = \frac{{x_2}^2}{2k\,\epsilon_0\, A_{plate}}. \tag{4.11}$$

The characteristic polynominal $\xi(x_1)$ is defined by substituting Eq. 4.10 in Eq. 4.11, solving for x_1 and setting $\xi(x_1) = 0$:

$$\xi(x_1) := -{x_1}^3 + 2{x_1}^2 x_{1_0} - {x_{1_0}}^2 x_1 + \frac{\epsilon_0 A_{plate} V_{in}}{2k}. \tag{4.12}$$

Physically, $\xi(x_1)$ is directly related to the accelerating force on the mobile plate: only when this force is zero, will there be an equilibrium of the forces on the plate. The zeros of this polynominal are the equilibrium points in the system, as we shall soon see in Fig.4.3(a) (points c_A and c_B).

Furthermore, it is interesting to find the voltage above which the mobile plate will snap onto the fixed plate, no matter it's position, charge or velocity. This is called the pull-in voltage. To find the pull-in voltage, we need to find the extreme values of $\xi(x_1)$, also called critical points. The critical points are found by solving $\frac{\mathrm{d}\xi}{\mathrm{x}_1} = 0$, as it will be explained graphically later on:

$$\frac{\mathrm{d}\xi\left(x_1\right)}{\mathrm{x}_1} = -3{x_1}^2 + 4x_1 x_{1_0} - {x_{1_0}}^2. \tag{4.13}$$

The two solutions are $x_a = \left[{x_1}_0, \infty, 0\right] \vee x_b = \left[\frac{1}{3}{x_1}_0, \frac{3V_{in}\epsilon_0 A_{plate}}{2{x_1}_0}, 0\right]$. Point x_a represents the situation where the plate distance vanishes and the amount of charge goes to infinity. More interesting is x_b. If we linearize the system around x_b and given $\bar{x}, \bar{u}$ to be the deviation from equilibrium, there holds: $\bar{x} = x - x_b$, $\bar{u} = u - u_b$.

The dynamics in the neighborhood of point can be found by linearization:

$$\dot{\bar{x}} = A\bar{x} + B\bar{u}, \text{ with } A := \frac{\partial f}{\partial x}\Big|_{x_b, u_b} \text{ and } B := \frac{\partial f}{\partial u}\Big|_{x_b, u_b}. \tag{4.14}$$

The two matrices are in this case:

$$A = \left.\begin{bmatrix} 0 & 0 & 1 \\ \frac{x_2}{R\epsilon_0 A_{plate}} & -\frac{\left({x_1}_0 - x_1\right)}{R\epsilon_0 A_{plate}} & 0 \\ -\frac{k}{m} & \frac{x_2}{\epsilon_0 A_{plate} m} & -\frac{b}{m} \end{bmatrix}\right|_{\left[\frac{{x_1}_0}{3}, \frac{3V_{in}\epsilon A_{plate}}{2{x_1}_0, 0}\right]} \quad \text{and} \quad B = \begin{bmatrix} 0 \\ \frac{1}{R} \\ 0 \end{bmatrix} \tag{4.15}$$

We can determine stability in this point by deriving $\det\left(A - \lambda I\right)$:

$$\left(A - \lambda I\right) = \begin{bmatrix} -\lambda & 0 & 1 \\ \frac{3V_{in}}{2R{x_1}_0} & -\frac{2{x_1}_0}{3R\epsilon_0 A_{plate}} - \lambda & 0 \\ -\frac{k}{m} & \frac{3V_{in}}{2m{x_1}_0} & -\frac{b}{m} - \lambda \end{bmatrix}. \tag{4.16}$$

The determinant of this matrix is:

$$\begin{aligned} \det\left(A - \lambda I\right) &= -\lambda^3 - \lambda^2\left(\frac{2{x_1}_0}{3R\epsilon_0 A_{plate}} + \frac{b}{m}\right) - \lambda\left(\frac{2b{x_1}_0}{3R\epsilon_0 A_{plate} m} + \frac{k}{m}\right) \\ &\quad - \left(\frac{2k{x_1}_0}{3R\epsilon_0 A_{plate} m} - \frac{9{V_{in}}^2}{4Rm{{x_1}_0}^2}\right). \end{aligned} \tag{4.17}$$

From basic control theory [19], the Routh-Hurwitz stability criterion implies that a necessary condition for stability is that all terms of the determinant have the same sign.

In Eq. 4.17, this is only possible if the last part of the determinant is smaller than zero. This condition gives us the region for which this critical point is stable:

$$\frac{2k{x_1}_0}{3R\epsilon_0 A_{plate} m} - \frac{9{V_{in}}^2}{4Rm{{x_1}_0}^2} > 0 \tag{4.18}$$

$$-\sqrt{\frac{8k{{x_1}_0}^3}{27\epsilon_0 A_{plate}}} < V_{in} < \sqrt{\frac{8k{{x_1}_0}^3}{27\epsilon_0 A_{plate}}}. \tag{4.19}$$

The pull-in voltage occurs exactly at the edge between stability and instability and is given by:

$$V_{pull-in} = \sqrt{\frac{8k{x_1}_0{}^3}{27\epsilon_0 A_{plate}}}. \tag{4.20}$$

This equation can be found in a variety of literature sources [29, 48, 64, 79].

Graphical interpretation

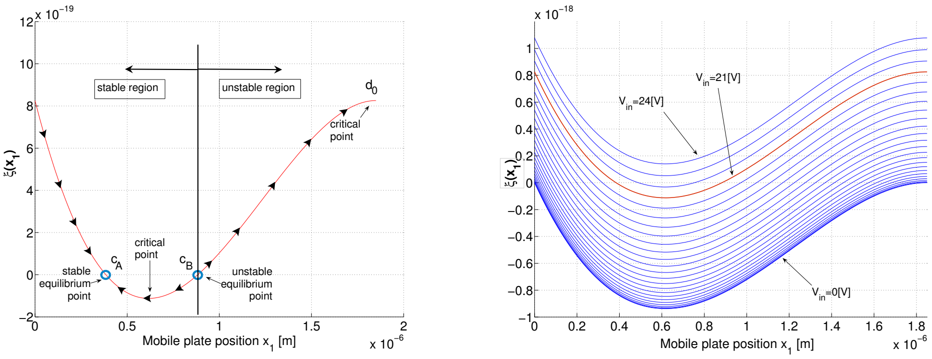

(a) Resultant force and stability for one case ($V_{in} = 21V$).

(b) Resultant force for different input voltages.

Figure 4.3: The region of stability varies as a function of the input voltage.

System stability can be investigated in a more intuitive way by explaining Fig. 4.3(a). This figure shows function $\xi(x_1)$ from Eq.4.12 in the case that a fixed voltage V_{in} ($V_{in} < V_{pull-in}$) is applied. Note that the standard μWalker parameters are used. The horizontal axis represents the mobile plate position x_1. Both plots show critical points at $x_1 = \frac{{x_1}_0}{3}$ and $x_1 = {x_1}_0 (= d_0)$ in line with the derivation shown earlier.

It is easy to see that $\xi(x_1)$ is closely related to the force exerted on mass m – in any case they have the same sign. Therefore we can derive (un)stability by inspecting $\xi(x_1)$ graphically.

First, let us consider Fig. 4.3(a) where a constant voltage $V_{in} = 21V$ is applied. This is just under the pull-in voltage of about 22.5V. Accordingly, a set of equilibrium points c_A (stable) and c_B (unstable) exists within $x_1 = [0 ... {x_1}_0]$. Again, these points are found by solving $\xi(x_1) = 0$ while $V_{in} = 21$.

When the system is in $0 < x_1 < c_A$ (see Fig. 4.3(a)), then $\xi(x_1)$ is positive. According to the convention chosen in Fig. 4.2(a), a positive force means that the mass undergoes an acceleration downwards. The force on the mass remains present until the stable equilibrium point c_A has been reached. As a consequence, the mobile plate position becomes $x_1 = c_B$.

In region $c_A < x_1 < c_B$ the mass is accelerated in the negative direction (upwards), so the system dynamics goes to c_B. For displacements larger than c_B the system jumps to the critical point $x_1 = d_0$ and pull-in occurs. To sum up, for all plate distances $x_1 < c_B$ the system settles to point c_A. For larger values, the system jumps to $x_1 = d_0$ and pull-in occurs.

In Fig. 4.3(b) we can see the values of $\xi(x_1)$ for all $V_{in} = [0 : 1 : 24]$. The plot indicates that $\xi(x_1)$ is lifted up when V_{in} increases. This in turn decreases the distance between c_A and c_B. Therefore, the stability region is decreasing with increasing voltage. When the pull-in voltage is reached, no stability region exists anymore and the force on the mass is positive along the whole trajectory of x_1 from 0 to x_{1_0}.

In contrast with many misconceptions around this topic found in literature, hopefully it is now clear to the reader that the stability region depends on the voltage applied and that it is not at all constant (two thirds of the steady-state distance). It cannot be repeated frequently enough that this derivation and the results only hold in the hypothetical case of linear components.

Plate thickness and pull-in

An interesting result from this study is that we can derive the relation between the pull-in voltage and plate thickness. Figure 4.4 shows the solutions of $\xi(x_1)$ for varying μWalker plate thickness, assuming that the plate shows bending only and thus the vertical stiffness k is linear. The vertical axis in the figure is shows the values of the characteristic equation for different voltages. The bifurcations appear exactly at the pull-in voltage and we can see that indeed the bifurcations appear when the variable plate position is at two thirds from the fixed plate.

The plot shows that the pull-in voltage can be decreased below $8V$ if the plate is about $0.6\mu m$ or thinner. A thinner plate does have a negative impact on the maximum force delivered by the μWalker, but in Chapter 5 we shall see that this force can be increased by altering the plate width. Note that plate width does not affect the pull-in voltage because both the capacitor plate and the vertical stiffness are assumed to be linearly dependent on the plate width (w_{plate}). This will be treated in more detail later in this chapter.

As a closing remark, the assumption that the value of the capacitor is constant with the plate dimensions, does not hold for the μWalker. As bending of the plate occurs, more and more of the μWalker plate has an influence as a capacitor, such that the value of the capacity depends on the applied voltage. The quest for a dynamical model of the μWalker plate is continued from page 89, with an infinite dimensional model featuring the plate stiffness and mass.

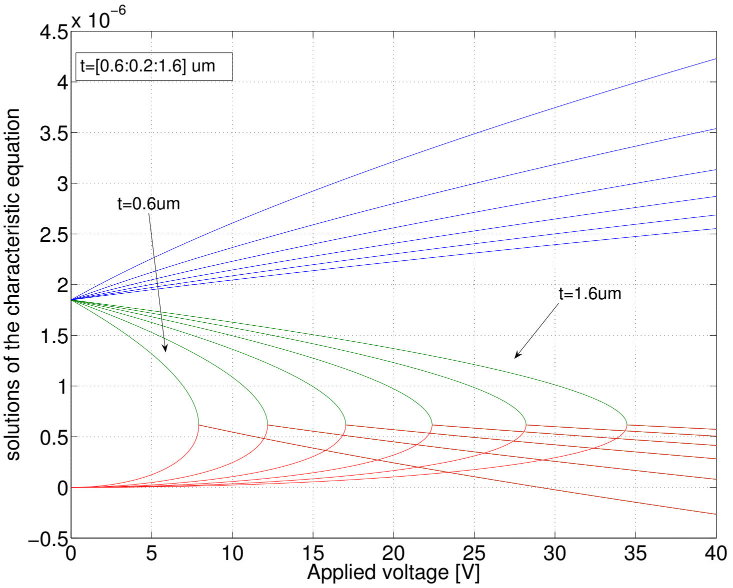

Figure 4.4: Solutions of the characteristic equation $\xi(x_1)$ for different plate thickness.

4.1.4 Plate resonance frequency and the variational method

An estimation of the plate resonance frequency tells us about the operation frequency where the highest plate efficiency is present. In this case, the vertical motion of the plate could be compared with a first order linear system vibrating at the eigen frequency [19].

The most frequently encountered method to calculate the first resonance frequency of a clamped-clamped beam or plate structure is like in Eq. 4.22, which is derived from Eq. 4.21 for a standard mass-spring system [27, 30, 36, 51, 77].

$$f_{res_1} = \frac{1}{2\pi}\sqrt{\frac{k}{m}} \tag{4.21}$$

$$f_{res_1} = \frac{\alpha h_{plate}}{L_{plate}^2}\sqrt{\frac{E_{poly}}{\rho_{pSi}}}, \tag{4.22}$$

with α sometimes omitted or denoted as a fitting parameter [99] and its value around 1.03.

A more precise manner to obtain the resonance frequency is by using Eq. 4.21 with $m = \rho_{pSi}L_{plate}h_{plate}w_{plate}$ and $k = \frac{\lambda^4 EI_{plate}}{L_{plate}^3}$ [87]. Here, $I = \frac{w_{plate}h_{plate}^3}{12}$ and $\lambda = 4.7300408$, which is a solution to the differential equation of a clamped-clamped beam [67]:

$$\cos(\lambda)\cosh(\lambda) = 1.$$

We obtain the relation [2, 87] (compare with 4.22):

$$f_{res_2} = \frac{1}{2\pi}\sqrt{\frac{\lambda^4 E_{poly}h_{plate}^2}{12\rho_{pSi}L_{plate}^4}} \tag{4.23}$$

Filling in the typical dimensions of the μWalker as summed up in Table B.2 on page 162, gives $f_{res_2} = 236.3kHz$.

There is another way to derive the resonance frequency, namely by considering the balance between the (maximum) potential and kinetic energy in the system while the plate is actuated in resonance. This is also called the variational method in [79]. Reconsidering Eq.4.2, the second term is small and therefore disregarded here. In line with [40], we start by defining a priori the shape of the plate $w(x)$ as a function of the plate position along the $x - axis$, in this case a fourth order polynominal of the form:

$$w(x) = d_0\left(\frac{2}{L_{plate}}\right)^4\left[\left(\frac{L_{plate}}{2}\right)^2 - \left(x - \frac{L_{plate}}{2}\right)^2\right]^2, \tag{4.24}$$

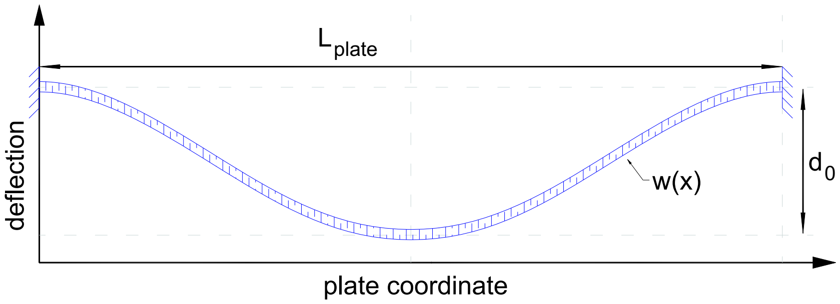

Figure 4.5: A polynominal shape of the plate, with $0 \leq x \leq L_{plate}$.

which can be reduced to:

$$w(x) = \frac{16d_0}{L_{plate}} \cdot \left(x^4 - 2L_{plate}x^3 + L^2_{plate}x^2\right) \tag{4.25}$$

The factor d_0 is the maximum bending of the plate at center while in resonance, which does not influence the resonance frequency as we shall see later. Figure 4.5 visualizes this shape.

Let us consider a harmonic actuation, then the position of all points with the same x–coordinate can be described in time by:

$$\hat{w}(x,t) = \hat{w}(x)\sin(\omega t), \tag{4.26}$$

with $\hat{w}(x)$ the maximum amplitude which appears at all points with the same x–coordinate while the plate is in resonance. Of course, if at a certain moment (in this case $t = \xi\frac{\pi}{\omega}$, $\xi \in I\!N$) there is a point $\hat{w}(x) = 0$, $x \neq \{0, L_{plate}\}$, then $\hat{w}(x) = 0\,\forall\, x \in [0 \ldots L_{plate}]$, or in other words the plate is straight and the velocity of each point is maximal at that moment.

Now we can define the maximum velocity $\frac{\partial\hat{w}(x,t)}{\partial t}$, which is used to calculate the maximum kinetic energy:

$$\left.\frac{\partial\hat{w}(x,t)}{\partial t}\right|_{t=0} = \hat{w}(x)\cdot\omega\cos(\omega t) \tag{4.27}$$

$$= \hat{w}(x)\cdot\omega \quad (\omega = 2\pi f) \tag{4.28}$$

The maximum kinetic energy in the plate (compare with $U_k = \frac{1}{2}mv^2$) is given by:

$$U_k = \frac{1}{2}\int_{vol.}\rho_{pSi}\left(\frac{\partial\hat{w}(x,t)}{\partial t}\right)^2 \mathrm{d}vol. \tag{4.29}$$

$$= \frac{1}{2}\int_{x=0}^{x=L_{plate}}\int_{y=0}^{y=w_{plate}}\int_{z=-\frac{h_0}{2}}^{z=\frac{h_0}{2}}\rho_{pSi}\cdot\left(\hat{w}(x)\cdot\omega\right)^2 \mathrm{d}x\mathrm{d}y\mathrm{d}z \tag{4.30}$$

$$\tag{4.31}$$

Solving for the proposed polynominal shape gives:

$$U_k = \frac{64}{315}\, w_{plate}\, h_{plate}\, L_{plate}\, \rho_{pSi}\, \omega^2\, d_0^2 \tag{4.32}$$

The potential energy due to bending of the plate is derived from the curvature κ in [21], see also Appendix F:

$$\kappa = \frac{M}{E_{poly} I_{plate}} = \frac{\partial^2 \hat{w}(x,t)}{\partial x^2}, \tag{4.33}$$

where M is the bending moment and $I = \frac{w_{plate}\, h_{plate}^3}{12}$ the moment of inertia.

Given that the bending strain ϵ is generally defined as [21]:

$$\epsilon = -\kappa \cdot z,$$

where z is the vertical position of the plate center with respect to rest, then the maximum potential energy is reached when the plate is maximally bent (compare with $U_p = \frac{1}{2}kx^2$ for a linear spring):

$$U_p \;=\; \frac{E_{poly}}{2} \int_{x=0}^{x=L_{plate}} \int_{y=0}^{y=w_{plate}} \int_{z=-\frac{h_0}{2}}^{z=\frac{h_0}{2}} \epsilon^2 \mathrm{d}x\mathrm{d}y\mathrm{d}z \tag{4.34}$$

For the chosen plate shape we obtain:

$$U_p = \frac{128}{15} \frac{E_{poly}\, h_{plate}^3\, w_{plate}\, d_0^2}{L_{plate}^3} \tag{4.35}$$

Setting $U_k = U_p$ (from Eq.4.32 and 4.35) and solving for the frequency $f = 2\pi\omega$ gives

$$f \;=\; \frac{h_{plate}}{\pi L_{plate}^2} \sqrt{\frac{21 E_{poly}}{2\rho_{pSi}}} \tag{4.36}$$

$$f \;\approx\; 237073 Hz \tag{4.37}$$

A plate resonance frequency of 237kHz has thus been derived given a polynominal plate shape. Actually, the exact shape does not matter much. Appendix H shows a more detailed list of steps used to derive the step frequency, where instead of a polynominal shape, a sinusoidal shape is used as starting point. It turns out that the resonance frequency is 240694Hz in this case, only about 1.5% different than the polynominal approach.

Note that [73] presents an expected resonance frequency of 304kHz. If we assume that a μWalker with 180μm plate was under attention, then the above presented method yields about 316.6kHz.

In reality, it is questionable whether any noticeable performance increase is present at the resonance frequency compared to lower frequencies. Fixing and releasing the μWalker legs during each step could be one reason. Another issue is air damping, which dramatically decreases performance – especially at the high resonance frequencies calculated for the plate.

4.1.5 Statical plate model

This subsection relies on work presented in [40] and concentrates around a statical model of the μWalker plate. It is implicitly assumed that there are no axial forces in the plate (Euler-Bernoulli beam), as at least one of the legs is free to move sideways. The main feature of the model is the presence of a stick region of the plate for voltages above pull-in, which affects the step size. Basically, the main results follow from considering equilibrium between the derivatives of the elastic and electrostatic energy potentials with respect to certain model variables variables, as will become clear below.

Plate shape

The starting point is to define the shape of the plate. To keep the equations tractable, it was chosen for a fourth order polynominal shape, however different basic shapes (trigonometric functions, etc) would yield results very close to the ones presented here. A simplified version of Eq. 4.24 is:

$$y(x) = d - a\left(1 \ - \ X^2\right)^2 \ , \tag{4.38}$$

where $y(X)$ is the vertical deflection, $X \in [-1,\ 1]$ is a parameterization of the shape and L_m is the Euclidean distance between the plate ends. The length of the plate is normalized in the beginning ($L_0 = 2$), to keep the tractability of the equations and thus increase the model clarity. The beam profile is assumed to be a function depending only on a, where $a < d$ and d is the distance at rest between the beam and the contact surface. Variable a is the distance between the rest position and the current position of the center of the beam (mode (b) in Fig.4.6(a)).

Figure 4.6(a) represents the three possible modes that the plate can be in. If the applied voltage is zero ($V_{plate} = 0$), then the plate is at rest. For voltages smaller than the pull-in voltage ($V_{plate} < V_{pull-in}$) the free mode is active and a is changes until equilibrium is found. For larger voltages a part of the plate sticks to the surface. Also in the third mode, the bending segments follow the same polynominal shape (Eq. 4.38).

Figure 4.6(b) shows the Euler and the Euler-Bernoulli approximations of a part of the bending plate, with $\mathrm{d}s$ an infinitesimal part of it. For the Euler model, the x-coordinate of the rightmost point remains the same, no matter the displacement, so that the length of $\mathrm{d}s$ varies with deflection. According to the sketch, the curvature is given by a relation between the angle $\mathrm{d}\phi$ and the infinitesimal plate length $\mathrm{d}s$:

$$\kappa(x) = \frac{\mathrm{d}\phi}{\mathrm{d}s} \ . \tag{4.39}$$

For the Euler-Bernoulli case which will be used further on, the plate has constant length and does not elongate due to a deflection, such that $\frac{\mathrm{d}s}{\mathrm{d}X} = 1$.

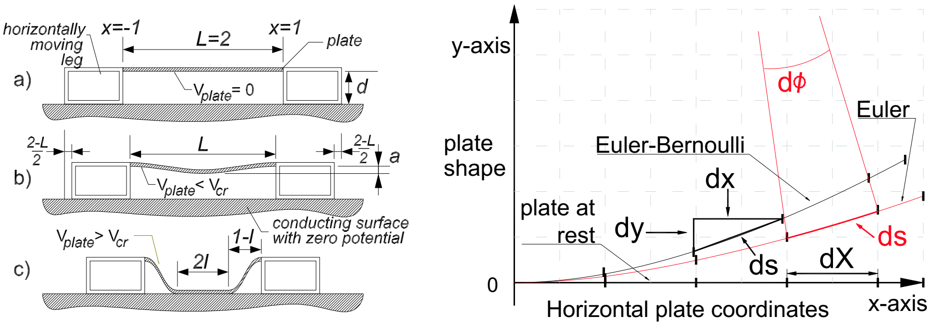

(a) The plate is always in one of the three modes: (a) at rest, (b) in free mode or (c) in stick mode.

(b) The Euler-Bernoulli approximation of a bending element.

Figure 4.6: Considerations of the plate shape proposed.

Thus for our case, $\mathrm{d}X$ and $\mathrm{d}s$ are equal. At this point, the Pythagoras Theorem [4] is used to derive $\partial_s x(s)$:

$$
\begin{aligned}
(\mathrm{d}x(X))^2 + (\mathrm{d}y(X))^2 &= (\mathrm{d}s(X))^2 && (4.40)\\
\left(\frac{\mathrm{d}x(X)}{\mathrm{d}s}\right)^2 + \left(\frac{\mathrm{d}y(X)}{\mathrm{d}s}\right)^2 &= \left(\frac{\mathrm{d}s(X)}{\mathrm{d}s}\right)^2 && (4.41)\\
(\partial_s x(X))^2 + (\partial_s y(X))^2 &= 1\,\forall s && (4.42)\\
\partial_s x(X) &= \sqrt{1-(\partial_s y(X))^2}\,. && (4.43)
\end{aligned}
$$

Then, from [69], we can approximate $\partial_s x(X)$ by the McLaurin series:

$$
(1+\upsilon)^n = 1 + n\upsilon + n(n-1)\frac{\upsilon^2}{2!} + n(n-1)(n-2)\frac{\upsilon^3}{3!} + \ldots\,, \tag{4.44}
$$

where $\upsilon := -(\partial_s y(X))^2$ and $n = \frac{1}{2}$. This gives:

$$
\begin{aligned}
\partial_s x(s) &= 1 - \frac{1}{2}\partial_s y(X)^2 - \frac{1}{2}\frac{1}{2}\frac{\partial_s y(X)^4}{2!} + \ldots && (4.45)\\
&\approx 1 - \frac{1}{2}\partial_s y(X)^2 \iff && (4.46)\\
\partial_s x(X) &\approx 1 - \frac{1}{2}\left(4aX\left(1-X^2\right)\right)^2 && (4.47)\\
&\approx 1 - 8a^2\left(1-X^2\right)^2 X^2\,, && (4.48)
\end{aligned}
$$

given that for $\partial_s y(X)$, the derivative of the shape with respect to the reference coordinate, holds:

$$\partial_s y(X) = 4a\left(1 - X^2\right)X\ . \tag{4.49}$$

If a (the deflection at the center) is known, then the distance between the plate ends equals:

$$\begin{aligned} L &= \int_{-1}^{1} \partial_s x(X)\mathrm{d}X && (4.50)\\ &\approx 2 - \frac{128}{105}a^2\ . && (4.51) \end{aligned}$$

Elastic energy

Now that the shape of the plate has been defined, we proceed by calculating the bending energy E_b, which is a function of the beam curvature κ. The equation for the curvature is taken from [23]:

$$\begin{aligned} \kappa(X) &= \frac{\partial y(X)}{\partial X} \cdot \frac{\partial^2 x(X)}{\partial X^2} - \frac{\partial x(X)}{\partial X} \cdot \frac{\partial^2 y(X)}{\partial X^2}\ ; && (4.52)\\ \kappa(X) &= \left[4a\left(1-X^2\right)X\right] \cdot \left[32a\left(1-X^2\right)X^3 - 16a^2\left(1-X^2\right)X\right] - \\ &\quad \left[1 - 8a^2\left(1-X^2\right)X^2\right] \cdot \left[-8aX^2 + 4a\left(1-X^2\right)\right] \\ &= 160a^3X^4 - 224a^3X^6 - 32a^3X^2 + 96a^3X^8 + 12aX^2 - 4a \\ \kappa(X) &\approx 12aX^2 - 4a, && (4.53) \end{aligned}$$

where the second order derivatives have been obtained from Eq. 4.43 and 4.49. The latter approximation is valid for a very small a like in our case. Thus,

$$\begin{aligned} E_b &= \int_{-1}^{1} \frac{E_{poly}I_{plate}}{2}\kappa(X)^2\,\mathrm{d}X && (4.54)\\ &= \frac{64}{5}E_{poly}I_{plate}a^2 && (4.55)\\ &= \frac{16E_{poly}w_{plate}h_{plate}^3a^2}{15}\ , && (4.56) \end{aligned}$$

with I_{plate} the moment of inertia as defined on page 71.

Electrostatic energy

Let us now consider the electrostatic energy stored in the plate-surface combination. First, the electric field of an infinitely long capacitor is parallel to the plate and can be written as:

$$E_{\|}(X) = \frac{V_{plate}}{y(X)}\ . \tag{4.57}$$

The charge density – also called electric displacement – $\rho(x)$ is:

$$\rho(X) = \epsilon_0 E_{\|}(X)\ . \tag{4.58}$$

This approximation can be used for our device as well, because $d \ll L_{plate}$ (see Fig.4.6(a)). In this way, the electrostatic energy density δE_e can be expressed as:

$$\begin{aligned} \delta E_e &= \frac{\epsilon_0}{2} E_{\|}(X)^2 \,\mathrm{d}_{Vol} & (4.59)\\ &= \frac{\epsilon_0 V_{plate}^2}{2y\left(X\right)^2} \,\mathrm{d}_{Vol}\ . & (4.60) \end{aligned}$$

By integrating over the volume between the plate and the surface, we obtain the electrostatic energy E_e:

$$\begin{aligned} E_e &= \int\limits_{Vol} \delta E_e \mathrm{d}_{Vol} & (4.61)\\ &= \int\limits_{-1+\frac{64a^2}{105}}^{1-\frac{64a^2}{105}} \int\limits_{0}^{y(X)} \int\limits_{0}^{w_{plate}} \delta E\big(\bar{x}\left(X\right), \bar{y}\left(X\right), \bar{w}\big) \mathrm{d}\bar{x}\ \mathrm{d}\bar{y}\ \mathrm{d}\bar{w}. & (4.62) \end{aligned}$$

To obtain the region to be integrated along the $\bar{x}$ axis, Eq.4.51 was used , which gives exactly the plate ends distance when the plate is bent at center by a. We proceed with eliminating the factor $\mathrm{d}x$ by using Eq.4.48:

$$\begin{aligned} \mathrm{d}x &= \frac{\mathrm{d}x(X)}{\mathrm{d}X} \cdot \mathrm{d}X & (4.63)\\ &= \partial_X x(X) \cdot \mathrm{d}X \\ &= \left(1 - 8a^2\ \left(1 - X^2\right)^2 X^2\right) \cdot \mathrm{d}X. \end{aligned}$$

Now the range of integration along $\bar{x}$ changes from $[-1 + \frac{64a^2}{105}\ ..\ 1 - \frac{64a^2}{105}]$ to $[-1\ ..\ 1]$ and the electrostatic energy E_e becomes:

$$\begin{aligned} E_e &= \int\limits_{-1}^{1} \int\limits_{0}^{y(X)} \int\limits_{0}^{w_{plate}} \frac{\epsilon_0 V_{plate}^2}{2y(X)^2} \left(1 - 8a^2\ \left(1 - X^2\right)^2 X^2\right) \mathrm{d}X\ \mathrm{d}\bar{y}\ \mathrm{d}\bar{w} & (4.64)\\ &= \frac{\epsilon_0 V_{plate}^2 w_{plate}}{2} \int\limits_{-1}^{1} \frac{1}{y(X)} \left(1 - 8a^2\ \left(1 - X^2\right)^2 X^2\right) \mathrm{d}X\ . & (4.65) \end{aligned}$$

To keep the equations tractable, we state that a is small; therefore the second term in Eq.4.65 is very small and as a consequence it is disregarded from here on:

$$E_e \approx \frac{\epsilon_0 V_{plate}^2 w_{plate}}{2} \int\limits_{-1}^{1} \frac{1}{d - a\left(1 - X^2\right)^2} \mathrm{d}X. \tag{4.66}$$

The integral in Eq. 4.66 is indefinite [10]. Using the symbolic package Maple^{TM}, the integrand IE_e is found:

$$\mathrm{I}E_e = \frac{a \operatorname{arctanh}\left[\frac{ax}{\sqrt{\left(a+\sqrt{ad}\right)\, a}}\right]}{2\sqrt{ad}\sqrt{\left(a+\sqrt{ad}\right)\, a}} + \frac{a \arctan\left[\frac{ax}{\sqrt{\left(-a+\sqrt{ad}\right)\, a}}\right]}{2\sqrt{ad}\sqrt{\left(-a+\sqrt{ad}\right)\, a}}\,. \tag{4.67}$$

We define $r := \sqrt{ad}$, $\Delta := \sqrt{\frac{d}{a}}$ and the integrand becomes:

$$\mathrm{I}E_e = \frac{1}{2r} \cdot \left[\frac{\operatorname{arctanh}\left[\frac{x}{\sqrt{\Delta+1}}\right]}{\sqrt{\Delta+1}} + \frac{\arctan\left[\frac{x}{\sqrt{\Delta-1}}\right]}{\sqrt{\Delta-1}}\right]\,. \tag{4.68}$$

The electrostatic energy (Eq. 4.66) becomes:

$$E_e = \frac{\epsilon_0\, V_{plate}^2\, w_{plate}}{2} \cdot \mathrm{I}E_e \Big|_{x=-1}^{x=1} \tag{4.69}$$

$$= \frac{\epsilon_0 V_{plate}^2 w_{plate}}{4r} \left[\frac{\operatorname{arctanh}\left[\frac{1}{\sqrt{\Delta+1}}\right]}{\sqrt{\Delta+1}} + \frac{\arctan\left[\frac{1}{\sqrt{\Delta-1}}\right]}{\sqrt{\Delta-1}}\right]\,. \tag{4.70}$$

This function is difficult to manipulate analytically, therefore an approximation is proposed which is based on a square root singularity[2]:

$$E_{e_{appr}} = \frac{\epsilon_0\, V_{plate}^2\, w_{plate}}{2d} \cdot \left[2.2\left(\frac{1}{\sqrt{1-\frac{a}{d}}} - 1\right) + 2\right] \tag{4.71}$$

$$= \frac{\epsilon_0\, V_{plate}^2\, w_{plate}}{d} \cdot \left(\frac{1.1}{\sqrt{1-\frac{a}{d}}} - 0.1\right)\,. \tag{4.72}$$

Note that this approximation is used in the case presented, when no insulation layer is taken into account. Figure 4.7(a) shows the relation between the exact energy function (Eq.4.70) and the approximation (Eq.4.72), both with respect to $\frac{a}{d}$. This relation is especially useful for the free mode of the plate, namely mode (b) in Fig. 4.6(a).

---

[2] This type of singularity is of the form $\frac{\alpha}{1-\sqrt{\beta}}$ with $\alpha \in \mathbb{R}$, $0 \leq \beta \leq 1$, such that the numerator becomes zero if $\beta = 1$ and we have a singularity.

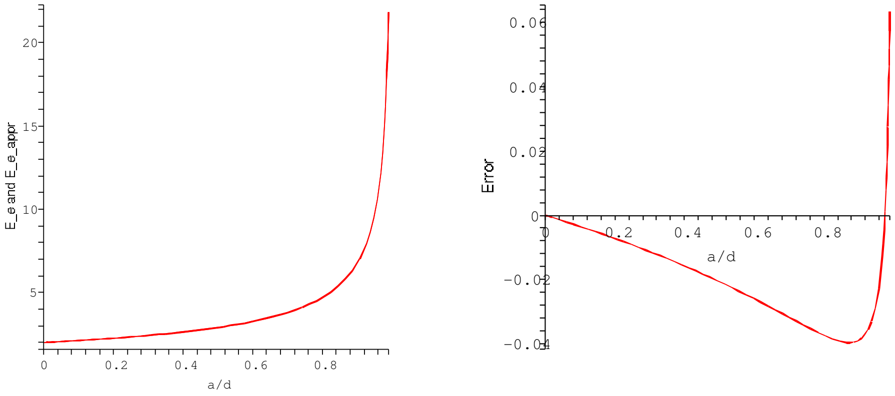

(a) E_e and the approximated electrostatic energy $E_{e_{appr}}$, when $\epsilon_0 V_{plate}^2 w_{plate}/2 = 1$.

(b) Error plot of $E_e - E_{e_{appr}}$.

Figure 4.7: Shape of the electrostatic energy as a function of the bending parameter a.

In this light, only the left part of the plot is relevant, since the plate reaches the critical point around $a = 0.4d$ (as will be shown shortly). The error plot (Fig.4.7(b)) confirms the fact that the estimation proposed matches the original function (E_e) well, as the error between the normalized energy functions does not exceed 0.04 for the range $0 < a < 0.9d$.

From Fig. 4.7(a) it also follows that the exact value of the coefficient a is rather hard to determine experimentally, especially given the noise and slight variations in the plate dimensions, material properties, as well as the exact value of the applied voltage. For instance, we know that the electrostatic energy E_e scales with the square of V_{plate}, and from Fig. 4.7(a) we see that a, in turn, is quite sensitive to changes in E_e. As a consequence, small changes in the voltage input will have a big impact on the exact magnitude of a, which makes it difficult to estimate the exact shape while the plate is in free mode.

Electroelastic energy and pull-in voltage

In this part, we consider balance between the electrostatic and bending energy potentials in the plate. A balance is reached between these potentials, when there is no net flow of energy between the electrical and mechanical domains. In other words, there must be a force balance.

An important remark here is that $E_{e_{appr}}$ given in Eq. 4.72 is strictly spoken not the electrostatic energy but the co-energy (denoted by E_e^* from here on), because it is expressed in the input variable (applied voltage V_{plate}) instead of the state variable (charge q). From the co-energy, we can derive the energy function E_e by the (inverse) Legendre transform [7, 9]:

$$E_e^* = -\mathfrak{L}\left\{E_e\right\} = -\left(E_e - \frac{\partial E_e}{\partial q}\, q\right). \tag{4.73}$$

The energy becomes:

$$E_e = V_{plate}\, q \; - \; E_e^*, \tag{4.74}$$

where we replace E_e^* by $E_{e_{appr}}$. The total energy E_{tot} in the system – also called the Hamiltonian – is the sum of the bending and the electrostatic energy:

$$E_{tot} = E_b + E_e. \tag{4.75}$$

The force balance from energy considerations is obtained by taking the derivative of E_{tot} with respect to state variable a:

$$\begin{aligned}
\frac{\partial E_{tot}}{\partial a} &= 0 && (4.76)\\
\frac{\partial\left(E_b + E_e\right)}{\partial a} &= 0 && (4.77)\\
\frac{\partial\left(E_b + \left(V\, q - E_e^*\right)\right)}{\partial a} &= 0 && (4.78)\\
\partial_a E_b - \partial_a E_e^* &= 0 && (4.79)\\
\frac{128}{5} E_{poly} I_{plate}\, a - \frac{0.55 w_{plate} \epsilon_0 V_{plate}^2}{d^2\left(1 - \frac{a}{d}\right)^{\frac{3}{2}}} &= 0\,. && (4.80)
\end{aligned}$$

Solving for V_{plate} yields the critical voltage V_{cr}, also called the pull-in voltage:

$$V_{cr} = \sqrt{\frac{128 E_{poly}\, h_{plate}^3\, a\, d^2}{33\epsilon_0}\left(1 - \frac{a}{d}\right)^{\frac{3}{2}}}\,. \tag{4.81}$$

Note that the critical voltage is defined for generalized plate length, i.e. the plate length is set to $L_{plate} = 2$. Moreover, now we deal with non-linear components, such that the pull-in voltage obtained here is not identical to the one in Eq. 4.20.

A maximum of this function is obtained at $a = \frac{2d}{5}$ by differentiating Eq. 4.81 with respect to a. In a nut shell, this means that for voltages initiating a deflection at the center of the plate which is larger than 40% of the distance between the plate and the ground, there will be no stable situation anymore. The plate will move towards the ground, into the stick region (mode (c) in Fig. 4.6(a)). Compare this to 33% deflection of the total distance, which holds for linear components (Section 4.1.3).

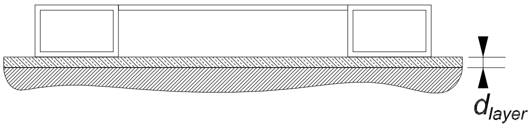

Figure 4.8: The walking surface of thickness d_{layer} is of great importance.

Stick region

Here we present a way to express the energy potential of the system both under and above the critical point. We will do this by introducing a configuration variable ξ but first let us introduce a small, yet important factor into the model, namely the silicon nitride layer (Fig. 4.8) which is represented by δ in the model.

With this addition, the effective distance between the plate and the other electrode, which is the bulk material under the walking surface, becomes (see also Figs. C.1, C.2 on page 165):

$$h = d + \frac{d_{layer}}{\epsilon_{Si_RN}} \Longleftrightarrow h = d\,(1+\delta)\,, \text{with } \delta = \frac{d_{layer}}{d\,\epsilon_{Si_RN}} \ll 1\,, \tag{4.82}$$

where ϵ_{Si_RN} is the electric permittivity of the insulating layer. Intuitively, the effective distance h between the plate center and the surface has increased due to the addition of the silicon nitride layer. The factor δ is small in general, because the layer thickness is small and because ϵ_{Si_RN} has a relatively high permittivity (around 7.6).

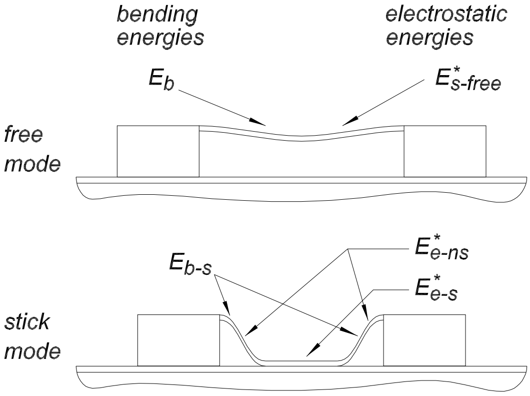

Figure 4.9: The electrostatic co-energy and bending energy potentials corresponding to the free mode and the stick mode.

Table 4.1: The mechanical energies and electrical co-energies for the free and stick mode.

	bending energy	electrostatic energy
free mode	E_b	E^*_{s-free}
stick mode	E_{b-s}	E^*_{e-ns}, E^*_{e-s}

Before deriving the various electrostatic co-energies and mechanical energies involved, let us shortly introduce them by means of Fig. 4.9 and Table 4.1. The bending energy and the electrostatic co-energy for the free mode are E_b and $^*E_{s-free}$, respectively. In the case of applied voltages above $V_{pull-in}$, there is a finite stick area and the (co-)energies are denoted as E_{b-s} for the bending and E^*_{e-ns}, E^*_{e-s} for electrostatics (here the total co-energy is composed of the co-energy in the bending parts and the co-energy in the stick part).

Incorporating the insulating walking layer (Fig. 4.8) into the equation for the electrostatic co-energy of the plate under free mode means replacing d in Eq. 4.72 by the effective distance h. This yields the electrostatic co-energy of the bending parts of the plate in free mode (plate does not touch the surface):

$$E^*_{s-free} = \frac{\epsilon_0 \, V^2_{plate} \, w_{plate}}{d(1+\delta)} \cdot \left[1.1 \left(\frac{1}{\sqrt{1-\frac{a}{d}}} - 1 \right) + 1 \right] \; . \tag{4.83}$$

If the plate does stick to the surface, then the electrostatic co-energy is split in one part for the two regions that bend and another for the section that sticks on the surface.

The co-energy density dE^*_{e-s} at the part of the plate which sticks – this is $2l$ in mode (c) of Fig. 4.6(a) – is:

$$dE^*_{e-s} = \frac{\epsilon_0 V^2_{plate}}{2\left(\frac{d_{layer}}{\epsilon_{Si_RN}}\right)^2} \mathrm{d}_{Vol} \Longleftrightarrow dE^*_{e-s} = \frac{\epsilon_0 V^2_{plate}}{2\;(d\,\delta)^2} \mathrm{d}_{Vol} \; . \tag{4.84}$$

Using again Eq. 4.61 yields the electrostatic co-energy for the sticking part, E^*_{e-s}:

$$E^*_{e-s} = \frac{\epsilon_0 l w_{plate} V^2_{plate}}{d\,\delta} \; . \tag{4.85}$$

The above presented energy is only for the sticking part. The bending parts of the plate also act as a capacitor. The electrostatic co-energy for one such part is denoted as E^*_{e-ns}:

$$E^*_{e-ns} = (1-l)E_e\big|_{(a=d)} \tag{4.86}$$

$$E^*_{e-ns} = \frac{(1-l)\,\epsilon_0 w_{plate} V^2_{plate}}{d\,(1+\delta)} \cdot \left[\frac{1.1}{\sqrt{1-\frac{a}{d(1+\delta)}}} - 0.1\right]\Bigg|_{(a=d)} \tag{4.87}$$

$$E^*_{e-ns} \approx \frac{(1-l)\,\epsilon_0 w_{plate} V^2_{plate}}{d} \cdot \left[\frac{1.1}{\sqrt{\delta}} - 0.1\right] . \tag{4.88}$$

In Eq. 4.86, $E_e\big|_{(a=d)}$ is from Eq. 4.66 where it is supposed that $a = d$. In the last step, we assume that δ is very small.

The bending energy in free mode (E_b) was derived in Eq. 4.56. For bending in the stick mode, the effective length of the bending parts is smaller than in free mode. To find E_{b-s}, we reuse Eq. 4.54, but now we substitute X by $\frac{X}{(1-l)}$ because the total plate length that bends is now smaller due to the stick region:

$$E_{b-s} = \int\limits_{1-l}^{-(1-l)} \frac{E_{poly} I_{plate}}{2} \kappa(X)^2 \mathrm{d}X \tag{4.89}$$

$$= \int\limits_{1-l}^{-(1-l)} 8 E_{poly} I_{plate} a^2 \left(9\left(\frac{X}{1-l}\right)^4 - 6\left(\frac{X}{1-l}\right)^2 + 1\right) \mathrm{d}X. \tag{4.90}$$

Also here holds $a = d$ because of stick. After solving the integral, it turns out that E_{b-s} can be written as:

$$E_{b-s} = \frac{E_b}{(1-l)^3}\Bigg|_{(a=d)} \iff \tag{4.91}$$

$$E_{b-s} = \frac{16 E w_{plate} h^3_{plate} d^2}{15\,(1-l)^3} . \tag{4.92}$$

The total energy is now given by the difference between the bending energy and the sum of the electrostatic co-energies acting on the straight and bending parts of the plate:

$$E_{tot} = E_{b-s} - (2E^*_{e-ns} + E^*_{e-s}). \tag{4.93}$$

The electrostatic co-energy in the bending parts ($2E^*_{e-ns}$) is assumed to be of small importance compared to E^*_{e-s}, because $\delta \ll \sqrt{\delta}$ and therefore $E^*_{e-s} \gg E^*_{e-ns}$. In an intuitive way, the electrostatic co-energy stored in the sticking part of the plate is much larger than in the bending parts, because the distance between the plate and the surface is much smaller for the stick part. Therefore, E^*_{e-ns} is disregarded from here on:

$$E_{tot} \approx E_{b-s} - E^*_{e-s} . \tag{4.94}$$

We can thus express the energy potential as a function which varies depending on l. To find the minimum energy potential and the minimum stick distance l_{min} for the minimum energy, we differentiate Eq. 4.94 with respect to l:

$$\frac{\partial E_{tot}}{\partial l} = 0 \Longleftrightarrow \frac{16 E_{poly} w_{plate} h_{plate}^3 d^2}{5\,(1-l)^4} - \frac{\epsilon_0 w_{plate} V_{plate}^2}{d\delta} = 0\,. \tag{4.95}$$

Solving for l yields the minimum stick distance l_{min}:

$$l_{min} = 1 - \sqrt[4]{\frac{16 E_{poly} h_{plate}^3 d^3 \delta}{5\epsilon_0 V_{plate}^2}}\,. \tag{4.96}$$

If $l_{min} < 0$, then the plate touches the surface only at only one point.

It is recalled here that the calculation of the Euclidean distance between the ends of the plate gives the step size. At this point, it is better to generalize the function which gives the Euclidean plate ends distance (Eq. 4.51) by using an arbritrary plate length L_0 instead of 2. In case we incorporate the stick mode, Eq. 4.51 becomes:

$$L = L_0 - \frac{128 d^2}{105} \cdot \alpha(d,l)\,. \tag{4.97}$$

Function $\alpha(d,l)$ is chosen such that if $l = 0$ (plate does not touch the surface) then $L = L_0 - \frac{128d^2}{105}$ and in the infeasible case that $l = \frac{L_0}{2} - d$ (for instance due to an infinite V_{plate}), then $L = L_0 - 2d$. A possible interpolating function which fulfills these requirements is:

$$\alpha(d,l) = \frac{\left(\frac{L_0}{2} - d\right) - l}{\left(\frac{L_0}{2} - d\right)} + \frac{105}{128 d^2} \cdot \frac{l}{\left(\frac{L_0}{2} - d\right)} \cdot 2d\,, \tag{4.98}$$

then L becomes:

$$\begin{aligned} L &= L_0 - \frac{128 d^2}{105}\left[\frac{\left(\frac{L_0}{2} - d\right) - l}{\left(\frac{L_0}{2} - d\right)} + \frac{105}{128 d^2} \cdot \frac{l}{\left(\frac{L_0}{2} - d\right)} \cdot 2d\right] && (4.99)\\ &= L_0 - \frac{4d}{105}\left[\frac{32\left(dL_0 - 2d^2 - 2dl\right) + 105 l}{L_0 - 2d}\right]\,. && (4.100) \end{aligned}$$

In the special case that $L_0 = 2$, there holds:

$$L = 2 - \frac{2d}{105}\left[\frac{32(2d - 2d^2 - 2dl) + 105 l}{1-d}\right]\,. \tag{4.101}$$

This equation is actually a better approximation of the Euclidean distance between the plate ends than the one presented in [40]. The reason is that inserting $l =$

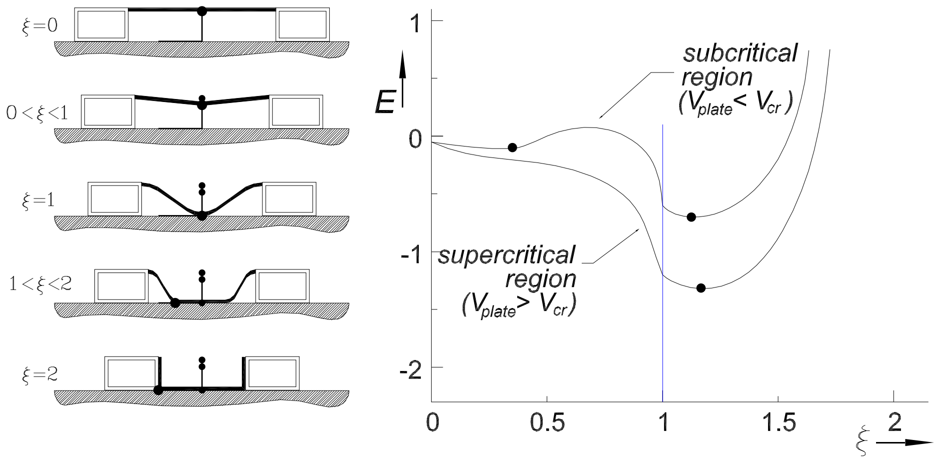

(a) A sketch of ξ, the configuration variable. The vertical path is the distance between the beam and the floor.

(b) A sketch of the energy as function of ξ for one sub- and one supercritical value of V_{plate}.

Figure 4.10: Towards a plate model that is valid both in free mode and in stick mode.

$\frac{L_0}{2} - d$ in [40] does not give the desired result $L = L_0 - 2d$ and moreover a fixed length ($L_0 = 2$) is taken into account, so the equations derived above are correct and more general.

To catch the stick and non-stick phenomena in one model, let us now introduce a configuration variable ξ where $0 \leq \xi \leq 2$:

$$\xi := \begin{cases} \frac{a}{d} & \text{if} \quad a < d \qquad (\xi < 1) \\ 1 + l & \text{if} \quad a = d \qquad (\xi \geq 1) \end{cases} \tag{4.102}$$

Figure 4.10(a) shows the shape of the plate for different values of ξ, from the minimum to the maximum value. Certainly, $\xi = 2$ is infeasible, as this value can only be reached when $V_{plate} \to \infty$.

As a prelude for Fig. 4.11, Fig. 4.10(b) is a sketch with two energy potentials of the system, each corresponding to an input voltage. Wherever a (local) minimum in the potential is reached, the system is in a stable point. In words, a (local) minimum of the energy potential means that there is no exchange of energy between the electrical and mechanical domain and the system is thus in equilibrium.

In one case – namely the subcritical region, there holds $V_{plate} < V_{cr}$. There are two possible local minima for the energy potential. The other case is called supercritical region and here we only have one stable minimum in the plot. Equation 4.81 is the boundary between the two regions.

The way in which the system jumps from the disappearing local minimum (left) to the absolute minimum (right) when $V_{plate} - V_{cr}$, depends on the voltage source characteristics and the plate dynamics. Here, we are mainly interested in the equilibrium points and hence the dynamics vanish. We continue by assuming without loss of generality that the jump happens instantaneously.

For the two sub- and supercritical cases in Eq. 4.102, the electroelastic energy potentials can be expressed as, respectively:

$$E_{<}(\xi, V_{plate}) = \frac{1}{2}K\xi^2 - \frac{1}{2}C\,V_{plate}^2\frac{1}{\sqrt{1+\delta-\xi}} \tag{4.103}$$

$$E_{>}(\xi, V_{plate}) = \frac{1}{2}\frac{K}{(2-\xi)^3} - \frac{1}{2}C\,V_{plate}^2\frac{\xi-1+\sqrt{\delta}}{\delta}\,, \tag{4.104}$$

where K and C were derived from Eq. 4.56 and Eq. 4.83, respectively:

$$E_b = \frac{16E_{poly}w_{plate}h_{plate}^3a^2}{15} \tag{4.105}$$

$$= \frac{1}{2}\cdot\frac{32E_{poly}\;w_{plate}\;h_{plate}^3\;a^2}{15} \tag{4.106}$$

$$= \frac{1}{2}\cdot\frac{32E_{poly}\;w_{plate}\;h_{plate}^3\;d^2}{15}\xi^2 \tag{4.107}$$

$$= \frac{1}{2}K\xi^2 \Longleftrightarrow K = \frac{32}{15}E_{poly}\;w_{plate}h_{plate}^3d^2 \tag{4.108}$$

and (4.109)

$$E_{s-free} = \frac{\epsilon_0 w_{plate}V_{plate}^2}{d\,(1+\delta)}\cdot\left[\frac{1.1}{\sqrt{1-\frac{a}{d(1+\delta)}}}-0.1\right]\Bigg|_{(a=d)} \tag{4.110}$$

$$\approx \frac{\epsilon_0 w_{plate}V_{plate}^2}{d\,(1+\delta)}\cdot\left[\frac{1.1-0.1}{\sqrt{1-\frac{a}{d}}}\right]\Bigg|_{(a=d)} \tag{4.111}$$

$$= \frac{\epsilon_0 w_{plate}V_{plate}^2}{h}\cdot\left[\frac{1}{\sqrt{1-\delta}}\right]\Bigg|_{(a=d)} \tag{4.112}$$

$$= \frac{\epsilon_0 w_{plate}V_{plate}^2}{h}\cdot\left[\frac{\sqrt{1+\delta}}{1+\delta^2}\right]\Bigg|_{(a=d)} \tag{4.113}$$

$$\approx \frac{1}{2}\cdot\left(2w_{plate}\epsilon_0\frac{\sqrt{1+\delta}}{h}\right)V_{plate}^2 \tag{4.114}$$

$$= \frac{1}{2}CV_{plate}^2 \Longleftrightarrow C = 2w_{plate}\epsilon_0\frac{\sqrt{1+\delta}}{h}\,. \tag{4.115}$$

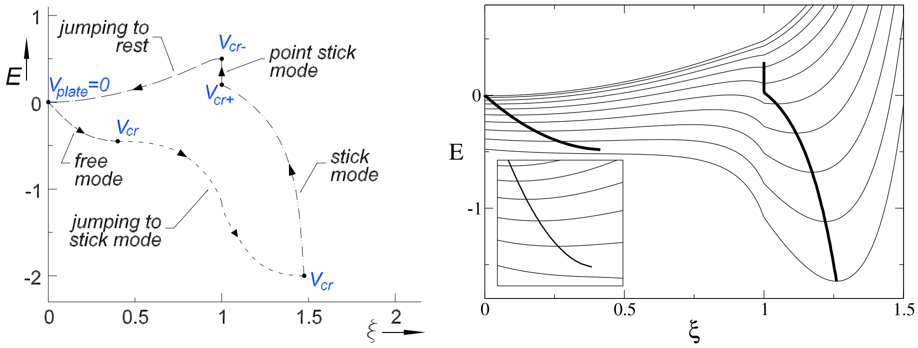

(a) Example of a possible trajectory for a certain set of design parameters.

(b) The two segments indicate the trajectory of the system (Property of N. E. Ligterink, co-author of [40]).

Figure 4.11: The total plate energy as a function of the configuration variable ξ and the input voltage V_{plate}.

In the general case where the length is L_0, we get:

$$K = \frac{256 E_{poly}\, w_{plate} h_{plate}^3 d^2}{15 L_0^3} \text{ and } C = \frac{\epsilon_0 L_0 w_{plate}\sqrt{1+\delta}}{h} \;. \tag{4.116}$$

Plate modes and hysteresis

According to the theory presented, we define five different modes, where the plate energy potential can be in. These modes are discussed next, after which some energy-related topics will follow.

Figure 4.11(a) shows a typical trajectory during the actuation of the plate to obtain one step. The first domain is the *free mode*. The voltage potential increases from zero up and there is a balance between the electrostatic co-energy and the bending energy, which is expressed by Eq. 4.103. Any point on this mode is a stable equilibrium and moving from one point to the other is achieved by slightly altering the input voltage.

As the voltage increases above a certain critical value (V_{cr} in Eq. 4.121), the electrostatic co-energy dominates and no equilibrium of the energy potential exists anymore. The value of the critical voltage follows by differentiating Eq.

4.103 with respect to ξ and solving for V_{plate}:

$$\begin{aligned}
\frac{\partial E_{<}(\xi, V_{plate})}{\partial \xi} &= 0 \qquad (4.117)\\
K\xi - \frac{C\,V_{plate}^{2}\,(1+\delta-\xi)^{-\frac{3}{2}}}{4} &= 0 \qquad (4.118)\\
V_{plate} &= \sqrt{\frac{4K\xi\,(1+\delta-\xi)^{\frac{3}{2}}}{C}}\,. \qquad (4.119)
\end{aligned}$$

Now in order to find the marginal value of ξ, we differentiate Eq.4.119 with respect to ξ and solve:

$$\frac{\partial V_{plate}}{\partial \xi} = 0 \quad \Longrightarrow \quad \xi = \frac{2}{5}(1+\delta). \tag{4.120}$$

Indeed, the added insulation layer has a linear effect on the critical value of ξ. Filling this into Eq. 4.119 yields the critical voltage in the presence of the insulation layer:

$$V_{cr} = \sqrt{\frac{8K(1+\delta)^{\frac{5}{2}} \cdot \left(\frac{3}{5}\right)^{\frac{3}{2}}}{5C}}\,. \tag{4.121}$$

Thus, this situation is reached at $\xi = \frac{2}{5}(1+\delta)$ and is called *jumping to stick mode*. As a consequence, the system suddenly jumps to another stable situation, where a part of the plate sticks to the surface. Here, we again have a local minimum of the energy potential (Eq. 4.95). During stick, ξ can be derived from Eq. 4.104:

$$\frac{\partial E_{>}(\xi, V_{plate})}{\partial \xi} = 0 \quad \Longrightarrow \quad \xi = 2 - \sqrt[4]{\frac{3K\delta}{CV_{plate}^{2}}}\,. \tag{4.122}$$

In the *stick mode*, the voltage is reduced more and more. This in turn decreases the stick length of the plate (decreasing ξ value). As the voltage is decreased, the stick length goes to zero, which is called *point stick mode*. The plate only sticks at one point. The range of points which make up the point stick mode can be found by filling in $\xi = 1$ in the equations of the energy derivative with respect to ξ for both under and above pull-in (Eq. 4.103 and 4.104):

$$\begin{aligned}
K\xi - \frac{C\,V_{plate}^{2}\,(1+\delta-\xi)^{-\frac{3}{2}}}{4}\bigg|_{\xi=1} = 0 \quad &\Longrightarrow \quad V_{cr}^{-} = \sqrt{\frac{4K\delta^{\frac{3}{2}}}{C}} \qquad (4.123)\\
\frac{3K}{2(2-\xi)^{4}} - \frac{CV_{plate}^{2}}{2\delta}\bigg|_{\xi=1} = 0 \quad &\Longrightarrow \quad V_{cr}^{+} = \sqrt{\frac{3K\delta}{C}}\,. \qquad (4.124)
\end{aligned}$$

For any point in the stick segment of Fig. 4.11(a), the following condition must hold:

$$\sqrt{\frac{4K\delta^{\frac{3}{2}}}{C}} < V < \sqrt{\frac{3K\delta}{C}} \,. \tag{4.125}$$

The presence of the point stick mode can also be derived from Fig. 4.11(b). In this plot, each isoline or segment of the waterfall (plotted from $0 \leq \xi \leq 1.5$) represents the energy potential in the system. This potential depends on ξ and is given for a fixed voltage V_{plate}. Actually, each isoline is composed of two parts, namely Eq.4.103 and 4.104: the first is valid for $0 \leq \xi \leq 1$ and the second for $1 \leq \xi \leq 2$.

Looking at the small vertical part which represents the system in the point stick mode, it becomes clear that locally, the left derivatives of the isolines ($\frac{\partial E_<}{\mathrm{d}\xi}$) are negative and the right derivatives ($\frac{\partial E_>}{\mathrm{d}\xi}$) are positive, which yields a local minimum. As the potential is decreased more and more, the size of the well in the energy potential decreases down to a singularity. After this, the local minimum vanishes due to the fact that $V_{plate} < V_{cr}^-$ and the system goes to the next and last mode, *jumping to rest*. This brings the system back at the starting point.

It must be said that in reality the point stick situation may not be visible or dissappear quickly due to dynamical effects and the small size of the local minimum. During measurements, decreasing V_{plate} did result in decreasing of the plate stick distance, but no point stick could be observed. Instead, the system jumped from a finite stick distance directly to the free mode (for the measured values, see Fig.3.7).

One of the interesting results is the total energy needed for one cycle. This energy loss is caused only by the second and last mode, when jumps occur. The energy lost while jumping to stick mode is calculated by taking the difference before and after the jump.

The energy $E_\downarrow(\xi, V_{plate})$ at the first jump (towards pull-in) is due to a change in the configuration parameter from the critical value $\xi_{before} = \frac{2}{5}(1+\delta)$ to $\xi_{after} = 2 - \sqrt[4]{\frac{3K\delta}{CV_{cr}^{+2}}}$:

$$\Delta E_\downarrow = E_>(\xi_{after}, V_{cr}) - E_<(\xi_{before}, V_{cr}) \tag{4.126}$$

$$\Delta E_\downarrow = \frac{3^{\frac{1}{4}}K}{6\zeta^{\frac{3}{4}}} \cdot \frac{CV_{cr}^2}{2\delta}\left[1 - (3\zeta)^{\frac{1}{4}} + \sqrt{\delta}\right] - \frac{2K}{25}(\delta+1)^2 + \frac{\sqrt{5}CV_{cr}^2}{2\sqrt{3}\sqrt{1+\delta}} \,, \tag{4.127}$$

with V_{cr} from Eq. 4.121 and $\zeta = \sqrt{\frac{K\delta}{CV_{cr}^2}}$. The energy at the second jump is

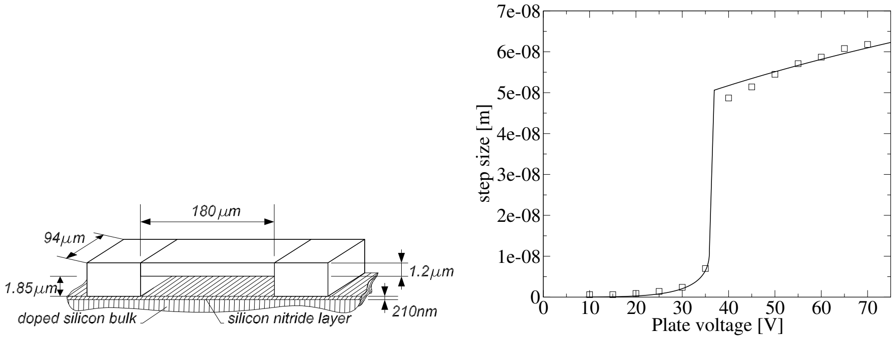

(a) Assumed dimensions.

(b) The squares represent measured step sizes (Property of E. Sarajlic). The solid line is the step size from the model, the dashed line is the step size for the adjusted plate thickness.

Figure 4.12: Model results and measurements of an existing μWalker.

calculated accordingly, as ξ goes from 1 to 0:

$$\begin{aligned} \Delta E_{\uparrow} &= E_{<}(0, V_{cr}^{-}) - E_{>}(1, V_{cr}^{-}) && (4.128) \\ &= -\frac{2K\delta^{\frac{3}{2}}}{\sqrt{1+\delta}} - \frac{K}{2}\left(1 - 4\,\delta\right)\ . && (4.129) \end{aligned}$$

In total, both jumps require:

$$\begin{aligned} \Delta E &= \Delta E_{\downarrow} + \Delta E_{\uparrow} && (4.130) \\ \Delta E &= \frac{3^{\frac{1}{4}}K}{6\zeta^{\frac{3}{4}}} - \frac{CV_{cr}^{2}}{2\delta} \cdot \left[1 - (3\zeta)^{\frac{1}{4}} + \sqrt{\delta}\right] - \frac{2K}{25}(\delta+1)^{2} + && (4.131) \\ & \frac{\sqrt{5}CV_{cr}^{2}}{2\sqrt{3}\sqrt{1+\delta}} - \frac{2K\delta^{\frac{3}{2}}}{\sqrt{1+\delta}} - \frac{K}{2}\left(1 - 4\,\delta\right)\ . && (4.132) \end{aligned}$$

Jumping energy loss – a case

This subsection is concluded by showing concrete results of the statical model proposed above. Consider the dimensions in Fig. 4.12(a), especially the shorter plate length[3].

An important remark here is that the effective value of δ is bigger than the layer thickness only. This could be explained by the fact that the plate is not a

---

[3] This set of dimensions was chosen because the measured data was readily available.

simple plate, but features bumps (Fig. 2.8 on page 19). Due to the presence of the bumps, δ cannot be determined accurately from the design and has been estimated to around $\delta = 0.22$, which is larger than the expected 0.014 if there were no bumps.

Additionally, it has been assumed that the effective thickness of the plate is $0.8\mu m$ instead of the original $1.2\mu m$. This leads to a decreased stiffness of the plate, which could be attributed to the structure of bumps –or better said holes– on the plate. The presence of such holes reduces the stiffness and thus the pull-in voltage.

Figure 4.12(b) shows measured and simulated values. The squares are measurements obtained from a real device. We can observe that the pull-in voltage is well-predicted by the model. The step size of about $50nm$ at pull-in voltage is well-estimated and also under and above pull-in a valid estimation results. Further, from the model follows that the exact thickness of the walking layer does not influence the results much.

The values for K and C are calculated from Eq. 4.116:

$$K \approx 7.71 \cdot 10^{-11} \quad \text{and} \quad C \approx 7.33 \cdot 10^{-14} \,. \tag{4.133}$$

Filling this into Eq. 4.121 yields a critical voltage of about $35.9V$.

Another interesting aspect is the amount of energy that is being lost at the moments when jumps take place. It is repeated here explicitly that this is not the amount of energy that is lost due to the impact (sudden change of the mass impulse), but the amount of charge that is being fed back to the actuation setup.

From Eq. 4.126, the total energy needed for one cycle is in this case:

$$\begin{aligned} E_{cycle} &\approx [E_{>}(\xi_{after}, V_{cr}) - E_{<}(\xi_{before}, V_{cr})] + \quad (4.134)\\ &\quad \left[E_{<}(0, V_{cr}^{-}) - E_{>}(1, V_{cr}^{-}]\right] \quad (4.135)\\ &= (-2.35 + 1.55) \cdot 10^{-10} + (-4.86 - 1.56) \cdot 10^{-11} \quad (4.136)\\ &= -1.45 \cdot 10^{-10} \,. \quad (4.137) \end{aligned}$$

Thus, about $0.15nJ$ is being lost for one cycle. This concludes the static modeling of the μWalker plate. To sum up, the step size, the energy consumption due to plate instability and the pull-in voltage are estimated with this model, which includes a number of energy modes for capturing the pull-in effect.

4.1.6 Towards a dynamical plate model

In the last subsection, we have seen how an energy-based model can predict several interesting parameters relevant for the μWalker design and actuation. A number of other (expected) issues are assumed relevant, amongst them the stick length of the plate, the plate dynamics and the axial forces in the plate which depend on the states of the two legs (clamped or free mode).

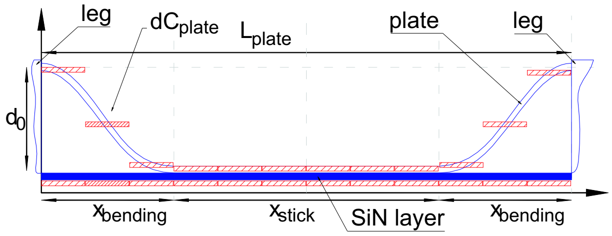

Figure 4.13: Non-linear plate capacitor.

For instance, according to the model, the stick region is about 41% of the total plate length in the case that $V_{plate} = V_{pull-in}$ and $\delta = 0.2$ (Eq. 4.96). Several related measurements were shown on page 34 Fig. 3.7. They suggest that the percentage of plate which sticks at pull-in is generally much lower than 41%. This fact emphasizes the need for a new, improved model, which solves this mismatch.

The electroelastic nature of the plate is modeled here by defining a non-linear capacitor like in Fig. 4.13. In line with the theory presented earlier for the sticking plate, for each small part dx there is a corresponding infinitesimal capacitor dC_{plate} and a counteracting spring force due to bending and axial forces in the plate. Moreover, the generated vertical force depends on the input voltage, as well as the plate shape. For instance, assume that the plate is straight, and at $t = 0$ we apply a voltage higher than the pull-in voltage. Due to the inertia of the plate mass, a stable situation with stick region will only be present after some time $t > 0$.

Assume again the polynominal plate shape $w(x)$ as in Eq. 4.24. The vertically generated infinitesimal force is calculated by:

$$\mathrm{d}F\left(w(x)\right) = \left.\frac{\partial \mathrm{d}E}{\partial w}\right|_{(x=x_l)} \quad \text{where } \mathrm{d}E = \frac{\mathrm{d}q^2}{2\mathrm{d}C_{plate}} \; . \tag{4.138}$$

The value of $\mathrm{d}C_{plate}$ varies and is composed of two parts in series:

$$\mathrm{d}C_{plate} = \left(\mathrm{d}C_{air}^{-1} + \mathrm{d}C_{Si_RN}^{-1}\right)^{-1} \text{ with} \tag{4.139}$$

$$\mathrm{d}C_{air} = \frac{\epsilon_0 \mathrm{d}A_{plate}}{d_0} \text{ and } \mathrm{d}C_{Si_RN} = \frac{\epsilon_0 \epsilon_{Si_RN} \mathrm{d}A_{plate}}{d_{layer}} \; . \tag{4.140}$$

The capacitor area is $\mathrm{d}A_{plate} = w_{plate}\mathrm{d}x$. The total electrostatic force becomes:

$$F_{el} = \int_0^{L_{plate}} \mathrm{d}F\left(w(x)\right) \mathrm{d}x \; . \tag{4.141}$$

The result is that we can now plot the net vertical force applied as a function of the applied voltage and the instantaneous beam shape:

$$F_{vert} = F_{el} - F_{bend} \; . \tag{4.142}$$

The bending force has been treated in the previous part for both with and without a stick region, and will not be repeated here.

With voltages higher than $V_{pull-in}$, a stick region is present at equilibrium. An estimation of the stick region as function of the applied voltage is interesting, because it the amount of the plate that sticks influences the plate capacitance (C_{plate}) considerably. The length of this stick region is derived by interpolation from measurements (Fig. 3.7, page 35):

$$x_{stick} = L_{plate} \frac{3V_{plate} + 10}{500} \; . \tag{4.143}$$

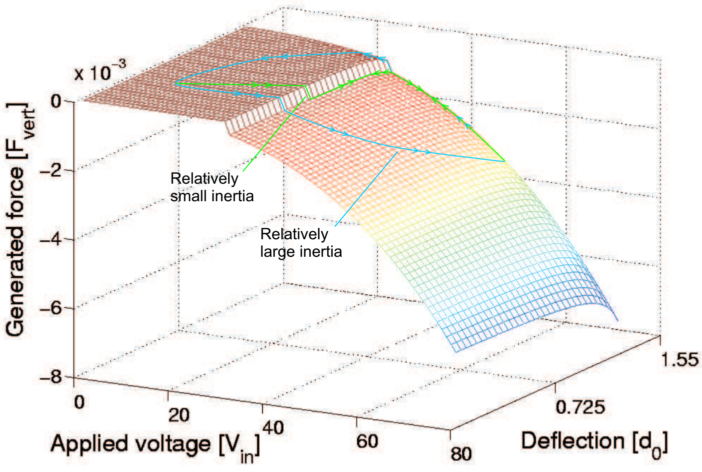

Figure 4.14: The net vertical force depends on the applied voltage and the deflection.

Figure 4.14 shows a mesh generated to calculate the force F_{vert} from the applied voltage and the deflection at the center of the plate. It was chosen to use a mesh for this sub-part of the μWalker model, in order to reduce the number of equations to be processed real-time during simulations.

In Fig. 4.14, we can see a step at the pull-in voltage of $32V$. For higher voltages, the net vertical force increases roughly with the square of the voltage, as expected. On the deflection axis, larger (instantaneous) bending for the same applied voltage yields a higher force.

During simulations, we attach an inertia to the mobile part of the plate, so that dynamics come into play. For very small inertia effects of the plate, the system trajectories on the mesh are very close in each other's proximity. The more the inertial effects play a role, the more the trajectory shapes are ellipsoidal. The inertia is not implemented in this part, which is the vertical part of the plate, but in the horizontal part of the plate, as will become clear in Subsection **Entire model** on page 101.

4.1.7 Beam stiffening

Depending on the conditions at the ends of a beam or plate (clamped, fixed in one direction or free), bending and sometimes axial forces oppose to the force that bends the structure. Axial forces are present when the beam is clamped at both sides and then bent. In this case, axially stress arises and the beam becomes a little longer. Because axial forces can be much larger than bending forces, they add considerably to the bending stiffness. The effect is called beam stiffening.

Some parts of the actuator system, especially the thin ones, cannot be modeled well by only taking into account the bending stiffness. This effect is generally present when the deflection of the specific part is in the same order of magnitude or bigger than its thickness.

A number of approximations have been suggested in literature [20, 45, 79], in order to avoid solving the Euler equation (Eq. 4.2). This results in reduced modeling complexity and simulation time without sacrificing too much from the point of view of accuracy.

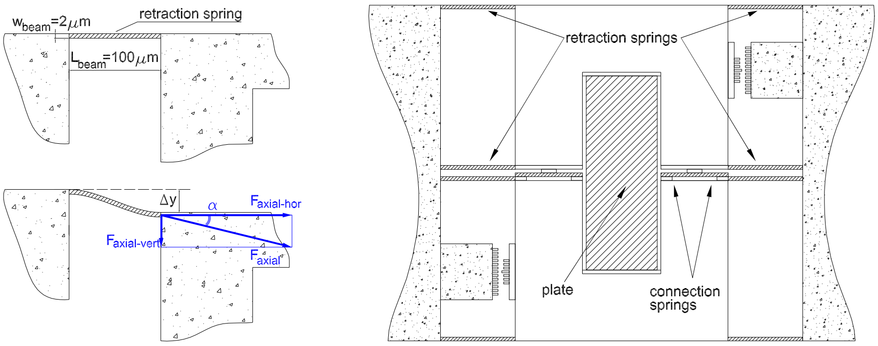

(a) Close-up of one retraction spring.

(b) Different bending components of the μWalker (top view).

Figure 4.15: Example where axial stresses dominate the bending stiffness.

Figure 4.15(a) illustrates a component which clearly shows beam stiffening behavior, namely a retraction spring in two dimensions (no out of plane movements considered at this stage). Assuming that the beam is fixed horizontally at both ends, and vertically only at the left end, the only unconstrained leg motion is vertical.

The other part of the leg is symmetric (see Fig. 4.15(b)), so that the leg can only move vertically and moments are being built at the connection between the retraction springs and the leg. The effect is now that the beams must become a little longer, as the present Euclidean distance between the ends of the beams has increased compared to the initial state. This elongation causes tension, also called tensile axial forces, in the retraction spring according to Eq.4.5.

The right part of Fig. 4.15 reveals the bending components of a standard μWalker. According to estimations derived from the theory presented below, only the retraction beams need special attention in this sense[4]. By measuring the deflection of these springs, we can derive the total horizontal force exerted by the μWalker at any moment in time, but more about this will be explained later.

The maximum deflection of the connection springs is only about one step size ($52nm$), hence the bending energy dominates here. The axial stiffness of the plate is too high for the plate to elongate noticeably (see Subsection 4.1.2 and Appendix G).

We can estimate upper and lower bounds of the axial force generated by the springs attached to one leg of the actuator (in Fig. 4.15(a) the force F_{axial}). As an upper bound, we calculate the force resulting from a fourth order polynominal of an S-shape. The lower bound is considered to be simply a string shape, which connects the ends of the springs by an Euclidean line segment.

If the axial tensile force applied by four springs of dimensions[5] $L.w.h = 100 \cdot 10^{-6}.2 \cdot 10^{-6}.5.5 \cdot 10^{-6}$ are plotted against the bending displacement, Fig. 4.16 results. As expected, if we assume pure tensile stress, then the string-like shape generates less counter force than the fourth order shape. The solution is actually somewhere in between, as we shall soon see.

Looking again at Fig. 4.15(a), the vertical component of the axial force is adding stiffness to the original bending force and follows from:

$$F_{axial-vert} = F_{axial} \arctan \alpha = F_{axial} \arctan \left(\frac{\Delta y}{L_{beam}} \right)$$

, where α is the angle between the horizontal component of the axial force ($F_{axial-hor}$) and the axial force (F_{axial}), from Fig. 4.15(a); Δy is the vertical deflection of the beam and L_{beam} is the beam length at rest.

---

[4] In Chapter 5, several other types of suspension are proposed, so that the beam stiffening effect is eliminated and the total stiffness of the retraction springs is reduced.

[5] The springs length was not chosen to be standard, to comply with the ANSYS simulation.

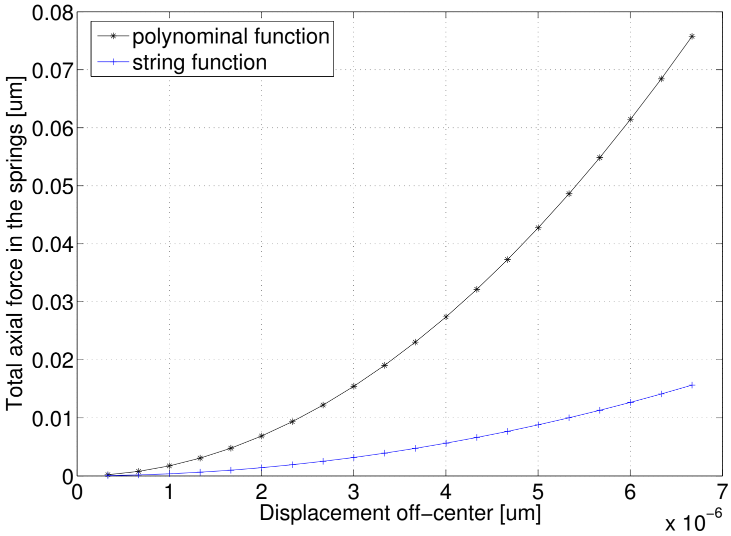

Figure 4.16: Resulting axial force depends on the assumed beam shape.

The values of $F_{axial-vert}$ of the two cases, the polynominal and the straight wire, can be seen further on in Fig. 4.17. Actually, in order to have a fair comparison with the other cases, the bending force was added to this force.

Unfortunately, the results from the two cases differ considerably, especially at the end of the travel distance of the μWalker. Therefore, a simplified model is proposed below (presented in [56]) in which $k_{bm.st.}$, the total stiffness (bending and axial stiffness), can be approximated by comparing the axial force to the buckling force of the structure (from [45]). The buckling force is the axially applied compressive force on a plate that is just enough make it buckle. The total stiffness $k_{bm.st.}$ is thus approximated by:

$$k_{bm.st.} \approx k_{tim}\left(1+\frac{F_{axial-vert}}{F_{buckling}}\right), \tag{4.144}$$

with k_{tim} the bending factor based on linear beam theory [21]:

$$k_{tim} = \frac{E_{poly} w_{beam}^3 h_{beam}}{L_{beam}^3}.$$

The vertical axial force $F_{axial-vert}$ can be written as ([45]):

$$F_{axial-vert} = \frac{3E_{poly} w_{beam} h_{beam} \left(\Delta y\right)^2}{5L_{beam}^3}$$

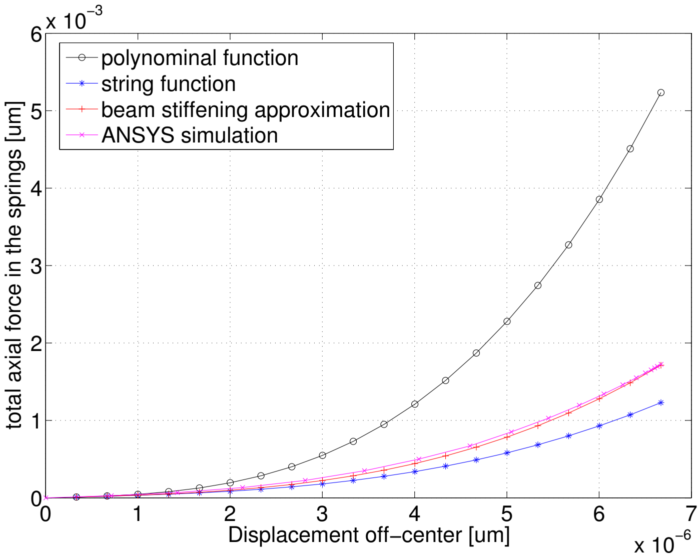

Figure 4.17: Comparison of the different estimations of counter force.

and the buckling force of the beam comes from [21]:

$$F_{buckling} = \frac{4\pi^2 E_{poly} w_{beam}^3 h_{beam}}{(2L_{beam})^2}.$$

Simplifying the above equations results in the equations for the total force due to bending of a beam with boundary restrictions like in Fig. 4.15(a):

$$F_{bm.st.} = k_{bm.st.}\, \Delta y \tag{4.145}$$

$$k_{bm.st.} = \frac{E_{poly} w_{beam}^3 h_{beam}}{L_{beam}^3} \left[1 + \frac{36\,(\Delta y)^2}{5\pi^2 w_{beam}^2} \right] \tag{4.146}$$

Figure 4.17 also shows a curve linking several points calculated with this approximation. Former simulations done by others [73] in ANSYS show a curve which is almost identical to the results from the approximation presented. Also, the ANSYS simulation and the derived force are clearly within the two bounds presented before (polynominal shape and simple wire), somewhat closer to the wire model than to the polynominal model. It can be concluded that the force derived is within the expected range. Therefore, the beam counter force derived here will be used throughout the models and simulations presented later on. A number of conclusions following from measurements in Chapter 3 imply the use of this approximation.

4.1.8 Contact model of the legs

The last important part of the sub-model is the contact between the legs and the walking surface. Parts of this subsection have been presented in [62, 60, 56].

The vast diversity of literature sources on tribology[6] has only grown more wild with the advent of micro and nano electromechanical systems. New terms are being introduced, while old ones are sometimes misused or reused. This and other factors lead to misconceptions and wrong interpretations which are found throughout the literature. For instance [78], while being generally considered a solid reference for MEMS design and modeling, presents a model on Coulomb friction which is proportional to velocity. This is clearly not in line with the general notions of friction, where the Coulomb force does not depend on velocity [25, 14, 65].

We start this subsection by a small survey of the basics of friction models, including pre-sliding, stick-slip, Coulomb friction, viscous friction and more. This theory is presented in much more detail in probably the most famous survey about friction up to date [25]. Then the friction model for the μWalker legs is enlighten, with an eye on simulation of the whole system.

Friction models

Friction is the overall process which takes place when two contact surfaces come into contact and slide with respect to each other. Lubrication may or may not be present. Roughly, the phenomenon of friction can be divided in the pre-sliding and the sliding mode. Let us first have a look at the pre-sliding regime, also called static friction or micro-slip.

The theory is mainly based on material asperities of both parts, which form temporary bonds, or imaginary springs. The amount of springs of the actual contact surface is very reduced compared to the apparent surface. This reduction becomes clear when regarding the μWalker legs. A texture of bumps is applied, so that actually only parts of a few bumps touch the walking surface instead of the whole leg area. The real contact surface is thus reduced to only a fraction of the apparent surface. A citation from [25] enlightens this:

In a BBC radio program, tribology pioneer F. P. Bowden observed that "putting two solids together is rather like turning Switzerland upside down and standing it on Austria – the area of intimate contact will be small" ..

In some models [25], these junctions between the materials at contact are modeled as linear springs, while in other they are non-linear [37]. Yet other models include a narrow dead zone around zero velocity, where the output velocity is set to zero [33, 8]. Note that the energy put into the system during pre-sliding is reversible, as it is stored in the imaginary springs. The stiffness of the imag-

---

[6] The study of friction, lubrication and wear.

inary springs depends on contact geometry, elasticity of materials and the applied normal force that pushes the materials together.

As the shear force on the springs increases above a certain value, the junctions break one by one. The force needed to break all connections and start sliding is called the breakaway force. The relation between the breakaway force and the applied force is given by the coefficient of stiction: $\mu_{stiction} = \frac{F_{breakaway}}{F_{applied}}$.

We are now in the sliding mode, where a number of phenomena can be distinguished. In the sliding mode, the boundary layer and possible lubrication or contamination particles play an important role. The boundary layer in the μWalker case is composed of mainly silicon oxide, which can resist a much lower shear stress[7] than the original material (polysilicon). This layer can become several tens of nm thick. For very low sliding velocities, the boundary layer lubricates the contact.

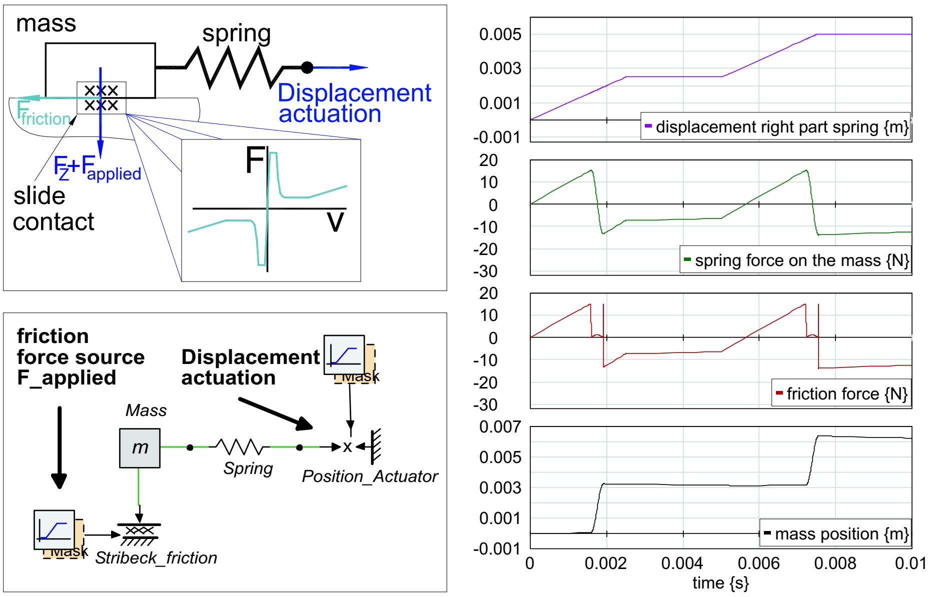

(a) Top: schematic view of the model. Bottom: 20-sim implementation of the mass-spring-stribeck model.

(b) From top to bottom: input position to the right part of the spring; spring force; generated friction force by the mass; mass position.

Figure 4.18: A hypothetical model to visualize the stribeck effect.

The velocity is now increased and we enter the stick-slip mode (Fig. 4.19).

---

[7] Shear stress acts tangential to the surface of a material.

This is an unstable mode, in the sense that the friction force decreases for larger velocities. For clarity, consider Fig. 4.18. The force on the sliding contacts is formed by gravity and an externally applied force $F_{applied}$, which is constant in this case. Another external signal is applied to the right part of the spring in order to increase the horizontal force on the mass. As soon as the force exerted by the spring on the mass exceeds $F_{friction}$, the mass comes into the stick-slip mode and starts to move. Figure 4.18(b) shows the applied position of the right part of the spring and the resulting force exerted on the mass as well as the mass displacement.

Due to the unstable nature of the stick-slip mode, the sliding contact dynamics arrives into a region where the motion opposing friction force does not change noticeably as a function of velocity. This is the Coulomb regime. Typically, the relation between the applied force (perpendicular on the contact surface) and the horizontally generated friction force ($F_{friction}$ in Fig. 4.18) is described by the constant factor $\mu_{sliding} = \frac{F_{sliding}}{F_{applied}}$. Only if $\mu_{sliding} << \mu_{stiction}$, will there a stick slip mode be present.

Finally as the velocity is increased and mostly due to full lubrication, the friction force increases linearly with sliding velocity, which is the viscosity regime.

With more and more experiments and model development taking place, some time-dependent phenomena like dwell time[8] and frictional memory[9] have been developed and are implemented in dynamical models concerning friction.

Dynamical models have some disadvantages. First, they may induce a change in causality at the border between the sliding and pre-sliding regime. In the pre-sliding regime, the decision for leaving the sliding regime depends on the magnitude of the breakaway force. In the sliding regime, the friction force is generally a function of the velocity. This issue can give raise to problems during implementation in simulation software.

Second, dynamical models add states to the system. One example is the length of the springs during the pre-sliding region. If the total model to be simulated is quite elaborated in terms of stiffness dynamics and simulation time – like it is the case with the μWalker model as we will see shortly – then a (dynamical) friction model can make the difference between a model that can be simulated and one that cannot be in reasonable time.

Another implementation issue is the fact that the states of these internal states must be reset each time the springs arrive into the pre-sliding region again – an operation which is not always possible with the available software due to energy discontinuity.

On the other hand, the measurements available at the time of writing do not indicate the presence of the above mentioned time-dependent dynamical

---

[8] The time between initiation and breakage of an imaginary spring like introduced earlier.

[9] A time delay between a change in velocity and the corresponding change in friction force.

effects, so that friction models including internal states are not considered necessary at this point.

The presence of drift in statical models refers to the fact that when the horizontal force on a sliding contact is under the break-away force, then the system is in stick mode, however the velocity is not zero but very small. As a result, the two contacts will slowly move with respect to each other in the simulations. This means that drift is introduced by the model, which is not present in the real system. This drift is inherently present in statical models and can become an issue, but generally it can be reduced to an acceptable value by changing some parameters in the statical friction model.

Legs friction implementation

The choice for a statical friction model of the contact between the μWalker legs and the walking surface is elaborated a little further. The vertically applied force on the contact is derived from the geometry, the electrostatic properties of the materials and the applied voltage. The applied voltage changes constantly between zero and a certain value (typically $30V$) and so does the vertically applied force. This means that the stribeck curve which models friction is actually being scaled according to the applied voltage: when the applied voltage is increased, then a larger horizontal force is required to bring the leg in slip mode. This can also be explained using a notion called 'cone of friction', however this is not treated further in this work.

Let us have a look at Fig. 4.19. No pre-sliding regime is present around zero velocity. Instead, the first regime consists of a smooth function which brings the system from zero velocity to the stick regime (second regime), where the stiction force is present. This way of modeling introduces some minor velocity-dependent damping, which is not existent in the system for these small velocities. By keeping the first regime small, the results of the friction model are not affected considerably by this has a big impact on simulation time and accuracy.

As the velocity increases even further, the third regime becomes valid, stick-slip. The name comes from the fact that this part makes stick-slip motion possible. Also this part is smooth and continuously differentiable. The fourth part is Coulomb friction. The friction force could not be obtained from measurements and had to be fitted during simulations. The last regime, which is the viscous regime, is virtually not reached during the simulations. The assumption is that no lubrication is present between the contact surfaces for normal operation speeds.

The implementation of legs friction model which will be used further on for simulations, is listed in Appendix I and is identical for both legs.

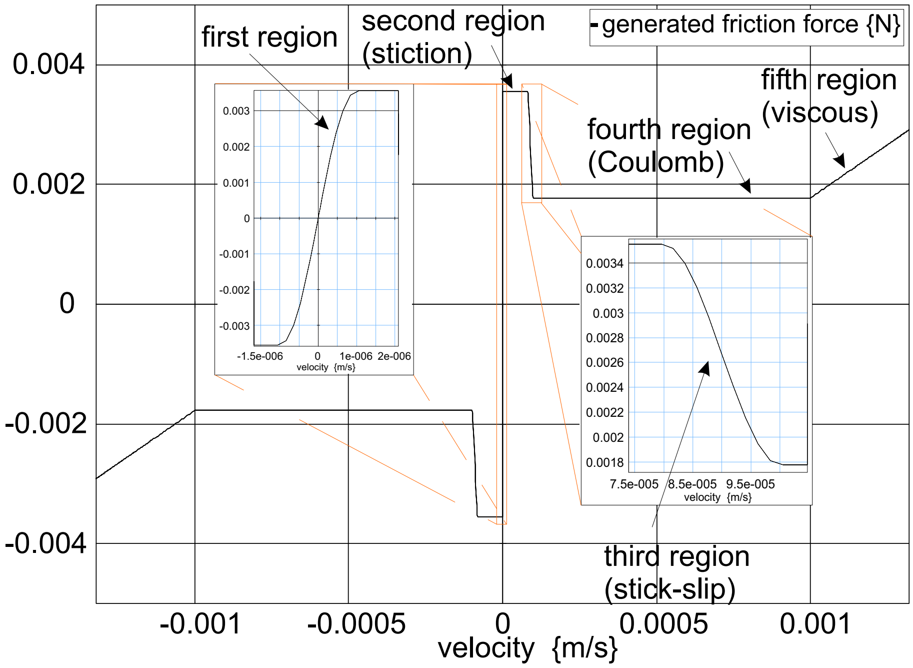

Figure 4.19: The F–v curve used for the friction of the legs, with five regimes.

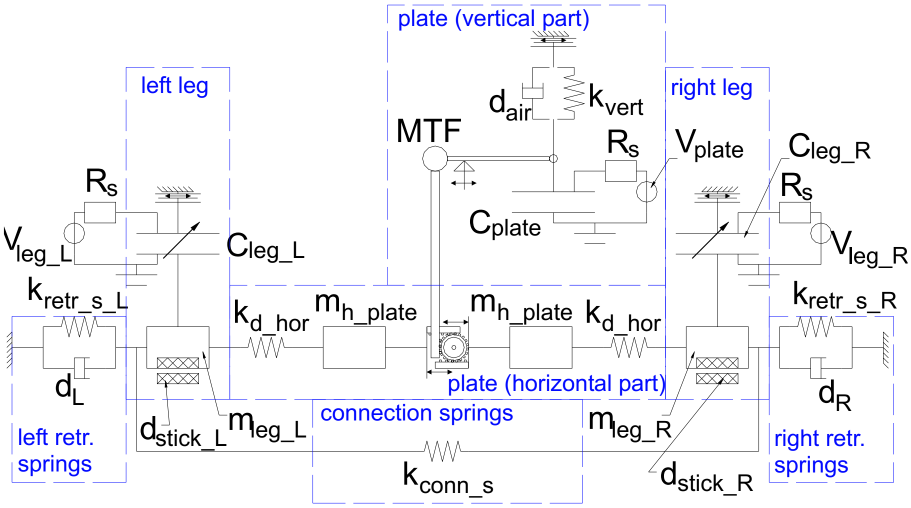

Figure 4.20: Schematic model of the μWalker model, with the plate as the central part.

4.1.9 Entire model

Here we aggregate the different parts shown in this chapter so far. The result is a (highly) nonlinear dynamical model including stick-slip of the legs, the pull-in phenomenon of the plate and beam stiffening in the retraction springs.

Figure 4.20 shows the main components of the total μWalker model. The simulations of this model will be shown in the following section, for now it is useful to review the overall model part by part.

We start by presenting the plate, which is divided into a horizontal and a vertical part. By applying a voltage V_{plate} via a cable with resistance R_s to the μWalker plate, and in combination with the instantaneous shape of the plate which influences C_{plate}, a vertical force is being generated in the plate. This electrostatic force, minus the force needed to bend the plate (k_{vert}) and to overcome the air friction force (d_{air}), is being converted by a modulated transformer (**MTF**) to the horizontal part of the model.

Regarding the transformer ratio, [85] mentions a ratio between 25 and ∞ for a device similar to the μWalker. This ratio decreases towards the minimum as the mid-plate deflection increases from zero to 2μm. The exact relation between the plate deflection at center and horizontal stepping is not relevant for very small deflections, which do not generate steps anyway in practice. Therefore, a transformer ratio of 29 was derived experimentally. Thus, the transformed ratio yields a smaller displacement, and a larger force.

The transformed vertical force is now converted to the horizontal part at a 1:1 ratio by the gear system, shown here only for orientation purposes (implicitly present in the 20-sim model shown later). The horizontal part of the plate consists of two symmetrical mass-spring pairs ($k_{d\_hor\_X}$ and $m_{h\_plate\_X}$), which together with the vertical part introduce plate dynamics[10]. The spring value $k_{d\_hor\_X}$ is chosen equal to the axial stiffness (expressed in Eq. 4.5). The value of the masses $m_{h\_plate\_X}$ was fitted such, that the eigen frequency of the mass-spring systems approximates the theoretically obtained result presented in an earlier subsection on page 4.1.4. The obvious assumption is made here, that the resonance frequency of the plate in vertical direction is the same as in the horizontal direction.

This approach of modeling the plate makes it possible to incorporate axial stiffness and more complex relations of the boundary conditions (the legs), which can slip or have a varying amount of stick force, depending on the applied voltages. This all translates into a boundary conditions dependent step size, which is indeed one of the targets of this model.

The legs are composed of a capacitor with one variable plate, C_{leg_X}, a mass m_{leg_X}, a vertical component of the retraction springs (not shown in the figure) and the stiction-friction model presented in the last subsection (d_{stick_X}). The same electroelastic model like for the plate applies to the legs, only here a simplified approach is more effective (linear spring and rigid capacitor plate). The legs are also interconnected via the four connection springs (k_{conn_s}), for more precise steps (see also Fig. 2.7).

It has been mentioned before that each of the legs is suspended above the ground by retraction springs ($k_{retr\_s\_X}$). These springs show the beam stiffening effect for in-plane deflections larger than one or two μm. Damping injection (d_X) is used to reduce the integration error in the integration solver during simulations. It does not have a great effect on the total system dynamics but it does decrease simulation time considerably.

In a more general context, two causes can be pointed for having difficulties during simulations. First, the simulation range covers several orders of magnitude, while the μWalker steps to be simulated are very small. Second, the plate dynamics has a high first order resonance frequency and the leg friction models show steep regions. Together, this means that the simulation accuracy must be very high to cope with the high order dynamics and on the other hand each simulation step in time is very small, so as to catch the dynamics to a sufficient degree of accuracy. To be concise, a lot of simulations are needed for a broad dynamics range and this requires very small errors during each step, otherwise the error accumulates rapidly above the error bound of the integration method and the simulation stops with an error message.

In the next section, a 20-sim model based on the model presented here will be introduced, after which simulation results follow.

---

[10] Here and further on, X is to be substituted by L and R; for instance, the stiffness becomes $k_{d\_hor\_L}$ and $k_{d\_hor\_R}$.

4.2 Simulations and models in 20-sim

It is important to justify the efforts done in modeling and simulation, as they represent a considerable part of the study. A better understanding of the walking principle of the μWalker has been of foremost importance. From this, ideas for improvement of performance emerged, like for instance increase of step size accuracy, larger total range and force. To be more precise, performance of new devices could be predicted well before fabricating. This decreases the design parameter space[11] a lot so that relatively few devices need to be designed on the wafer and characterized after fabrication. Last but certainly not least, using the software to simulate controllers in the absence of sensor in the real setup further increases the usefulness of accurate and fast simulations. The latter is subject of Chapter 6.

With time, the number of models (and model versions) has grown in such a way, that it would be very hard to present all results and all improvements obtained in each model or sub-model. Actually, each sub-model of the μWalker could lie at the heart of a future research in the hope to understand ever more about the fundamentals of friction, charge distribution and field densities at the micro scale.

Instead, only two of all models will be presented here. In the first model, the accent lies on power, energy dissipation and efficiency. The target of the second model is to capture the main dynamics of the μWalker motion and give estimations about position, step size, maximum force and so on.

Although the two models certainly show some overlap and they could be merged, the choice to keep them separated has one main reason. The simulation speed has become an increasingly worrying issue, because of the dynamics complexity of some μWalker parts. Combining the two models would yield even slower simulations without any substantial improvement in the accuracy or model understanding.

4.2.1 Power and efficiency

This is the first of the two models, which is used to estimate the power consumption and other related issues for the single μWalker design and for estimating the consumption of a whole μSPAM prototype. In the following results, only the dissipation effects of the μWalker parts are considered, while the electrostatic energy of the parts is supposed to flow back and be dissipated into the power source.

The capacity of the load (plate or leg) is varying between two values, one is under pull-in ($0V$) and the other above ($55V$ and $50V$, respectively). The pull-in

---

[11] This is the amount of dimensions and material properties that can be varied from prototype to prototype on the wafer, like for instance plate length or thickness.

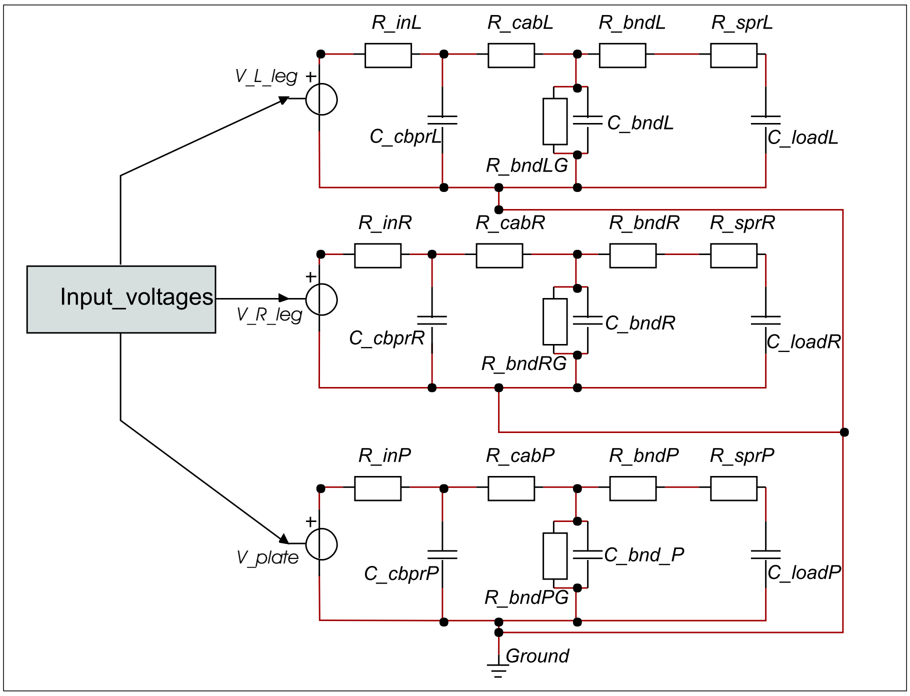

Figure 4.21: Model of the actuation system.

voltage of the plate is $32V$ and for the legs $10V$[12].

Figure 4.21 introduces the lumped model of the electrical actuation system for the three sub-parts that act as capacitors, from top to bottom the left, the right leg and the plate. The link between the lumped parts and the respective physical components is depicted in Fig. 4.22. In contrast with Fig. 3.6, which was a concise representation of one channel, the resistance value of the bond and of the retraction spring is now divided in R_{bndXG}, R_{bndX} and R_{sprX}. Again, X stands for L, R and P, or left leg, right leg and plate, respectively. The first term represents the resistance of the silicon nitride layer between the bond pad and the underlying wafer bulk, typically in the order of $M\Omega$ or higher. R_{bndX} is the resistance between the point where the probe touches the bond to the area where the retraction spring is connected to the bond and R_{sprX} is simply the ohmic resistance of the retraction spring between the bond and the μWalker part.

A first estimation of the load is a capacitor C_{loadX}. The value of the capacitor depends on the applied input voltage. No mechanical dynamics were included

---

[12] The legs pull-in voltage ($\approx 10V$), is only an estimation, as in reality this value is not always easy to derive. partial pull-in, plate bending and the number of retraction springs play a role.

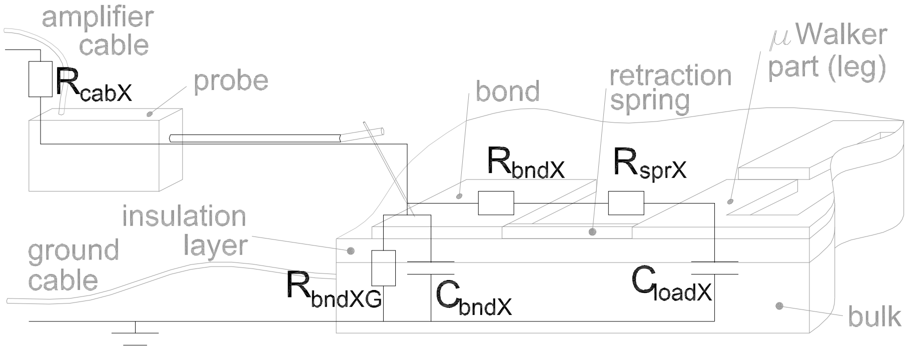

Figure 4.22: Lumped model and physical components.

here for the sake of simulation speed and because the exact vibrations of the μWalker sub-parts are not very crucial at this point, where we seek to roughly estimate the total device consumption. The signals offered to the legs and plate are plotted in Fig. 4.23(a), compare with Fig. 2.6(b) on page 17. The resulting (peak) power delivered to the μWalker is just under $0.1W$ (Fig. 4.23(b)). This relatively high estimated peak power is caused mainly by the rapid charging of the plate or leg. The momentary peak power could be reduced at the expense of performance. It is easy to see that higher resistances in the model decrease the peak power but also delay the charging process of the μWalker parts, modeled as capacitors. As a consequence, reaching plate pull-in would take more time for a higher resistance value, so that smaller μWalker operating frequencies are necessary. It is implicitly assumed that the only dissipative elements are the retraction springs, which act as resistors here (R_{sprX}). Figure 4.24 presents some interesting signals from a simulation with the above mentioned input signals. As the right leg signals are identical to the ones of the left leg but only slightly shifted in time, they are omitted here. Due to the slightly larger area of the leg compared to the plate and to the fact that $R_{sprL} \approx 3R_{sprP}$, the main power is used by the legs The difference in resistance between R_{sprL} and R_{sprP} is due to the length of the conducting channel from the bond all the way to the plate, which is approximately $590\mu m$ (see Fig. 2.7). In contrast to the leg, not only the retraction spring represents the resistance, but also the whole conducting path around one side of the leg, which is necessary to reach the plate.

In Fig. 4.24(a), the maximum charge current is approximately $2mA$ for one leg and $0.74mA$ for the plate, which is considerably at this scale. The dissipated peak power is about $53\mu W$ for the leg and $4.5\mu W$ for the plate. Per step the lost energy is about $1.87pJ$ and $0.063pJ$ for leg and plate, respectively. The energy in the system is shown in Fig 4.25. Clearly, most of the energy is buffered in the legs, while the dissipated energy is about three orders of magnitude larger,

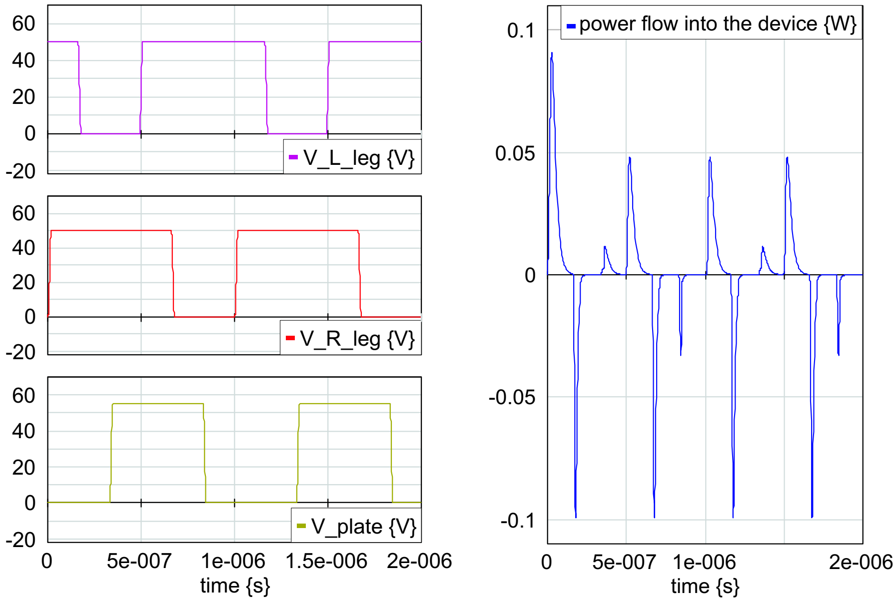

(a) Actuation voltages used here.

(b) Momentary power of all three inputs together.

Figure 4.23: Input signals and momentary power of the simulated μWalker model.

compared to the plate. The total energy dissipated in the system is about 3.8pJ per step.

At a theoretical rate of 1 million steps and 400 μWalkers working in parallel as proposed in Chapter 2, an amount of 1.52mJ would be dissipated per second, or a constant power of 1.52mW. This is acceptable from the point of view of overall system specifications (Table 2.1). The reader should note, however, that the design of dedicated power source circuitry is crucial, as a part of the energy will dissipate there as well.

Looking from an efficiency point of view, there are numerous ways to determine the efficiency and just as many results. From Chapter 3 – especially Fig. 3.14, we know that the maximum range of the typical μWalker has been reached after about 350 steps. This induces a total dissipated energy E_{dis} of 1.33nJ in the retraction springs, from the electrical domain.

Using the beam stiffening theory presented earlier (Eq. 4.145 and 4.146), the potential energy contained by the eight retraction springs when the device

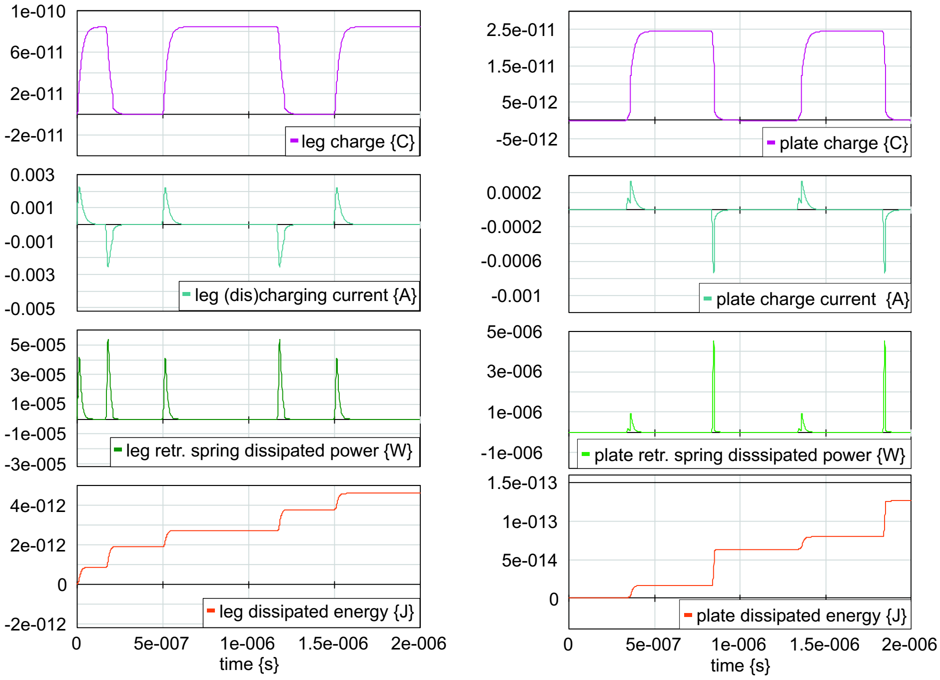

(a) Simulations of the left leg, from top to bottom: the amount of charge, the current, the dissipated power and the dissipated energy.

(b) The same signals for the plate.

Figure 4.24: Interesting sub-system signals.

is at the maximum range, is:

$$E_{pot} = 8 * \int\limits_{0}^{12\cdot 10^{-6}} F_{bm.st} \mathrm{d}x \quad \Longleftrightarrow \quad E_{pot} \approx 7.16nJ\ . \tag{4.147}$$

In words, integrating the position dependent spring counter-force $F_{bm.st}$ from steady-state to the maximum range yields the total potential energy that can be stored, E_{pot}. According to the above, the efficiency of the electrical domain is about 84%.

There is another category of losses, in the mechanical domain. Friction and energy los due to impact of the μWalker sub-parts to the walking surface are the primary causes. These losses cannot be estimated from the experiments

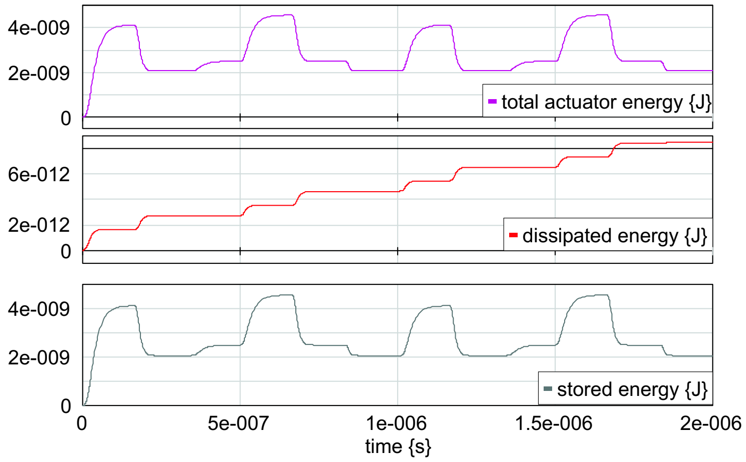

Figure 4.25: The estimated energy in the system, from top to bottom: the total energy, the dissipated energy and the buffered energy.

made nor by simulation, because the tribology aspects at the contact points are still an open discussion. An estimation of the efficiency based on pure modeling would therefore be premature from this respect.

4.2.2 Dynamic plate model

From static to dynamic plate models

It has been remarked before that due to space and time constraints, only one of the various models is being presented. Before proceeding, let us justify the model presented in this subsection by having a short review of the statical plate model, the ancestor of the dynamic μWalker model. The name already suggests that plate dynamics is not present and this model is a straight-forward implementation of Subsection 4.1.5. The basic idea is that given the input voltage, a corresponding step is calculated. The statical model gives useful information about energy losses due to the impact of the μWalker plate and legs on the walking surface. More important, the effect of varying design dimensions and material properties on the pull-in voltage and step size is important for future μWalker prototypes. With this model, such predictions could be made easily and without excessive computational effort.

There are number of deficiencies of the statical model, however. The step size is assumed independent of the boundary conditions – or more specifically the device off-center position. This approximation is only acceptable for a very small range around the initial position, say one or two micrometer, which is less than 10% of the total range. Another issue is that the model contains a number of fitting parameters (for example δ in the presented model), which disturb the physical nature of the model in the sense that they do not influence the simulation outcome in a physically comprehensive manner. These and other less relevant issues have led to the development of the dynamic plate model as presented below.

Model highlights

The model is presented in a top-down approach and where necessary, more details are shown about the exact implementation of the sub-parts. At the top level, the device is split in three parts: the horizontal part (including all sub-parts but the vertical part of the plate), the vertical part (a part of the plate) and the leverage coupling between the two (see Fig. 4.26). The coupling is a transformer with a constant ratio of 29, which converts the vertically obtained force into a useful horizontal force.

The vertical part has two interconnected sub-parts, `Vert_bending` and `Electrostatic_actuation`. `Vert_bending` contains the bending stiffness of the plate and a damping component, for which the physical interpretation could be squeezed damping of the air film between the plate and the surface. `Electrostatic_actuation` uses the data mesh in Fig. 4.14 to derive the electrostatic force which corresponds to the plate deflection and applied plate voltage at each point throughout the simulations.

The horizontal part of the model contains the same components as presented earlier schematically in Fig. 4.20, but now expressed in bond graph language. Damping injection was added on some points in the system for improving simulation stability and decreasing simulation time (dL, dR, d_hor1 and d_hor2), see also the remarks of the previous section, page 102.

Simulation and validation

The final μWalker model presented above was simulated. In this part, the reader is confronted with only a few of the many simulations which were carried out.

To start with, the applied voltages and the legs position as a function of time can be seen in Fig. 4.27, for a displacement of five steps. The choice for a relatively large time scale has a number of reasons. First, some measurements which are used to validate the model were carried out at a low step rate per second, in order to grab enough details about the shape of each step. Therefore, the simulations had to be correlated to this rate. Second, the numerical integration method[13] sometimes had difficulties with solving the high dynamics of the model. To solve this, distance between the steps was increased and damping

---

[13] The method used was the Backwards Differentiation Method (BDF).

was added so that high-frequency internal system vibrations are damped out. Third, as one second corresponds to one step in the plots, it is more convenient to directly derive the number of steps until an event occurs.

One of the disadvantages of this choice is that the model slips towards steady state during the long waiting periods between the steps. In the case when the device is off-center for a long period of time, this slippage makes simulations inaccurate and not very useful for dynamic analysis. Some more attention will be given to this shortcoming and a way to solve it later on.

Figure 4.27 confirms that the simulated step size corresponds to the measured step size (measurements show a mean of 52 nm for the first 20 steps, see Chapter 3, page 47) for this type of μWalker, namely about 55nm.

The meaning of the friction states of Fig. 4.28 has been treated in 4.1.8. In general, a higher state value means higher velocity of the leg and a negative value means a velocity in the opposite direction. The close-up at the upper-left part of the figure shows the friction state of the left leg, when it is shifted to a new position. For a short time, state four (Coulomb region) is being reached. In contrast, the shift of the right leg (the upper-right plot) shows much more chattering. The reason for this difference is again the actuation principle: when the left leg is shifted to the right, the cause is that the electrostatic force pulls the plate towards the ground. The electrostatic force does not contain much dynamics. When the right plate is released and moves to the right, however, the dynamics is ruled mostly by the double mass-spring system which has high resonance frequencies. The potential energy which is now stored in the plate is released, yielding a certain number of oscillations before the system settles into a new equilibrium state.

After a time, both states stabilize to -1, which is the expected situation when both legs clamp the μWalker somewhere at the right of the zero position, and the μWalker slips very slowly back to the zero position.

A run of 500 steps into one direction (Fig. 4.29 shows that the total range is limited to 8.0μm, compared to about 12μm from the measurements. Unfortunately, this difference could not be alleviated by changing the parameters of the friction models, because then simulation problems like discussed earlier occur, which impede reaching the maximum range. In the zoom-ins, we can distinguish the different shapes of each step near the center, at mid-range and at the end of the range. The slip of the actuator is here responsible for the decreasing step size with increasing off-center distance. In reality, the effect of slip is combined with the limited buckling force, which together give a reduced step size as well.

The end of the range is reached after about 300 steps, which is comparable to the measurements in Fig. 3.14 (maximum range measured after 350 steps).

The same slipping effect just presented above is also seen in Fig. 4.30. This figure shows simulation and measurements of an identical actuation pattern, consisting of 40 steps into one direction, a six-second hold, then 20 steps followed by another identical hold action and finally release of the device after 78s. The two plots are quite similar and represent the position of the right leg while the device moves to the right direction.

Regarding the zoom-in at the beginning of the actuation, a small dip can be observed around 6.5s, which is not present in the simulations. It is not clear what triggers this curiosity, but one of the possibilities is the fact that the first time when the left leg is clamped, the right leg – a part of which is used by the video grabbing setup to record the displacement – gently shifts either to the back of out of plane about 20nm. Later on, this effect is not present anymore, because then at least one of the legs is clamped at all times.

Two interesting remarks about the close-up at the end of the actuation follow. First, note the decaying position of the simulated position with respect to the measurements. Second, due to the long device actuation with the same potential while holding at the same position (between 70 and 78s in the figure), charge build-up takes place. This charge keeps the μWalker from going back directly to center, as the simulations (and also intuition without considering the charge phenomenon) indicate. Instead, the actuator falls back from 3.26 to 3.05μm and only after a time it goes back completely to the zero position (not shown in the figure).

If we change a parameter of the Stribeck-curve, instead, the discrepancy between the simulation and measurements[14] is improved (Fig. 4.31). For example, consider parameter `p_leg` of the legs contact model (see Appendix I for the exact implementation of the Stribeck curve). We can tune this parameter so that the influence of the vertically applied force on the μWalker plates is increased and the legs slip less. In turn, there are less transition changes between stick and slip, resulting in reduced integration errors of the numerical integration solver.

Although changing parameter `p_leg` is a little un-orthodox because the vertically applied force should remain the same but the Stribeck parameters should change instead , it turned out to be the only option. Choosing more aggressive parameters for the Stribeck curve itself resulted in unacceptable integration errors and canceled simulation. From the right close-up up of Fig. 4.31 we clearly see that the simulation with `p_leg`=3 now resembles the measured end value much more.

4.3 Review and concluding remarks

This chapter has informed the reader about the modeling choices taken in order to obtain simulation results that are in conformity with measurements. The road from the effect of pull-in of the μWalker sub-parts and up to simulation of

---

[14] The same measurement data as in Fig. 4.31 used here.

a scanning motion has been shortly presented, omitting details about the many types of models which were developed with time.

At a certain point, the (purely physical) models showed some discrepancy with the measurements (especially regarding the stick distance of the plate at pull-in) and therefore the model was extended to better fit experimental data. In this case a simple equation showing the relation between applied voltage and stick distance was incorporated into the model.

Furthermore, a part of the plate model was processed a priori into a 3D mesh, for increasing simulation speed. This part would need to be recalculated for every other μWalker with different plate dimensions than the standard set presented in Chapter 2.

The next chapter is on device optimization. New types of 1D and 2D actuators based on the standard μWalker are introduced and shortly described. Some combinations of MEMS sensors and actuators in one design are presented.

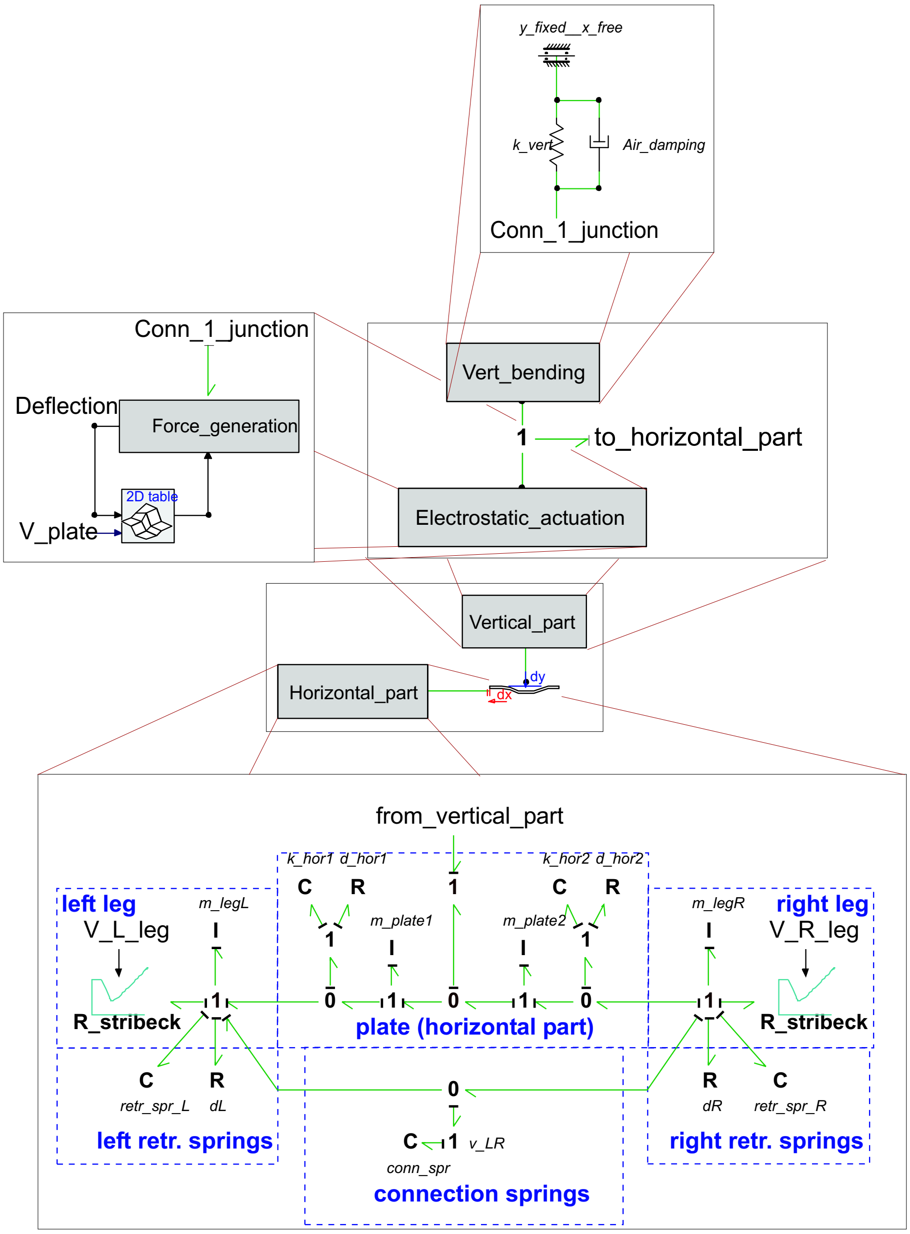

Figure 4.26: Top view and main sub-models of the 20-sim model.

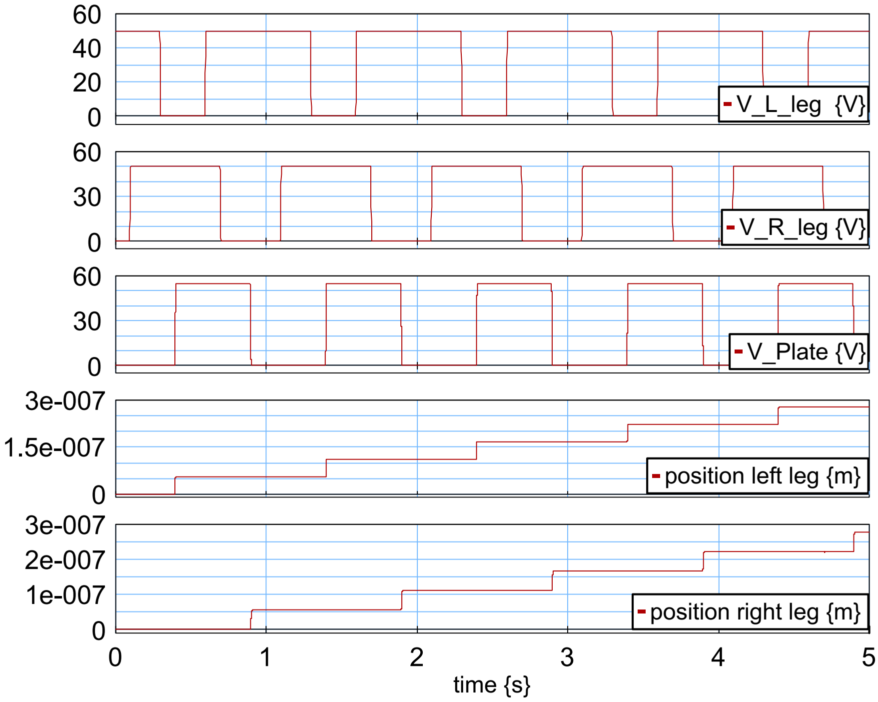

Figure 4.27: Offered input voltages and corresponding displacement of the legs.

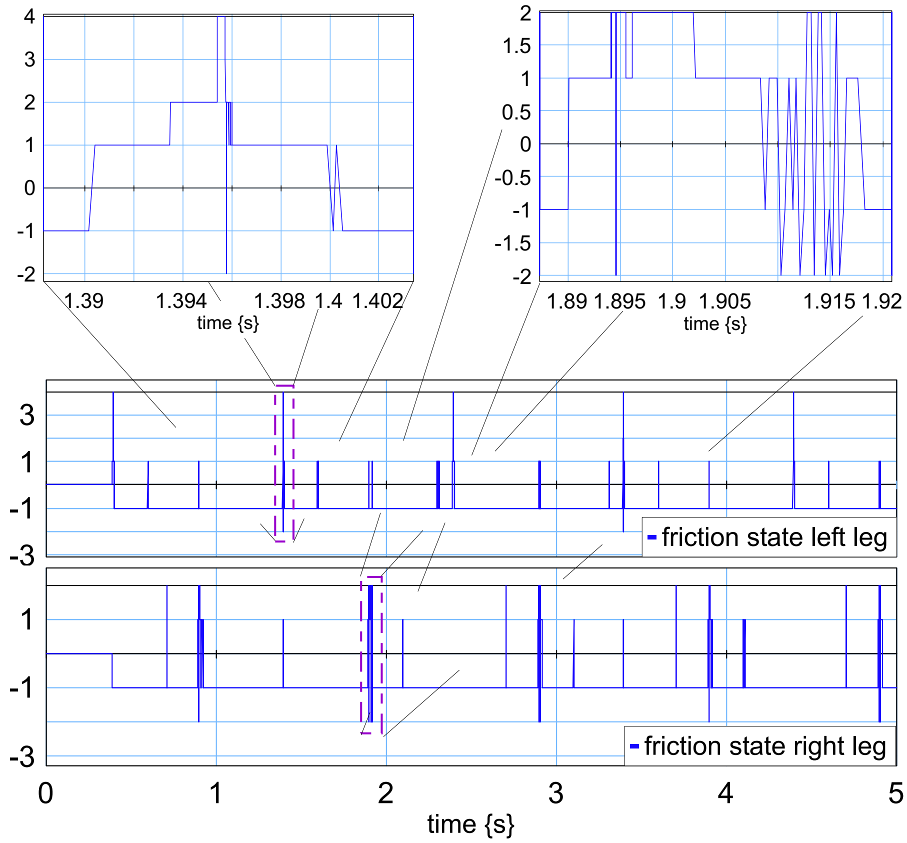

Figure 4.28: Friction states of both legs, with a close-up of two important regions.

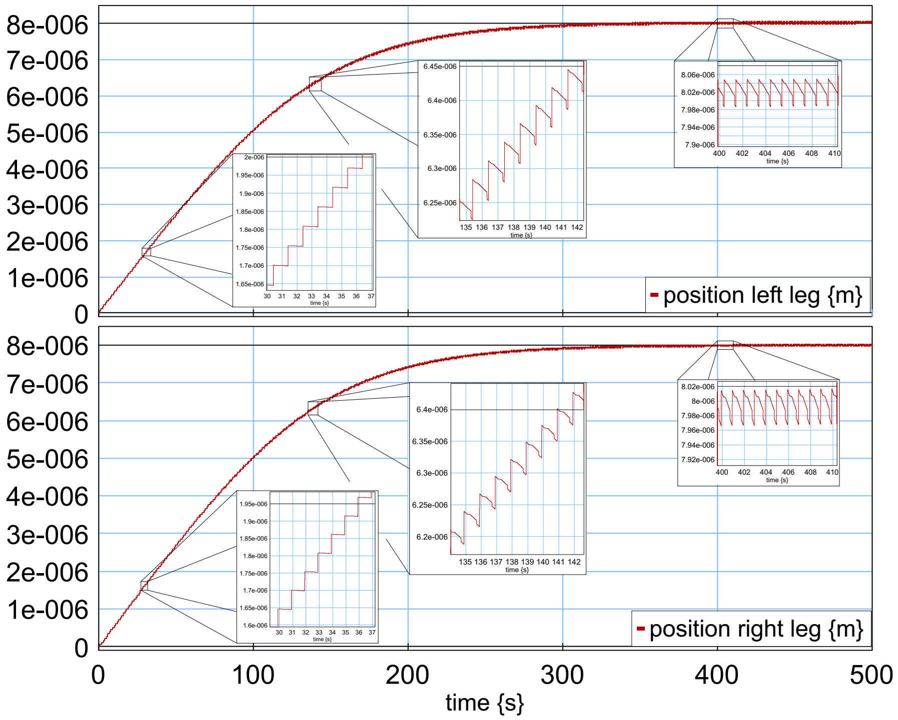

Figure 4.29: Simulation of 500 steps showing the position of both legs and a number of close-ups.

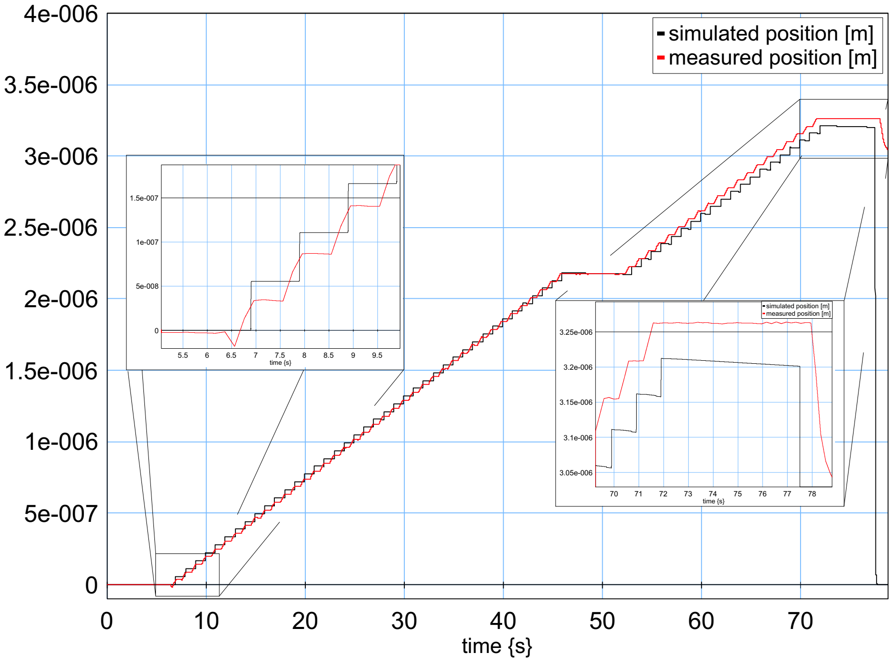

Figure 4.30: Simulation and measurement of a typical movement of the μWalker.

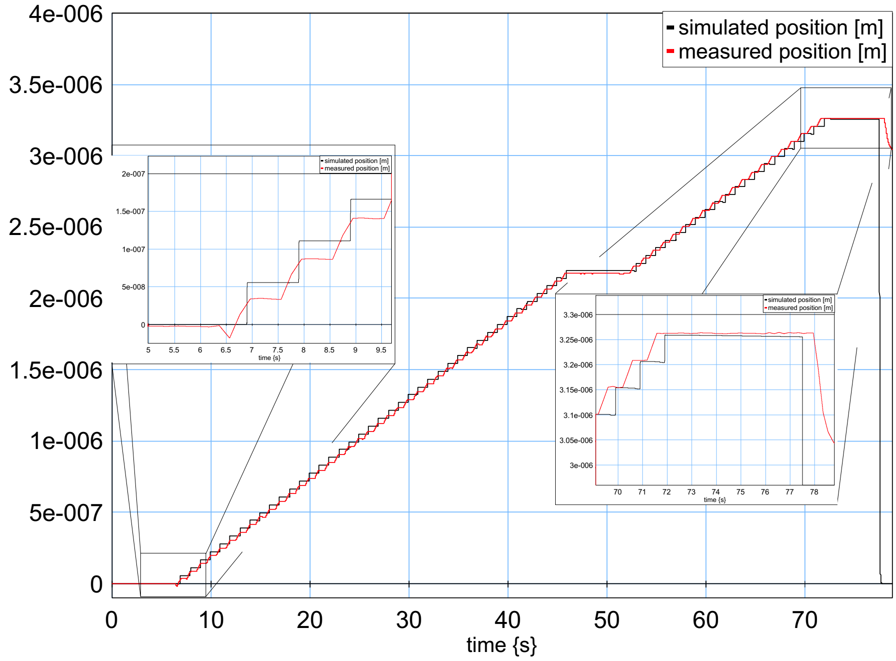

Figure 4.31: Simulation with altered parameters and measurement of a typical movement of the μWalker.

Chapter 5

Design optimization

After a short motivation, the processing background is discussed shortly, to introduce to the reader the challenges and the limitations of the current way of processing. Also, some attention is paid to statistical information about the produced wafers. Then some designs and experiments of several exotic μWalkers and other devices follow. The last part is about the first μWalker-based actuators with a real application potential in the near future, namely 1D and 2D actuated tables. References [54, 59] contain a part of the optimized structures introduced in this chapter.

5.1 Motivation

Improvement of the properties of an actuator depends strongly on the set of dimensions of the device. For the μWalker case and according to the models presented, varying the length or width of the actuation plate influences the total generated output force linearly. At the same time, the output force goes with the third power of the plate thickness!

There is an optimum between maximum force, low voltage, restricted dimensions and fabrication steps in the clean-room. Especially the last term makes it hard to define this optimization problem in a trivial way. To give a small example, imagine that the thickness of the plate needs to be increased. Then, not only will other sub-parts change shape as well, but also the variation of material thickness will change, because a larger processing time is needed for deposition of a thicker plate. This increase of the thickness could involve stress build-up in the plate, leading to a drastically different behavior than expected. It must be noted here that clean-room products are known to show variations over different runs, which makes the task of optimization all but an easy one.

As remarked in earlier chapters, is evident that the making of test structures cannot be avoided totally, nor should it. Instead, there should exist an iteration between models and simulations, and test runs. Prototypes should be used to

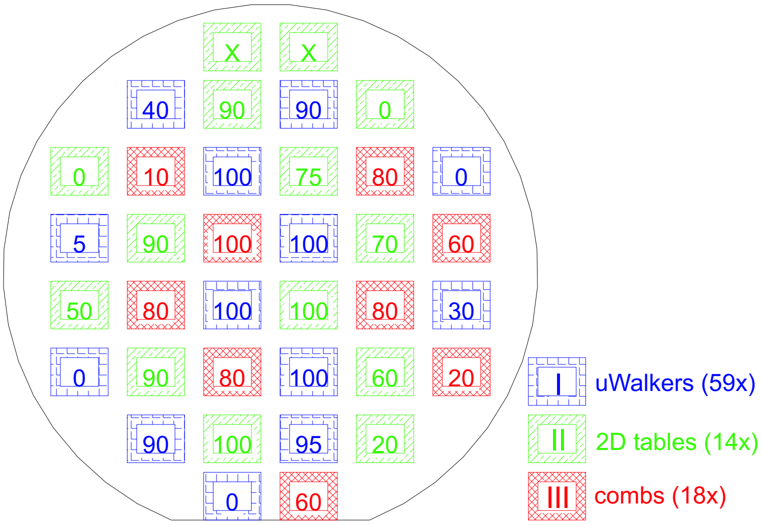

Figure 5.1: Estimated yield after measurements of the first wafer.

get insight of the actual processes and to validate models, while models and simulations should use this information and suggest new changes for the next run. These two worlds should form a synergy. The accomplishments are then both a sufficiently good working MEMS device and a valid model from which other devices can be simulated and optimized directly.

Due to the extended nature of the measurements and time constraints, only a limited number of devices are presented. Although most of the experiments were repeated five or ten times, the reader should keep in mind that more needs to be done for obtaining more accurate data.

5.2 Processing background

Although the processes involved in the fabrication of μWalkers and related devices is not topic of this thesis, they are shortly elucidated here as their effect is omnipresent in the device dimensions and performance. For more information about specific design issues, the reader is referred to [73, 74].

Due to its length and relevance, the process document is presented in Appendix J. Almost 100 clean-room steps are needed to finish the fabrication, which involves lithographic processes for four masks. In the same appendix, the main fabrication steps are described and represented schematically for the front and back side of the wafer (Fig. J.1 and J.2, respectively). Regarding the design, a total of 91 different types of actuators were designed. Only one of

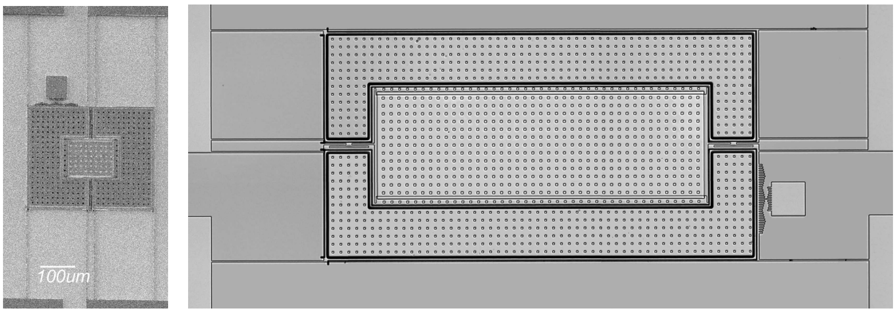

(a) μWalker with short plate.

(b) A wider plate provides more force.

Figure 5.2: Diversified shapes of μWalkers.

these devices malfunctions due to a design mistake, which led to over-etching during processing.

Figure 5.1 shows an estimation of the yield of the first successfully tested wafer. There are two main reasons for the reduced yield in the different clusters. First, short circuits appear due to mask overlapping and the shape of the nitride trenches. Second, some structures were not totally freed from the substrate and some silicon oxide was still present under the actuator. When freeing it, parts of the device broke resulting in failure.

Although no hard estimations have been made for the wafer produced during the second and last run, there is a strong belief that the yield is considerably higher, as most devices are totally free and no short circuits occurred so far.

5.3 "Exotic" actuators

Plate length and width effects

We start the survey of the new actuators by presenting μWalkers with altered plate length and width. The device plate lengths vary from 124μm to 208μm. Figure 5.2(a) shows an example of a μWalker with a 124μm long plate.

Table 5.1 shows typical values of the pull-in voltage, maximum range and related force and the step size. The pull-in voltage indeed decreased with increasing plate length. Furthermore, the maximum range, generated force and step size were measured for the 152μm device. This indicates the presence of the maximum step size and range for a plate with length between 124 and

Table 5.1: The effect of the plate length on pull-in voltage, maximum displacement and step size.

	$124\mu m$	$152\mu m$	$180\mu m$	$208\mu m$
pull-in voltage $[V]$	73	49	37	28
maximum range $[\mu m]$	10.17	14.13	13.12	10.30
generated force $[mN]$	1.42	3.72	2.99	1.48
step size $[nm]$	55.3	58.2	51.3	50.7

$180\mu m$.

Another possibility to increase the performance is to choose a wider plate (Fig 5.2(b)). The expected linear relation between plate width and maximum force could not be observed. Increasing the plate width from the standard value ($94\mu m$) to $610\mu m$ boosts the maximum force to $4.82mN$ instead of about $19mN$ which are expected if the relation would indeed have been linear like predicted from the models. An explanation for this is the absence of enough clamping force of the legs. This force is needed to prevent slippage and is not sufficiently high for forces larger than mentioned above. The plate does deliver enough force but the legs cannot be clamped strong enough to permit a larger range. In other words, the effective legs contact area should be increased to allow for better fixing the legs. The device with the wide plate has a mean step size of $65.9nm$.

Weak retraction springs and maximum range

Figure 5.3(a) shows a μWalker where the retraction springs do not show stiffening effects: the design makes it possible to alleviate axial (tensile) stress in the retraction springs. Therefore, the stiffness is reduced even for large off-center positions of the actuator, like in Fig. 5.3(b). The displacement in one direction is about $285\mu m$, with step sizes of $51.2nm$. The maximum range can be further improved by decreasing the retraction springs even more (Fig. 5.4(a)). The highest achieved range in one direction is about $430\mu m$, see Fig. 5.4(b).

Although the target range of $1mm$ was not achieved due to stiction effects of the long sliders, the reader is hopefully convinced of the fact that the range can be increased deliberately. The main problem to be addressed is improved performance of the retraction springs, such that long range movements show repeatable behavior.

Connection springs variation

Increasing the stiffness of the four short connection springs (Fig. 5.5) from $261N/m$ to $7040N/m$ does theoretically increase the elastically stored energy

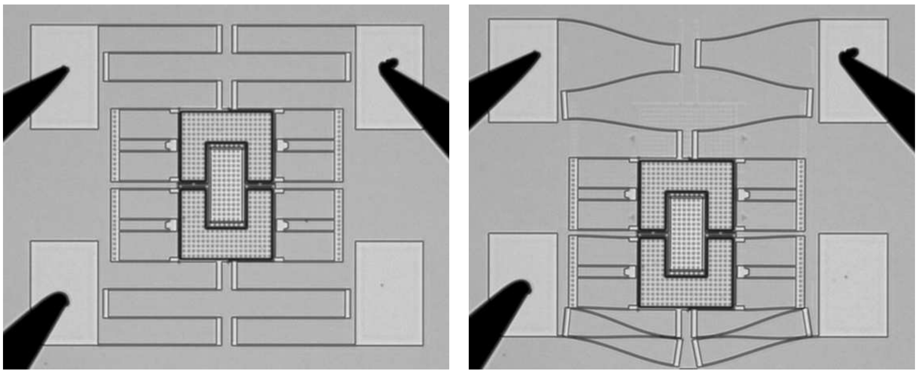

(a) Actuator with weak retraction springs stiffness at rest.

(b) The same μWalker, but now at maximum range.

Figure 5.3: Maximization of the range for small devices.

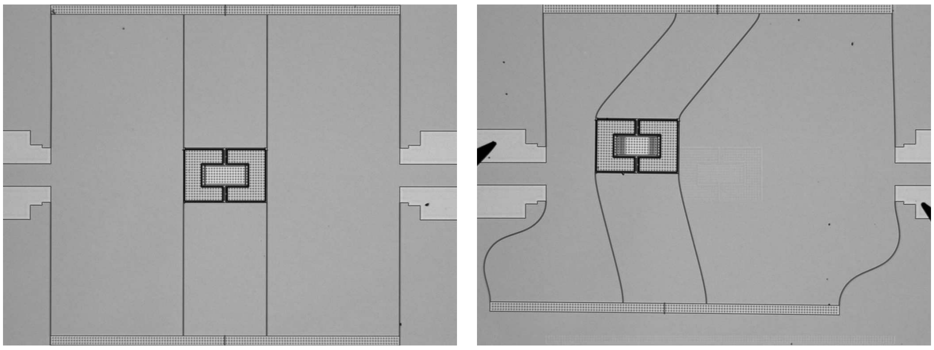

(a) Device with large retraction springs...

(b) ...reaching the maximum range...

Figure 5.4: A new record of the μWalker design maximum range.

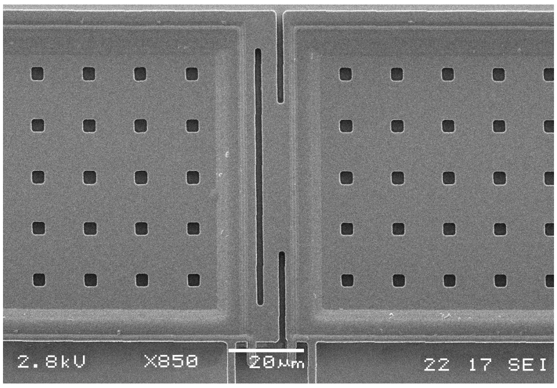

Figure 5.5: Increased stiffness of the connection springs.

in the system. The drawback is that the step size is smaller. Measurements show that the step is generally smaller than 32.1nm, whereas the maximum range is 9.33μm, or about 1.1mN of maximum force. More accurate measurements should be performed to determine the optimal shape of the connection springs. In this context, by optimal we mean to achieve the necessary step size and thereby maximize the total actuator force.

One and both legs fixed

By not releasing one or both legs of the μWalker during fabrication, we believed it would become possible to approximate the clamped-free and clamped-clamped boundary conditions which are also present when the μWalker makes steps. For the clamped-free case, the pull-in voltage measured is 26V and a step size of 55nm.

The pull-in voltage of the clamped-clamped case is unexpectedly low, about 16V. This could be explained by the presence of internal stress in the plate, which makes it bend and this reduces the pull-in voltage. Bending was also observed from microscope views and is present at all times, also when the device is not connected. Therefore, a clamped-clamped stress-free plate turns out to be very difficult to realize for μWalker plate dimensions and given the polysilicon deposition method used during processing (LPCVD, see Appendix J).

L-shaped legs

For increasing the step accuracy and repeatability, it is important to reduce unwanted modes when the μWalker is in action. Figure 5.6(a) illustrates one of these modes, where the actuator could rotate around the plate center (in-plane motion), for instance due to a slight asymmetry in the plate height which

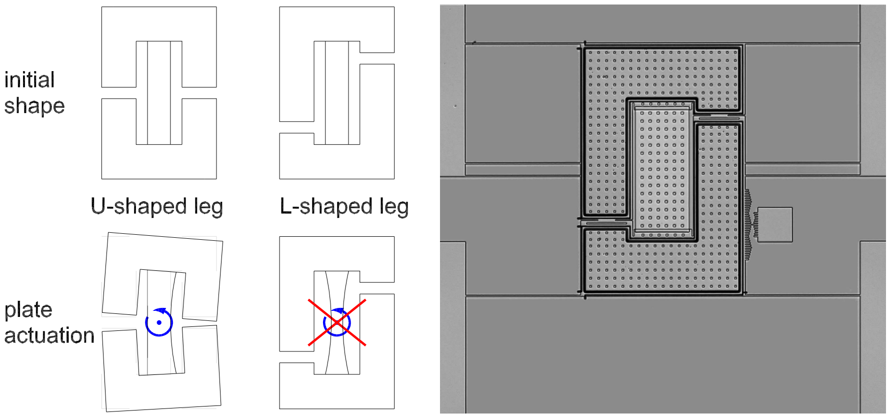

(a) L-shaped legs prevent in-plane rotations around the center point of the plate.

(b) Realization in MEMS.

Figure 5.6: Altering the basic shape of the legs from U to L shape.

makes one part of the plate touch the ground, while the other does not.

Altering the U-shape of the legs to an L-shape can in this case prohibit this mode. The reason is that for the U-shape, the (relatively low) bending force of the connection springs must prevent in-plane rotation of the actuator parts. If we use an L-shape instead, then in-plane rotation of the μWalker legs is much more difficult to realize, due to the fact that the force induced in the the connection springs is now mainly axial and thus much higher.

Figure 5.6(b) is an illustration of one actuator with such legs. The step size around zero position is about 46.1nm but paradoxically, the deviation between nine repetitive measurements of each 20 steps is much worse than for the U-shaped μWalker, namely 113nm. Compare this with the results of the standard μWalker in Fig. 3.19, where the standard deviation was 6.52nm. Some reasons for this discrepancy follow. First, the devices measured come from different wafers, which were fabricated with slightly different processes and process parameters. Second, the L-shaped device might indeed feature a reduced unintended in-plane rotation, but now the out-of-plane rotation due to the asymmetry of applied electrostatic force is even worse. This is depicted in Fig. 5.7. Actually, the long part of each leg always touches the ground first. As the legs are now point-symmetrical around the center of the plate, the plate could start to show torsion effect, which would dramatically decrease performance, because now the clamping force of the legs is seriously compromised.

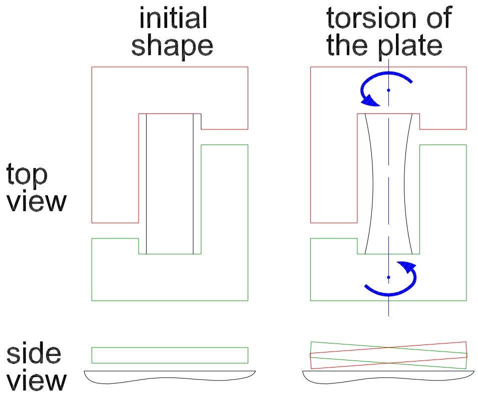

Figure 5.7: Plate torsion can decrease the performance dramatically.

μWalker and comb drive hybrids

With an eye on miniaturization and MEMS sensor-actuator aggregation, a number of six different devices were designed and fabricated which are composed of one μWalker and one or two comb drives. Figures 5.8(a) and 5.8(b) are two examples. The μWalker is used to actuate, while the comb drives sense the position. Double comb drives can be used to increase the accuracy by measuring the position in a differential way. Although the range for a double comb drive is reduced to $8\mu m$ in each direction to prevent jamming of the comb fingers, the combination does move successfully and without any visible asymmetry of the fingers along each comb structure. The first capacitive measurements done with the comb drive system (Fig. 5.9(a)) clearly show the same pattern as the position derived off-line from the video file which was recorded at the same time (Fig. 5.9(b)).

Although the exact axis parameters of the comb drive measurement in Fig. 5.9(a) are still under investigation at the moment of writing, the results represent a leap step towards closed-loop control and sensor-actuator aggregation.

Stiction measurement devices

The purpose of the type of devices like in Fig. 5.10 is to measure the coefficient of stiction for different configurations. We are able to derive the applied force of the actuating μWalkers by measuring the bending force of the springs which in turn gives an indication of the axial force through the horizontal or vertical part of the stiction system.

The basic idea is that we actuate the vertical μWalker until a certain bending force of the springs is reached and the three points of the moving slider touch the upper fixed square. After this, the μWalker for horizontal position is actu-

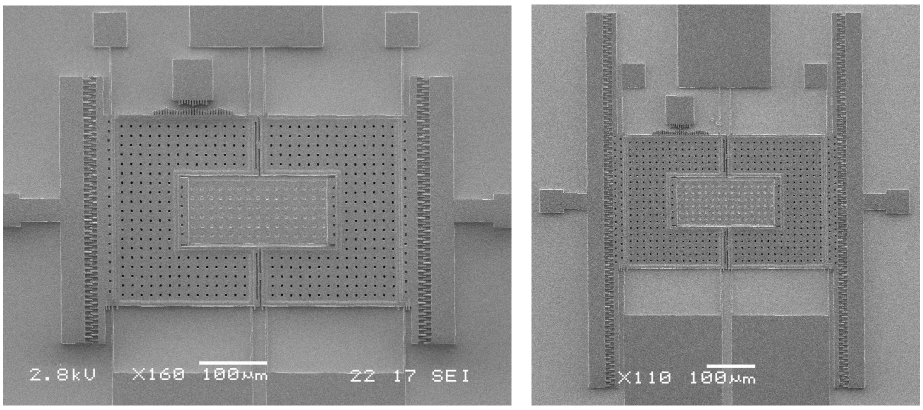

(a) The μWalker as actuator and two comb drives (40 finger pairs each) as sensors.

(b) Here the comb drives feature 80 finger pairs each.

Figure 5.8: Sensor and actuator processed with thin film technology at the **MESA+** facility.

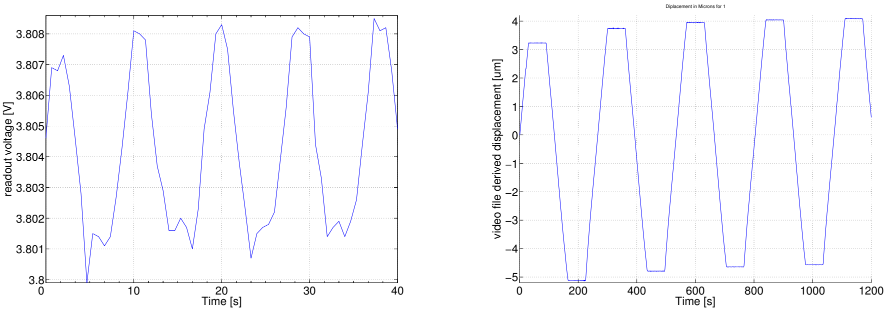

(a) Capacitive displacement measurements from one comb drive, done in collaboration with W. Zhou, CE Dept, Univ of Twente.

(b) Corresponding displacement derived off-line from a video file.

Figure 5.9: Two different ways of measuring μWalker displacements.

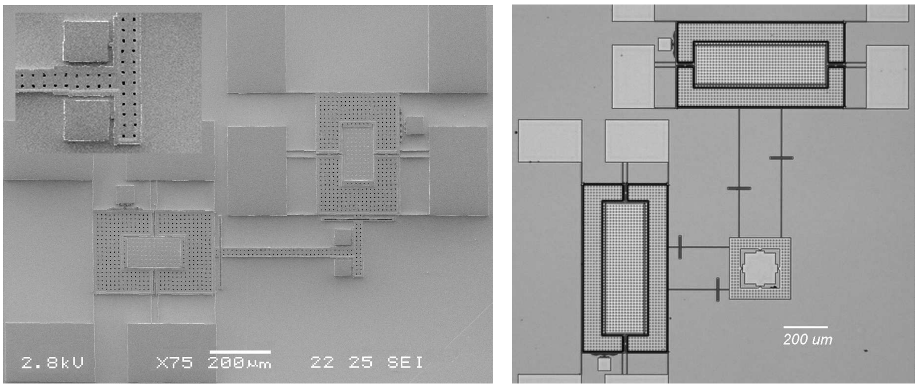

(a) Two actuators and a T-like structure for stiction coefficient measurements (note the zoom in the upper-left part of the picture).

(b) Due to the longer connections to the square, a better xy decoupling can be reached.

Figure 5.10: Two types of devices designed to measure stiction of a Hertzian contact (rounded pin against a plane surface).

ated, until the three points of the stiction device start to shift with respect to the fixed square. This is the moment when the vertically applied stiction force is not high enough anymore to keep the moving part from sliding due to the horizontally applied force.

No successful experiments could be performed due to the lack of height of the device layer, which is only $5.5\mu m$ tall. The consequence of the reduced height is that the moving part of the friction component (long T-like structure) sometimes snaps over the the two squares which are fixed on the bulk. Moreover, the horizontal versus vertical decoupling of some devices needs to be slightly improved.

Comb drives for real-time positioning

The last part of this subsection is about comb drives fabricated within the same run and thus with thin film technology. The devices are intended to be actuated electrostatically and move frictionless above the surface. In reality, with increased actuation time, stiction effects started to occur, which indicate that the devices touch the surface underneath. Again, charge effects in the insulation layer are probably the cause. Due to the reduced height of the comb fingers (only $5.5\mu m$), relatively high actuation voltages are necessary to produce high enough forces to give noticeable displacements.

The device in Fig. 5.11(a) can either be used as an actuator with moving

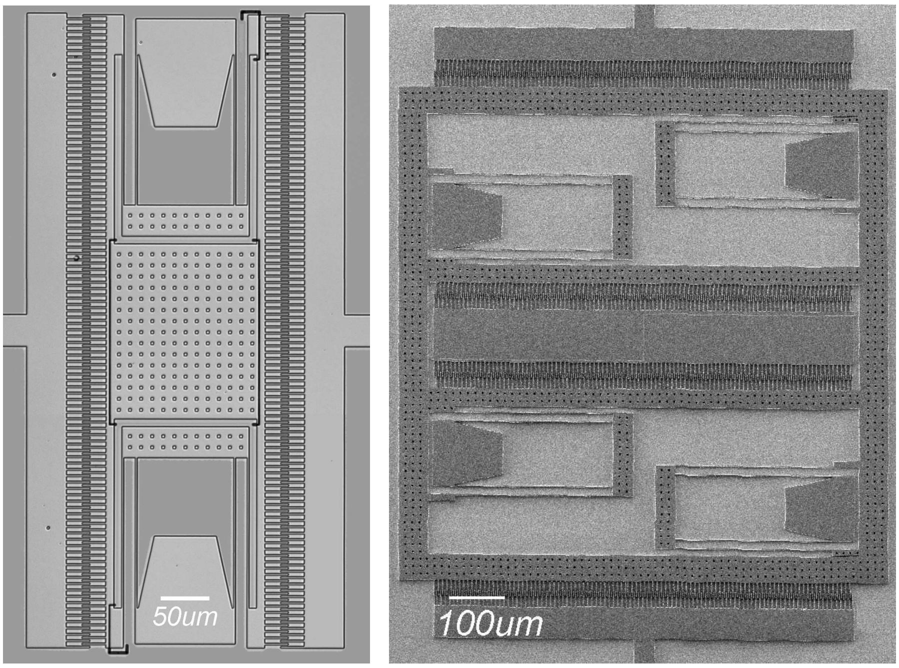

(a) Comb drive with two finger arrays.

(b) Four arrays can be used to actuate in both directions and measure differentially.

Figure 5.11: Comb sensors and actuators, where the array textured sub-parts are free to move, and the plain parts are fixed to the wafer bulk underneath.

range in both directions, or as a sensor and actuator device but with half the range[1].

This limit is not present in the design of Fig. 5.11(b), where the sensor-actuator combination uses the whole range and where the position can be measured differentially. In this concept, when the mobile part moves in either direction, the capacity will increase for one sensor and decrease for the other. In this way, we can obtain double the sensitivity compared to the single sensor case.

Both devices have successfully passed basic testing procedures. To be more specific, repetitive motion resulted from harmonic actuation at $40V$.

5.4 1D and 2d prototypes

5.4.1 1D tables

With an eye on force maximization and also linearization along the range, a new table which can move along one axis is proposed here. In Chapter 3 page 37, we have seen that the push and pull forces of the plate are not identical and that the push force is the limiting factor. Moreover, Chapter 4 treated in detail the dynamics of the plate. The models presented there confirm the statement that the push and pull force feature completely different dynamics. Practically, this means that the μWalker behaves differently when it pushes or pulls against the retraction springs. As we are interested in a step size which is as linear as possible along the range, one possible improvement is to combine the push force with the pull force by using two μWalkers which work in parallel.

Figure 5.12(a) shows one of the produced types of such actuators. The table in the middle can be used as a basis to connect the μSPAM medium or other objects. To obtain the intended linear motion, the actuation sequence for the two μWalkers must be closely matched. This is necessary in order to prevent that one μWalker does not load the other.

For instance, let us consider a sequence of 20 steps to the right, starting from rest. According to Fig. 5.12(b), we first actuate the starting sequence $T_{s1}..T_{s3}$ in order to have the actuators' parts in the correct states for taking steps. Then, the first step is made by processing $T_1..T_6$. After this, the second step can follow directly. Once the 20 steps have been completed in this way, the sequence must be ended by three more actions, namely $T_{e1}..T_{e3}$.

Now the 1D table is in a neutral position. From this position, one can initiate a sequence to the left, a hold sequence to keep the table at this position or a release command to return to zero position. The different ways of actuating the 1D table are listed in Appendix E.

---

[1] This holds because only attractive forces can be generated electrostatically, so in one direction.

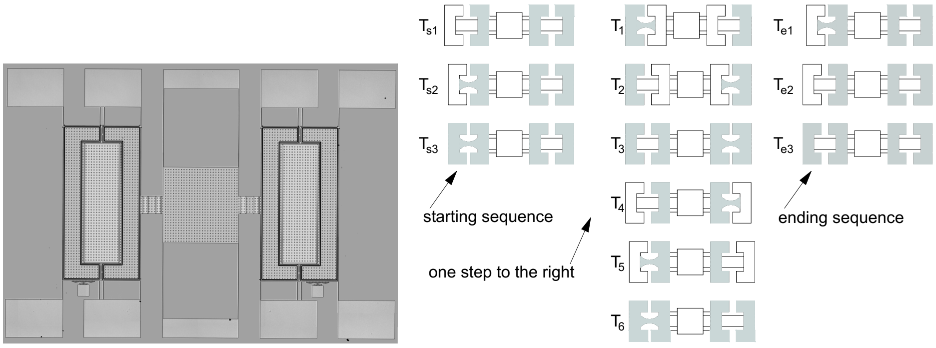

(a) Implementation of the 1D table concept.

(b) Actuation sketch for 1D propulsion with two μWalkers (grey part = actuated).

Figure 5.12: One dimensional positioning system.

5.4.2 2D scanners

A number of different concepts were combined in order to realize 2D tables with decoupled horizontal and vertical motion (Fig. 5.13). Additional to the push and pull strategy presented above for the 1D table, some structures are needed which feature a large buckling force in one direction, let's say the vertical, while the bending force in the other direction – the horizontal one – is reduced. The concept in Fig. 5.14(a) is used for this purpose, and the implementation can be seen in Fig. 5.14(b). Another important issue is the prevention of the rotation of the table, in other words reduction of parasitic effects, which reduced the practical application of an earlier 2D actuator based on the shuffle motor [74]. The idea implemented in Fig. 5.15 is to keep the two sub-parts at all times parallel to each other. Finally, the out-of-plane movement of the table related to the up and down movement of the uWalkers during each step can be tackled by reducing the vertical coupling between the vertical motion of the independent actuators and the table in the center. The sectional sketch in Fig. 5.16(a) and the top-view SEM picture clarify this. The decoupling structure is attached on the left side to the μWalker leg and on the right side to the 2D table suspension.

Two dimensional actuation of this device shows decoupled x-y motion and the practically an absence of a rotation angle of the table. Even if no exact measurements were taken to quantify rotation, no visible rotation can be observed, which indicates that the rotation angle is smaller than 0.5°.

The range is about $10\mu m$ in both directions and is limited by the combined stiffness of both the μWalker retraction springs and the anti-buckling construc-

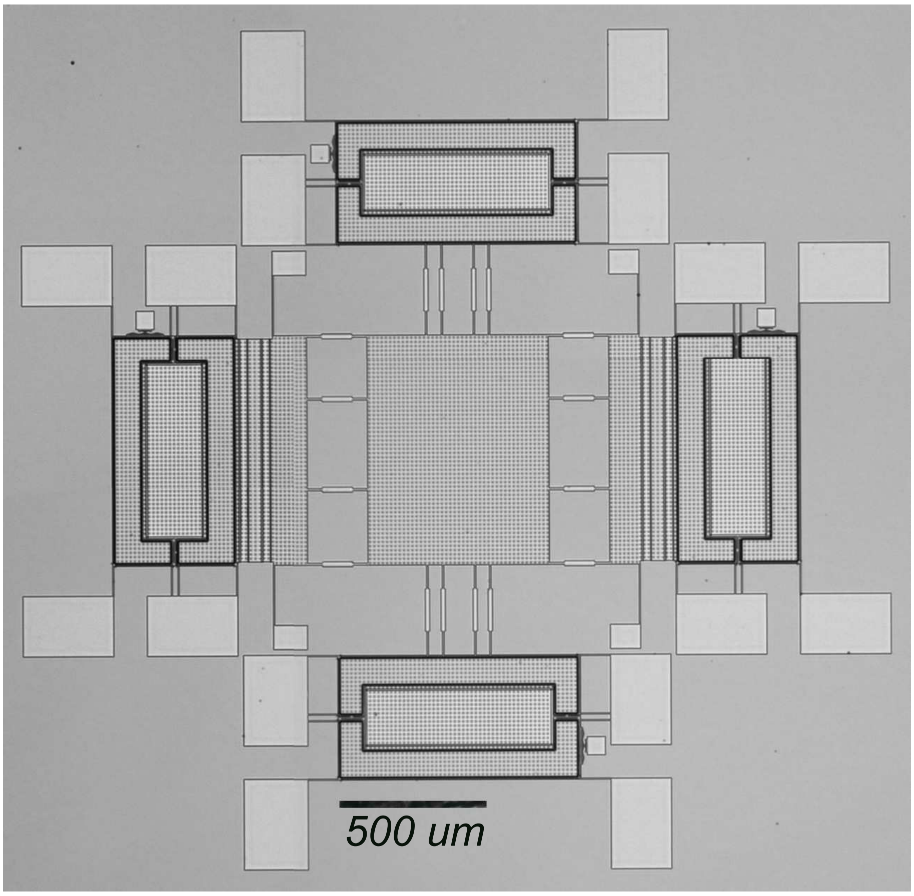

Figure 5.13: Snapshot of a 2D table with four μWalker actuators.

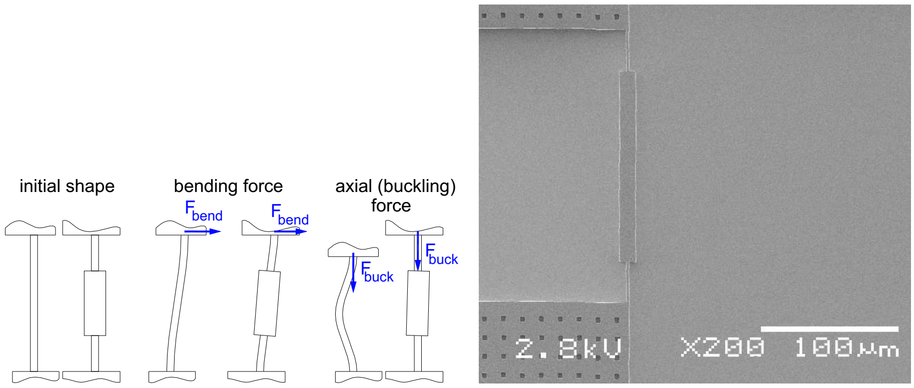

(a) Sketch of the main advantage of a thicker beam at the center.

(b) SEM picture of one such anti-buckling structure for the 2D table.

Figure 5.14: To prevent buckling, the thickness of some springs in the system is locally increased.

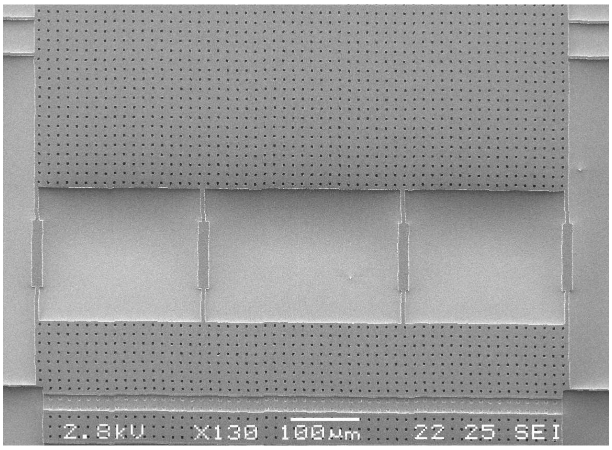

Figure 5.15: A number of anti-buckling structures – especially at the corners of the 2D table – reduce the the rotation of the table when it is actuated in diagonally.

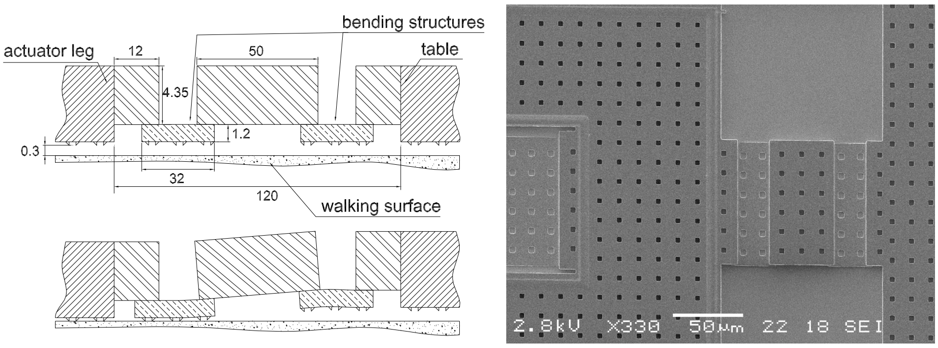

(a) Sectional sketch indicating the coupling between the out-of-plane motion of the μWalker legs and the table.

(b) SEM picture of such a decoupling structure..

Figure 5.16: One way to reduce the up and down motion of the legs on the center table.

tion of the table. The step size is about $40nm$ in the case that only one μWalker is activated for each axis. As remarked before, increasing the range by decreasing the stiffness of the spring values in the system has a negative impact on accuracy.

The tables designed can move into eight directions, orthogonal on the x and y axis as well as diagonal. It can be fixed at a certain position for some time or be released to return to zero position. Different track following actions were offered to the device. The result is a motion which closely follows the intended path. Amongst others, tracks were tested which mimic a square motion with a lattice of $4\mu m$, the shape of an eight-points star and a scanning sequence consisting of scanning four streams of $4\mu m$ long of (virtual) bits separated by $0.5\mu m$ each and consequently returning to zero position and repeating the scan.

5.5 Review

This chapter has introduced to the reader some of the devices which were designed and fabricated with as target on one hand to pave a way towards integrated sensor-actuator systems, and on the other hand to investigate possible improvements of the standard μWalker design presented in Chapter 2.

However all devices shown above can perform (and sometimes sense) motion, it must be said that it is hard to draw any hard conclusions on altering the dimensions of the standard μWalker. It is indeed true for example that a larger plate width does increase the actuator force considerably, but less than linear as expected from the models. A shorter plate does bring up the need for higher pull-in voltages, but there seems to be an optimum between the plate size and the maximum range and maximum force. A new record range of $430\mu m$ in one direction was obtained, which can be further improved by slightly improving the design with respect to parasitic electrostatic forces on the connections from the bonds to the μWalker parts. Legs of other forms than U-shaped can be used to reduce unwanted rotations but at the cost of step accuracy and of increased torsional forces on the actuator plate. The first successful combination of a μWalker actuator with one or two comb drive sensors has been presented, a study which is subject to further research.

About the 1D and 2D tables, successful fabrication and testing has taken place. The actuator follows a given track path without showing unintended rotation and/or axis coupling.

In the next chapter, control of the μWalker within the μSPAM framework is being investigated. Both open and closed-loop schemes are reviewed.

Chapter 6

Control

To increase the operating performance in terms of access time, positioning accuracy and actuation sequence scheduling, the use of two types of controllers is investigated in this chapter. The open-loop type is elucidated first, accompanied by measurements to confirm validity. The following section is closed-loop control by combining a controller in software and a sequence generator in FPGA. The implementation of the controller is enlighten by an example of a tracking sequence, which is processed by the control system. The results of this chapter have been presented to a large extent in [54, 55].

6.1 Control in MEMS systems

The main problems concerning open- and closed-loop control of MEMS sensor and actuator systems have received a large interest in the recent literature [6, 39, 41, 52]. On one hand, open-loop control is more convenient due to reduced complexity of both the setup and the control algorithm. Yet when large device parameter variations are present or when a higher performance is needed than what is achievable with an open-loop configuration, closed-loop is an option. For servo systems in general, implementation of a closed-loop design is necessary. In reality, both methods are often present.

Regarding control systems, there are some substantial differences between macroscopic and MEMS-fabricated systems. First, the typical resonance frequencies of the dynamics of MEMS actuators are generally one or more orders of magnitude higher. The corresponding bandwidth which is necessary for closed-loop control makes it hard to control the system dynamics by using most of the tools available for 'normal-size' systems.

Unlike with macro systems, the sensors for MEMS applications are reduced to only a few categories, are not standardized and must often be specially designed and incorporated in the MEMS actuator fabrication process, as aggregation at a later stage is not convenient or possible. Frankly, few other sensing methods have been mentioned in literature except electrostatic and magnetic position measurements along with optics. Out of these possibilities only electrostatic sensors can be produced efficiently and cheap with the MEMS technology available today.

Furthermore, the mechanical and electronic noise levels play a more important role, due to the reduced sensor size. In the case of an electrostatic actuator, the signal from the actuator is in the same order of magnitude as the noise level. This calls for dedicated amplifier systems which are on the actuator or in close vicinity, so that noise is minimized.

Another specific problem concerning actuators like the μWalker is the fact that the system dynamics is highly nonlinear, as opposed to the typical mass-spring-damper-capacitor modeling of comb drives, where the electrostatically applied force depends on the square of the input voltage. In our case, a sequence of input voltages must be offered to three inputs of the actuator in order to obtain motion (see Fig. 2.6(b)). We have seen in Chapter 4 that pull-in, contact friction and beam stiffening in the retraction springs induce many non-linear effects in the model.

An additional issue is that the steps obtained are very small and should be repeated a large number of times in order to get the displacements needed. As mentioned in earlier chapters, the sensing system in this case was chosen to be a camera setup, which delivers position information with every frame. The data from the sensor is thus sampled at $30fps$ (or $33ms$) and there is no guarantee that the sensor data sampling frequency is constant.

The discrepancy between the high actuation rate needed to to generate displacement by taking many steps and the low sampling frequency of the sensing setup calls for a totally different approach, which includes different sampling frequencies across the feedback loop. Although the main approach of feed-forward and feed-back remains similar to the original situation [90], the non-linearity of the actuator and sensor systems raise a number of challenges, as we will soon explain.

6.2 μWalker open-loop control

Again, it must be noted that many sources in literature concentrate on feed-forward controllers for (piecewise) linear or linearizable plants [24, 50]. In our case, due to the lack of the ability to describe system parts in terms of transfer functions, a great deal of the basic linear control theory cannot be addressed straightforwardly in order to investigate stability and other interesting properties.

Open-loop control is applicable in our case, because a high step repeatability can be achieved with the μWalker actuator (Chapter 3), despite the complex highly non-linear friction and pull-in phenomena which are present at sub-part level (Chapter 4). Moreover, if the device dynamics only varies a little from actuator to actuator, then a valid open-loop model does give fast and accurate enough results without the need of a feedback signal. This holds only if no external disturbances are present.

6.2.1 Model implementation

The model relies purely on experimental data, which can be obtained statistically for all flavors of μWalkers. Indeed, each type of μWalker has typical performance properties and a database could be built that comprises the most commonly used types of μWalkers.

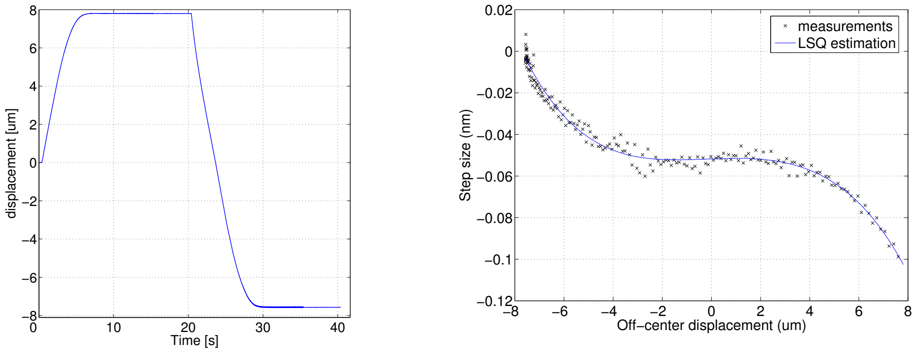

(a) Position of the μWalker as function of time.

(b) Measurements and linearization of the step size relation.

Figure 6.1: Experimental characterization of one μWalker for open-loop control.

The strategy used for defining the feed-forward model is to let the actuator perform a sweep-like full range motion, to be precise from one extremity to the other – like in Fig. 6.1(a). A μWalker with plate length of 208μm and four 100μm long springs is under study here.

Now, by making sure that at least one data point is available for each step, the step size can be derived as a function of the off-center displacement. In Fig. 6.1(b), the data points of the rising as well as the falling part in Fig. 6.1(a) are used to characterize this relation. Intuitively, when the μWalker is off-center, the step size is smaller when the moving direction acts against the springs and larger when the device moves towards the rest position in the center. With the eye on validation, we chose not to use modeling knowledge from the previous chapters.

A least-squares method (LSQ) linear in the parameters is found for the given data points, where the relation between step size s and off-center position m is estimated by:

$$s(m) = \alpha_5\, m^5 + \alpha_4 m^4 + \alpha_3\, m^3 + \alpha_2\, m^2 + \alpha_1\, m + \alpha_0, \text{ with} \tag{6.1}$$

$$\begin{bmatrix} \alpha_0 \\ \alpha_1 \\ \alpha_2 \\ \alpha_3 \\ \alpha_4 \\ \alpha_5 \end{bmatrix} = \begin{bmatrix} -5.1770 \cdot 10^{-2} \\ +4.2190 \cdot 10^{-4} \\ -6.1314 \cdot 10^{-5} \\ -9.5807 \cdot 10^{-5} \\ +1.4910 \cdot 10^{-6} \\ +3.5155 \cdot 10^{-7} \end{bmatrix}.$$

By changing the sign of α_0, we obtain an estimation of the step while moving from the same position but in the other direction. This polynominal is the information used by the system in order to predict the position as a function of time.

6.2.2 Open-loop validation

To test the validity of the proposed open-loop model, a scanning sequence was composed where the device passes four times over six different positions on its range, followed by one scan over the whole range. A part of the command file is listed in Tab.6.1.

Table 6.1: Actuation command for scanning (part).

Command (table)	Repeat x times
WAIT	2
2 STEPS RIGHT	20
HOLD (2x)	50
2 STEPS LEFT	5
2 STEPS RIGHT	5
2 STEPS LEFT	5
2 STEPS RIGHT	5
HOLD (2x)	50
....	..

Now we can offer the same command file to the model and the real device. Fig. 6.2(a) shows the results of both the estimated and the measured plots, which show considerable resemblance.

Figure 6.2(b) is the error plot between the measured and estimated signals. The reader should mind that the error plot has some particularities. First, the sample frequency of the measured displacement equals the frame rate (30

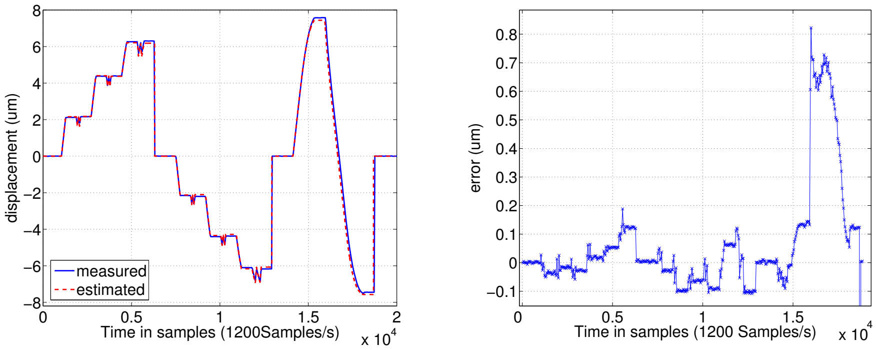

(a) Measured and estimated position of the test sequence.

(b) The error between measured and estimated signals.

Figure 6.2: The LSQ estimation closely matches measurements.

$Samples/s$), whereas the model output is estimated each sample, in this case 1200$Samples/s$. Furthermore, the operating system is not real-time so that the time spacing between different frames is not exactly equal. Another issue is the presence of frame drops in the video data, which happens randomly. A slight delay in time between the measured and estimated data yields high peaks in the error. Especially around $1.87{\cdot}10^4$, one such negative error peak is several μm.

If these effects are disregarded, then the difference between the two signals in Fig. 6.2(a) is at most 140nm and generally under 100nm. If we consider the total range of 15.38μm, then the maximum error is only 0.91%. This rate can be improved even more by using more data for characterization and taking higher order estimations in Eq. 6.1.

The open-loop model is used in the next section in order to improve the performance of the proposed closed-loop system.

6.3 Towards closed-loop control

6.3.1 Switching control

Figure 6.3 illustrates the relevant blocks of the proposed system. The reference tracking signal represents the desired μWalker position trajectory as a function of time and can be defined in terms of table rows or piecewise affine trajectories. The signal offered here and described in more detail later in this section is a seek-and-scan example, where the positioning system is supposed to move

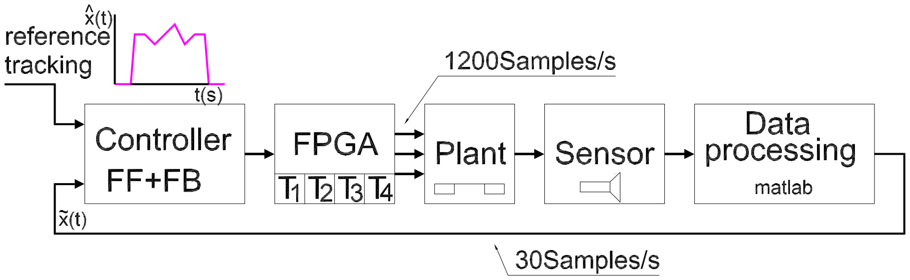

Figure 6.3: Control design of the present setup.

to a certain position as soon and accurate as possible, after which a scanning sequence follows. In the end, the system goes to zero position again.

The controller correlates in time the desired tracking signal to the actual position and then generates a sequence of commands for the FPGA. Effectively, the FPGA contains a number of tables – each of them represents an actuation sequence like for instance 'Table Go To Right' – which can be sent to the actuator in a repetitive fashion, such that the desired motion is obtained (Appendix E). Thus, for obtaining a desired position which is $2\mu m$ off-center and to the right, the controller compares the actual position with the target, then generates a proper sequence (for instance to repeat : "Table Go To Right 50x"). This sequence is passed on to the FPGA, which then executes the respective table 50 times consecutively.

A sensor, in our case a fire-wire camera, passes position information to a computer on which a Matlab routine calculates the achieved displacement for each data point. This data is then used by the controller to adjust the position if necessary before proceeding to the next part of the signal.

It has been remarked before that the FPGA output sample rate (typically $1200Hz$ or higher) is generally much higher than the sensor bandwidth (only $30Hz$). The negative impact of the reduced sensor bandwidth on performance calls for a control approach based on switching between closed- and open-loop.

Basically, in our case we have only two possible velocities, for seek and scan. The seek speed must be as high as possible and bring the device close to the read/write target area. The scan speed is much slower, and does not strictly require feed-back. This speed is closely related to the data density on the recording medium and the cantilever eigen frequency [92].

The feedback information is used only after a seek command in order to position the device accurately on the read/write area, after which the feedforward model in the controller takes over during the effective scanning process. This control paradigm is studied further on by means of a case but first let us have a look at the implementation of the controller.

6.3.2 State diagram-based controller

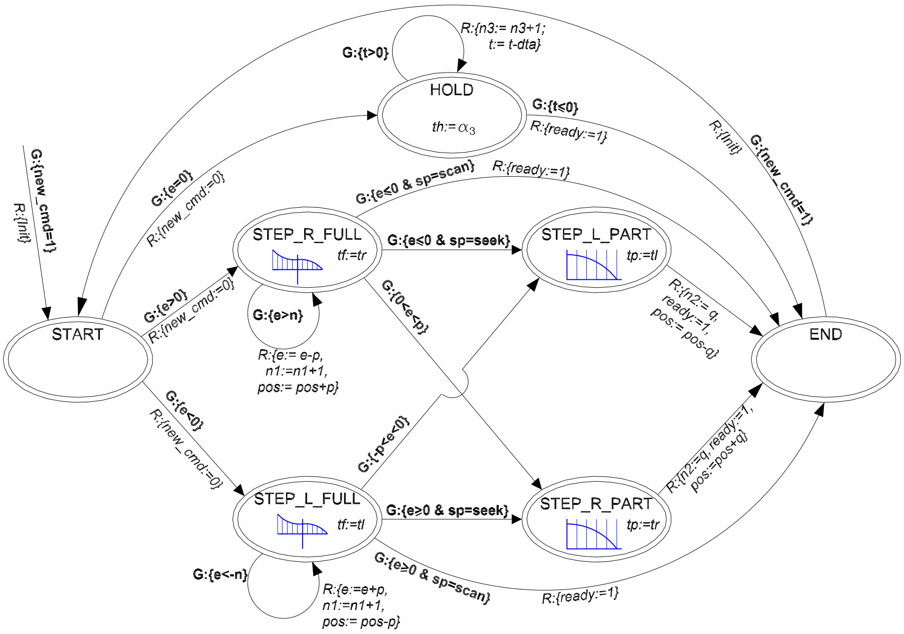

Figure 6.4: State diagram of the proposed controller.

Seven modes have been defined for the controller automaton in Fig.6.4: besides the `START` and `END` mode, there is a `HOLD` mode, and a full- and partial-step mode for each direction. The full-step mode contains the feed-forward function of Eq. 6.1, which gives the corresponding step size as a function of position and direction. As the desired position cannot be achieved by full steps only in general, after the calculated position is within one full step of the desired position, a partial step is performed which can be obtained by using data similar to Fig.3.21(b). For this application, the data can be quantized in a number of sub-regions, which are all represented by a specific table in the FPGA. For instance, a partial step of 0-25% the magnitude of the nominal step can be obtained by table T0-25, a step of 25-50% by using table T0-50, and so on.

In Fig. 6.4, G:{...} represent the guards which can be present at the transition between two states. Generally, the guards test the value of the position error e. R:{...} are resets which change elements in the state vector during the respective transition. For convenience, some elements of this vector also change in a mode itself (t_f and t_p).

The (initial) state vector (*Init*) of this automaton is described by:

$$\begin{bmatrix} t_f \\ t_p \\ t_h \\ dir \\ sp \\ pos \\ t \\ e \\ dta \\ ready \\ n_1 \\ n_2 \\ n_3 \end{bmatrix} = \begin{bmatrix} \alpha_1 \\ \alpha_2 \\ \alpha_3 \\ \alpha_4 \\ \alpha_5 \\ \alpha_6 \\ \alpha_7 \\ \alpha_8 \\ \alpha_9 \\ \alpha_{10} \\ 0 \\ 0 \\ 0 \end{bmatrix} \quad \text{meaning} \quad \begin{bmatrix} \text{pointer towards table for full steps} \\ \text{pointer towards table for partial steps} \\ \text{pointer towards table for hold} \\ \text{direction of movement} \\ \text{speed} \\ \text{position} \\ \text{motion sub-part duration} \\ \text{position error signal} \\ \text{sample duration} \\ \text{communicate with upper layer} \\ \text{nr. of full steps} \\ \text{type of partial step} \\ \text{nr. of hold steps} \end{bmatrix} \tag{6.2}$$

Let us shortly describe the variables present in the state vector. Variables t_f and t_p have a tri-state, namely $\alpha_1, \alpha_2 \in \{0, t_r, t_l\}$. The three possible values mean: no value defined[1], steps to the right and steps to the left, respectively.

t_h is a boolean for the `HOLD` mode ($\alpha_3 \in \{0, 1\}$). The variables dir and sp represent the direction and magnitude of the velocity. They can be found by performing a $sign$ test on the desired velocity function ($\alpha_4 \in \{-1, 0, 1\}$) and by a readout of the magnitude ($\alpha_5 \in \{hold, seek, scan\}$), see also Fig.6.6. pos is the momentary estimated position; initially, $\alpha_6 := \mathring{x}(t_{start})$, where t_{start} is the first data point of the sub-sequence under consideration.

Next, by implementing a trigger on the same velocity plot, we can discriminate between different sequences and define a time t for each sequence ($\alpha_7 \in \mathbf{R}^+$).

The closed-loop part comes in the model with variable e which is initialized as α_8 and represents the position error, which is defined as follows:

$$\begin{aligned} \alpha_8 &= \text{reference tracking} - \text{measured position} \qquad (6.3) \\ &= \hat{x}(t) - \mathring{x}(t), \text{with} \qquad (6.4) \\ \mathring{x}(t) &= \begin{cases} \tilde{x}(t) & : \text{ last sequence was seek} \\ \hat{x}(t-1) & : \text{ otherwise} \end{cases} \qquad (6.5) \end{aligned}$$

Variable dta stands for the time needed for one table to be run:

$$\alpha_9 = \frac{\text{samples per table}}{\text{output samples per second FPGA}}.$$

In our case, $\alpha_9 \approx \frac{12}{1200} = 0.01$.

The $ready$ signal informs a higher controller layer that the automaton is ready for the next part of the signal ($\alpha_{10} \in \{0, 1\}$). Finally, the n_1, n_2 and n_3

---

[1] Do not generate a command of full (t_p) or partial (t_p) steps during this part.

define the number of full steps, the specific table to be used for the partial step and the number of hold sequences.

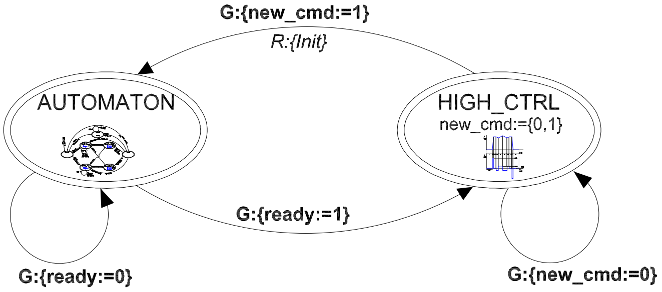

Figure 6.5: Signal interchange between the formerly presented automaton and a higher order control which delivers the initial vector for each sub-sequence.

This automaton outputs one or more commands for the FPGA once it has reached `END` state. As soon as the new_cmd is tested high by the higher controller `HIGH_CTRL` in Fig. 6.5, the automaton is being reset and a new part of the tracking signal is transformed into table rows for the FPGA. The commands are thus stored in a buffer of the FPGA, where they wait for execution.

To better understand the way of working of this automaton-based controller, we will consider a hypothetical seek and scan motion in the next subsection.

6.3.3 Case: seek and scan sequence

In this subsection we study a possible motion tracking scheme, where the probe storage device is supposed to go with 'seek speed' to a certain position, scan over a region and then return to the initial position (Fig. 6.6). The accent lies on feedback and the generation of table rows for the FPGA. The table with actuation commands is listed in Tab. 6.2.

Assuming that all desired signal parts $\hat{x}(t)$ from **A** to **J** are available for execution before starting the automaton – or at least the next sub-part to be executed, we can also derive the velocity profile $\hat{v}(t)$. From this profile, we detect the velocity type (sp) and direction (dir), along with a trigger which defines the time length of each individual sub-part of the signal (α_7).

We start by considering the first part of the proposed tracking signal, namely **A**. Table 6.2 indicates that during this part, the μWalker should hold the present position. In Fig.6.4, the automaton starts processing in mode `START`. As $e = 0$, the guard towards `HOLD` is triggered. In this mode, the automaton calculates the number of times n_3 that the hold table (Appendix E) in the FPGA will be repeated, so as to keep the device at the desired position for the given time pe-

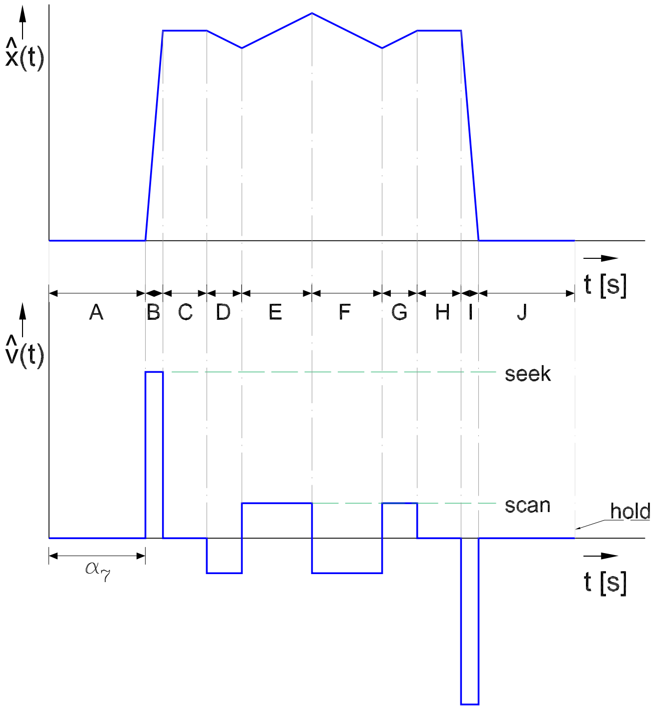

Figure 6.6: Desired position and velocity as a function of time.

riod α_7. When the time is up ($t \leq 0$), the guard to `END` becomes valid. During the jump between modes, the $ready$ variable is set to 1, such that the higher order controller now can read the state vector for next sub-sequence and issue a new command (part **B** of the signal).

We are now at the second and third row in the table. In part **B**, the target is to move as fast as possible to a desired position using seek speed. New values for the state vector (Eq. 6.2) are derived and the vector is loaded before the automaton restarts. The reference tracking $\hat{x}(t)$ is now positive whereas the loop is open: $\mathring{x}(t) = \hat{x}(t-1) = 0$ so that $e > 0$. We arrive in mode `STEP_R_FULL` and using the feed-forward data about step size as function of direction and position, we derive the number of steps n_1 until either the error becomes smaller than one step, or it becomes negative. In the first case the system jumps to mode `STEP_R_PART`, in the latter it has already passed the target value and it must go back a bit (`STEP_L_PART`). In our case, we assume that `STEP_R_PART` is initiated, because $0 < e < p$ holds[2]. Here, based on the remaining distance to be realized – more precise the value of e, a choice is made between several ta-

---

[2] p is the nominal step size calculated from the feed-forward relation (Eq. 6.1).

Table 6.2: Generated table with commands for the FPGA. The **FB**-rows are generated dynamically according to feedback data.

Sub-sequence	Table	Nr. repeats/ Partial table	Speed
A	t_h	n_3	hold
B1	t_r	n_1	seek
B2	t_p	n_2	seek
FB	$\mathbf{t_r}$	$\mathbf{n_1}$	**seek**
FB	$\mathbf{t_p}$	$\mathbf{n_2}$	**seek**
C	t_h	n_3	hold
D	t_l	n_1	scan
E	t_r	n_1	scan
F	t_l	n_1	scan
G	t_r	n_1	scan
H	t_h	n_3	hold
I1	t_l	n_1	seek
I2	t_p	n_2	seek
FB	$\mathbf{t_l}$	$\mathbf{n_1}$	**seek**
FB	$\mathbf{t_p}$	$\mathbf{n_2}$	**seek**
J	t_h	n_3	hold

bles which together cover the whole region of interest between a full step and a step with zero displacement (see again Fig. 3.21(b)). The flag for the partial table is set to the right direction ($t_p := t_r$) and the proper table for the partial step is passed to variable n_2. The seek motion is hereby completed and rows for **B1** and **B2** are written to the commands table (Tab. 6.2).

After this cycle, we want to correct – if necessary – the position by using sensor data. The loop is closed and after a predefined delay, the sensor output is read ($\hat{x}(t) := \tilde{x}(t)$). In this way, we make sure that the scanning position is indeed reached so that we address the target region. The error e is calculated again and if there is a difference between the desired end position of **B** and $\tilde{x}(t)$, then $e \neq 0$. As a result, the automaton is being reset and an additional sequence is processed, which adds another row or set of rows to the FPGA table (**F1, F2** in Tab. 6.2).

Then follows sequence **C**, which is a hold sequence similar to **A**. **D** is the first scanning sequence, during which data should be read from or written to the medium of μSPAM. The tracking velocity is reduced ($sp := scan$), the direction is negative ($dir := -1$) and the automaton only produces full-steps to the left. Note that scanning does not use feedback signals.

The explanation for parts **E** to **J** in Tab. 6.2 is similar and is left as an exercise to the reader.

6.4 Discussion

Even though the practical implementation of the controller presented above is under attention at the moment, both software (20sim) and FPGA (VHDL code) are candidates to host the automaton. In the beginning the controller will be built in software, which interacts with the FPGA code generation by means of a DLL. Information about the current position will be provided to the software controller by a Matlab script which processes $30fps$ real-time, or close to real-time.

The performance of the control system would increase if the interaction between the controller and the FPGA comprises a buffer with multiple rows. In this way, each row can be passed on to the FPGA as soon as it becomes available, while at the same time the FPGA processes the oldest row in the buffer and then the next row.

Substantial improvement can be realized by using a different type of sensor (laser-based or incorporated capacitive sensor), provided that the sensor electronics is fast enough and measurement noise is reduced. Still, the basic structure of the controller scheme will remain identical because no matter how fast the sensor reading electronics is, the feedback loop cannot be closed at the FPGA operating frequency (which can be as high as $3MSamples/s$). Even if there could exist such a fast controller for this purpose, its advantage compared to the present scheme would be minimal, provided that our models of the feed-forward loop are accurate. To be concise, the feeling of the author is that the proposed control scheme can be further studied and implemented in the final μSPAM prototype.

Regarding stability, a number of studies have to be initiated in order to characterize the delay in the loop, to avoid unstable behavior and erroneous sensor readout during feedback. In principle, instability can be avoided if the actuation rate is much faster than the rate at which position data is available.

As a last remark, note that data about the current position does not necessarily have to imply complex sensors and readout circuitry. Like is the case with the hard-disk architecture, coded data on the medium itself could be used to retrieve positioning data. For instance, a number of dedicated probes could be used to keep track of each tile (Fig.2.3). Both position and rotation errors of each tile with respect to the medium underneath are detectable by using four or more dedicated probes per tile. In this hypothetical case, the sensor update interval would be several tens of $kSamples/s$. The challenge of designing and integrating a high-rate, reduced-size controller into the μSPAM system is still an open problem.

Chapter 7

Discussion and recommendations

In the last part of this work, we start by having a retrospective of the thesis objective on page 9. Then we review the main results of each chapter and propose some new directions of research for the future of probe storage, especially the μSPAM project.

7.1 Thesis objective validation

The need for physical modeling of the μWalker has a central place in the thesis objective (pg. 9) and it is clearly the principal topic of this work. Several reasons can be given for the accent that was put into modeling:

- improvement of the actuator for better performance;
- control design and implementation;
- knowledge about phenomena like stick-slip and pull-in at the micro scale.

Like it is the case with all physical systems, very soon in the modeling process it became clear that the models needed to be fed with measurements. Much of this data was not available and as a consequence, a series of measurements were conducted to characterize the micro actuator. Additionally, the characterization results helped to acquire a feeling about the motion principle, device geometry and material properties.

New devices were developed, based on the knowledge from the characterization procedure. The first steps towards closed-loop control have been presented. Let us review the results from each chapter before presenting possible directions for further research.

7.2 Summary and Conclusions

7.2.1 Chapters 1 and 2

A general introduction of data storage was presented, where we proposed a sandwich-like structure of the read/write heads, the medium, the positioning actuators and the driving/readout electronics.

The μSPAM project was shortly described and compared to the state-of-the-art Millipede prototype. One small part of the project is about the positioning device for read and write. A concise comparison between three MEMS actuators made clear that the μWalker is a good positioning device to concentrate on.

7.2.2 Chapter 3

This chapter started by a survey on scaling from the macro world towards MEMS and beyond. Especially when partly unknown friction phenomena are involved in motion of MEMS components, scaling does not prove very useful.

After reviewing the μSPAM setup for characterizing the μWalker, two methods were introduced for position measurements: sub-pixel resolution videos [96] and fringes based on Michelson interferometry [4]. With these methods, a number of results were obtained:

- the relation between the percentage of the μWalker plate that touches the surface and the applied voltage;

- the actuator push and pull force were measured to determine which of the two is limiting the performance; in accordance with models (Chapter 4) and intuition, the pull force is limiting the maximum range of the μWalker; increasing this force would enlarge the maximum range;

- it was shown that bi-polar actuation can alleviate the negative effects that the charged silicon nitride walking surface has on motion repeatability;

- the coefficient of stiction between two contact parts made of silicon nitride – of which one is a neat surface and the other consists of sharp contacts – ranges between 0 and 0.5, depending on the applied voltages and device configuration. For zero applied voltage, the device is supposed to be suspended above the surface, whence no friction is present and the coefficient of stiction approaches zero.

- the optimal actuation voltages for the legs and the plate are $55V$ and $60V$, respectively; the criteria were maximum range and minimization of stiction effects due to the insulator on the walking surface;

- an open-loop motion of 20 steps was repeated 100 times and the standard deviation was only $6.5nm$;
- the relation between step size and springs counter force is linear, in conformity with [73];
- steps smaller than the nominal step size (≈50nm) were measured reproducibly; they are very useful for accurate positioning when the final positioning error should be smaller than half the step size ($<25nm$);
- wear patterns and device life time were investigated by letting several μWalkers run continuously until failure; at the end of the life time, short circuits and welding points occurred between the μWalker parts and the bulk under the walking surface; the number of steps until the first recoverable failure was in one case $4.25 \cdot 10^9$; the same device performed a total of $18.3 \cdot 10^9$ steps before going to oblivion.

7.2.3 Chapter 4

The models presented in literature so far did not predict the pull-in voltage well enough, nor did they give clear relations between step size and device dimensions or material properties. Only by using a physical model, could the μWalker performance be investigated in a structured way.

The first model was on a capacitor with a mobile plate. From this, we found several issues:

- the relation between the pull-in voltage and the stability region was derived from energetical considerations;
- plate thickness has a great impact on pull-in voltage: decreasing the thickness to $0.6\mu m$ yields a pull-in voltage just under $8V$, which makes the adapted device appropriate for mobile applications;
- the plate resonance frequency ($237kHz$) was derived from energy considerations and is in line with other studies in literature.

The second model was quasi-static and concentrated on the μWalker plate. It included the presence of a silicon nitride walking surface between the μWalker parts and the wafer bulk. This model could predict the stick region, the pull-in voltage, the step size and the energy loss during one step of the actuator.

The retraction springs were modeled by considering the relation between the springs force and their deviation from zero position. Both axial and bending forces were incorporated in the model. The simulation results are in agreement with finite element simulations.

The μWalker legs show stick-slip behavior and therefore a friction model without pre-sliding was implemented using a Stribeck curve description. The parameters for this curve were chosen to fit initial measurements.

At last, a dynamical model including the above-mentioned components was simulated in the 20sim package. Some useful data resulted:

- the expected peak power is under $100mW$ for the μSPAM 2D positioning device, if 100 independently working 2D actuators are considered;
- per step, $4pJ$ of energy is used by each μWalker;
- at the moment, the efficiency of the electrical domain is about 84%;
- regarding a comparison between the model simulations and measurements, the error – for a motion composed of 40 steps and after a short break another 20 steps – is at all times smaller than one step.

7.2.4 Chapter 5

Only a part of the 91 actuators designed and fabricated were described in this chapter. Amongst the most interesting optimization questions was the effect of the plate length on the pull-in voltage, maximum range, generated force and on step size (Table 5.1).

Increased plate width did not increase the μWalker force linearly like predicted from models: the maximum measured force was only $5mN$ instead of about $20mN$. This difference was then attributed to the lack of grip in the legs.

Changing the U-shape of the legs into L-shape does not improve motion repeatability. A possible cause for this was pointed to be twisting of the actuator plate.

An alternative retraction system made it possible for a μWalker to establish a new range record: it moved $430\mu m$ away from the center position. The positioning accuracy however was not regarded during design.

Because the video setup can only be used for characterization and not in the future μSPAM device, alternative ways to measure position resulted in a combination between an actuator (μWalker) and a sensor (comb drive), fabricated with the same process. Successful experiments showed that the position of the μWalker can indeed be measured by the comb drive. The noise from the measurements obtained with the comb drive is unfortunately higher than from the video analysis method.

The first step towards 2D actuators was a one-dimensional table actuated by two μWalkers. The need for two actuators arose for two reasons:

- first, having two actuators instead of one does increase the force exerted considerably; this becomes important when a mass needs to be accelerated (i.e. the medium with the data bits in the μSPAM case), because a large force decreases the positioning time and thus the access times;
- second and more important, according to page 36 the μWalker can pull better than it can push; to have a more linear range, the table is moved at all times by two actuators: one pushes while the other pulls.

After the 1D tables were successfully tested, MEMS actuators for 2D motion were the next step. Here, two actuators are present for each axis (four in total). The main issue here was decoupling the motion from one actuator axis to the other. In this way 2D planar motions were realized, where the table could move in eight directions: along the orthogonal axes and diagonally.

7.2.5 Chapter 6

It has been stated that closing the loop for our MEMS positioning system is not straight-forward, because:

- there was a lack of a sensor and actuator of proper size and aggregated together;
- the sensor signal could not be fetched in real-time;
- the actuator behavior is highly non-linear;
- for enough accuracy and due to the geometry, the steps are small; if the range is large, then many steps need to be taken; typically, the μWalker actuation voltages need to be updated about 1200 times per second, whereas the real time sensor data (if any) can be fetched only at $30fps$.

The first approach was to investigate open-loop control. This method is fast and accurate. For a complex motion, the error was at all times smaller than 1% of the total range.

If better accuracy is desired – in the order of tens of nm – then closed-loop control is an option. The model information obtained from the open-loop model can be used in a state diagram controller to improve positioning accuracy and thus decrease seek and track times. In this design, the actuation signals are generated much faster than the rate at which the sensor data comes in. Moreover, steps smaller than $50nm$ can be performed for high-accuracy positioning. Although no closed-loop results have been obtained so far, the hardware implementation should be ready soon.

This concludes the review of the thesis. In the last part of this chapter, possible future work is investigated.

7.3 Future work and the μSPAM perspective

The development of the positioning actuators for μSPAM does not end here. On one hand, this research successfully answered a range of questions regarding actuator design and improvement of performance. On the other hand, a numerous range of research directions are pointed out, which are related to actuator design and aggregation into the system. Some of these directions are listed below and could be regarded as necessary check-points on the way towards a fully working μSPAM prototype – at least from the positioning system point of view.

7.3.1 Setup

- There is a need for automation of the setup used for characterizing electrostatic MEMS actuators. In this way, the amount of experimental data increases, leading us to a better understanding of various phenomena at the micro and nano scales.

- For user convenience, increased life time and measurement data reliability, the whole setup including the amplifier and the data generation and acquisition equipment should be located in the clean environment. The user should not need to enter and leave the clean-room while doing measurements or replacing the actuator to be tested. This in turn would decrease the amount of wafer contamination due to particles in the air. In the present setup, the constrained size of the clean environment is the bottleneck.

- Moreover, the experimental setup including the protective environment should be placed in a room with reduced size, no windows and an air conditioning system instead of a large laboratory. There are multiple advantages to this investment: the air temperature can be kept constant within one or two degrees Celsius, the same air is ventilated through the filters so that maintenance is reduced, no sunshine or open windows can influence measurements, et cetera.

- The projected closed-loop experiments should be performed, as soon as the setup is ready for real-time position acquisition and control.

7.3.2 Models and measurements

- According to the author, new types of measurements should be performed to better characterize stiction, friction and charge phenomena.

- The 2D actuator composed of four μWalkers should be characterized. Especially coupling between the two motion axes must be quantified. At the moment, software is being developed for this purpose.

- Friction models with pre-sliding regime should be implemented into the system, keeping an eye on simulation performance.

- Based on the 1D μWalker models and on measurements from the 2D actuator (yet to be completed), a two dimensional model would become useful to study and correct positioning irregularities at either end of the two axes of motion.

7.3.3 MEMS actuators design

- Amongst the most appealing topics in the design of MEMS data storage actuators, the challenge is to combine a sufficiently large range ($\approx 100\mu m$) with accurate positioning ($<10nm$ error). This work did present actuators with large range and others with very accurate motion, but finding a good compromise between the two is still an open problem.

- Operating voltages could be decreased by using a thinner μWalker plate. This would yield a smaller moving range and actuation force, however this can be compensated by increasing the plate width.

- Increasing the area of the legs will allow the μWalker to exert forces larger than $5mN$. The reason is not because of a larger effective contact area – this will be about the same – but is due to a larger area of the leg. In turn, larger area means a greater vertical force available to keep the leg fixed to the surface. Theoretically, the vertical force on the contact grows linearly with area.

- A very important issue is the decrease or elimination of the up-down (out-of-plane) motion of the legs during motion. The magnitude of the up-down motion is about $350nm$, namely the distance between the bumps and the Si_RN layer in Fig. 2.8. A decrease of this distance could be accomplished by using a thinner SiO sacrificial layer during fabrication and increasing the height of the retraction springs, i.e. the thickness of the device layer. With the current fabrication processes, the device layer thickness is limited.

- Also comb drives for position measurement would be improved if the device layer could be made thicker. The sensitivity of the combs increases linearly with the thickness.

- Two-dimensional actuators and incorporated comb drive sensors should be designed for 2D real time closed-loop positioning. This presents new challenges regarding axis decoupling.

- The attachment of the medium or another load on 1D and/or 2d actuators should be investigated.

- The useful life time of the μWalker can be further increased by having a thicker insulating layer above the bulk. In this way, it would take more time until the bulk is exposed due to wear. Moreover, possible discharges between the bulk and μWalker parts are postponed.

- When looking at data storage from a general point of view, there is no strict need for symmetry between the two orthogonal axes of motion of the positioning device. To the contrary, in literature [76] it is suggested that the data bits are best arranged in arrays, such that they can be read row by row. In this context, it would be useful to investigate the combination of a comb drive and a μWalker. The comb drive is then used to obtain a regular, harmonic motion with large range that reads data from one row (horizontally), whereas the μWalker-like structure moves from row to row (vertically) with positioning high accuracy.

7.3.4 μSPAM perspective

- Regarding the μSPAM project, it is clear that some effort must be put into aggregation of the different subparts (positioning system, medium, probes, controller, packaging and so on). According to the author, severe consequences could result if this matter is not coped with effectively.

- Another possibility for the near future is a steadily interaction between the different data storage projects around the world. For instance, whereas the μSPAM project has advantages such as the potential to fabricate parallel working, further miniaturizable two dimensional actuators, the Millipede project is more successful in the read/write technology, system aggregation, packaging, closed-loop control and other. A synergy between such related projects would increase the chance of success and help develop new fabrication technologies for data storage.

- About one hundred years ago, it has been pointed out by Pointcaré (see beginning of this thesis) that experience – in the form of measurements and observations – lies at the heart of science. In the μSPAM project and especially regarding positioning, it is an urgent necessity to increase the rate of measurements so as to characterize effects that are not fully understood and to quantify positioning accuracy in terms of noise.

- In line with Chapter 2, let us hope that the μSPAM project will become a perspective and will not be degraded to idealism in the future.

Chapter 8

Acknowlegdments

How else could I start this chapter, but by mentioning Stefano, my supervisor? Whenever he was there, he passed his full impulse to the μSPAM project and also guided me within the error bounds. The knowledge I received on physical systems is largely based on talks with Stefano. As a constant watchdog, he has learnt me many things. Amongst the most vital ones I want to mention diplomatic behavior and dealing with 'sleeping dogs'. Stefano, may your future humanoid robots rule the Department and always keep the Department clock on time! Unfortunately, I cannot wait for that moment but will you!?..

In his work, Stefano was of course supported by the head of our department, Job, which I wish to thank for so many things: from his advices on picture and video quality related topics to more general talks and of course also discussions related to my project. Being at the core of a department is not trivial, I am sure; but such a core does have some means to steer the whole in the good direction. I think you did a very good job all these years and I wish you very much strength for the years to come.

Leon Abelmann, leader of the μSPAM project, thank you for your fruitful advices. Your optimistic spirit can now be felt all over the project and in other projects as well. Without your personality, I doubt that our project would have gained so much success and popularity.

Gijs Krijnen and Edin Sarajlic from TST, it was a pleasure to learn so many things about MEMS technology from you. If I would not have considered your knowlegde, technical input and results, it would not have been possible to conduct research on MEMS – for sure not the way it was done during my research.

From the same department (TST), Theo Lammerink is acknowledged for giving me the opportunity to think more about modeling issues while I had to wait for the amplifier. Theo, even if a little late delivered, your amplifier works great and it fulfilled with honour its important place in the characterization of the MEMS devices I presented in this work.

When it came down to doing MEMS measurements, it was Wei Zhou, my room mate, who often cooperated. Wei, thanks for the times we played table-tennis and tennis after work. It was fun to have you around and hopefully I have not misused your friendly character too much.

Spoken about MEMS, I want to give a special word of thanks to Meint and Rik de Boer from TST. Their intensive efforts in the MESA+ clean-room resulted in successful fabrication of the wafers with MEMS devices. I owe you one! Again from TST: Remco and Henk, your help was very welcome. From data cards to microscope systems, you helped me all the way to build the measurement setup. From SMI, Thijs Bolhuis and Jos Pasop supported me with computer software and hardware at times when the situation seemed lost. Jos, keep the wheels rolling! To close the circle of the technical staff, I want to thank Marcel, Gerben and Alfred for their input. Especially Marcel, which has put a lot of effort in the design of setup electronics for the μSPAM setup.

From Mechanical Engineering, Dik Schipper and Erik de Vries helped me characterize tribology-related effects of the μWalker. Every now and then, I also played tennis with Peter Breedveld, which unfortunately I could only beat once, namely the first time. After that it went monotonously bad for me. Anyway, Peter, your 'slices' gave me reason to think what I was doing wrong. Your advice regarding bond graphs and physical systems was quite useful.

I am very merciful for our physics database at the Control Department, which is represented by Norbert Ligterink. It was surprisingly difficult to find a topic in the large sea of physics where this database could not give a fast and appropiate answer to. Norbert, it was a relief for me to know I can contact you each time I felt physics was behaving weird! For all software related problems, I always knew where to find Marcel Groothuis. Rob Quentemeijer helped me maintain the μSPAM project website and more, thank you Rob.

Valer, moving to Brabant became easier with your advices. I thank my former students, Chr. Vriend, Martin Scheppers and especially Martin Lootsma for their contribution to the project. My thanks also goes to the CE Laboratory as a group, the AIOs and to our restless secretary, Carla. To the rest of the μSPAM/A4 team I give kind regards and I hope that team-play will lead to a great prototype somewhere in the near future. I wish to thank STW for funding the project and for their input during the meetings. Alexander, Mink, Jos and Arnout, my car and motorcycle now have a better future because of you!..

Lavinia, my wife, thank you so much for your support and strength all these years. My parents deserve my complete gratitude for bringing basic ingredients into my life, amongst them: religion, education and joy of living. My brothers Gabi and Andrei, go for the best.

There is probably a legion of people who added their input to my work and whose names I failed to mention above. To all these people I apologize and I would like to thank them more than proportionally for their efforts in supporting me and the project.

Appendix A

Optical resolution of the setup

The topic of this appendix is to elaborate the resolution and the limiting factors of the optical measurements done in Chapter 3. The data used here was taken from the data sheets of the respective components. Only measurements with the 50x objective from Mitutoyo are considered here. Please see Figure A.1 for more details.

A.1 Microscope optical path resolution

Defining r as the smallest detail that can be observed, then:
$r \approx \frac{\lambda}{2N.A._{obj}}$, where
λ is wavelength of light, typically $>400nm$ and
$N.A._{obj}$ the numerical aperture of the lens, here 0.42 for the 50x M Plan Apo SL objective. Thus $r > 0.48\mu m$, which means roughly that details smaller than $0.5\mu m$ cannot be seen purely due to the resolving power of the objective.

Taking a lens with higher numerical aperture would definitely increase image sharpness, because a magnification of 50x results in a spot size of $25\mu m$ on the CCD chip, which is about 5 pixels wide.

A.2 Digital camera resolution

The CCD chip of the XCD-X710 Sony camera contains square pixels with dimensions of $4.65\mu m$ and a resolution of 1024x758 pixels. Up to 30fps can be recorded (non-interlaced) in 8 bits grey tints.

Assuming again the 50x magnification, then about $93nm/pixel$ resolution results. This resolution was also verified and confirmed experimentally.

If the camera were to be replaced by another one with a higher pixel density, then the measurement accuracy would increase, because now one pixel

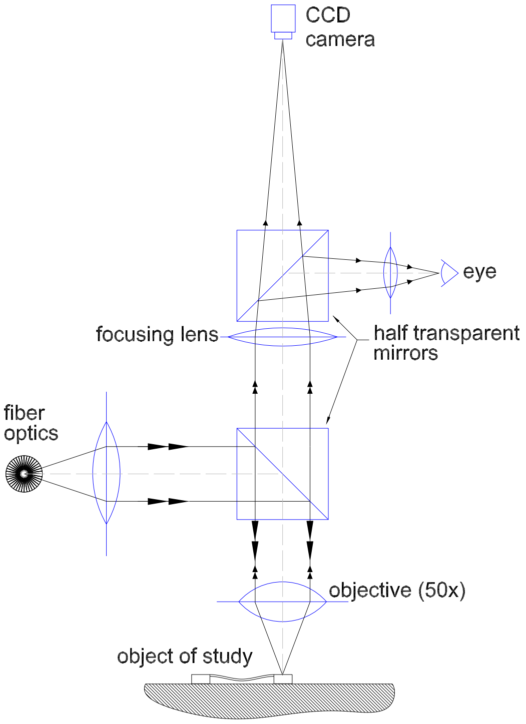

Figure A.1: Schematic view of the optical path through the microscope.

corresponds to a smaller movement of the actuator – irrespective whether the microscope resolution is increased or not.

Appendix B

Tables

Table B.1: Typical values of the lumped parts in Figure 3.6, Section 3.2.

V_{source}	source voltage [V]	-10 ... +10
R_{source}	internal resistance source [Ω]	<50
R_{term}	terminator resistance [Ω]	0/50
R_{in_amp}	input resistance amplifier [Ω]	≈9.4k
V_{out_amp}	amplifier output voltage [V]	-100 ... +100
R_{out_amp}	output resistance amplifier [Ω]	≈220
$C_{cab+prb}$	capacitance of the cable, probe and BNc connection [F]	102.3p
R_{cable}	cable resistance [Ω]	0.265
$R_{bnd+spr}$	resistance of the probe-bond contact, bond and retraction springs [Ω]	≈ 2k
$C_{bnd+spr}$	bond and retr. springs capacitance [F]	19.2p
C_{load}	load capacitance [F]	<1.5p

Table B.2: Dimensions of the basic μWalker type in μm.

L_{total}	overall device length	440
w_{total}	overall width	286
h_{total}	overall height	5.5
L_{leg}	leg length	216
w_{leg}	leg width	286
L_{n_leg}	notch length	110
w_{n_leg}	notch width	106
L_{plate}	plate length	208
w_{plate}	plate width	94
h_{plate}	plate height	1.2
h_{retr_s}	retraction springs height	5.5
L_{retr_s}	retr. springs length	200
w_{retr_s}	retr. springs width	2
h_{conn_s}	connection springs height	5.5
L_{conn_s}	conn. springs length	15
w_{conn_s}	conn. springs width	2
$N_{bumps_{leg}}$	number of bumps for leg	204
$N_{bumps_{plate}}$	number of bumps for plate	102
r_{bump}	estimated bump radius	2.5
h_{bump}	estimated bump height	0.22
d_{leg}	distance leg surface	0.33
d_{plate}	distance plate surface	1.88
d_{Si_RN}	silicon nitride layer thickness	0.16

Appendix C

Calculation of loads of the actuation scheme

C.1 Amplifier cable and probe

Low capacitance cables are strictly necessary in order to minimize signal alteration from amplifier to the load. The actuation signals passing through the cables are pulses up to $100V$ at a high rate, up to one million pulse signals per second or more.

Cables with reduced (parasitic) capacitance ($45pF/m$) and small outer diameter (≈$2.6mm$) are used to connect the amplifer to the probes. For a $1/1.5m$ cable[1] and a probe, spectrum analyzer measurements reveal a capacitance of $75.1pF$ and $102.3pF$, respectively.

The resistance has been estimated from the dimensions and material properties:

$$R_{cable} = \rho_{Cu} * \frac{L_{cable}}{\left(\frac{\pi * d_{core}}{4}\right)^2},$$

with

$$\rho_{Cu} = 1.78\,10^{-8}\,\Omega m^2/m, \quad L_{cable} = 1.0/1.5\,m, \quad d_{core} = 0.35\,10^{-4}\,m^2.$$

This gives a resistance value of 0.185Ω for a $1m$ cable or 0.278Ω for $1.5m$.

---

[1] sets of cables of these dimensions have been made

C.2 Bonds and retraction springs

The resistance of the contact between the probe tip and the bond is not a trivial thing to measure or calculate. During measurements, the resistance continuously varied one or two orders of magnitude, due to complex phenomena like temporary welding points at the contact area between the tip and the polysilicon bond. Actually, these complications can be attributed to the silicon oxide layer above which grows above the polysilicon bond. This is a well-known problem in MEMS, but the effects are not very well understood. A few effective measures consist in taking sharp, clean tips and making sure that the preload on the probe tips is always equal.

The conductivity of the boron-doped poly silicon retraction springs (and the trail leading from the retraction spring towards the mid plate) can be estimated by using the same formula as above for the cable. Considering a boron concentration of 10^{17} to 10^{18} atoms per mol polysilicon [2], the specific resistance is around 0.01 Ωm, which would mean that a spring of typical dimensions (Lwh = $200\mu m$x$2\mu m$x$5.5\mu m$) would have a resistance of around $200k\Omega$! Resistive measurements confirm the idea that this high resistance is not realistic. The descrepancy can be partly explained by the fact that the boron doping is not unformly distributed as a function of material depth, but is exponentially instead. However the exponential distribution cannot be too pronounced, otherwise stress gradients would form in the poly silicon layer, bending the MEMS structure beyond a usable shape. Clearly, this is not the case with the current devices. About 500Ω have been measured for a resistor of length $200\mu m$(legs), and 1500Ω for the total length of the connection from the bond to the plate. This yields an estimated $2.5\Omega/\mu$ length, which is valid for all connections of the μWalker devices produced.

C.3 Capacitance of the μWalker sub-parts

Fig. C.1 and C.2 reveal which estimations have been made while calculating the effective value of the capacitance of the legs and of the plate, both in and out of pull-in situation. The assumption is here that the electostatic field is parallel on the part and on the surface, such that no field lines are found in the center of a bump, only on the edges of bumps and outside.

Let us consider the dimensions in Table B.2 and also in Fig. 2.8. The total effective area of one part is:

$$A_{leg_{eff}} = \Big(L_{leg}w_{leg} - L_{n\_leg}w_{n\_leg}\Big) - N_{bumps_{leg}}\big(\pi r_{bump}^2\big),$$

---

[2] higher boron concentration would give rise to surface cristals, which make upcoming etching processes during fabrication useless.

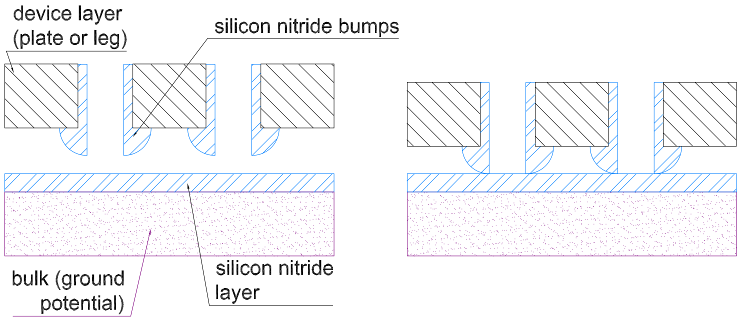

Figure C.1: Section of a part of the μWalker (left: no pull-in; right: pull-in).

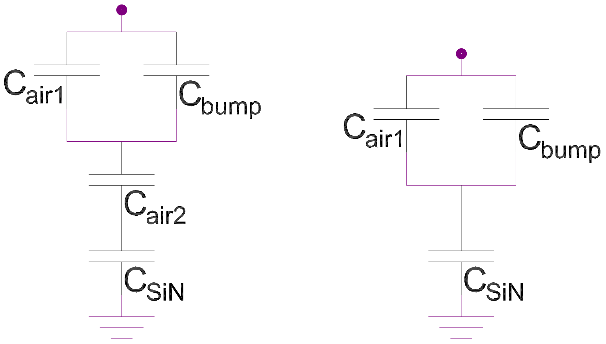

Figure C.2: Lumped parts derived from the μWalker geometry (left: no pull-in; right: pull-in).

$$A_{leg_{eff}} = 4.61 \cdot 10^{-8}\, m^2$$

for the legs and for the plate:

$$A_{plate_{eff}} = \left(L_{plate} w_{plate}\right) - N_{bumps_{plate}} \left(\pi r_{bump}^2\right),$$

$$A_{plate_{eff}} = 1.75 \cdot 10^{-8} m^2$$

We can calculate the capacitance of the parts both when they touch the surface due to pull-in, and when they are not actuated. These values are the lower and upper bounds for the load capacitances: Fig. C.2 shows the lumped parts for these two cases.

C.3.1 Legs capacitance

Starting with the situation when no actuation is applied (left), we have:

$$C_{air1} = \frac{\epsilon_0 A_{leg_{eff}}}{h_{bump}};$$

$$C_{bump} \lll C_{air1} \quad \Rightarrow \quad C_{bump} \approx 0;$$

$$C_{air2} = \frac{\epsilon_0 A_{leg_{eff}}}{d_{leg}};$$

$$C_{SiN} = \frac{\epsilon_0 \epsilon_{Si_R N} A_{leg_{eff}}}{d_{Si_R N}};$$

The corresponding capacitance $C_{leg_{nopull-in}}$ is:

$$C_{leg_{no\,pull-in}} = \left(\frac{1}{C_{air1}} + \frac{1}{C_{air2}} + \frac{1}{C_{SiN}}\right)^{-1} \Rightarrow$$

$$C_{leg_{no\,pull-in}} = 7.14 \cdot 10^{-13}\, F$$

In case the applied voltage causes pull-in and the leg sticks to the surface, the equivalent capacitance becomes:

$$C_{leg_{pull-in}} = \left(\frac{1}{C_{air1}} + \frac{1}{C_{SiN}}\right)^{-1} \Rightarrow$$

$$C_{leg_{pull-in}} = 1.69 \cdot 10^{-12}\, F$$

C.3.2 Plate capacitance

The case with no actuation is identical to the legs:

$$C_{air1} = \frac{\epsilon_0 A_{plate_{eff}}}{h_{bump}};$$

$$C_{bump} \lll C_{air1} \quad \Rightarrow \quad C_{bump} \approx 0;$$

$$C_{air2} = \frac{\epsilon_0 A_{plate_{eff}}}{d_{plate}};$$

$$C_{SiN} = \frac{\epsilon_0 \epsilon_{Si_RN} A_{plate_{eff}}}{d_{Si_RN}};$$

This results in:

$$C_{plate_{no\,pull-in}} = \left(\frac{1}{C_{air1}} + \frac{1}{C_{air2}} + \frac{1}{C_{SiN}}\right)^{-1} \Rightarrow$$

$$C_{plate_{no\,pull-in}} = 7.32 \cdot 10^{-14}\,F$$

For the pull-in case, the situation is slightly more complex, as the capacitance is dependent on the voltage applied. A higher voltage will increase the percentage of the plate which sticks to the surface and thus the capacitance. This interesting subject is treated in Chapter 4, where relation between the electrostatic force and the percentage of stick in the plate and the distance between the plate and the walking surface is derived. The higher bound would be reached by applying an infinite actuation voltage, which then would theoretically pull the whole plate to the ground. In this hypothetical case, we would have:

$$C_{plate_{max\,pull-in}} = 6.44 \cdot 10^{-13}\,F$$

Typically, the capacitance would be lower than about $\frac{2}{3} C_{plate_{max\,pull-in}}$ for most applicable voltages (amplitude smaller than $80V$).

C.4 Simplifications

A number of simplifications were introduced above, which do not have a great effect:

- no cross-coupling channels via isolation tranches; this is permitted, because the height of the channels – and thus the rate of the coupling capacitance – is very reduced

- the retraction springs do not add any remarkable value to the total capacitance
- the resistance of the bond is much smaller than the resistance of the retraction spring(s) in series with it, so it is disregarded.
- the internal resistance of the legs and of the plate is much smaller than of the retraction springs

Appendix D

Principal mechanisms of wear

In this appendix, four main mechanisms of wear are elucidated shortly. The four types of wear are: adhesive, abrasive, corrosive wear and fatigue. The information presented here was derived from [91],[95].

D.1 Adhesive wear

Adhesive wear is the result of contact friction between two surfaces of about the same hardness. In the μWalker case, the material is silicon nitride. Material is being transferred from one part to the other. This kind of wear takes place when the boundary layer cannot protect the two surfaces anymore. Cold welding is a category of adhesive wear and takes place when identical or compatible materials are cleaned and rubbed together with sufficient force. This phenomenon creates a bond between the two materials which is practically as strong as the parental material.

The effect of cold welding might be an important factor concerning the life time of the μWalker actuator. As the bumps and the walking surface are made of the same material, the oxide in between is slowly and surely moved away by continous actuation. The ideal condition for cold welding are present. This has actually been observed in practice very often, expecially after applying a high voltage and/or actuating a device for several days.

D.2 Abrasive wear

When the hardness of the contact material differs a lot, the hard material will plough into the soft one, thus creating traces and finally removing or replacing parts of the soft material.

In our MEMS actuator case, this type of wear could happen as soon as one or more leg bumps have suffered from adhesive wear and are worn out. The ploughing that might have occured to the walking surfaces now attacks the device material around the bumps, which is made of polysilicon – a more soft material.

D.3 Corrosive wear

Oxidation of the polysilicon layer is a good example of corrosive wear. Because oxidation increases with temperature, it is expected that a certain balance will occur between corrosive and adhesive wear. An increased rate of actuation will thus also increase the production of the boundary layer. As such, corrosive wear does not have a negative effect on the μWalker life time.

D.4 Fatigue

In rolling contacts, fatigue plays a role. This is expecially the case when relatively large normal forces are present at the contact. Although the materials seem to hold the applied loads, small fissures appear just under the surface. With time, these microscopic cracks grow towards the surface and large pits are formed, a phenomenon which is called pitting.

The presence of fatigue during operation of the μWalker could not be confirmed by any measurements or observations. The reason for this is the high material hardness of silicon nitride and also the fact that the adhesive and abrasive wear take place at a much more pronounced rate.

Appendix E

Actuation sequences

E.1 General

A basic bi-polar step like the one in Fig. 3.12 can be expressed in a compact way as in Table E.1 A step in the opposite direction is composed of the signal in Table E.2. This is exactly the sequence offered to the data generation card to complete one step. More steps can be generated by repeating the sequence a desired number of times. In fact, there are a number of tables, each of them with a function. The most important are:

- hold a position (H)
- go one step to one direction (Go+)
- go one step to the opposite direction (Go-)
- release (R)

By using some simple code, one can generate a data file of deliberate length from the tables. For instance, the command file *dummy.cmd* (Table E.3) generates a signal which takes 20 steps to the right[1], then waits, then takes 50 steps in the opposite direction, then waits again and finally the device returns to

---

[1] note that each sequence is composed of two steps

Table E.1: Basic, bi-polar step to the right, where x stands for the typical voltage of $55V$ (Go+).

Left leg	x	0	0	-x	-x	-x	-x	0	0	x	x	x
Right leg	x	x	x	x	0	0	-x	-x	-x	-x	-0	0
Plate	0	0	x	x	x	0	0	0	-x	-x	-x	0

Table E.2: Basic, bi-polar step to the left (Go-).

Left leg	x	x	x	x	0	0	-x	-x	-x	-x	0	0
Right leg	x	0	0	-x	-x	-x	-x	0	0	x	x	x
Plate	0	0	x	x	x	0	0	0	-x	-x	-x	0

Table E.3: Command file to generate a walking pattern.

Table	R	Go+	H	Go-	H	R
Repeat x times	5	10	5	25	5	5

steady-state due to the release at the end. The result is a *dummy.sig* file, typically a long file with all the actuation signals (Table E.4). The file can now be loaded into a data generation card (NI data card and Labview™ or FPGA), which is then connected to the μWalker via the voltage amplifier. In this example, only the first three channels are used.

Note that by implementing the actuation in this way, a road is paved towards feedback control, where the FPGA choses between a number of predefined tables, and where the choice is based on the difference between the desired position and the current or the estimated position of the μWalker.

E.2 Push and pull signals

In line with the above presented way of signal generation, the Tables E.5, E.6, E.7 and E.8 are useful for push and pull actuation.

The command files used to capture the push and pull displacement are listed in Tables E.9 and E.10, respectively.

E.3 1D and 2D table signals

In this section, we show the sequences needed for actuation a one dimensional table, or a 2D table by actuating both μWalkers for one direction. Because the amount of charge induced in the wafer during actuation should be minimized, bipolar signals are used. Let us first consider the one dimensional case now,

Table E.4: Part of the resulting signal file $dummy.sig$.

Left leg	0	0	0	0	0	x	0	0	-x	-x	-x	-x	...
Right leg	0	0	0	0	0	x	x	x	x	0	0	-x	...
Plate	0	0	0	0	0	0	0	x	x	x	0	0	...

Table E.5: Positive actuation for capturing the push displacement (Psh+).

Left leg	x	x	x	x	x	x	x	x	x	x	x	x
Right leg	0	x	0	0	0	0	0	-x	0	0	0	0
Plate	x	x	x	0	0	0	-x	-x	-x	0	0	0

Table E.6: Negative actuation for capturing the push displacement (Psh-).

Left leg	x	0	-x	-x	-x	-x	-x	-x	-x	-x	-x	-x	-x	-x	-x	-x	-x	0	x	x
Right leg	x	x	x	0	0	x	0	0	0	0	0	-x	0	0	0	0	-x	-x	-x	0
Plate	0	0	0	0	x	x	x	0	0	0	-x	-x	-x	0	0	0	0	0	0	0

Table E.7: Positive actuation for capturing the pull displacement (Pll+).

Left leg	x	x	x	x	x	x	x	x	x	x	x	x	x	x
Right leg	x	0	0	x	0	0	0	0	0	-x	0	0	0	0
Plate	x	0	x	x	x	0	0	0	-x	-x	-x	0	0	0

Table E.8: Negative actuation for capturing the pull displacement (Pll-).

Left leg	-x	-x	-x	-x	-x	-x	-x	-x	-x	-x	-x	-x	-x	-x	-x	0
Right leg	x	x	0	x	0	0	0	0	0	-x	0	0	0	0	x	x
Plate	0	0	x	x	x	0	0	0	-x	-x	-x	0	0	0	0	0

Table E.9: Command file to capture the push displacement.

Table	R	Go+	Psh+	Go+	Psh-	Go+	Psh+	...
Repeat x times	1	5	1	5	1	5	1	...

Table E.10: Command file to capture the pull displacement.

Table	R	Go-	Pll+	Go-	Pll-	Go-	Pll+	...
Repeat x times	1	5	1	5	1	5	1	...

Table E.11: 1D actuation with two μWalkers: starting one step (or a sequence of more steps) in the positive direction (sp).

Act.1-L	0	0	x
Act.1-R	x	x	x
Act.1-P	0	x	x
Act.2-L	x	x	x
Act.2-R	x	x	x
Act.2-P	0	0	0

Table E.12: 1D actuation with two μWalkers: processing one step in the positive direction (p).

Act.1-L	x	x	x	0	0	-x	-x	-x	-x	0	0	x
Act.1-R	0	0	-x	-x	-x	-x	0	0	x	x	x	x
Act.1-P	x	0	0	0	-x	-x	-x	0	0	0	x	x
Act.2-L	0	0	-x	-x	-x	-x	0	0	x	x	x	x
Act.2-R	x	x	x	0	0	-x	-x	-x	-x	0	0	x
Act.2-P	0	x	x	x	0	0	0	-x	-x	-x	0	0

keeping in mind that wihout added complexity, a 2d device can be actuated by using the same tables.

There are eight tables that can be used for (for each axis) and they are shown below. It is supposed that one actuator (Act.1) is sided left (or below) the table, whereas the other (Act.2) is right (above) it. To illustrate with an example, Act.1-L represents the signal for the left leg of the actuator left (or below) the table. Please (re)visit Chapter 5 for more information.

Table E.13: 1D actuation with two μWalkers: ending one step (or a sequence of more steps) in the positive direction (ep).

Act.1-L	0	0	x
Act.1-R	x	x	x
Act.1-P	x	0	0
Act.2-L	x	x	x
Act.2-R	x	x	x
Act.2-P	0	0	0

Table E.14: 1D actuation with two μWalkers: starting one step (or a sequence of more steps) in the negative direction (sn).

Act.1-L	x	x	x
Act.1-R	x	x	x
Act.1-P	0	0	0
Act.2-L	x	x	x
Act.2-R	0	0	x
Act.2-P	0	1	1

Table E.15: 1D actuation with two μWalkers: processing one step in the negative direction (n).

Act.1-L	x	x	x	0	0	-x	-x	-x	-x	0	0	x
Act.1-R	0	0	-x	-x	-x	-x	0	0	x	x	x	x
Act.1-P	0	x	x	x	0	0	0	-x	-x	-x	0	0
Act.2-L	0	0	-x	-x	-x	-x	0	0	x	x	x	x
Act.2-R	x	x	x	0	0	-x	-x	-x	-x	0	0	x
Act.2-P	x	0	0	0	-x	-x	-x	0	0	0	x	x

Table E.16: 1D actuation with two μWalkers: ending one step (or a sequence of more steps) in the negative direction (en).

Act.1-L	x	x	x
Act.1-R	x	x	x
Act.1-P	0x	0	0
Act.2-L	x	x	x
Act.2-R	0	0	x
Act.2-P	x	0	0

Table E.17: 1D actuation with two μWalkers: holding the same position (h).

Act.1-L	x	x	0	-x	-x	-x	-x	-x	0	x	x	x
Act.1-R	x	x	0	-x	-x	-x	-x	-x	0	x	x	x
Act.1-P	0	0	0	0	0	0	0	0	0	0	0	0
Act.2-L	x	x	x	x	0	-x	-x	-x	-x	-x	0	x
Act.2-R	x	x	x	x	0	-x	-x	-x	-x	-x	0	x
Act.2-P	0	0	0	0	0	0	0	0	0	0	0	0

Table E.18: 1D actuation with two μWalkers: going to steady-state (ss).

Act.1-L	0	0	0	0	0	0	0	0	0	0	0	0
Act.1-R	0	0	0	0	0	0	0	0	0	0	0	0
Act.1-P	0	0	0	0	0	0	0	0	0	0	0	0
Act.2-L	0	0	0	0	0	0	0	0	0	0	0	0
Act.2-R	0	0	0	0	0	0	0	0	0	0	0	0
Act.2-P	0	0	0	0	0	0	0	0	0	0	0	0

Table E.19: Command file which generates a square motion in two dimensions.

Table (horiz.)	sp	p	ep	h	h	h	sn	n	en	h	h	h
Table (vert.)	sp	h	h	sn	n	en	h	h	h	sp	s	ep
Repeat x times	1	75	1	1	75	1	1	75	1	1	75	1

For full 2D actuation –all four μWalkers of the 2D table, a total of 12 actuation signals are needed. Although fully actuating a 2D table might seem complex at first, the axes are actuated separately. The matlab scripts used to generate the actuation file from the tables below support signal generation for 2D devices. For instance, generating a two dimensional square movement with the lattice of 150 steps would require the command file in Tab. E.19

Appendix F

Bending equations for the Timoshenko beam

This Appendix is based on [21] and the theory holds for very small deflections such that the axial stress due to the clamped-clamped situation does not become dominant.

If we consider a prismatic beam (Fig. F.1 which suffers from a force F_{in} at the center, then the whear force, moment, slope and deflection can be derived. In the figure, $\mathbf{M}$ and $\mathbf{F}$ are the reference momentum and force, respectively; $\mathbf{R_L}$ and $\mathbf{R_R}$ are the counter forces and $\mathbf{M_L}$ and $\mathbf{M_R}$ the counter momenta exerted by the walls at the ends. Actually, the load distribution could be seen as the spatial counter part of the Dirac (time) impulse, namely $q(x) = c_1 \delta\left(x - \frac{L_{plate}}{2}\right)$.

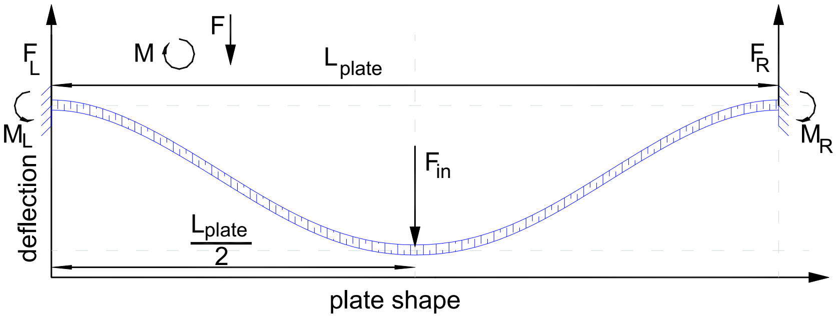

Figure F.1: Side-view of a prismatic beam with an impulse-like load distribution.

For the load distribution, we can write:

$$E_{poly}\ I_{plate}\frac{\partial^4 y(x)}{\partial x^4} = c_1\ \delta(x - \frac{L_{plate}}{2}) \tag{F.1}$$

$$\tag{F.2}$$

The shear force follows by integration:

$$\begin{aligned} E_{poly}\ I_{plate}\frac{\partial^3 y(x)}{\partial x^3} &= \int c_1\ \delta\left(x - \frac{L_{plate}}{2}\right)\mathrm{x} && \text{(F.3)} \\ &= c_1 && \text{(F.4)} \end{aligned}$$

Integrating once more with respect to position gives the moment equation:

$$\begin{aligned} E_{poly}\ I_{plate}\frac{\partial^2 y(x)}{\partial x^2} &= \int c_1\mathrm{dx} && \text{(F.5)} \\ &= c_1\ x + c_2 && \text{(F.6)} \end{aligned}$$

The slope follows in the same way:

$$\begin{aligned} E_{poly}\ I_{plate}\frac{\partial y(x)}{\partial x} &= \int c_1\ x + c_2\mathrm{dx} && \text{(F.7)} \\ &= \frac{1}{2}c_1\ x^2 + c_2\ x + c_3 && \text{(F.8)} \end{aligned}$$

The deflection of the plate appears after four integrations:

$$\begin{aligned} E_{poly}\ I_{plate}\ y(x) &= \int \frac{1}{2}c_1\ x^2 + c_2\ x + c_3\mathrm{dx} && \text{(F.9)} \\ &= \frac{1}{12}c_1\ x^3 + \frac{1}{2}\ c_2\ x + c_3\ x + c_4 && \text{(F.10)} \end{aligned}$$

Now, let's consider the boundary equations involved for Eq. F.4:

$$c_1 = \frac{F}{2} = R_L = R_R$$

This follows from the force equillibrium equation. Next is the equillibrium of the momenta (Eq. F.6), where:

$$c_1\ x + c_2 = -M_L = M_R$$

Looking in x=0, we get:

$$c_2 = -M_L = M_R$$

For the slope (Eq. F.8, we know that due to clamping, in $x = \left\{0, \frac{L_{plate}}{2}, L_{plate}\right\}$ yield a value of zero for the slope:

$$c_3 = 0\ (x = 0)\ \&\ \frac{1}{2}\frac{F_{in}}{2}\frac{L_{plate}^2}{4} + M\frac{L_{plate}2}{+}c_3 = 0\ (x = \frac{L_{plate}}{2})$$

The last equation gives the moment:

$$M_R = -M_L = \frac{F_{in}\ L_{plate}}{8}$$

Finally, for the deflection $y(x)$ holds in $x = 0$:

$$c_4 = 0,$$

such that:

$$c_1 = \frac{F_{in}}{2}\ ,\ c_2 = -\frac{F_{in}\ L_{plate}}{8}\ ,\ c_3 = c_4 = 0 \tag{F.11}$$

These results from the boundary conditions are now inserted into the differential equations:

$$\begin{align} E_{poly}\ I_{plate} \frac{\partial^3 y(x)}{\partial x^3} &= \frac{F_{in}}{2} \tag{F.12}\\ E_{poly}\ I_{plate} \frac{\partial^2 y(x)}{\partial x^2} &= \frac{F_{in}\ x}{2} - \frac{F_{in}\ L_{plate}}{8} \tag{F.13}\\ E_{poly}\ I_{plate} \frac{\partial y(x)}{\partial x} &= \frac{F_{in}\ x^2}{4} - \frac{F_{in}\ L_{plate\ x}}{8} \tag{F.14}\\ E_{poly}\ I_{plate} y(x) &= \frac{F_{in}\ x^3}{12} - \frac{F_{in}\ L_{plate\ x^2}}{16} \tag{F.15} \end{align}$$

Looking at $x = \frac{L_{plate}}{2}$, we get the maximum deflection:

$$\begin{align*} y_{max} &= \left| y\left(\frac{L_{plate}}{2}\right) \right| \\ &= \left| \left(\frac{F_{in}}{12} \frac{L_{plate}^3}{8} - \frac{F_{in}\ L_{plate}}{16} \frac{L_{plate}^2}{4} \right) \frac{1}{E_{poly}}\ I_{plate} \right| \\ &= \frac{1}{192} \frac{F_{in}\ L_{plate}^3}{E_{poly}\ I_{plate}} \end{align*}$$

Conversely, the point force exerted due to a deflection y_{defl} at the center is:

$$F_{in} = k_{lin}\ y_{defl}, \qquad k_{lin} = \frac{192 E_{poly} I_{plate}}{L_{plate}^3} \tag{F.16}$$

This is, the stiffness of the plate is independent on the deflection for small deflections.

Appendix G

Calculation of the axial force in a plate

The aim of this appendix is to show that the elongation of the μWalker plate cannot be significant for altering the step size for the set of standard dimensions of the actuator plate – therefore the axial stiffness is too high. More information about line integrals can be found in [10].

We start by defining a polynominal shape $w(x)$ of the plate in Fig. G.1,

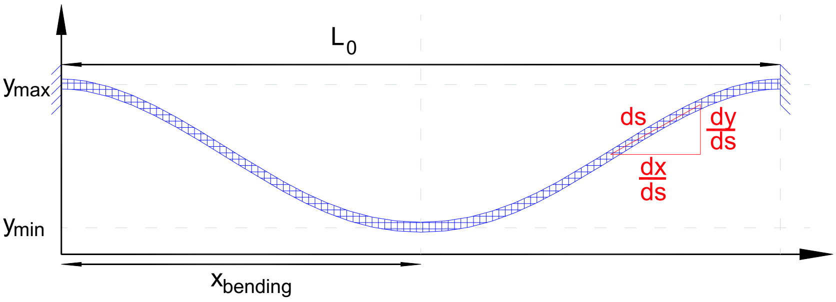

Figure G.1: Illustration of the integral over an arc problem.

which can be written in one of the equivalent forms:

$$\begin{aligned}
w(x) &= d_0 \left\{ 1 - \left(\frac{2}{L_0}\right)^4 \cdot \left[\left(\frac{L_0}{2}\right)^2 - \left(x - \frac{L_0}{2}\right)^2 \right]^2 \right\} \\
w(x) &= \frac{16 d_0}{L_0^4} \cdot \left(\left(\frac{L_0}{2}\right)^4 - x^4 + 2L_0 x^3 - L_0^2 x^2 \right) \\
w(x) &= d_0 - \frac{16 d_0}{L_0^4} x^4 + \frac{32 d_0}{L_0^3} x^3 - \frac{16 d_0}{L_0^2} x^2 \\
w(x) &= \alpha x^4 + \beta x^3 + \gamma x^2 + \delta,
\end{aligned}$$

with α, β, γ, δ defined as appropriate terms. The amplitude d_0 depends on the input force and can be at most 2.05μm (from Fig. 2.8), while the total beam length L_0 is constant, namely 208 μm.

The first step is to parameterize function $w(x)$ in s, such that $L = \int ds$. Using the transformation

$$\begin{aligned}
x(s) &= x, \\
y(s) &= \alpha s^4 + \beta S^3 + \gamma s^2 + \delta
\end{aligned}$$

and the Pythagorean theorem (see again Fig. G.1), yields:

$$\begin{aligned}
ds &= \sqrt{\left(\frac{\partial x}{\partial s}\right)^2 + \left(\frac{\partial y}{\partial s}\right)^2} \\
ds &= \sqrt{1 + \left(4\alpha s^3 + 3\beta s^2 + 2\gamma s\right)^2}
\end{aligned}$$

Then, for the total length L holds:

$$L = \int_{l=0}^{l=L_0} \sqrt{(4\alpha s^3 + 3\beta s^2 + 2\gamma s) + 1} dl$$

If we take the assumption that the plate only touches the walking surface at a line segment (in the center), then for the given values holds $L \approx 208,0492515 \cdot 10^{-6} m$, or a difference of $\approx 49.25 nm$ with respect to L_0. The strain is:

$$\frac{L - L_0}{L_0} \approx 2.3678 \cdot 10^{-4},$$

which leads to the total axial force due to elongation:

$$\begin{aligned}
F_{axial} &= E_{poly} w_{plate} h_{plate} \frac{L - L_0}{L_0} \\
F_{axial} &\approx 4.2735 \cdot 10^{-3} [N],
\end{aligned}$$

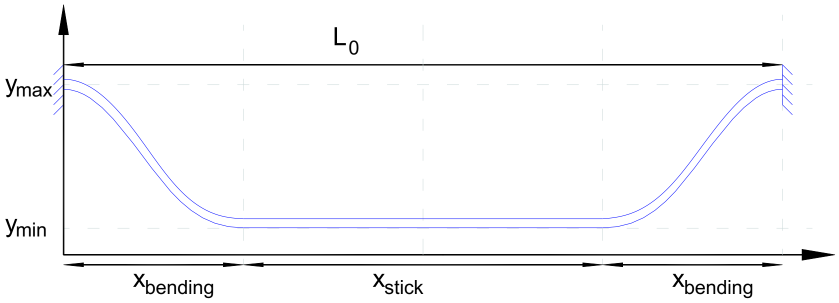

Figure G.2: Pull-in increases the horizontal pull force on the legs.

assuming variables as in Table B.2 and . This result means, that a horizontal force of about $4.3mN$ would be exerted on both legs. From extensive measurements (Chapter 3), we know that the legs cannot sustain such a horizontal force but will start to slip instead.

In reality the situation is even worse, as during pull-in of the plate the center part of the plate is straight on the ground surface (Fig. G.2). In case we consider 50% of the plate touching the surface, then the next equations can be used to determine the axial force:

$$\begin{aligned} y(x) &= d - a(b - x^2)^2 \\ a &= (y_{max} - y_{min})\,/x_{bending}^4 \\ b &= x_{bending}^2 \\ d &= d_0 \\ x_{bending} &= (L_0 - x_{stick})\,/2 \end{aligned}$$

The elongation of the plate would become about 72.6nm, which means a horizontal force of $\approx 8.54mN$ on the legs.

Appendix H

Resonance frequency by the variational method

H.1 Introduction

In this part, the resonance frequency of a plate with standard μWalker dimensions is calculated, assuming a sinusoidal bending shape according to Eq. H.1:

$$w(x) = d_0 \left[1 - \cos\left(\frac{2\pi}{L_{plate}} \right) \right] \tag{H.1}$$

H.2 Maximum velocity

The maximum velocity is calculated like in Eq. 4.27 and is only reviewed here. The assumption is that given that the position in time of one point on the plate (Eq. 4.26), the maximum velocity of that point is reached whenever that point passes the equillibrium, such that:

$$\left. \frac{\partial \hat{w}(x,t)}{\partial t} \right|_{max.vel} = \hat{w}(x) \cdot \omega \quad (\omega = 2\pi f) \ ,$$

with $\hat{w}(x)$ the maximum position off-center of the respective point and ω the angular velocity.

H.3 Kinetic energy

First we calculate the maximum kinetic energy by assuming $\hat{w}(x) = w(x)$:

$$\begin{aligned}
U_{kin} &= \frac{1}{2}\int_{vol.} \rho_{pSi} \left(\frac{\partial \hat{w}(x,t)}{\partial t}\right)^2 \, \mathrm{d}vol. \\
&= \frac{1}{2}\int_0^{L_{plate}} \int_0^{w_{plate}} \int_{-\frac{h_0}{2}}^{\frac{h_0}{2}} \rho_{pSi} \cdot (\hat{w}(x) \cdot \omega)^2 \, \mathrm{d}x \, \mathrm{d}y \, \mathrm{d}z \\
&= \frac{1}{2} \, w_{plate} \, h_{plate} \, \rho_{pSi} \, \omega^2 \int_0^{L_{plate}} \left[1 - \cos\left(\frac{2\pi}{L_{plate}} x\right)\right]^2 \mathrm{d}x \\
&= \frac{1}{2} \, w_{plate} \, h_{plate} \, \rho_{pSi} \, \omega^2 \cdot \left(\frac{3}{2} L_{plate} \, d_0^2\right) \\
U_{kin} &= \frac{3}{4} w_{plate} \, h_{plate} \, L_{plate} \, \rho_{pSi} \, d_0^2 \, \omega^2
\end{aligned}$$

H.4 Potential energy

According to page 71, the curvature κ becomes:

$$\begin{aligned}
\kappa &= \frac{\partial^2 \hat{w}(x,t)}{\partial x^2} \\
&= \frac{4\pi^2}{L_{plate}^2} \cdot \hat{w}(x,t) \; ,
\end{aligned}$$

such that the strain ϵ is:

$$\begin{aligned}
\epsilon &= -z \, \kappa \\
&= -\frac{4\pi^2 z}{L_{plate}^2} \cdot \cos\left(\frac{2\pi}{L_{plate}} x\right)
\end{aligned}$$

The maximum potential energy is reached when the plate is at maximum deflection, or conversely when the velocity of each point on the plate is zero:

$$\begin{aligned}
U_{pot} &= \frac{E_{poly}}{2} \int_0^{L_{plate}} \int_0^{w_{plate}} \int_{-\frac{h_0}{2}}^{\frac{h_0}{2}} \epsilon^2 \mathrm{d}x \mathrm{d}y \mathrm{d}z \\
&= \frac{E_{poly}}{2} \cdot \frac{h_{plate}^3 \, w_{plate}}{12} \int_0^{L_{plate}} \frac{16\pi^4 d_0^2}{L_{plate}^4} \left[\cos\left(\frac{2\pi}{L_{plate}}\right)\right]^2 \mathrm{d}x \\
&= \frac{E_{poly}}{2} \frac{h_{plate}^3 \, w_{plate}}{12} \frac{8\pi^4 \, d_0^2}{L_{plate}^3} \\
U_{pot} &= \frac{1}{3} \frac{E_{poly} \, h_{plate}^3 \, w_{plate} \, \pi^4 \, d_0^2}{L_{plate}^3}
\end{aligned}$$

H.5 The resonance frequency

By reasoning that the maximum kinetic energy and the maximum potential energy are equal while at resonance frequency, which is basically called the Rayleigh-Ritz Method [79], we calculate the corresponding frequency f_{res}:

$$\begin{aligned}
U_{kin} &= U_{pot} \\
\frac{1}{3}\frac{E_{poly}\; h_{plate}^3\; w_{plate}\; \pi^4\; d_0^2}{L_{plate}^3} &= \frac{3}{4} w_{plate}\; h_{plate}\; L_{plate}\; \rho_{pSi}\; d_0^2\; (2\pi\; f_{res})^2 \\
3 f_{res}^2\; \pi^2\; L_{plate}\; \rho_{pSi} &= \frac{1}{3}\frac{E_{poly}\; h_{plate}^2\; \pi^4}{L_{plate}^3} \\
f_{res}^2 &= \frac{1}{9}\frac{E_{poly}\; h_{plate}^2\; \pi^2}{\rho_{pSi}\; L_{plate}^4} \\
f_{res} &= \frac{\pi\; h_{plate}}{3 L_{plate}^2}\sqrt{\frac{E_{poly}}{\rho_{pSi}}} \\
f_{res} &\approx 240694\, Hz
\end{aligned}$$

In conclusion, the resonance frequency is about $241 kHz$ for a plate with sinusoidal shape and standard μWalker dimensions, which is within 2% from the frequency of the polynominal shape proposed in Eq. 4.25, page 70.

Appendix I

20sim implementation of contact friction

```
parameters
real global eps_0;
real global eps_SiNi;
real global d_bumps {m};
real global d_SiNi {m};
variables
real global V_in_R_LEG {V};
real global A_leg;
real global mu_col;
real global mu_stiction;
real global psi_0_stribeck;
real global psi_stiction_coulomb;
real global psi_stribeck_viscous;
real global v_stribeck_coulomb;
real Fn_applied {N};
real v_linear_stiction, v_stiction_stribeck, v_coulomb_viscous;
real hidden xA,xB,xC,xD,yA,yB,yC;
real hidden X[4,4], y[4,1], abcd[4,1];
real hidden M[4,4], p[4,1], klmn[4,1];
real hidden P[4,4], q[4,1], pqrs[4,1];
real friction_state; //variable in order to keep track of friction regimes
real F_coulomb; // Coulomb force, independent of velocity (input)
real F_stiction; // stiction force that is a consequence of a (small enough) velocity
real hidden C {F};
real hidden p_leg; // to regulate the force under pull-in

initialequations//DEFINING FORCES, VELOCITIES AND OTHER VARIABLES
friction_state=0;
v_linear_stiction = psi_0_stribeck * v_stribeck_coulomb;
v_stiction_stribeck = psi_stiction_coulomb * v_stribeck_coulomb;
v_coulomb_viscous = psi_stribeck_viscous * v_stribeck_coulomb;
C = eps_0*A_leg/(d_bumps+d_SiNi/eps_SiNi) ;
xA = v_stiction_stribeck; yA = mu_stiction;
xB = v_stribeck_coulomb;
yB = mu_col;
y  = [yA; yB; 0; 0];
X = [xA^3, xA^2,xA,1; xB^3, xB^2,xB,1;  3*xA^2, 2*xA,1,0;  3*xB^2,2*xB,1,0];
abcd = inverse(X) * y;
xC = -v_stiction_stribeck;
yC = -mu_col;
p  = [yC; yB; 0; 0];
M =  [xC^3, xC^2,xC,1; xB^3, xB^2,xB,1;  3*xC^2, 2*xC,1,0;  3*xB^2,2*xB,1,0];
klmn = inverse(M) * p;
xD = v_linear_stiction;

code
if V_in_R_LEG<10 then p_leg=(V_in_R_LEG/10)^2; else p_leg=1;
end;
Fn_applied =C* V_in_R_LEG^2 / (2* (d_bumps+d_SiNi/eps_SiNi) ) * p_leg;  //capacity is fixed, plate sticks to surface and distance is
constant
F_coulomb = mu_col*Fn_applied; //Coulomb force, where in general 0.1<mu_col<1
F_stiction = mu_stiction*Fn_applied; //Stiction force, where mu_stiction=1 in general
//THIS IS THE FIRST REGIME, (reduces chatter but adds some minor dissipation)
if (abs(p.f)<=abs(v_linear_stiction ))
then p.e = F_stiction * sin(2*pi/(4*xD)*p.f);
Friction_state=1*sign(p.f);
end;
//THE SECOND REGIME IS CONSTANT (stiction)
if  (abs(p.f)>abs(v_linear_stiction) and abs(p.f)<=v_stiction_stribeck)
then p.e = sign(p.f) * F_stiction;    friction_state=2*sign(p.f);
end;
//THE THIRD REGIME DECAYS SMOOTHLY (gives rise to stick-slip)
if (abs(p.f)>v_stiction_stribeck and abs(p.f)<=v_stribeck_coulomb)
then p.e = Fn_applied* (abcd[1,1]*p.f^3 + sign(p.f)*abcd[2,1]*p.f^2 + abcd[3,1]*p.f + sign(p.f)*abcd[4,1]) ;
friction_state=3*sign(p.f);
end;
//THE FOURTH REGIME IS CONSTANT (Coulomb)
if (abs(p.f)>v_stribeck_coulomb and abs(p.f)<=v_coulomb_viscous)
        then p.e= sign(p.f) * F_coulomb;   friction_state=4*sign(p.f);
end;
//THE LAST REGIME IS LINEAR WITH SPEED (viscous friction)
if (abs(p.f)>v_coulomb_viscous)
        then p.e = (2*F_coulomb/v_coulomb_viscous) * p.f - sign(p.f)*F_coulomb;
        friction_state=5*sign(p.f);
end;
```

Figure I.1: 20-Sim code of the Stribeck curve, consisting of five distinct regions in each direction of the velocity.

Appendix J

Process document

Figure J.1 contains the main steps during fabrication. Please recall that a fabrication procedure almost identical to the one below was used earlier by E. Sarajlic [74],[73].

Generally, one starts by choosing heavily boron-doped polysilicon wafers (0.015-0.025Ωcm), which are then coated with a thin silicon nitride layer (steps 1a and 1b). A layer of silicon oxide (the sacrificial layer) is deposited and the positions where the legs will appear, are etched away; then, a second layer of oxide is deposited for ground clearance of the legs (steps 1c/d/e). For the device material, poly silicon is deposited in two sequences, with a burried silicon oxide in between (steps 2a/b/c/d).

In the next three steps (3a/b/c), the silicon nitride trenches used for insulation are formed.

Steps 4a, 5a/b/c produce equidistant holes in the legs and the mid plate, to be able to remove the sacrificial layer in the last step. Moreover, the contour of these holes is enhanced with silicon nitride, which leads to bumps underneath the device components.

In 6a, the nitride layer on the outer part of the wafer is removed, to be able to make contact with the wafer bulk (ground connection). Finally, the sacrificial layer is removed by using a freeze-drying process, so that components do not stick to the surface due to capillary forces of the remaining etchant.

The back side of the wafer needs processing as well, in order to reduce stresses which could lead to bending of the wafer or even cracks at wafer level (Figure J.2). Therefore, step BS_01 removes the nitride layer just added in the step before. In BS_01, the device layer on the back side is removed and in BS_03 the lastly deposed silicon nitride layer is removed. At last, the outer part of the nitride layer can be removed in step BS_02, although this step is not strictly necessary.

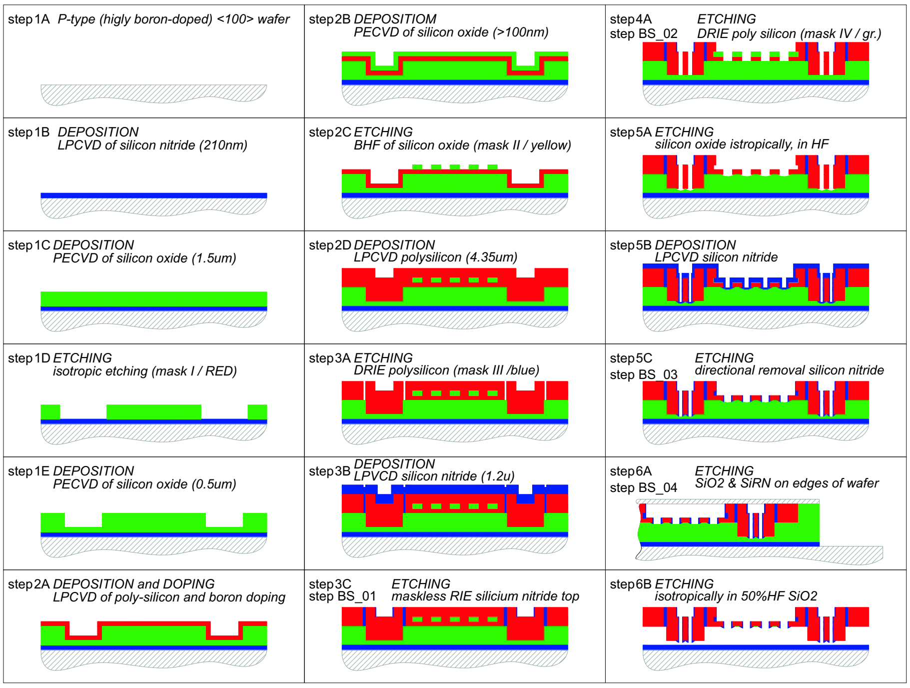

Figure J.1: The basic processing steps of the actuator devices (red=poly silicon, green=silicon oxide, blue=silicon nitride and hatched area = doped silicon bulk). The steps are divided in six parts: 1-walking layer and sacrificial layer deposition; 2-polysilicon (device layer) with burried mask; 3-insulation trenches; 4-bumps extrusion; 5-adding nitride to the extrusions' contours of the bumps; 6-expose bulk potential and release the structures.

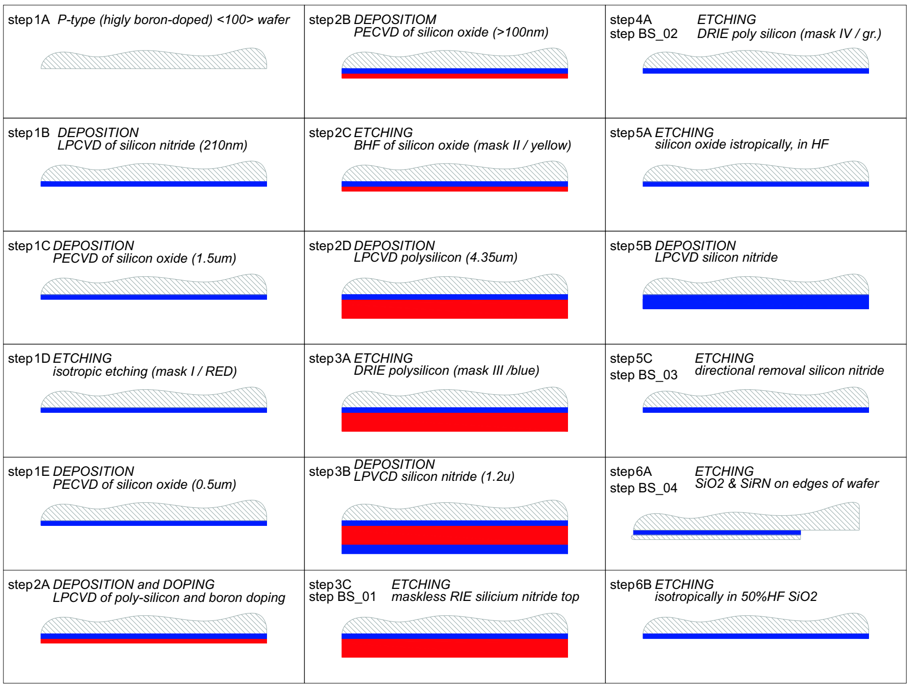

Figure J.2: Processing of the back side of the wafer. Four extra steps are additionally needed (BS_01/02/04/04) to maintain wafer symmetry and thus reduce stress built-up between the front and back part of the wafer.

```
10                                   <<STEP XX>>  refers to fabrication
                                     steps in the accompanying process
                                     layout figure
20  subs008  Substrate selection     <<STEP 1A>> ˜ 7 wafers + 13 dummies;
             Silicon <100> OSP       take LOW resistivity wafers
             (low resist.)           <<STEP 1A>>
30  clean003 Cleaning Standard
40  depo001  LPCVD Si3N4             <<STEP 1B>> 210nm; walking surface;
             stoichiometric          a flush of 2hr (!!) is needed before
                                     starting the deposition;
                                     NO STRANGE PARTICLES ALLOWED!
50  char007  Ellipsometer            dummy 01; investigate surface
             Measurement             flatness and presence of particles
                                     in SiN; VERY IMPORTANT
60  clean003 Cleaning Standard       <<STEP 1C>> 1.55um; 1st part of
70  depo032  PECVD of SiO2 (OXFORD) sacrificial layer; Cap.=850 APC=33
80  char007  Ellipsometer            dummy 02; wafer thickness
             Measurement             measurement
90  clean002 Cleaning short          Optional cleaning
100 anne002  Annealing at 800C     30min
             with N2 for diffusion
             of B or P
110 lith003  Lithography - Priming  <<STEP 1D>>, first mask (III / RED);
              (Gamma 60)             only where the legs will come
120 lith008  Lithography - Coating  4 4k. txt
             Olin907-17 (Gamma 60)
130 lith018  Lithography - Align-
             ment & Exposure Olin
             907-17 (Karl Sss)
140 lith011  Lithography -Develop-
             ment Olin Resist
150 etch024  Etching BHF (1:7) SiO2 stop on SiRN

160 clean003 Cleaning Standard       stripping of F-C (Fluor-Carbon)
170 depo026  Dry Oxidation (DOX)
             at 800C of Silicon
180 depo032  PECVD of SiO2 (OXFORD) <<STEP 1E>> 0.50um
190 char007  Ellipsometer            dummy 03
             Measurement
200 anne008  Annealing at 800C
             with N2 of CVD SiO2
210 clean003 Cleaning Standard       optional
220 char006  Micro Balance           dummy 4; weighting the wafer
             Measurement             before deposition
230 depo005  LPCVD Poly-Silicon-     <<STEP 2A>> 1.15um
             590C
240 char006  Micro Balance           dummy 04;
             Measurement
250 etch027  Etching HF (1%)         120s; on hydrophobic surface
             Native Oxide
260 dopi004  Solid Source            1hr; BE CAREFUL, NOT TOO HIGH
             Diffusion (SSD) of      A CONCENTRATION OF BORON!!
             Boron at 1050C          RIGHT PROCESS? @1050C !!!
270 etch026  Etching BHF (1:7) B2O5 15 min to be sure
```

280	clean003	Cleaning Standard	5 min
290	depo026	Dry Oxidation (DOX) at 800C of Silicon	30 min; transform by-product Si-B into B2O5 and get rid of it
300	etch026	Etching BHF (1:7) B2O5	15 min
310	clean002	Cleaning short	
320	depo032	PECVD of SiO2 (OXFORD)	<<STEP 2B>> burried mask, estimated 200nm; for exact thickness, search selectivity HARS, which will be needed in <<STEP 4A>>; ask Meint
330	char007	Ellipsometer Measurement	dummy 05
340	clean003	Cleaning Standard	OPTIONAL, if you do next step one day later than the former one
350	anne002	Annealing at 800C with N2 for diffusion of B or P	
360	lith003	Lithography - Priming (Gamma 60)	<<STEP 2C>> second mask (IV/yellow); only has plate shapes
370	lith008	Lithography - Coating Olin907-17 (Gamma 60)	
380	lith018	Lithography - Alignment & Exposure Olin 907-17 (K. Sss)	
390	lith011	Lithography - Development Olin Resist	
400	lith009	Lithography - Postbake standard	postbake needed because wet etching will follow
410	etch024	Etching BHF (1:7) SiO2	200nm
420	clean003	Cleaning Standard	
430	etch027	Etching HF (1%) Native Oxide	for polysilicon layer to attach well to underlying (polysilicon / SiO2)
440	char006	Micro Balance Measurement	measure weight before deposing the second polysilicon layer
450	depo005	LPCVD Poly-Silicon - 590C	<<STEP 2D>> 4.35um
460	char006	Micro Balance Measurement	dummy 07
470	etch027	Etching HF (1%) Native Oxide	1.5min
480	dopi004	Solid Source Diffusion (SSD) of Boron @1050C	1050C, 1hr!!
490	etch026	Etching BHF (1:7) B2O5	15 min (instead of 3)
500	clean003	Cleaning Standard	
510	depo026	Dry Oxidation (DOX) at 800C of Silicon	30 min
520	etch026	Etching BHF (1:7) B2O5	15 min
530	clean002	Cleaning short	
540	depo032	PECVD of SiO2 (OXFORD)	capping for uniforming doping
550	char007	Ellipsometer Measurement	dummy 08
560	anne008	Annealing at 800C with N2 of CVD SiO2	Meint?
570	anne006	Annealing at 1100C with N2 for diffusion	3hr, 1100C strip oxide; Meint?

```
             of B or P annealing
             for Silicon-Silicon
             bonding
580 etch024  Etching BHF (1:7) SiO2 capping
590 depo026  Dry Oxidation (DOX) at
             800C of Silicon
600 etch024  Etching BHF (1:7) SiO2
610 clean002 Cleaning short
620 char009  Sheet Resistance       specific values, Meint?
             Measurement
630 lith003  Lithography - Priming  <<STEP 3A>> third mask (I / blue);
             (Gamma 60)             thin, long trenches for SiRN filling
640 lith008  Lithography - Coating
             Olin907-17 (Gamma 60)
650 lith018  Lithography -
             Alignment & Exposure
             Olin 907-17 (K. Sss)
660 lith011  Lithography - Deve-
             lopment Olin Resist
670 etch058  B-HARS-1: High Apect   new process; ask Meint;
             Ratio process for      use dummy 09 to check profile
             Silicon
680 clean003 Cleaning Standard
690 depo026  Dry Oxidation (DOX)    for removal of F-C;
             at 800C of Silicon
700 etch027  Etching HF (1%)        HF dip
             Native Oxide
710 clean003 Cleaning Standard
720 char002  Optical microscopic    measure line width of the trenches
             inspection
730 etch027  Etching HF (1%) Native
             Oxide
740 char006  Micro Balance          dummy 10; measure weight before
             Measurement            deposing the SiRN layer
750 depo002  LPCVD SiRN - low       <<STEP 3B>> deposition time depends
             stress                 on the line width of the trenches
                                    (#char002); MAKE SURE THE TRENCHES
                                    ARE TOTALLY FILLED!
760 char007  Ellipsometer           dummy 10
             Measurement
770 etch019  Plasma etching of      <<STEP 3C>> + <<STEP BS_01>> --->
             Quartz - SF6 (Plasma   BACK SIDE etch away the second SiRN
             Therm)                 layer on the back side
780 clean003 Cleaning Standard
790 lith003  Lithography - Priming  <<STEP 4A>> fourth mask (II / green);
             (Gamma 60)             device masks, shapes of all devices
800 lith008  Lithography - Coating
             Olin907-17 (Gamma 60)
810 lith018  Lithography -
             Alignment & Exposure
             Olin 907-17 (K. Sss)
820 lith011  Lithography - Deve-
             lopment Olin Resist
830 etch058  B-HARS-1: High Apect   dummy 11; new process - ask Meint
```

		Ratio process for Silicon	for etch rate; etching through polysilicon, STOP on SiRN; + <<STEP BS_02>> BACK ETCH ---> remove the polysilicon layer (5.5um) on the back side as well
840	clean003	Cleaning Standard	
850	depo026	Dry Oxidation (DOX) at 800C of Silicon	30min; for removal of FC
860	etch027	Etching HF (1%) Native Oxide	HF dip for removal of by-products
870	clean003	Cleaning Standard	
880	etch024	Etching BHF (1:7) SiO2	<<STEP 5A>> 100nm plate mask (SiO2) must disapppear and bumps shape should be well formed, with bumps height of about 210nm, VERY important! Mink? Meint? Rik?
890	char003	SEM inspection	dummy 12; destructive measurement to see if etching of the bumps is ok
900	clean003	Cleaning Standard	
910	etch027	Etching HF (1%) Native Oxide	
920	depo002	LPCVD SiRN - low stress	<<STEP 5B>> (partially) filling the trenches with nitride; bump height ~210nm; thickness of the nitride layer. Mink, Meint?
930	char007	Ellipsometer Measurement	dummy 13
940	etch019	Plasma etching of Quartz - SF6 (Plasma Therm)	<<STEP 5C>> nitride bumps must be hollow at the center; VERY IMPORTANT Edin? Niels? Mink? + <<STEP BS_03>> BACK ETCH ---> etch some of the SiRn layer, exactly thickness of STEP 5B
950	etch019	Plasma etching of Quartz - SF6 (Plasma Therm)	<<STEP 6A>> remove SiO2 and SiRN on the edges of wafer for electrical connection to bulk; use a smaller wafer (3inch with SiRNi layer) which covers the devices. + <<STEP BS_04>> BACK ETCH ---> back side idem
960	etch024	Etching BHF (1:7) SiO2	<<STEP 6B>> etching away sacrificial layer completely (!) time?? Edin? Mink? Niels? Note: here the wafer remains one piece!
970	etch001	Freeze Drying for Combdrive devices after Sacrificial Layer Etching of SiO2	to prevent stick of suspended parts on the wafer; Note: here the wafer remains one piece! Time? Edin?
980	char003	SEM inspection	1) nice photos of all types of components (1D, 2D, 1d+comb, 1D friction, 2xcomb, etc); 2) mid plate thickness; 3) dimensions (thickness+height) horizontal and vertical retraction springs; 4) distance between mid plate and

	ground; 5) thickness SiN layer under devices 6) shape of trenches SAFE TO DO THIS STEP BEFORE "Freeze Drying" (#970), TO AVOID CHARGING OF SiRN PARTS!
990	END

Bibliography

[1] L. Abelmann, T. Bolhuis, A. M. Hoexum, G. J. M. Krijnen, and J. C. Lodder. Large capacity probe recording using storage robots. *IEE Proc.-Sci. Meas. Technol*, 150(5):218–221, September 2003.

[2] J. R. Banerjee. Dynamic stiffness formulation and its application for a combined beam and a two degree-of-freedom system. *Journal of Vibration and Acoustics*, 125:351–358, 07 2003.

[3] B. Bechevet, Y. Samson, et al. IMST White Paper 2005. January 2005.

[4] W. Benenson, J. W. Harris, H. Stocker, and H. Lutz. *Handbook of Physics*. Springer-Verlag, 2002. ISBN: 0-387-95269-1.

[5] M. Bolks, F. Hanssen, L. Abelmann, P. Havinga, P. Hartel, P. Jansen, C. Lodder, and G. Smit. Micro Scanning Probe Array Memory (uSPAM). *Proceedings of the Second Progress Workshop, Veldhoven, The Netherlands*, pages 17–26, October 2001. ISBN: 90-73461-26-X.

[6] B. Borovic, A. Q. Liu, D. Popa, H. Cai, and F. L. Lewis. Open-loop versus closed-loop control of MEMS devices: choices and issues. *Journal of Micromechanics and Microengineering*, 15:1917–1924, 2005.

[7] P. C. Breedveld. *Physical systems theory in terms of bond graphs*. PhD thesis, 1984. ISBN: 90-900059-4.

[8] P. C. Breedveld. An alternative model for static and dynamic friction in dynamic system simulation. *1st IFAC Conference on Mechatronic Systems*, 2:717–722, September 2000.

[9] P. C. Breedveld. Modeling and simulation of dynamic systems using bond graphs. *Control Systems, Robotics and Automation*, pages 1–36, 2004.

[10] I. N. Bronshtein, K. A. Semendyayev, G. Musiol, and H. Muehlig. *Handbook of Mathematics*. Springer, 2003. ISBN: 3-540-43491-7.

[11] L. F. Byard. Hard disk drive guide: History of the hard disk drive. May 2005.

[12] L. R. Carley, J. A. Bain, G. K. Fedder, D. W. Greve, D. F. Guillou, L. Abelmann, and S. Min. Single-chip computers with microelectromechanical systems-based magnetic memory (invited). *Journal of Applied Physics*, 87(9):6680–6685, 05 2000.

[13] M. P. de Boer, D. L. Luck, W. R. Ashurst, R. Maboudian, A. D. Corwin, J. A. Walraven, and J. M. Redmond. High-performance surface-micromachined inchworm actuator. *Journal of Microelectromechanical Systems*, 13(1):63–74, February 2004.

[14] G. V. Dedkov. Nanotribology: experimental facts and theoretical models. *Uspekhi Fizicheskikh Nauk*, (43):541–572, 2000.

[15] E. Eleftheriou, P. Bächtold, G. Cherubini, A. Dholakia, C. Hagleitneand T. Loeliger, and e.a. A. Pantazi. A nanotechnology-based approach to data storage. *VLDB 2003, Proc.*, 29:3–9, August 2003.

[16] L.-S. Fan, Y.-C. Tai, and R. S. Muller. IC-processed electrostatic micromotors. *Tech. Digest, IEEE Int. Electron Decices Meeting, San Francisco, CA, 1988*, pages 666–669, December 1988.

[17] R. S. Fearing. Survey of sticking effects for micro parts handling. *IEEE/RSJ International Conference on Intelligent Robots and Systems 95. 'Human Robot Interaction an*, 2:212–217, August 1995.

[18] A. Ferreira and J.-G. Fontaine. Optimized friction drive controller for a multi-DOF ultrasonic nanopositioner. *Proceedings of the 2003 IEEE/ASME International Conference on Advanced Intelligent Mechatronics*, pages 1315–1320, 2003.

[19] G. F. Franklin, J. D. Powell, and A. E. Naeïni. *Feedback control of dynamic systems*. 3rd edition, 1994.

[20] L. D. Gabbay, J. E. Mehner, and S. D. Senturia. Computer-aided generation of nonlinear reduced-order dynamic macromodels - I: non-stress-stiffened case. *Journal of Microelectromechanical Systems*, 9(2):262–269, June 2000.

[21] J. M. Gere. *Mechanics of materials*. Nelson Thornes, 5th si edition edition, 2002. ISBN 0-7487-6675-8.

[22] H. Goldstein. The race to the bottom. *Spectrum*, pages 26–33, March 2005.

[23] H. W. Guggenheimer. *Differential Geometry*. McGraw-Hill, New York, 1963.

[24] L. Guo and M. Tomizuka. High-speed and high-precision motion control with an optimal hybrid feedforward controller. *IEEE/ASME Transactions on mechatronics*, 2(2):110–122, June 1997.

[25] B. A. H˙ A survey of models, analysis tools and compensation methods for the control of machines with friction. *Automatica*, 30(7):1083–1138, 1994.

[26] E. Hecht. *Optics*. Addison Wesley, 4th edition, 2002. ISBN: 0-8053-8566-5.

[27] G. K. Ho, R. Abdolvan, and F. Ayazi. Through-support-coupled micromechanical filter array. *17th IEEE Int. Conf. on MEMS*, pages 769–772, 2004.

[28] D. A. Horsley, R. Horowithz, and A. P. Pisano. Microfabricated electrostatic actuators for hard disk drives. *IEEE/ASME Transactions on mechatronics*, 3(3):175–183, September 1998.

[29] E. S. Hung and S. D. Senturia. Extending the travel range of analog-tuned electrostatic actuators. *Journal of Microelectromechanical Systems*, 8(4):497–505, December 1999.

[30] T. Iizuka and H. Fujita. Fabrication of electrostatic micro-actuators for a hard disk drive application. *Journal of Micromechatronics*, 2(1):47–64, 2003.

[31] J. D. Jacobson, S. H. Goodwin-Johansson, S. M. Bobbio, C. A. Bartlett, and L. N. Yadon. Integrated force arrays: theory and modeling of static operation. *Journal of Mecroelectromechanical Systems*, 4(3):139–150, September 1995.

[32] H. V. Jansen, N. R. Tas, and J. W. Berenschot. MEMS-based nanotechnology. *Encyclopedia of Nanoscience and nanotechnology*, 5:163–275, 2004.

[33] D. Karnopp. Computer simulation of stick-slip friction in mechanical dynamic systems. *Transactions of the ASME*, 107, 1985.

[34] F. H. Kreuger. *Industrial High Voltage*. Delft University Press, 1991. ISBN: 90-6275-561-5.

[35] A. A. Kuijpers. *Micromachined capacitive long-range displacement sensor for nano-positioning of microactuator systems*. PhD thesis, University of Twente, The Netherlands, 2004. ISBN: 90-365-2119-X.

[36] T. Lamminmäki, K. Ruokonen, I. Tittonen, T. Mattila, I. Jaakkola, A. Oja, H. Seppä, P. Seppälä, and J. Kiihamäki. Electromechanical analysis of micromechanical SOI-fabricated RF resonators. *Technical Proceedings of the 2000 International Conference on Modeling and Simulation of Microsystem*, pages 217–220, 2000. ISBN: 0-9666135-7-0.

[37] V. Lampaert, F. Al-Bender, and J. Swevers. A generalized Maxwell-slip friction model appropriate for control purposes. page 8 pages.

[38] A. J. le Fèbre, J. C. Lodder, and L. Abelmann. Tip-sample distance control for magnetic probe recording. *Proceedings of IMST2006*, 05 2006. Accepted for publication.

[39] Y. Li and R. Horowitz. Mechatronics of electrostatic microactuators for computer disk drive dual-stage servo systems. *IEEE/ASME Transactions on mechatronics*, 6(2):111–121, June 2001.

[40] N. E. Ligterink, M. Patrascu, P. C. Breedveld, and S. Stramigioli. An energy-based electroelastic beam model for MEMS applications. *Sensors and Actuators A: Physical*, 121(2):500–507, June 2005.

[41] M. S.-C. Lu and G. K. Fedder. Position control of parallel-plate microactuators for probe-based data storage. *Journal of Microelectromechanical Systems*, 13(5):759–769, October 2004.

[42] Y. Lu. Patterned PMMA media for MEMS XY micro-stage in probe storage. *Proc. 2nd Int. Conf. Technological Advances of Thin Films and Surface Coating, Singapore, 13-17 July*, 2004.

[43] M. J. Madou. *Fundamentals of Microfabrication*. CRC Press, 2nd edition, 2002. ISBN: 0-8493-0826-7.

[44] H. J. Mamin, R. P. Ried, B. D. Terris, and D. Rugar. High-density data storage based on the atomic force microscope. *Proceedings of the IEEE*, 87(6):1014–1027, June 1999.

[45] J. E. Mehner, L. D. Gabbay, and S. D. Senturia. Computer-aided generation of nonlinear reduced-order dynamica macromodels - II: stress-stiffened case. *Journal of Microelectromechanical Systems*, 9:270–278, June 2000.

[46] J. Q. Mou. Compact electrostatic XY micro-stage for probe data storage. *Digest of ASME Info. Storage and Proc. Systems conference, Santa Clara, CA, 14-16 June*, 2004.

[47] R Murillo, H. A. van Wolferen, L. Abelmann, and J. C. Lodder. Fabrication of patterned magnetic nanodots by laser interference lithography. *Journal of Microelectronic Engineering*, 78:260–265, 2005.

[48] Y. Nemirovsky and O. Bochobza-Degani. A methodology and model for the pull-in parameteres of electrostatic actuators. *Journal of Microelectromechanical Systems*, 10(4):601–615, December 2001.

[49] online: http://www.hp.com/hpinfo/abouthp/iplicensing/ars.html. ARS program at Hewlett-Packard.

[50] G. Otten, T. J. A. de Vries, J. van Amerongen, A. M. Rankers, and E. W. Gaal. Linear motor motion control using a learning feedforward controller. *IEEE/ASME Transactions on mechatronics*, 2(3):179–187, September 1997.

[51] D. Paci, K.-U. Kirstein, C. Vancura, J. Lichtenberg, and H. Baltes. A behavioural model of resonant cantilevers for chemical sensing. *Analog Integrated Circuits and Signal Processing*, 44(2):7 pages, August 2005. ISSN: 0925-1030.

[52] A. Pantazi, M. A. Lantz, G. Cherubini, H. Pozidis, and E. Eleftheriou. A servomechanism for a micro-electromechanical-system-based scanning-probe data storage device. *Nanotechnology*, 15:612–621, 2004.

[53] M. Patrascu, L. Abelmann, G. J. M. Krijnen, and S. Stramigioli. Opslagmedia voor toekomstige mobiele toepassingen. *Agroinformatica*, 19(3), September 2006.

[54] M. Patrascu, L. Abelmann, and S. Stramigioli. Modeling and control of the uWalker, a MEMS micro stepper for data storage. *IEEE Trans. on Control Systems Technology*, 2006. Submitted.

[55] M. Patrascu, M. Lootsma, M. de Boer, G. J. M. Krijnen, and S. Stramigioli. Nanometer range closed-loop control of a microWalker for probe storage. *IEEE MEMS*, 2007. Submitted.

[56] M. Patrascu and S. Stramigioli. Physical modelling of the uWalker, a MEMS linear stepper actuator. *SYROCO 2006*, 11 2005. Submitted.

[57] M. Patrascu and S. Stramigioli. Stick-slip actuation of electrostatic stepper micropositioners for data storage- the uWalker. *ICMENS*, July 2005.

[58] M. Patrascu and S. Stramigioli. Characterization of stiction effects of an electrostatic micro positioner for probe storage. *Journal of Physics: Conference Series, Institute of Physics (IOP)*, 34:818–823, 2006. online: http://www.iop.org/EJ/abstract/1742-6596/34/1/135.

[59] M. Patrascu and S. Stramigioli. Electrostatic micro-actuators for probe storage. *Proceedings of PPTC2006*, 2006. Submitted.

[60] M. Patrascu and S. Stramigioli. Modeling and simulating the stick-slip motion of the uWalker, a MEMS-based device for uSPAM. *Microsystem Technologies*, (161):1432–1858, June 2006.

[61] M. Patrascu, S. Stramigioli, G. Krijnen, and E. Sarajlic. Modeling and characterization of the uWalker, a MEMS positioner for uSPAM. *International Probe Storage Workshop III*, February 2005.

[62] M. Patrascu, S. Stramigioli, and J. van Amerongen. Modeling, design and control of the uWalker, a MEMS-based storage medium for uSPAM. *IMST*, pages 1–2, 2004. abstract.

[63] M. Patrascu, S. Stramigioli, and J. van Amerongen. MEMS-fabricated actuators for data storage - from physical modeling to control. *Fysica 2006*, April 2006. Poster.

[64] J. A. Pelesko and D. H. Bernstein. *Modeling MEMS and NEMS*. Chapman & Hall/CRC, 2003. ISBN: 1-58488-306-5.

[65] K. J. Åström. Control of systems with friction.

[66] D. Ratner and M. A. Ratner. *Nanotechnology and homeland security*. Prentice Hall, 2nd printing edition, 2004. ISBN 0-13-145307-6.

[67] J. W. S. Rayleigh. *The theory of sound*, volume 1. Dover, 2nd edition, 1945. ISBN: 486-60292-2.

[68] K. J. Rebello. Applications of MEMS in Surgery. *Proceedings of the IEEE*, 92(1):43–55, 01 2004. Invited paper.

[69] K. F. Riley, M. P. Hobson, and S. J. Bence. *Mathematical methods for physics and engineering*. Cambridge University Press, 2003. ISBN: 0 521 89067 5.

[70] D. Litvinov S. Khizroev. Perpendicular Magnetic Recording. January 2004. ISBN: 1402026625, 174 pages.

[71] H. Saito, A. G. van den Bos, L. Abelmann, and J. C. Lodder. High-resolution MFM: simulation of tip sharpening. *IEEE Trans. Magn.*, 39(5):3447–3449, 2003.

[72] J. Samitier, A. Errachid, and G. Gomila. Nanoelectromechanical systems. *Encyclopedia of Nanoscience and nanotechnology*, 6:643–663, 2004.

[73] E. Sarajlic. *Electrostatic microactuators fabricated by vertical trench isolation technology*. PhD thesis, University of Twente, The Netherlands, 2005. ISBN: 90-365-2212-9.

[74] E. Sarajlic, E. Berenschot, H. Fujita, G. Krijnen, and M. Elwenspoek. Bidirectional electrostatic linear shuffle motor with two degrees of freedom. *MEMS 2005 - 18th IEEE International Conference on Micro Electro Mechanical Systems, Miami*, pages 391–394, January 2005.

[75] E. Sarajlic, E. Berenschot, N. Tas, H. Fujita, G. Krijnen, and M. Elwenspoek. High performance bidirectional electrostatic inchworm motor fabricated by trench isolation technology. *TRANSDUCERS 05 - Int. Conf. on Solid State Sensors and Actuators - Seoul, Korea*, June 2005.

[76] S. W. Schlosser. *Using MEMS-based storage devices in computer systems*. PhD thesis, 05 2004. PhD Thesis.

[77] J. S. Schmidt, R. Knobel, D. R. Schmidt, C. S. Yung, and A. N. Cleland. Nanoelectronic and nanomechanical systems. *Proc. SPIE*, 4591:11–21, November 2001.

[78] S. D. Senturia. Simulation and design of microsystems: a 10-year perspective. *Sensors and Actuators A*, 67:1–7, 1998.

[79] S. D. Senturia. *Microsystem Design*. Kluwer Academic Publishers, 2001. ISBN 0-7923-7246-8.

[80] P. G. Slade and E. D. Taylor. Electrical breakdown in atmospheric air between closely spaced (0.2um-4u m) electrical contacts. *IEEE Transactions on Components and Packaging Technologies*, 25(3):390–396, September 2002.

[81] J. J. Slotine and W. Li. *Applied nonlinear control*. Prentice Hall. ISBN: 0-13-040890-5.

[82] Online staff. CE Growth Supercharging MEMs Market. August 2005.

[83] N. Tas, T. Sonnenberg, H. Jansen, R. Legtenberg, and M. Elwespoek. Stiction in surface micromachining. *Journal of Micromechanics and Microengineering*, pages 385–397, 1996.

[84] N. Tas, J. Wissink, L. Sander, T. Lammerink, and M. Elwenspoek. Modeling, design and testing of the electrostatic shuffle motor. *Sensors and Actuators A*, 70:171–178, 1998.

[85] N. Tas, J. Wissink, L. Sander, T. Lammerink, and M. Elwenspoek. Modeling, design and testing of the electrostatic shuffle motor. *Sensors and Actuators A*, pages 171–178, 1998.

[86] N. R. Tas. *Electrostatic micro walkers*. PhD thesis, University of Twente, The Netherlands, 2000. ISBN: 90-365-1435-5.

[87] S. Timoshenko, D. H. Young, and W. Weaver Jr. *Vibration problems in engineering*. Wiley, 4th edition, 1974. ISBN: 0-471-87315-2.

[88] M. Treder. Accelerating Paradigm Sifts in Information Storage and Retrieval. *Extropy - Journal of Transhumanist solutions*, September 2002.

[89] W. S. N. Trimmer. Microrobots and micromechanical systems. *Sensors and Actuators*, 19(3):267–287, September 1989.

[90] J. van Amerongen and P. Breedveld. Modelling of physical systems for the design and control of mechatronic systems. *Annual Reviews in Control*, 27:87–117, 2003.

[91] A. van Beek. *Machine lifetime performance and reliability*. 2004. ISBN: 90-3700-208-0.

[92] A. G. van den Bos. *CantiClever - Planar fabrication of probes for magnetic imaging*. PhD thesis, 2003. ISBN: 90-365-1988-8.

[93] A. G. van den Bos, I. R. Heskamp, M. H. Siekman, L. Abelmann, and J. C. Lodder. The CantiClever: a dedicated probe for magnetic force microscopy. *IEEE Trans. Magn.*, 38(5):2441–2443, 2002.

[94] A. G. van den Bos, A. C. J. van Dijk, I. R. Heskamp, L. Abelmann, and J. C. Lodder. A new concept in magnetic force microscope cantilevers. *Magnetic Storage Systems Beyond 2000, NATO Science Series 2: Mathematics, Physics and Chemistry*, 41:307–312, 2001.

[95] M. van Drogen. *The transition to adhesive wear of lubricated concentrated contacts*. PhD thesis, 2005. ISBN: 90-365-2286-2.

[96] S. Vanapalli. Techniques for characterization of in-plane displacement for microactuators. Master's thesis, Department of Electrical Engineering, University of Twente, The Netherlands, 2004.

[97] P. Vettiger, G. Cross, M. Despont, U. Drechsler, U. Dürig, B. Gotsmann, W. Häberle, and M. A. Lantz e.a. The "Millipede" - nanotechnology entering data storage. *IEEE Trans. Nanotechnol.*, 1:39–55, 2002.

[98] M. Vincken and M. Patrascu. Micromotor voor een nieuw type geheugen. *Bits-n-Chips*, (14), September 2006.

[99] K. Wang, Y. Yu, A.-C. Wong, and C. T.-C. Nguyen. VHF free-free beam high-Q micromechanical resonators. *Technical Digest, 12th International IEEE Micro Electro Mechanical Systems Conference*, pages 453–458, January 1999.

[100] S. Zappe, M. Baltzer, Th. Kraus, and E. Obermeier. Electrostatically driven linear micro-actuators: FE analysis and fabrication. *J. Micromech. Microeng.*, 7:204–209, 04 1997.